19 Higgs Bosons

19.1 Introduction

The experimental observation of one or several Higgs bosons [19-1] will be fundamental for a better understanding of the mechanism of electroweak symmetry-breaking. In the Standard Model [19-2], one doublet of scalar fields is assumed, leading to the existence of one neutral scalar particle H. On the basis of present theoretical knowledge, the Higgs sector in the Standard Model remains largely unconstrained. The Higgs-boson mass, m_H, is not theoretically predicted. From unitarity arguments an upper limit of ~1 TeV can be derived [19-3]. The requirements of the stability of the electroweak vacuum and the perturbative validity of the Standard Model allow to set upper and lower bounds depending on the cutoff value chosen for the energy scale Λ up to which the Standard Model is assumed to be valid [19-4]. Such analyses exist at the two-loop level for both lower [19-5] and upper [19-6] Higgs mass bounds. If the cutoff value is chosen at the Planck mass, which means that no new physics appears up to that scale, the Higgs-boson mass is required to be in the range between $130 < m_H < 190$ GeV. This bound becomes weaker if new physics appears at lower mass scales. If the cutoff is chosen to be 1 TeV, the Higgs-boson mass is constrained to be in the range $50\ \text{GeV} < m_H < 800$ GeV. Experimentally, constraints on the Standard Model Higgs-boson mass are derived directly from searches at LEP2, which presently lead to $m_H > 90$ GeV [19-7]. It is expected that the sensitivity of LEP2 will be extended to ~105 GeV over the coming years [19-8], if the centre of mass energy of the LEP collider is raised to 200 GeV. Indirectly, high precision electroweak data constrain the Higgs-boson mass via their sensitivity to loop corrections. Assuming the overall validity of the Standard Model, a global fit to all electroweak data leads to $m_H = 76^{+85}_{-47}$ GeV [19-9].

In supersymmetric theories, the Higgs sector is extended to contain at least two doublets of scalar fields. In the minimal version, the so-called MSSM model [19-10], there are five physical Higgs particles: two *CP*-even Higgs bosons h and H, one *CP*-odd Higgs boson A, and two charged Higgs bosons $H^{\pm}$. Two parameters, which are generally chosen to be m_A and $\tan\beta$, the ratio between the vacuum expectation values of the two Higgs doublets, determine the structure of the Higgs sector at tree level. However, large radiative corrections affect the Higgs masses and couplings. The lightest neutral scalar Higgs-boson mass, m_h, is theoretically constrained to be smaller than ~150 GeV [19-11].

Alternative manifestations of electroweak symmetry-breaking mechanisms would probably involve a strongly interacting electroweak sector [19-12]. In this case, significant deviations from the Standard Model predictions would be observable in final states consisting of gauge boson pairs.

The aim of this Chapter is to review and assess the performance of the ATLAS detector in the search for a Standard Model Higgs boson, for the various supersymmetric Higgs bosons, and for alternative signals of electroweak symmetry breaking. Many results are based on studies which have been presented in earlier documents [19-13][19-14][19-15][19-16]. The main differences with respect to previous studies are:

- The significance of a Higgs discovery is evaluated for the final ATLAS detector configuration, as presented in the various Technical Design Reports.
- Improvements on theoretical calculations of cross-sections, branching ratios *etc*., which have appeared since the Technical Proposal, are taken into account.

- The study of the MSSM Higgs sector is extended by several channels, which had not been considered in the Technical Proposal. In addition, cases where SUSY particles are light and appear in Higgs decays and cases where Higgs bosons are produced in decays of SUSY particles are considered in some detail here.
- Finally, it is discussed how accurately Higgs boson parameters, such as mass, width, spin, and couplings to fermions and bosons, can be measured in the ATLAS detector.

The results presented in this Chapter are obtained predominantly from fast detector simulations [19-17] (see Section 2.5), where the detector response and resolution functions have been taken into account. However, the crucial detector-dependent performance parameters such as the mass resolutions, reconstruction and identification efficiencies for the signal events and the most important background rejections, were obtained from a detailed GEANT simulation of the ATLAS detector. Many of them have already been presented in the corresponding performance chapters of this document. Wherever relevant, they have been used for the evaluation of the signal significance.

Physics processes have been simulated with the PYTHIA Monte Carlo program, including initial- and final-state radiation, hadronisation and decays. The signal and background production cross-sections are affected by uncertainties due to higher-order corrections, structure function parametrisations and event generation. Over the recent years, there has been considerable progress in the calculation of higher-order QCD corrections to the cross-sections for the Higgs-boson production [19-18]. However, the higher-order QCD corrections to the production cross-sections are not known for all signal and background processes. Therefore, the present Higgs studies have consistently and conservatively refrained from using *K*-factors, resorting to Born-level predictions for both signal and backgrounds.

This Chapter begins with a discussion of the discovery potential of the ATLAS detector for the Standard Model Higgs boson (Section 19.2), followed by the discussion of the Higgs boson searches in the MSSM (Section 19.3). Searches in the framework of a strongly interacting Higgs sector are described in Section 19.4. A short summary and conclusions are given in Section 19.5.

19.2 Standard Model Higgs boson

19.2.1 Introduction

In this Section, the expected performance in the search for the Standard Model Higgs boson with ATLAS is discussed over the mass range from 80 GeV to 1000 GeV. Although the present LEP2 mass limit for a Standard Model Higgs boson is already higher than 90 GeV [19-7], masses as low as 80 GeV have been considered in the studies reported here in order to assess the detection capabilities in these difficult conditions. Such low masses remain relevant in some regions of the MSSM parameter space, where the same final state topologies from Higgs boson decays occur as in the Standard Model case. The Standard Model Higgs boson is searched for at the LHC in various decay channels, the choice of which is given by the signal rates and the signal-to-background ratios in the various mass regions.

These channels are:

- $H \rightarrow \gamma\gamma$ direct production;
- $H \rightarrow \gamma\gamma$ from the associated production WH, ZH and $t\bar{t}H$, using a lepton (e, μ) tag from the vector boson or top quark decay;
- $H \rightarrow b\bar{b}$ from the associated production WH, ZH and $t\bar{t}H$, using a lepton (e, μ) tag and b-tagging;
- $H \rightarrow ZZ^* \rightarrow 4l$;
- $H \rightarrow ZZ \rightarrow 4l$ and $H \rightarrow ZZ \rightarrow llν\nu$;
- $H \rightarrow WW \rightarrow lνjj$ and $H \rightarrow ZZ \rightarrow lljj$.

The search strategies and background rejection methods have been established through many studies over the past years. In addition to the well established channels listed above, the discovery potential is also reported for less promising channels, such as $H \rightarrow Z\gamma$. The associated production of a Higgs boson with QCD jets, where the Higgs boson decays to $\gamma\gamma$, has been also investigated. In addition, the discovery potential of the Higgs boson in the recently suggested $H \rightarrow WW^* \rightarrow lνlν$ channel [19-19] has been studied.

The total Higgs-boson production cross-section has contributions from various subprocesses, of which gg fusion and WW fusion are the most important ones. The WW fusion process is significant only in the high-mass region. The processes of $q\bar{q}$ and ZZ fusion also contribute to the total cross-section. For all Higgs studies reported here, the CTEQ2L structure function parametrisation has been used. The variation in the cross-section has been estimated [19-15] using four different sets of structure function parametrisations (namely the CTEQ2L, CTEQ2MS, CTEQ2M and MRSD sets); in the low-mass region ($m_H < 180$ GeV), a spread of only ~5% in the Higgs-boson production rates has been found. The decay branching ratios have been calculated using the program of Ref. [19-20], which includes all higher-order corrections presently available.

19.2.2 $H \rightarrow \gamma\gamma$

The decay $H \rightarrow \gamma\gamma$ is a rare decay mode, only observable over a limited Higgs boson mass region, where the production cross-section and the decay branching ratio are both relatively large. It is a promising channel for Higgs searches in the mass range $100 < m_H < 150$ GeV and places severe requirements on the performance of the EM Calorimeter. Excellent energy and angular resolution are needed to observe the narrow mass peak above the irreducible prompt $\gamma\gamma$ continuum. Powerful particle identification capability is also required to reject the large QCD jet background as well as the potentially dangerous resonant background from $Z \rightarrow ee$ decays, in the case where $m_H \approx m_Z$.

In the following, the search for $H \rightarrow \gamma\gamma$ decays is described separately for direct production of the Higgs boson (Section 19.2.2.1), for associated production of a Higgs boson with a W or Z boson or a $t\bar{t}$ pair (Section 19.2.2.2), and for production of a Higgs boson in association with QCD jets (Section 19.2.2.3). In each case, the signal reconstruction, the reducible and irreducible backgrounds and the signal observability are discussed.

19.2.2.1 Direct production

The direct production of a low-mass Higgs boson is dominated by the *gg* fusion process. The production cross-sections and the branching ratios for the $H \rightarrow \gamma\gamma$ decay are listed in Table 19-1 for $80 < m_H < 150$ GeV.

Signal Reconstruction

Very detailed and complete simulations have been performed to evaluate the reconstruction of photons in the ATLAS detector [19-21]. In the simulations done for this TDR, the most relevant changes and up-to-date details of the Inner Detector and of the calorimeters (*e.g.* the barrel cryostat) have been included. The impact of photon conversions on the mass resolution and on the signal reconstruction efficiency has thus been realistically evaluated.

Isolated photons have been reconstructed by applying the standard photon identification criteria, as described in Section 7.5.1. Both unconverted and converted photons have been used and the electromagnetic shower energy has been reconstructed using the procedures described in Chapter 7. The photon identification efficiency has been found to be 80%, approximately independent of p_T in the region of interest.

Simple kinematic cuts, which optimise approximately the significance of the $H \rightarrow \gamma\gamma$ signal over the mass range considered, have been applied:

- The photon candidates, ordered in p_T, were required to have transverse momenta in excess of 40 and 25 GeV ($p_T^1 > 40$ GeV and $p_T^2 > 25$ GeV).
- Both photon candidates were required to be in the pseudorapidity interval $|\eta| < 2.4$. Events with one or more photons in the region of the electromagnetic barrel/end-cap transition in an interval of $\Delta\eta = 0.15$, were rejected.

The acceptance of these kinematic cuts increases with m_H and ranges from 29% for $m_H = 80$ GeV to 58% for $m_H = 150$ GeV. It should be noted that, in comparison to the study presented in [19-14], the cut on the p_T-balance between the two photons has been removed [19-22]. This increases the signal acceptance by ~16% and the irreducible background by ~9%. The acceptance of the kinematic cuts is given in Table 19-1 as a function of m_H. In order to compute signal event rates, these numbers still have to be multiplied by the photon reconstruction efficiency. For $m_H = 90$ GeV, the photon reconstruction efficiency is somewhat lower than the nominal 80% because of the stringent cuts applied to remove the background from $Z \rightarrow ee$ decays (see the discussion of the $Z \rightarrow ee$ background below).

Table 19-1 Cross-sections (σ), branching ratios (BR), cross-sections times branching ratios ($\sigma \times$ BR), acceptances and expected mass resolutions at high luminosity for $H \rightarrow \gamma\gamma$ decays as a function of m_H.

Higgs mass (GeV)	80	90	100	110	120	130	140	150
Cross-section (pb)	38.4	32.4	27.8	24.2	21.2	18.8	17.0	15.4
Branching ratio (%)	0.089	0.119	0.153	0.190	0.219	0.222	0.193	0.138
$\sigma \times$ BR (fb)	34.2	38.6	42.5	46.0	46.4	41.8	32.8	21.2
Acceptance	0.29	0.38	0.44	0.48	0.51	0.53	0.55	0.58
Mass resolution (GeV)	1.11	1.20	1.31	1.37	1.43	1.55	1.66	1.74

The invariant mass of the two photons is reconstructed using the combined information of the EM Calorimeter and the Inner Detector, as discussed in Section 7.8.1.

An example of a reconstructed Higgs mass distribution, obtained after applying the kinematic and photon identification cuts as well as the photon conversion and primary vertex reconstruction algorithms, is shown in Figure 19-1. It has been obtained from a fully simulated sample of $H \rightarrow \gamma\gamma$ decays with m_H = 100 GeV, including the minimum-bias pile-up expected at high luminosity. The overall mass resolution, σ, is found to be 1.31 GeV. The various contributions to the total mass resolution are discussed in detail in Section 7.8.1. The interval of $\pm 1.4\sigma$ around the nominal Higgs mass, which is used for the evaluation of the signal significance, contains 79% of the fully simulated $H \rightarrow \gamma\gamma$ events. For a Gaussian distribution, this fraction is expected to be 83.8%. At low luminosity, the $\gamma\gamma$ mass resolution can be improved, since the pile-up contribution to the energy resolution of the calorimeter is largely reduced and the vertex can be reconstructed from the associated tracks. For example, for m_H = 100 GeV the mass resolution improves from 1.31 GeV to 1.10 GeV.

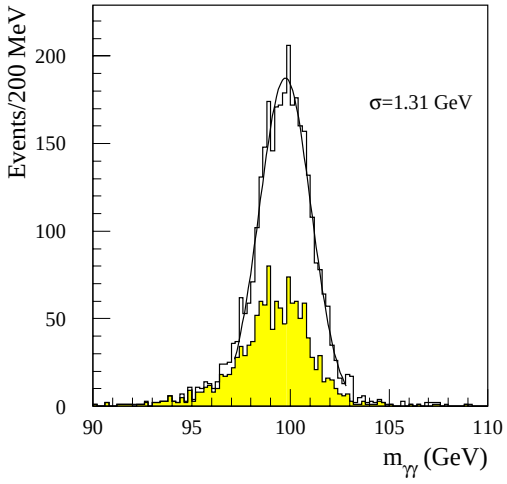

Figure 19-1 Reconstructed two-photon invariant mass for $H \rightarrow \gamma\gamma$ decays with m_H = 100 GeV at high luminosity. The shaded histogram represents events containing at least one converted photon.

Irreducible background

The irreducible background consists of genuine photon pairs produced via the following three processes: Born ($q\bar{q} \rightarrow \gamma\gamma$), box ($gg \rightarrow \gamma\gamma$), and quark bremsstrahlung ($qg \rightarrow q\gamma \rightarrow q\gamma\gamma$). The production cross-section for the sum of the Born and box processes is of the order of 1 pb / GeV in the two-photon mass range around 100 GeV. In the bremsstrahlung process, only the small fraction of events with isolated photons in the final state pass the selection criteria. It has been demonstrated [19-23] that their contribution, as generated using PYTHIA, is in good agreement with semi-analytical calculations [19-24]. After isolation cuts, this background amounts to about 50% of the combined Born plus box contribution, and has been included in the simulations by correspondingly scaling these backgrounds. The expected numbers of $\gamma\gamma$ background events in the relevant mass windows are given in Table 19-2.

Reducible background

In addition to the irreducible $\gamma\gamma$ background, other potentially large background sources have to be considered. These include jet-jet and γ-jet events in which one or both jets are misidentified as photons, as well as $Z \rightarrow ee$ decays, where both electrons are mistaken as photons. Since the production cross-sections for these processes are many orders of magnitude larger than the signal cross-sections, excellent photon / jet and photon / electron discrimination are required.

For pairs of calorimeter clusters which pass the kinematic cuts and have an invariant mass in the range from 70 GeV to 170 GeV, the ratios of the jet-jet and γ-jet cross-sections to the irreducible $\gamma\gamma$ cross-section are 2×10^6 and 8×10^2 respectively. There are large uncertainties on these ratios and on the fraction of jets which are expected to satisfy the photon identification criteria, arising

from higher-order corrections and from uncertainties in jet fragmentation. In order to reduce these backgrounds to a level well below that of the irreducible $\gamma\gamma$ continuum, rejection factors of $2\text{x}10^7$ and $8\text{x}10^3$ are required.

These rejection factors have been realistically evaluated by using large samples of fully simulated two-jet events, as described in Section 7.6. The rejection factors were then applied to estimate the cross-sections for the reducible jet-jet and γ-jet backgrounds relative to the irreducible $\gamma\gamma$-background. The results are shown in Figure 19-2 as a function of the two-photon invariant mass $m_{\gamma\gamma}$. After applying the full photon identification cuts from the calorimeter and the Inner Detector, the residual jet-jet and γ-jet backgrounds are found to be at the level of approximately 15% and 20%, respectively, of the irreducible $\gamma\gamma$ background over the mass range relevant to the $H \rightarrow \gamma\gamma$ search.

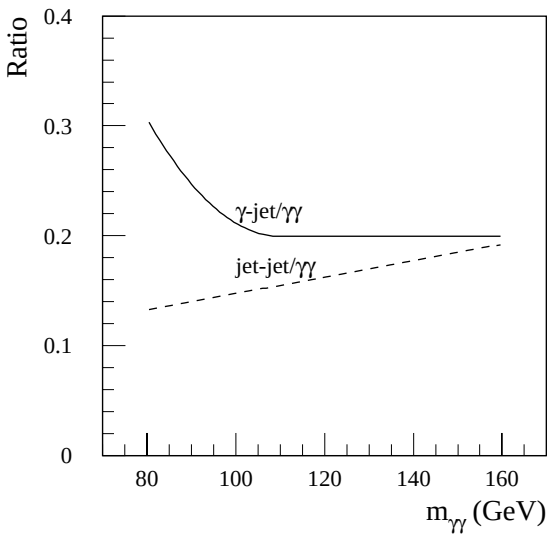

Figure 19-2 Expected ratios of the residual reducible jet-jet and γ-jet backgrounds to the irreducible $\gamma\gamma$-continuum background as a function of the invariant mass of the pair of photon candidates at high luminosity.

$Z \rightarrow ee$ background

For Higgs boson masses close to m_Z, the resonant background from $Z \rightarrow ee$ decays is potentially very dangerous. This background has a production cross-section roughly 25 000 times larger than that of the $H \rightarrow \gamma\gamma$ signal. Therefore, a rejection of ~ 500 per electron is needed to reduce it to a level below 10% of the expected $H \rightarrow \gamma\gamma$ signal. This requires that the Inner Detector vetoes electron tracks with very high efficiency.

Two classes of Z-decays have been studied with particular care in order to evaluate the expected veto efficiency. The first class consists of $Z \rightarrow ee$ (or $\mu\mu$) radiative decays with one or two photons in the final state. A careful study of these decays, which included initial- and final-state photon radiation [19-25], has shown that they produce final states for which the invariant mass of the $\gamma\gamma$ (or γe pair) is no longer resonant, as shown by the dashed histogram in Figure 19-3. If an electron veto efficiency of 99.8% is assumed, approximately equal contributions from $\gamma\gamma$ and γe radiative pairs are found. The contribution from $Z \rightarrow \mu\mu\gamma\gamma$ decays corresponds to about 20% of the total contribution from $Z \rightarrow ee$ radiative decays. Since the Z radiative decay background is smooth above 80 GeV, and is much smaller than the irreducible $\gamma\gamma$ background, it can be neglected.

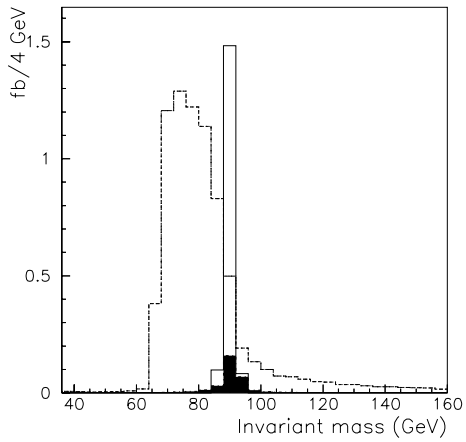

Figure 19-3 Reconstructed two-photon invariant mass for $H \rightarrow \gamma\gamma$ decays with m_H = 90 GeV (full histogram), for $Z \rightarrow ee\gamma$ (γ) and $Z \rightarrow \mu\mu\gamma\gamma$ decays (dashed histogram) and for $Z \rightarrow ee$ decays (black area) after electron veto cuts.

The second class of background from $Z \rightarrow ee$ decays consists of events where both electrons are misidentified as photons after undergoing very hard bremsstrahlung in the material of the Inner Detector at small radius (beam pipe and vertexing layers). As discussed in Section 7.7, detailed studies on the reconstruction of electrons with a p_T of 40 GeV over the full pseudorapidity coverage have been performed. Using an electron / photon separation algorithm based on two complementary pattern recognition programs and a photon conversion finder, an electron veto inefficiency as low as 0.19% can be reached for $Z \rightarrow ee$ events at the expense of an additional inefficiency for photon identification. The efficiency loss for photons depends on the luminosity. For a sample of $H \rightarrow \gamma\gamma$ events, it has been estimated to be 3.3% at low luminosity and 5.6% at high luminosity. The loss of signal efficiency has been included in the calculation of the expected event rates for m_H = 90 GeV. Figure 19-3 shows the expected $\gamma\gamma$ mass distribution for the remaining $Z \rightarrow ee$ events after applying the track veto described above. The rms width of the peak is found to be 4.4 GeV, which is therefore significantly larger than the expected one for normal $Z \rightarrow ee$ events and for $H \rightarrow \gamma\gamma$ events in this mass range. Although the residual $Z \rightarrow ee$ background remains resonant, its contribution to the $H \rightarrow \gamma\gamma$ signal for $m_H = m_Z$ is less than 10%.

Signal Observability

The expected $H \rightarrow \gamma\gamma$ signal significances, defined for each mass point as $S/\sqrt{B}$ where S and B are the numbers of accepted signal and background events in the chosen mass window of $\pm 1.4\sigma_m$, are given in Table 19-2 for an integrated luminosity of 100 fb^{-1}. The contributions from the irreducible and reducible backgrounds are accounted for in these estimates. In addition to the signal events from direct production, events from the associated production of a Higgs boson with a W or Z boson or a $t\bar{t}$-pair have been included in the signal. Due to the larger hadronic activity in the events arising from associated production, the efficiency of the photon isolation cuts is slightly lower than the values found for the direct production (see Section 19.2.2.2).

Table 19-2 Observability of the $H \rightarrow \gamma\gamma$ signal (direct and associated production) for 80 < m_H < 150 GeV. The expected numbers of signal and background events in the mass window, chosen to be $m_H \pm 1.4\sigma$, are given for an integrated luminosity of 100 fb^{-1}. The signal significances are given for integrated luminosities of 100 fb^{-1} (high luminosity) and 30 fb^{-1} (low luminosity).

Higgs mass (GeV)	**80**	**90**	**100**	**110**	**120**	**130**	**140**	**150**
Signal events (direct production)	502	655	947	1110	1190	1110	915	617
Signal events (WH, ZH, $t\bar{t}H$ production)	85	76	98	97	93	76	58	35
$\gamma\gamma$ background	41 700	41 000	41 400	35 000	29 000	24 700	20 600	16 900
Jet-jet background	5400	5600	5950	5300	4600	4100	3550	3050
γ-jet background	12500	10600	9100	7000	5800	4900	4100	3400
$Z \rightarrow ee$ background	-	< 70	-	-	-	-	-	
Stat. significance for 100 fb^{-1}	2.4	3.1	4.4	5.6	6.5	6.5	5.8	4.3
Stat. significance for 30 fb^{-1}	1.5	1.9	2.7	3.4	3.9	4.0	3.5	2.6

For an integrated luminosity of 100 fb^{-1}, a Standard Model Higgs boson in the mass range between 105 GeV and 145 GeV can be observed with a significance of more than 5σ by using the $H \rightarrow \gamma\gamma$ channel alone. Table 19-2 also contains the estimated significances of the $H \rightarrow \gamma\gamma$ channel for an integrated luminosity of 30 fb^{-1}, corresponding to the first three years of LHC operation. The significances at low luminosity have been evaluated by taking the resulting improvements in mass resolution and background rejection into account. A signal in the $\gamma\gamma$ channel can only be seen in this case with a significance of ~ 4σ over a narrow mass range between 120 and 130 GeV.

The significances quoted in Table 19-2 are slightly higher than the ones given in the Technical Proposal. The main reason for this is the removal of the so called p_T-balance cut, which was applied in order to suppress bremsstrahlung background. Although without this cut the background increases, there is a net gain in the significance. Another reason is the slightly improved mass resolution which is mainly due to a more sophisticated photon energy reconstruction, separating converted and non-converted photons. These gains are somewhat offset by the higher reducible background.

As an example of signal reconstruction above background, Figure 19-4 shows the expected signal from a Higgs boson with m_H = 120 GeV for an integrated luminosity of 100 fb^{-1}. The $H \rightarrow \gamma\gamma$ signal is clearly visible above the smooth $\gamma\gamma$ background, which is dominated by the irreducible continuum of real photon pairs.

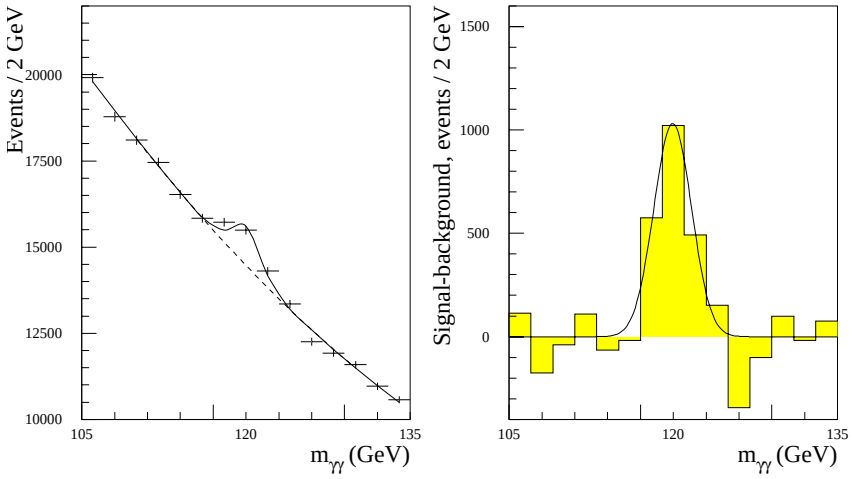

Figure 19-4 Expected $H \rightarrow \gamma\gamma$ signal for m_H = 120 GeV and for an integrated luminosity of 100 fb^{-1}. The signal is shown on top of the irreducible background (left) and after subtraction of this background (right).

19.2.2.2 Associated production: *WH*, *ZH* and $t\bar{t}H$

The production of the Higgs boson in association with a W or a Z boson or with a $t\bar{t}$ pair can also be used to search for a low-mass Higgs boson. The production cross-section for the associated production is almost a factor 50 lower than for the direct production, leading to much smaller signal rates. If the associated W / Z boson or one of the top quarks is required to decay leptonically, thereby leading to final states containing one isolated lepton and two isolated photons, the signal-to-background ratio can nevertheless be substantially improved with respect to the direct production. In addition, the vertex position can be unambiguously determined by the lepton charged track, resulting in better mass resolution at high luminosity than for the case of direct $H \rightarrow \gamma\gamma$ production.

There are many sources of reducible and irreducible backgrounds, which have been evaluated in a recent study [19-26]. The signal reconstruction proceeds along similar lines to the case of direct production. Two isolated photons and one lepton are searched for over $|\eta| < 2.4$. Simple kinematic cuts are applied, requiring that the transverse momenta of the photons and of the lepton exceed 25 GeV. As for direct $H \rightarrow \gamma\gamma$ production, events with one or more photons or the lepton in the crack region between the barrel and the end-cap calorimeter, in a region of $\Delta\eta = 0.15$, are rejected. In order to suppress the reducible background from QCD jet and $t\bar{t}$ production and from final-state photon radiation, additional isolation criteria are applied: the distance ΔR between each photon and each reconstructed jet cluster is required to be larger than 0.4. This separation criterion is also applied to the $\gamma\gamma$ and γl separation, *i.e.* $\Delta R_{\gamma\gamma} > 0.4$ and $\Delta R_{\gamma l} > 0.4$. After applying these cuts, the signal acceptance for $m_H = 100$ GeV is found to be 31% for WH and ZH events and 29% for $t\bar{t}H$ events. The slightly lower acceptance for $t\bar{t}H$ events is due to the larger jet activity in these events, which affects the efficiency of the separation criteria described above. These acceptances have to be multiplied by the reconstruction efficiencies for the photons and leptons. These have been estimated using fully simulated signal events and found to be compatible with those assumed for direct $H \rightarrow \gamma\gamma$ production, thereby indicating that the separation criteria quoted above lead to reconstructed final states with well isolated photons and leptons. The mass dependence of the acceptance is given in Table 19-3 for Higgs boson masses in the range between 80 and 140 GeV.

The irreducible background has been evaluated by considering the $W\gamma\gamma$, $Z\gamma\gamma$, $t\bar{t}\gamma\gamma$ and $b\bar{b}\gamma\gamma$ processes. In particular, radiation of photons from the leptons in the final state has been found to be important. They have been evaluated using the PYTHIA event generator in conjuction with the PHOTOS program [19-27]. After the kinematic cuts described above, the $Z\gamma\gamma$ background, where one photon is radiated from a final-state lepton, is dominant. This background has been further suppressed by requiring the lepton-photon mass, $m_{\gamma l}$, to be above a given threshold, $m_{\gamma l} > 25$ GeV, for any lepton-photon combination and to be outside a mass window of ± 8 GeV around the Z-boson mass. To further improve this rejection, events with a second lepton of the same flavour and opposite charge with $p_T > 10$ GeV are vetoed. These additional cuts reject the dominant $Z\gamma\gamma$ background by a factor 3.6, whereas the signal efficiency for $m_H = 100$ GeV is found to be 74%. The efficiency values as a function of m_H are given in Table 19-3.

There are also many sources of reducible backgrounds. Final states containing one, two or three jets in association with a lepton or a photon, such as $\gamma\gamma$-jet, γl-jet, γ-jet-jet, l-jet-jet and jet-jet-jet, have been considered [19-26]. In each case, the γ/jet or lepton/jet rejection factors, as determined from the full detector simulation (see Sections 7.4 and 7.6), have been applied. The total reducible background is estimated to be at the level of 20 - 30% of the irreducible one over the mass range considered, as shown in Table 19-3. The main contributions to the remaining reducible background arise from $t\bar{t} \rightarrow \gamma l$-jet final states, from associated $\gamma\gamma$-jet production, and from associated $W\gamma$+jet $\rightarrow l\gamma$+jet final states.

For the determination of the signal significance, only events in the mass window $m_H \pm 1.4\sigma$ are considered. Compared to direct $H \rightarrow \gamma\gamma$ production, the mass resolution at high luminosity is slightly improved, due to the precise determination of the z-position of the vertex by the lepton track. As an example, for $m_H = 100$ GeV, the mass resolution improves from 1.31 GeV to 1.23 GeV. Results from full simulation described in Section 19.2.2 show that, the acceptance in the mass window is 79%.

Table 19-3 Cross-sections times branching ratios, σ x BR, (sum of *WH*, *ZH* and $t\bar{t}H$), acceptances and expected numbers of signal and background events for associated Higgs production with $H \rightarrow \gamma\gamma$ decay and for $80 < m_H < 140$ GeV at high luminosity. The expected numbers of events and the statistical significances are given for an integrated luminosity of 100 fb^{-1}.

Higgs mass (GeV)	**80**	**100**	**120**	**140**
$\sigma \times$ BR (fb)	1.55	1.44	1.22	0.65
Acceptance of kin. cuts	0.24	0.30	0.31	0.32
Acceptance of mass cuts	0.70	0.74	0.78	0.79
Signal events	12.2	14.7	13.2	7.5
Irreducible background	6.0	5.7	4.4	3.2
Reducible background	1.3	1.4	1.3	1.3
Statistical significance	3.7	4.3	4.3	2.8

Using Poisson statistics, the probability to observe a statistical fluctuation in the background such that the total number of observed events would be larger than the sum of signal and background events, has been evaluated. The results, expressed in the usual units of Gaussian standard deviations, are given in the last row of Table 19-3. The statistical significances in this channel are found to be around 4.3σ for masses in the range between 100 and 120 GeV. The observation of this channel therefore represents an independent confirmation of a possible Higgs boson discovery for integrated luminosities above 100 fb^{-1}. It would also provide valuable information for the determination of the Higgs couplings to vector bosons and to the top quark. Because of the very small signal rate, this channel is not believed to have any discovery potential at low luminosity.

19.2.2.3 Associated production: *H* + jet $\rightarrow \gamma\gamma$ + jet

It has been argued that the observability of a Higgs boson in the γγ decay mode can be improved at the LHC by considering the associated production of a Higgs boson with one or two hard jets [19-28][19-29].

In addition to higher-order corrections to direct Higgs production (*e.g.* $gg \rightarrow Hg$), there are other production mechanisms which lead to the associated production of a Higgs boson with high-p_T jets. First there is the *WW* fusion process, which produces Higgs bosons in association with two jets which appear as tag jets in the forward regions of the detector (see Section 19.2.10). For a low-mass Higgs boson, this contribution to the total production cross-section is, however, only ~ 10%. Secondly, there is the associated production (*WH*, *ZH*, and $t\bar{t}H$), where jets from hadronic decays of the vector bosons or the top quarks are present in the final state. For these processes, jets appear in association with the Higgs boson already at the Born level, whereas they appear as a result of the higher-order QCD corrections for the dominant *gg* fusion process. Given the large contribution of the *gg* fusion to the total Higgs production cross-section, these higher-order QCD contributions are nevertheless expected to give a large contribution to inclusive *H*+jet production.

A study of the observability of *H+jet* with $H \rightarrow \gamma\gamma$ production has been recently carried out for the ATLAS detector [19-30]. The cross-sections for the associated production of a Higgs boson with a *W/Z* and a $t\bar{t}$ pair as well as for the *WW* fusion process have been obtained from the standard PYTHIA event generator. For the *gg* fusion process, the available first-order QCD ma-

trix-element calculation, *i.e.* at order α_s^3, [19-31] has been used. Unfortunately, such calculations are not available now for the dominant irreducible $\gamma\gamma$ background. A calculation exists for the $q\bar{q}$ subprocess, but not for the *gg* box-contribution. Due to the lack of a complete calculation for the $\gamma\gamma$ background, any such study would suffer at present from large uncertainties in the background estimates. A consistent treatment of the signal and the background can only be done when appropriate higher-order calculations will be available for both. In the analysis presented below, the signal contribution from direct $H \rightarrow \gamma\gamma$+jet production is estimated by using both the parton-shower approach and the available first-order matrix-element calculation. The results from both these approaches are used to estimate the uncertainties on the signal significance in this channel.

In the analysis, H+jet $\rightarrow \gamma\gamma$+jet final states are selected by applying the following criteria:

- Two isolated photons with $p_T^1 > 60$ GeV and $p_T^2 > 40$ GeV, within $|\eta| < 2.4$. As for the direct $\gamma\gamma$ analysis, events with photons in the barrel / end-cap transition region ($\Delta\eta = 0.15$) are rejected. In addition, a threshold on the transverse momenta of the photon system is also required $p_T^{(\gamma 1+\gamma 2)} > 50$ GeV.
- At least two reconstructed jets with:

  $E_T > 40$ GeV over $|\eta| < 2.4$ or $E > 800$ GeV over $2.4 < |\eta| < 4.6$.
- The distance ΔR between the jet and each photon is required to be $\Delta R > 1.5$. This cut is introduced to suppress bremsstrahlung contributions, where photons are radiated from the final-state quarks.

The expected numbers of signal and background events after applying this selection are given in Table 19-4 for an integrated luminosity of 100 fb^{-1}. The numbers shown in Table 19-4 for the expected signal rates demonstrate clearly that they depend strongly on the method chosen to generate the events. If the matrix-element approach is used, the *gg* fusion process accounts for most of the signal rate. The respective contributions of *WW* fusion and associated production amount to 35% and 10% of the total signal rate. In contrast, if the parton-shower approach is used, the contribution to the signal from direct H+jet production via *gg* fusion is decreased by a factor of 10, resulting in a total signal which is lower by a factor of two.

The dominant background contribution arises from quark bremsstrahlung. It should, however, be noted that, due to the lack of a complete higher-order calculation, the contribution from the $\gamma\gamma$ irreducible background has been estimated using the parton-shower approach, which most likely leads to an underestimate of the real contribution, as indicated by the results obtained for the signal.

Estimates of the signal significance are given in Table 19-4 for both approaches (matrix-element and parton-shower). In the absence of an appropriate $\gamma\gamma$ background calculation in the case of the matrix-element approach, the parton-shower estimate for this background has been scaled up by the same factor of 10 as found for the signal. In all cases, the significances shown in Table 19-4 are lower than those obtained for the inclusive direct $H \rightarrow \gamma\gamma$ signal, in addition to being affected by large theoretical uncertainties.

In summary, it might be possible to enhance the significance of a low-mass Higgs boson discovery in the $\gamma\gamma$ channel at the LHC, by looking for the associated production of $H \rightarrow \gamma\gamma$ decays with two jets. The simulated signal rate itself is very sensitive to the method used to generate the events. Given the large uncertainties reported here, this channel may be of interest as a confir-

Table 19-4 Expected rates for signal and background processes contributing to $\gamma\gamma$ + two jet final states for an integrated luminosity of 100 fb^{-1}. The signal contributions and statistical significances are given separately for the matrix-element and the parton-shower calculations of direct production of Higgs bosons associated with jets.

Higgs mass (GeV)	**100**	**120**	**140**
$gg, qg, q\bar{q} \rightarrow H + g\ (q)$ (matrix-element)	36	56	52
$gg, q\bar{q} \rightarrow H$ (parton-shower)	3	6	9
WW fusion ($qq \rightarrow qq\ H$)	24	35	30
Associated production ($WH/ZH, t\bar{t}H$)	9	10	8
Total signal (matrix-element)	70	101	90
Total signal (parton-shower)	36	51	47
$\gamma\gamma$ irreducible background	16	30	39
Bremsstrahlung: $qq \rightarrow g\ \gamma$, $qg \rightarrow q\ \gamma$	113	67	100
Total background	129	97	139
Total background (scaled, see text)	273	367	490
Statistical significance (matrix-element and scaled background, see text)	4.2	5.3	4.1
Statistical significance (parton-shower)	3.2	5.2	4.0

mation of a potential signal, but cannot at present be considered as a discovery channel. More solid conclusions may be drawn when higher-order calculations for all background processes and / or measurements from the Tevatron become available.

In a similar analysis, the associated production of a Higgs boson with a single jet, as suggested in [19-29], has also been investigated and the details are reported in [19-30]. In this case also, a better theoretical understanding is needed before large signal significances can be claimed.

19.2.3 $H \rightarrow Z\gamma$

$H \rightarrow Z\gamma$ is another rare decay mode of the Standard Model Higgs boson. As in the case of the $\gamma\gamma$ decay, the branching ratio for this channel is only significant in the limited mass range between 100 and 160 GeV. In addition, it has to be multiplied by the $Z \rightarrow ll$ branching ratio, which is about 6.6% (electrons and muons). The production cross-section times branching ratio is below 2.6 fb in the mass range 120 - 160 GeV. Both the signal and the backgrounds have been evaluated using the fast simulation, and the sensitivity is found to be below 1.4 σ with a signal-to-background ratio of 2.5% [19-32].

19.2.4 $H \rightarrow b\bar{b}$

19.2.4.1 General considerations

If the mass of the Standard Model Higgs boson is lighter than 2 m_W, the $H \rightarrow b\bar{b}$ decay mode is dominant with a branching ratio of ~ 90 %. The observation of such a characteristic signature would be important for both the Higgs discovery and for the determination of the nature of any resonance observed in this mass region. Since the direct production, $gg \rightarrow H$ with $H \rightarrow b\bar{b}$, cannot be efficiently triggered nor extracted as a signal above the huge QCD two-jet background, the associated production with a W or Z boson or a $t\bar{t}$ pair remains as the only possible process to observe a signal from $H \rightarrow b\bar{b}$ decays. The leptonic decays of the W boson or semi-leptonic decays of one of the top quarks provide an isolated high-p_T lepton for triggering. In addition, requiring this high-p_T lepton provides a large rejection against background from QCD jet production. The Higgs-boson signal might thus be reconstructed as a peak in the invariant jet-jet mass spectrum of tagged b-jets.

Both the WH and the $t\bar{t}H$ channels have already been studied for the ATLAS Technical Proposal [19-14]. The analysis was complex and it became clear that excellent b-tagging capabilities are needed. The major difficulties in extracting a reliable signal from either of these two channels are the combination of a small signal and the need for an accurate control of all the background sources. The analyses have been repeated for this document, using the expected performance of the final ATLAS detector configuration. In the case of the $t\bar{t}H$ channel, the analysis has also been significantly improved. In the new analysis presented here, both top-quark decays are completely reconstructed. This provides a significantly better signal-to-background ratio and a reduction of the combinatorial problem in the b-jet assignment to the Higgs boson decay.

Other channels involving $H \rightarrow b\bar{b}$ decays have been suggested in the literature [19-33]. They have so far not been considered by ATLAS for the following reasons:

- ZH production with $Z \rightarrow ll$: this channel would provide a rate about six times lower than the WH channel. In addition, although $t\bar{t}$ production does not contribute significantly to the background in this channel, gg $\rightarrow$ Z$b\bar{b}$ production with $Z \rightarrow ll$ is only a factor 1.8 smaller in rate than the W$b\bar{b}$ background with $W \rightarrow l\nu$, and the signal-to-background ratio would therefore not be significantly improved with respect to the WH channel.
- ZH production with Z $\rightarrow \nu\nu$: it would be difficult to trigger efficiently on such final states. In addition, this channel suffers from potentially very large experimental backgrounds, given the rather low E_T^{miss} expected for the signal.
- $b\bar{b}H$ production: this process is also difficult to trigger on with high efficiency. However, $b\bar{b}H$ production may be significantly enhanced in supersymmetric extensions of the Standard Model and a detailed study has been carried out in the MSSM framework (see Section 19.3.2.8). This study has shown that, even if the trigger problem is ignored, a signal can only be extracted for large values of tanβ, where the enhancement is large. Therefore, this channel does not provide any discovery potential for the Standard Model Higgs boson.

In the following, the main features of the analyses of the WH (search for $l\nu b\bar{b}$ final states [19-34]) and $t\bar{t}H$ (search for $l\nu jjb\bar{b}b\bar{b}$ final states [19-35]) channels are summarised. These analyses have been performed using the fast simulation (see Section 2.5). Crucial aspects of the b-tagging performance (see Section 10.6) and of the invariant mass reconstruction of b-jet pairs (see Section 9.3) are in agreement with the results obtained from the full detector simulation.

Table 19-5 shows the production cross-sections for the signal with m_H = 100 GeV and for some important background processes. The signal cross-sections for $l\nu b\bar{b}$ (WH production) and $l\nu jjb\bar{b}b\bar{b}$ ($t\bar{t}H$ production) final states are of the same order. The reducible backgrounds from W+jet and $t\bar{t}$ production are huge, with cross-sections orders of magnitudes larger than the signal cross-sections. In addition to the large non-resonant backgrounds, there is also WZ production, which constitutes a dangerous resonant background for the WH signal.

Table 19-5 Cross-sections times branching ratios for WH and $t\bar{t}H$ production and for various background processes. All relevant branching ratios ($W \to l\nu$, $W \to jj$, $H \to b\bar{b}$ and $Z \to b\bar{b}$) are included.

Final state: $l\nu b\bar{b}$ + X	**σ (pb)**
WH (m_H = 100 GeV)	0.40
WZ	0.86
W$b\bar{b}$	70
$t\bar{t}$	247
$W^* \to tb$	1.4
$qg \to tbq$	45
Wjj (two jets with p_T > 15GeV, $\|\eta\|$ < 3.2)	4640
Final state: $l\nu$ jj $b\bar{b}$ $b\bar{b}$ + X	
$t\bar{t}H$ (m_H = 100 GeV)	0.29
$t\bar{t}Z$	0.02

Some of the features of the event topology are common to both channels:

- One trigger lepton with p_T > 20 GeV (electron) or p_T > 6 GeV (muon) within $|\eta|$ < 2.5. At high luminosity, these respective p_T-thresholds are raised to 30 GeV and 20 GeV.
- Jets from $H \to b\bar{b}$ decay with p_T > 15 GeV and within $|\eta|$ < 2.5. Reconstructed jet energies are recalibrated on average back to the original parton energies. After recalibration, the jet-jet mass peak from $H \to b\bar{b}$ decays is positioned at the nominal Higgs-boson mass. About 85% of the events are reconstructed inside a mass window of ±22 GeV around the nominal Higgs-boson mass. The b-tagging performance is simulated assuming the nominal efficiencies of respectively 60% and 50% at low and high luminosity. It should be noted, that the expected numbers of signal and background events, and, in particular, the ratio of reducible to irreducible background, depend on the optimisation of the b-tagging efficiency versus the rejection of non-b jets. A detailed study of this important issue is presented in Chapter 10.

Because of the quite different final-state topologies and of the different backgrounds in the WH and $t\bar{t}H$ channels, the final selection criteria are different for each channel and are described in the following.

19.2.4.2 *WH* channel

The background to the WH channel can be divided into three classes.

- Irreducible background from $WZ \to l\nu b\bar{b}$ and from $Wb\bar{b}$ production. The former produces a peak at m_Z in the $b\bar{b}$ mass distribution, and is therefore of special concern. The latter is dominated by $q\bar{q} \to Wg \to Wb\bar{b}$, and also has a small contribution from $q\bar{q} \to W^* \to \bar{t}b \to Wb\bar{b}$.
- Reducible background with at least two b-quarks in the final state, which arises predominantly from $t\bar{t} \to WWb\bar{b}$ and, to a lesser extent, from single top production through $gq \to t\bar{b}q \to l\nu b\bar{b} + q$.
- Reducible background containing jets misidentified as b-jets, which arises mainly from W+*jet* production. Its magnitude depends critically on the quality of the b-tagging.

In order to reduce these large backgrounds, the following selection criteria are applied:

- At least one isolated trigger lepton, fulfilling the pre-selection requirements described above.
- Two tagged *b*-jets fulfilling the pre-selection requirements described above.
- Lepton veto: no additional lepton is reconstructed with $p_T > 6$ GeV and within $|\eta| < 2.5$.
- Jet veto: no additional jets are reconstructed with $p_T > 15$ GeV within $|\eta| < 5.0$. This veto is applied mostly to reject the large $t\bar{t}$ background.
- Mass cut: events are kept if the invariant mass of the two tagged *b*-jets is reconstructed in a mass window of ±22 GeV (*i.e.* around $\pm 2\sigma_m$) around the nominal Higgs-boson mass.

The total expected kinematic acceptances, excluding the *b*-tagging and lepton identification and reconstruction efficiencies, are 12.5% for signal, 1.4% for *Wjj* and 0.2% for $t\bar{t}$. The jet veto alone reduces the $t\bar{t}$ background by a factor of 30. The signal acceptance has been estimated to be 82% in a mass window of ±20 GeV from full simulation studies (see Section 9.3.2).

The expected numbers of signal and background events in the chosen mass window are given in Table 19-6 for three different Higgs-boson masses and for an integrated luminosity of 30 fb^{-1}. The background is dominated by *Wjj* events and decreases rapidly with increasing mass. Over the mass range considered here, the ratio between the reducible and irreducible background is about 70 %. With increasing m_H, the signal production cross-section decreases, but the backgrounds from W$b\bar{b}$, *Wjj* and *Wjb* are also about a factor of two lower for $m_H = 120$ GeV than for $m_H = 80$ GeV.

Table 19-6 Expected WH, $H \rightarrow b\bar{b}$ signal and background rates inside the mass window for three different Higgs-boson masses, assuming the nominal b-tagging performance and an integrated luminosity of 30 fb^{-1}.

Higgs mass (GeV)	**80**	**100**	**120**
$WH, H \rightarrow b\bar{b}$	650	416	250
$WZ, Z \rightarrow b\bar{b}$	540	545	220
$Wb\bar{b}$	3400	3650	2000
$t\bar{t} \rightarrow WWb\bar{b}$	2500	3700	3700
tb, tbq	500	740	740
Wbj, Wjj	12500	7600	4160
$R_{\text{red/irred}}$	0.75	0.70	0.65
Total background	19440	16235	10820
S/B	3.3%	2.5%	2.3%
$S/\sqrt{B}$	4.7	3.3	2.4
$S/\sqrt{B}$ incl. syst. (see text)	3.0	1.9	1.7

The invariant $b\bar{b}$ mass distributions for the signal and background events passing the selection criteria are shown in Figure 19-5. The residual $t\bar{t}$ and *Wjj* background distributions are reasonably flat. The W$b\bar{b}$ background peaks however around 60 GeV and the *WZ* resonant background obviously peaks around m_Z.

The expected *WZ* background contribution is shown above the sum of the non-resonant continuum backgrounds in Figure 19-6, for an integrated luminosity of 30 fb^{-1}. An example of the expected $H \rightarrow b\bar{b}$ signal is shown in Figure 19-7 for $m_H = 100$ GeV. These figures illustrate the difficulty of extracting a resonant signal from $b\bar{b}$ pairs in this mass range, due to the low expected signal-to-background ratios and the rapidly varying shape of the summed background, which for the present selection is peaked around 80 GeV. For more details see [19-36].

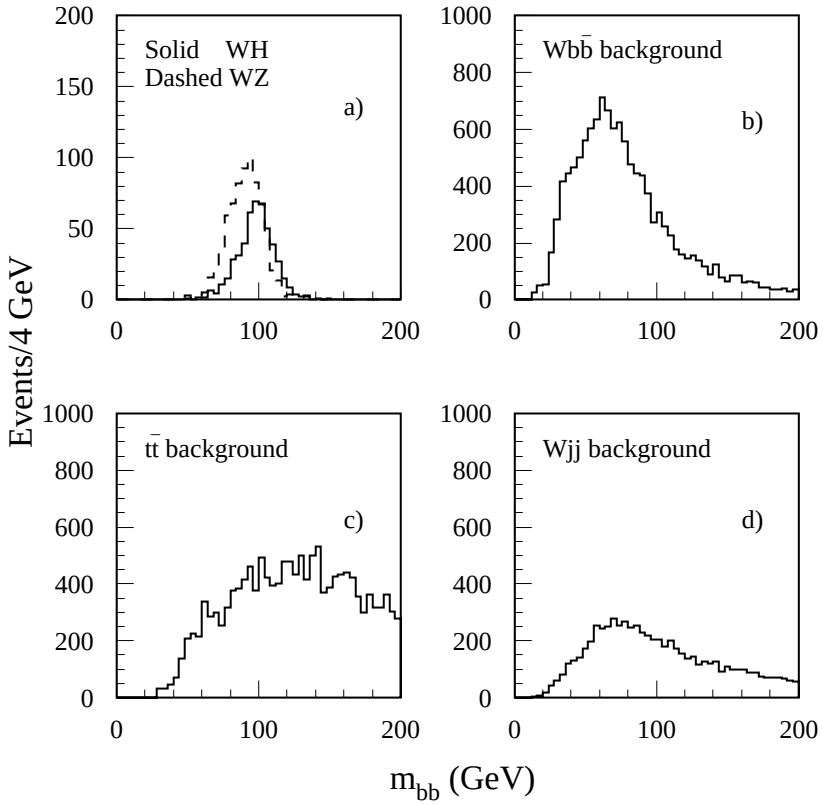

Figure 19-5 Invariant $b\bar{b}$ mass distributions for the *WH* signal and background events, after applying all selection criteria and for an integrated luminosity of 30 fb^{-1}: a) *WH* signal with m_H = 100 GeV (solid line) and resonant *WZ* background (dashed line), (b) $Wb\bar{b}$ background, (c) $t\bar{t}$ background, and (d) *Wjj* background.

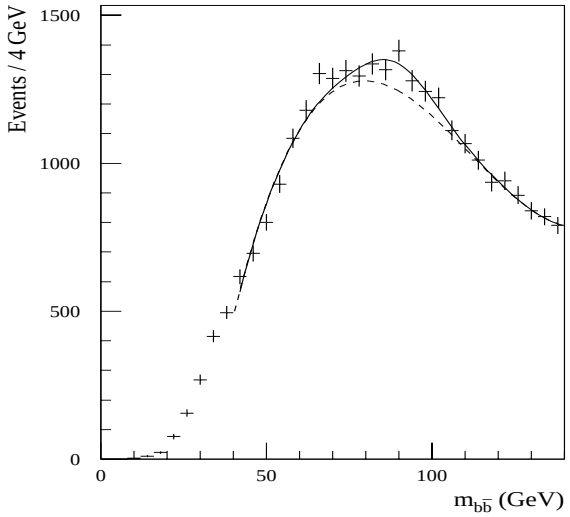

Figure 19-6 Expected *WZ* signal with $Z \rightarrow b\bar{b}$ above the summed background, for an integrated luminosity of 30 fb^{-1}. The dashed line represents the shape of the background.

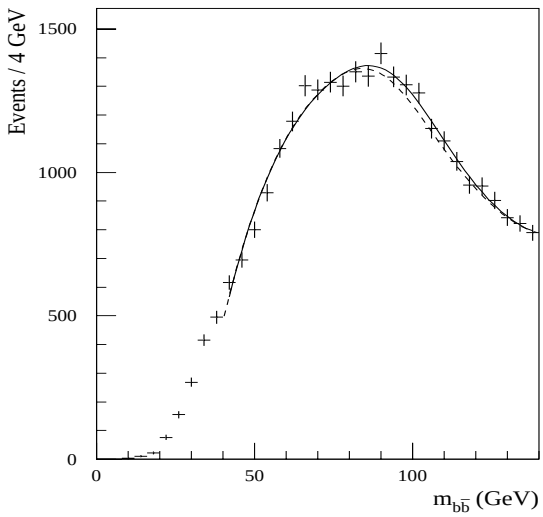

Figure 19-7 Expected *WH* signal with $H \rightarrow b\bar{b}$ above the summed background for m_H = 100 GeV and for an integrated luminosity of 30 fb^{-1}. The dashed line represents the shape of the background.

As shown in Table 19-6, a WH signal might be extracted if one assumes that the various background distributions are all perfectly known. Even in this optimistic scenario, the signal significance is at best 4.7σ for $m_H = 80$ GeV and is below 3σ for values of m_H above the ultimate sensitivity expected for LEP2. These numbers correspond to an integrated luminosity of 30 fb^{-1} expected to be reached over three years of initial operation at low luminosity. It is not clear in all cases how to achieve an accurate knowledge of the various backgrounds from the data.

- The most dangerous background from WZ production will be rather precisely measured through the background-free $WZ \rightarrow l\nu ll$ final states. Clearly, the observation of the WZ, $Z \rightarrow b\bar{b}$ final state above the continuum backgrounds would be an important first step in demonstrating the feasibility of extracting a WH signal at larger values of $m_{b\bar{b}}$.
- The shape and magnitude of the Wjj background can be constrained by varying the b-tagging cuts, assuming that this does not bias the $b\bar{b}$ mass distribution.
- The shape and magnitude of the $t\bar{t}$ background can be constrained by varying the jet-veto cuts, since it has by far the largest sensitivity to these cuts.
- The shape and magnitude of the W$b\bar{b}$ background cannot be obtained directly from the experimental data and one will have to rely on Monte Carlo simulations, which can to some extent be normalised to the experimental data in the mass regions where no signal from $H \rightarrow b\bar{b}$ decays is expected. If a systematic uncertainty of ±5% on the shape of the W$b\bar{b}$ background is assumed in the $H \rightarrow b\bar{b}$ signal region, the statistical significances are reduced considerably, as shown in Table 19-6.

Searches for WH, $H \rightarrow b\bar{b}$ final states at high luminosity will be further complicated by the impossibility of applying the tight jet-veto cuts described here (this would result in a substantial increase of the $t\bar{t}$ background) and by the need to increase the jet p_T threshold from 15 GeV to 30 GeV. In addition, the $H \rightarrow b\bar{b}$ mass resolution will be also somewhat degraded and this channel is not considered promising for searches at high luminosity.

In conclusion, the extraction of a signal from $H \rightarrow b\bar{b}$ decays in the WH channel will be very difficult at the LHC, even under the most optimistic assumptions for the b-tagging performance and calibration of the shape and magnitude of the various background sources from the data itself.

19.2.4.3 $t\bar{t}H$ channel

The cross-section for associated $t\bar{t}H$ production [19-34][19-35] is about the same as for WH production (see Table 19-5). The final state is however considerably more complex, since it consists of two W bosons and four b-jets. The W bosons and two b-jets come from the top-quark decays, and the other two b-jets from the Higgs boson decay. For trigger purposes, one of the W bosons is required to decay leptonically, whereas the other one is assumed to decay into a $q\bar{q}$ pair. In order to reliably extract the signal, the analysis requires that both top quarks be fully reconstructed. This method reduces considerably the large combinatorial background in the signal events themselves, since two of the b-jets are associated to the top decays, and therefore the remaining two should come from the Higgs boson decay. The signal should appear as a peak in the $m_{b\bar{b}}$ distribution, above the various background processes, which are classified as follows:

- Irreducible backgrounds, such as resonant $t\bar{t}Z$ and continuum $t\bar{t}b\bar{b}$ production. Since the $t\bar{t}Z$ cross-section is much smaller than the signal cross-section (see Table 19-5), the resonant background is not a problem in this channel.

- Reducible backgrounds containing jets misidentified as *b*-jets, such as $t\bar{t}jj$, *Wjjjjjj*, $WWb\bar{b}jj$, *etc*. The *Wjjjjjj* and $WWb\bar{b}jj$ backgrounds are suppressed to a large extent by the reconstruction of both top decays.

The following basic selection is applied before the *W* and top decay reconstruction are performed:

- One trigger lepton, fulfilling the pre-selection requirements described above.
- At least six jets with $p_T > 15$ GeV. The p_T threshold is raised to 30 GeV at high luminosity.
- Exactly four jets tagged as *b*-jets.

The *W* bosons are reconstructed from the jets not tagged as *b*-jets and from the reconstructed lepton and the neutrino. In the case of the leptonic decay, the *W* mass constraint is used to determine the longitudinal component of the neutrino. In order to improve the mass resolution for the reconstructed top quarks, the jet-jet invariant mass (within a ±25 GeV window around m_W) is also corrected to the nominal *W* mass, by scaling the corresponding four-vectors. Ambiguities arise in the pairing of the two *W* bosons with two of the four *b*-jets. These ambiguities are resolved by selecting from all *lνb-jjb* combinations the one which minimises $\chi^2 = (m_{jjb} - m_t)^2 + (m_{l\nu b} - m_t)^2$. It has been checked using the background samples [19-35], that this procedure does not introduce artificial peaks in the reconstructed mass spectrum of the two remaining *b*-jets. It should be noted that the reconstruction of the top signal is used to suppress background from *W+jet* events, but mainly to minimise the combinatorial background from the signal events themselves.

Most of the results presented below come from fast simulation of signal and background events. The quoted resolutions and acceptances have been confirmed with the full simulation of signal events for low-luminosity operation, see Section 9.3.4 and Section 2.5.

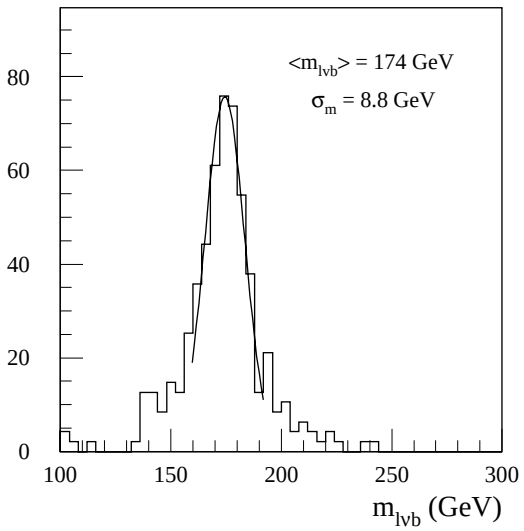

Figure 19-8 For fully simulated and reconstructed events (the $W \to l\nu$ reconstructed with fast simulation) the reconstructed top mass from $t \to l\nu b$ decays in $t\bar{t}H$ signal events with $m_H = 100$ GeV and for low-luminosity performance after the χ^2 selection (see text).

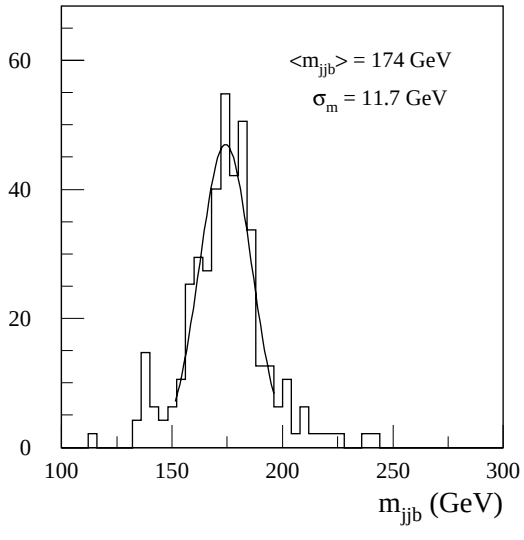

Figure 19-9 Same as Figure 19-8, but for the reconstruction of $t \to jjb$ decays.

The distributions of the reconstructed top masses ($m_{l\nu b}$ and m_{jjb}) for fully simulated events are shown in Figures 19-8 and 19-9 for $t\bar{t}H$ signal events with m_H = 100 GeV (see also Section 9.3.4). It should be noted that, due to the χ^2 selection, the mass distributions are somewhat biased towards the nominal top mass and therefore do not represent a true measure of the mass resolution. To further reject wrongly reconstructed top decays, only those events are kept, for which both top masses have been reconstructed to lie within ±20 GeV (*i.e.* ~ ±2σ) around the nominal top mass. This requirement is fulfilled by 66% of the reconstructed events. This acceptance must be convoluted with the acceptance of the kinematic cuts, which is 21.9%. This has still to be multiplied by the lepton and *b*-tagging efficiencies, for which the nominal values of 90% and 60% at low luminosity have been assumed. Multiplying these numbers leads to a total acceptance of 1.7% for $t\bar{t}H \rightarrow l\nu\, jj\, b\bar{b}\, b\bar{b}$ events at low luminosity.

At high luminosity, the p_T thresholds for the lepton and the jets are raised to 30 GeV. This results in a decrease of the acceptance of the kinematic cuts to 88% of their low luminosity value. In addition, the *b*-tagging efficiency is reduced from 60% to 50%. The top reconstruction efficiency is not significantly affected, and the total acceptance for $t\bar{t}H \rightarrow l\nu\, jj\, b\bar{b}\, b\bar{b}$ events is reduced to 0.7% at high luminosity.

For events passing all cuts, the $b\bar{b}$ invariant mass, $m_{b\bar{b}}$, is computed and a final cut is applied to select events in a mass window around the nominal Higgs-boson mass. The $m_{b\bar{b}}$ distribution of reconstructed fully simulated signal events is shown in Figure 19-10 for a Higgs-boson mass of 100 GeV at low luminosity. In the fast simulation used in this analysis, the Higgs-boson mass is reconstructed with a resolution of σ = 19 GeV, in good agreement with the results obtained from full simulation, σ = 20 GeV, which are discussed in Section 9.3.4 . For a significant fraction of the signal events, the assignment of the various jets is not correct, and results in the presence of non-negligible combinatorial background from the signal itself as shown in Figure 19-10. The shaded histogram represents those events for which the jet assignments in the Higgs boson reconstruction are correct.

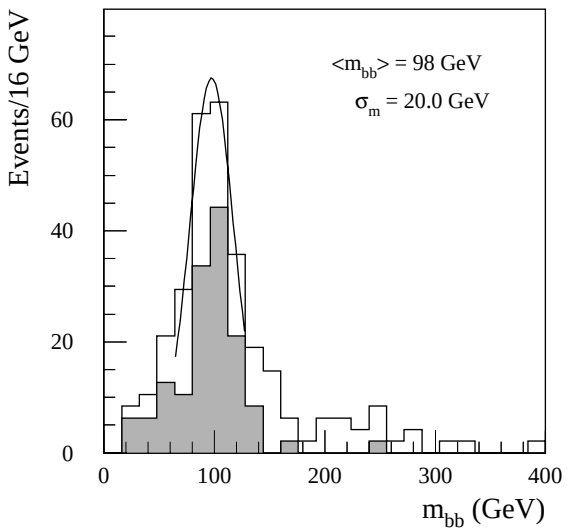

Figure 19-10 For fully simulated events, the reconstructed $m_{b\bar{b}}$ distribution for $t\bar{t}H$ with $H \rightarrow b\bar{b}$ signal events with both top-quarks being reconstructed inside a mass window m_{jjb}, $m_{l\nu b} = m_t \pm 20$ GeV and for low-luminosity performance. The shaded area denotes those events for which the jet assignment in the Higgs boson reconstruction is correct.

At low luminosity, the mass window cut is chosen to be ±30 GeV, and has an efficiency of 41% for signal events. For 64% of the events in this mass window, the jet assignment is correct. At high luminosity, the mass resolution is degraded from 19 GeV to 22 GeV. In this case, a mass window of ±45 GeV around the nominal Higgs-boson mass has been used, resulting in an acceptance of about 50%. At high luminosity, the fraction of events in the mass window, for which the jet assignments are correct, is reduced to about 50%. Detailed numbers for the fraction of correctly reconstructed $H \rightarrow b\bar{b}$ events in the signal are included in Tables 19-7 and 19-8, where the expected numbers of signal and background events are given at low and high luminosity, respectively.

The $m_{b\bar{b}}$ distributions for the summed signal and background events are shown in Figures 19-11 and 19-12, respectively for Higgs-boson masses of 100 and 120 GeV and for an integrated luminosity of 100 fb^{-1} (30 fb^{-1} with low-luminosity operation and 70 fb^{-1} with high-luminosity operation). The summed background is shown by the dashed line, and the points with error bars represent the result of a single experiment.

The expected numbers of signal and background events accepted by the full reconstruction chain are given in Tables 19-7 and 19-8, for Higgs-boson masses of 80, 100 and 120 GeV, and for integrated luminosities of 30 and 100 fb^{-1} respectively. The dominant background after these selection and reconstruction criteria is the irreducible, non-resonant $t\bar{t}jj$ background. Since top-quark production will be studied extensively in ATLAS (see Section 18.1), the shape of this background will be measured. To reject any potential contribution of a Higgs-boson signal in the determination of the background shape, a *b*-jet veto will most likely have to be used. Assuming that the shape of this background is known, the significance for the Higgs boson discovery in this channel exceeds 5σ in the low-mass range up to about 100 GeV for an integrated luminosity of 30 fb^{-1}.

Table 19-7 Expected *ttH* signal and background rates for three different Higgs-boson masses and for an integrated luminosity of 30 fb^{-1}. The numbers of events are given after all cuts, including the $m_{b\bar{b}}$ mass window cuts. The fraction of true $H \to b\bar{b}$ events ($S_{H \to b\bar{b}}/S_{\text{total}}$) in the signal peak is also given.

Higgs mass (GeV)	**80**	**100**	**120**
Signal *S*	81	61	40
$t\bar{t}Z$	7	8	2
Wjjjjjj	17	12	5
$t\bar{t}jj$	121	130	120
Total background *B*	145	150	127
S/B	0.56	0.41	0.32
$S/\sqrt{B}$	6.7	5.0	3.6
$S_{H \to b\bar{b}}/S_{\text{total}}$	0.67	0.64	0.59

The numbers given in Table 19-8 assume high luminosity performance. If the significance for an integrated luminosity of 100 fb^{-1} is computed from a combination of the significances reached for 30 fb^{-1} at low luminosity and for 70 fb^{-1} at high luminosity, the discovery window for a Standard Model Higgs boson, where the significance exceeds 5σ can be extended up to about 120 GeV. An ultimate integrated luminosity of 300 fb^{-1} at the LHC would extent the Higgs boson discovery window in this channel by another 10 GeV to about 130 GeV.

Table 19-8 Same as Table 19-7 for an integrated luminosity of 100 fb^{-1} (high luminosity operation).

Higgs mass (GeV)	**80**	**100**	**120**
Signal *S*	140	107	62
$t\bar{t}Z$	13	13	5
*W*jjjj	35	15	10
$t\bar{t}jj$	247	250	242
Total background *B*	295	278	257
S/B	0.47	0.38	0.24
$S/\sqrt{B}$	8.2	6.4	3.9
$S_{H \to b\bar{b}}/S_{\text{total}}$	0.57	0.53	0.50

It should be stressed that, due to the complete reconstruction of both top decays, the signal-to-background ratio has improved significantly compared to earlier studies [19-14], and lies in the range between 32% and 56% at low luminosity and between 24% and 47% at high luminosity.

In conclusion, the extraction of a Higgs-boson signal in the $t\bar{t}H$, $H \to b\bar{b}$ channel appears to be feasible over a wide range in the low Higgs-boson mass region, provided that the two top-quark decays are reconstructed completely with a reasonably high efficiency. This calls for excellent *b*-tagging capabilities of the detector. Another crucial item is the knowledge of the shape of the main residual background from $t\bar{t}jj$ production. If the shape can be accurately determined

using real data from $t\bar{t}$ production, a Higgs-boson signal could be extracted with a significance of more than 5σ in the mass range from 80 to 130 GeV, assuming an integrated luminosity of 300 fb^{-1}. For an uncertainty of ±5% on the absolute normalisation of the background shape, the discovery window would be reduced to the range between 80 and 125 GeV.

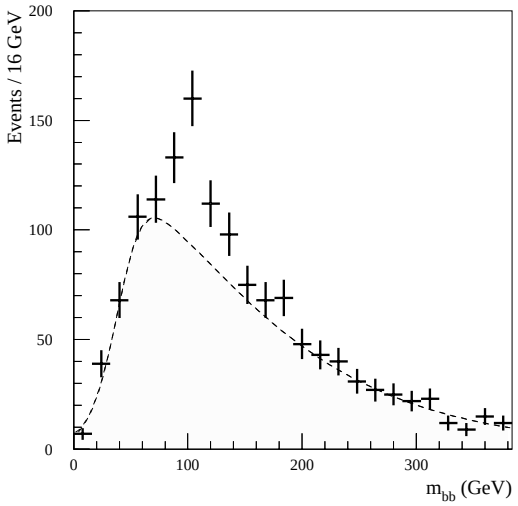

Figure 19-11 Invariant mass distribution, $m_{b\bar{b}}$, of tagged *b*-jet pairs in fully reconstructed $t\bar{t}H$ signal events with a Higgs-boson mass of 100 GeV above the summed background (see text), for an integrated luminosity of 100 fb^{-1} (30 fb^{-1} with low-luminosity operation and 70 fb^{-1} with high-luminosity operation). The points with error bars represent the result of a single experiment and the dashed line represents the background distribution.

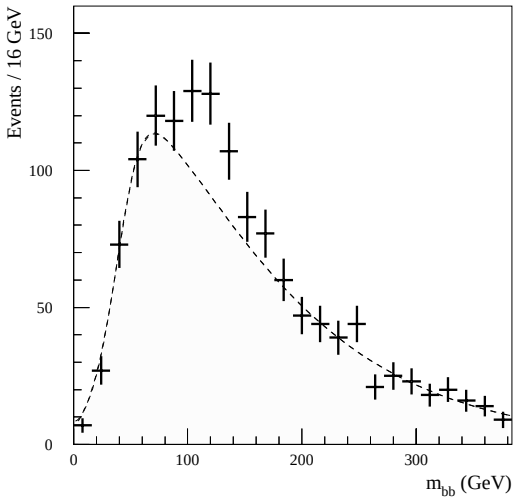

Figure 19-12 Same as Figure 19-11, but for a Higgs-boson mass of 120 GeV.

19.2.5 $H \rightarrow ZZ^* \rightarrow 4l$

The decay channel $H \rightarrow ZZ^* \rightarrow 4l$ provides a rather clean signature in the mass range between ~120 GeV and 2 m_Z, above which the gold-plated channel with two real Z bosons in the final state opens up. The branching ratio is larger than for the $\gamma\gamma$ channel and increases with increasing m_H up to $m_H \sim 150$ GeV. A pronounced dip appears, however, for $150 < m_H < 180$ GeV, because of the opening of the $H \rightarrow WW$ channel. In addition to the irreducible background from ZZ^* and $Z\gamma^*$ continuum production, there are large reducible backgrounds from $t\bar{t}$ and $Zb\bar{b}$ production. Because of the large top production cross-section, the $t\bar{t}$ events dominate at production level; the $Zb\bar{b}$ events contain, however, a genuine Z in the final state, which makes their rejection more difficult. In addition, there is a background from ZZ continuum production, where one of the Z bosons decays into a τ–pair, with subsequent leptonic decays of the τ–leptons, and the other Z decays into an electron or a muon pair.

In this Section, the potential for a Higgs boson discovery in the $H \rightarrow ZZ^* \rightarrow 4l$ channel is presented. Both electrons and muons are considered in the final state, thus yielding *eeee*, *ee*$\mu\mu$ and $\mu\mu\mu\mu$ event topologies. Since the detector performance is expected to be somewhat different for these various final states, they have been treated separately in the following. All results on the lepton and Higgs-boson mass reconstruction have been obtained from a full detector simula-

tion. Bremsstrahlung effects have also been taken into account, by using PYTHIA together with the PHOTOS package [19-27]. Background events have been generated using the exact matrix-element calculation [19-37] for the process $gg \rightarrow Zb\bar{b}$, which accounts for about 90% of the total $Zb\bar{b}$ cross-section. For both the $t\bar{t}$ and $Zb\bar{b}$ reducible backgrounds, leptons from cascade decays of *b*-quarks, *i.e.* not directly produced through *W*-boson or *b*-quark semi-leptonic decays, also contribute significantly to the background and have therefore been included in the event generation.

19.2.5.1 First stage of event selection

The signal reconstruction proceeds by selecting four leptons which pass the standard electron and muon identification criteria, as described in Sections 7.2 and 8.1, followed by the simple kinematic cuts:

- Two leptons with $p_T > 20$ GeV and $|\eta| < 2.5$ are required to trigger the experiment.
- Two additional leptons with $p_T > 7$ GeV and $|\eta| < 2.5$ are required.
- One pair of leptons of appropriate charge and flavour is required to have an invariant mass in a window around the *Z* mass, defined as $m_Z \pm m_{12}$. This cut rejects most of the non-resonant $t\bar{t}$ background.
- The other pair of leptons is required to have an invariant mass, above a certain threshold, defined as m_{34} threshold. This cut considerably reduces both the contributions from $t\bar{t}$ and $Zb\bar{b}$ cascade decays and from the $Z\gamma^*$ background.

The p_T thresholds for the leptons have been optimised to maintain a good acceptance for the signal at low m_H. By optimising the size of the m_{12} window as a function of the Higgs-boson mass, it is possible to recover partially acceptance losses due to $H \rightarrow ZZ^* \rightarrow 4l$ decays, which contribute significantly at the low end of the mass range [19-38]. The optimised values of m_{12} window and m_{34} threshold, used for the various Higgs-boson masses, are given in Table 19-9, together with the acceptance of the kinematic cuts, which is found to vary between ~27% and ~54% for masses between 120 and 180 GeV. The acceptance numbers are averaged over the three possible final-state topologies.

Table 19-9 For $H \rightarrow ZZ^* \rightarrow 4l$ final states, mass window, m_{12}, used around the Z mass and threshold, m_{34}, applied to the mass of the other lepton pair, together with the acceptance of the kinematic cuts as a function of m_H. The statistical error on the acceptances is ±0.003.

Higgs mass (GeV)	120	130	150	170	180
m_{12} window (GeV)	± 20	± 15	± 10	± 6	± 6
m_{34} threshold (GeV)	15	20	30	45	60
Acceptance of kinematic cuts	0.265	0.335	0.415	0.466	0.535

The Higgs-boson production cross-section times branching ratio to four leptons is given in Table 19-10 as a function of m_H, together with the cross-sections for the irreducible and reducible background contributions. The background cross-sections are given after the kinematic cuts have been applied and are integrated over a mass window of ±5 GeV around the corresponding Higgs-boson mass. Without further cuts, the reducible background is dominant, and a signifi-

cant fraction of these background events comes from cascade decays [19-39]. They can be further rejected by exploiting lepton isolation and vertexing criteria, as described in Section 19.2.5.3.

Table 19-10 Cross-section (σ) times branching ratio (*BR*) for $H \to ZZ^* \to 4l$ decays and for the various background processes (integrated over a mass window of ±5 GeV around the Higgs-boson mass) as a function of m_H. The acceptance of the kinematic cuts is included for all background processes.

Higgs mass (GeV)	**120**	**130**	**150**	**170**	**180**
$\sigma \times$ BR for Higgs signal (fb)	1.29	2.97	5.53	1.40	3.26
$\sigma \times$ BR for $ZZ^* \to 4l$ (fb)	0.16	0.28	0.28	0.26	0.24
$\sigma \times$ BR for $ZZ \to \tau\tau\, ll \to 4l$ (fb)	0.04	0.03	0.03	0.02	0.01
$\sigma \times$ BR for $t\bar{t} \to WbW\bar{b} \to 4l$ (fb)	1.2	1.9	2.5	1.9	1.7
$\sigma \times$ BR for $Zb\bar{b} \to 4l$ (fb)	0.9	1.3	1.7	1.3	1.2

19.2.5.2 Higgs-boson mass reconstruction

The results obtained from the full detector simulation and reconstruction of four-lepton final states are presented below. The reconstruction is based on the algorithms presented in Section 7.8.2 for electrons and Section 8.6.3 for muons. The following effects have been included in the evaluation of the mass resolution:

- Inner bremsstrahlung, *i.e.* radiative photon emission in Z decays, is included in the event generation; high-p_T photons ($p_T > 5$ GeV), which are identified and reconstructed, are included in the calculation of the four-lepton mass.
- Since the contribution from the experimental mass resolution is larger than that from the intrinsic width of the Z boson, a Z-mass constraint is applied, if the mass of the lepton pair is inside a window of ±6 GeV around the nominal Z-mass (see Section 7.8.2).
- Unlike the case of the $H \to \gamma\gamma$ analysis, where events are rejected if one or more photons are in the transition region between the barrel and end-cap calorimeters, events are not rejected for the $H \to ZZ^* \to 4l$ analysis (in the $H \to \gamma\gamma$ case, the quality of the γ/jet separation is crucial and tighter fiducial cuts are applied). Electrons in the transition region are measured with a somewhat worse energy resolution, and therefore they increase the non-Gaussian tails in the mass distributions.

The results are determined from full simulation at low and high luminosity for Higgs-boson masses of 130 GeV and 170 GeV. Based on these results, those for other masses are obtained by appropriate scaling of the results from the fast simulation. The results are discussed separately for the various final-state configurations, and a summary of all mass resolutions and of the relevant acceptances is given in Tables 19-11 and 19-12.

$H \to ZZ^* \to eeee$

An example of a reconstructed four-electron invariant mass distribution is shown for a Higgs-boson mass of 130 GeV in Figure 19-13. The mass resolution, obtained from a Gaussian fit in a window from -1.5σ to +2.5σ around the peak, is found to be (1.54 ± 0.06) GeV at low luminosity and (1.81 ± 0.07) GeV at high luminosity. Inner bremsstrahlung leads to a degradation of the mass resolution by about 0.1 GeV.

Within a mass window of $\pm 2\sigma$ around m_H, $(83.3 \pm 0.6)\%$ and $(84.7 \pm 0.6)\%$ of the events are retained at low and high luminosity respectively. This acceptance is about 12% lower than what is expected from a Gaussian distribution. The additional acceptance losses arise from inner bremsstrahlung (3%), from external bremsstrahlung in the Inner Detector (3%), from events for which no Z-mass constraint could be applied (5%), and from events for which one or more electrons are in the transition region between the barrel and end-cap calorimeters (1%). These individual fractions have been determined from the full detector simulation and reconstruction for $m_H = 130$ GeV. Most of these acceptance losses decrease as m_H increases.

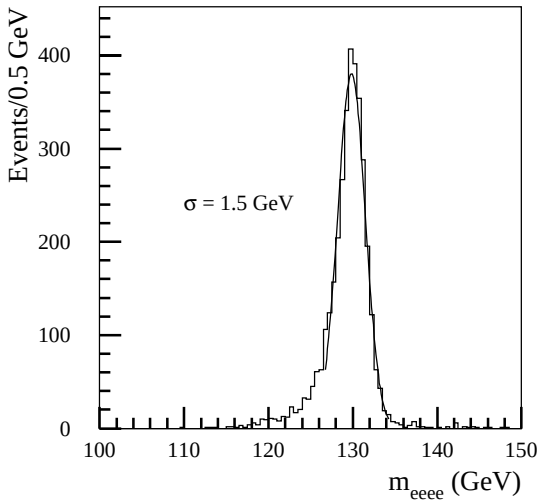

Figure 19-13 For fully simulated and reconstructed $H \rightarrow ZZ^* \rightarrow eeee$ decays with $m_H = 130$ GeV, four-electron invariant mass distribution at low luminosity (a Z mass constraint is applied).

The efficiency for the four-electron identification and reconstruction is found to be 69%, corresponding to an average of about 91% per electron.

$H \rightarrow ZZ^* \rightarrow \mu\mu\mu\mu$

The muon reconstruction is performed both in the Muon Spectrometer and in the Inner Detector. Details on the mass resolution obtained for the reconstruction in these two independent systems are given in Section 8.6.3. For the analysis presented here, the combination of the muon reconstruction in both systems has been used. In this case, the four-muon mass resolution is found to be (1.42 ± 0.04) GeV for a Higgs-boson mass of 130 GeV. The acceptance in the mass window of $\pm 2\sigma$ around m_H is about 83%. The individual contributions to the non-Gaussian part of the acceptance losses have been determined from full simulation and reconstruction: 4% of the events are lost due to inner bremsstrahlung, 5% are lost due to events for which no Z-mass constraint could be applied, and the remaining 3% are lost mainly due to non-Gaussian tails in the muon-momentum reconstruction. The effect of the inner bremsstrahlung is found to be slightly larger than in the four electron case, since low-energy photons, which are often recovered in the electron energy measurement in the EM Calorimeter, cannot be recovered in the track momentum measurement. For four-muon final states, the mass resolution is not affected by pile-up and is therefore identical at high luminosity.

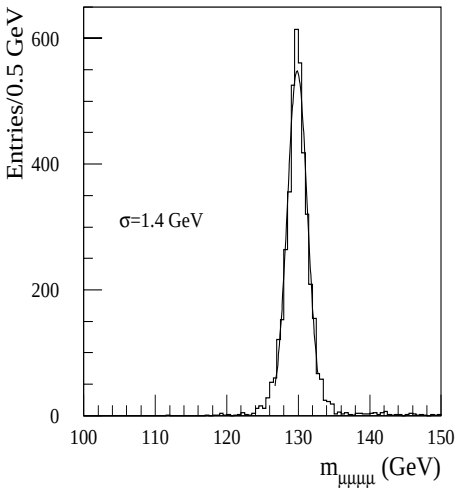

Figure 19-14 For fully simulated and reconstructed $H \rightarrow ZZ^* \rightarrow \mu\mu\mu\mu$ decays with $m_H = 130$ GeV, four-muon invariant mass distribution at low luminosity (a Z mass constraint is applied).

An example of a reconstructed mass peak for a Higgs-boson mass of 130 GeV is shown in Figure 19-14. The efficiency for the four-muon reconstruction is found to be 83.7%.

$H \rightarrow ZZ^* \rightarrow ee\mu\mu$

The $ee\mu\mu$ final state occurs in about one half of the total $H \rightarrow ZZ^* \rightarrow 4l$ event sample. The four-lepton mass resolution is found to be (1.39 ± 0.06) GeV for events where the on-shell Z decays to electrons, and (1.74 ± 0.07) GeV for events where it decays to muons. The difference between these two cases comes from the fact that the leptons from the on-shell Z have a harder p_T spectrum and that for the EM Calorimeter electron energy measurements, the relative resolution improves with increasing p_T, whereas it degrades for the magnetic muon-momentum measurements.

The average mass resolution at low luminosity is found to be (1.51 ± 0.06) GeV. The corresponding reconstructed four-lepton mass is shown in Figure 19-15 for a Higgs-boson mass of 130 GeV. In this case, (85.4 ± 0.6)% and (85.3 ± 0.6)% of the events are reconstructed within $m_H \pm 2\sigma$ at low and high luminosity, respectively. The non-Gaussian acceptance losses arise from inner bremsstrahlung (3%), from external bremsstrahlung in the Inner Detector (2%), from events for which no Z-mass constraint could be applied (4%), and from events for which one or more electrons are in the transition region between the barrel and end-cap calorimeters (0.5%).

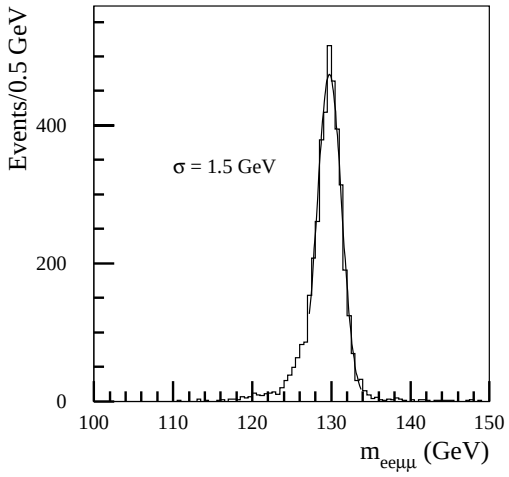

Figure 19-15 For fully simulated and reconstructed $H \rightarrow ZZ^* \rightarrow ee\mu\mu$ decays with $m_H = 130$ GeV, four-muon invariant mass distribution at low luminosity (a Z mass constraint is applied).

Summary of results

The results for the mass resolutions obtained for the various four lepton final states, for the overall efficiency for identifying and reconstructing them, and for the acceptances in the chosen mass windows, are summarised in Tables 19-11 and 19-12. As an example, for a Higgs-boson mass of 130 GeV, mass resolutions in the range between 1.42 GeV (in the case of four-muon final states) and 1.81 GeV (in the case of four-electron final states at high luminosity) are obtained. Electrons are more affected by pile-up effects than muons. In the four-muon final states, nearly all high-p_T photons from inner bremsstrahlung can be recovered and included in the four-muon invariant mass. In the electron case, this is only possible if the photons can be identified as separate clusters in the EM Calorimeter. Soft bremsstrahlung is, however, mostly recovered for electrons, since it is most often collinear and therefore automatically included in the EM Calorimeter energy measurement.

Table 19-11 Mass resolutions for the various four-lepton final states from $H \rightarrow ZZ^* \rightarrow 4l$ decays at low and high luminosity as a function of m_H. Bremsstrahlung effects are taken into account and a Z mass constraint is applied. The mass resolutions are obtained from full simulation and reconstruction for the events passing the kinematic cuts described in the text. The statistical error on the quoted resolution values is about ± 0.06 GeV.

Higgs mass (GeV)	Luminosity	120	130	150	170	180
σ(4*e*) (GeV)	Low	1.50	1.54	1.71	1.97	2.21
σ(4*e*) (GeV)	High	1.81	1.81	1.98	2.17	2.37
σ(4μ) (GeV)	Low / High	1.32	1.42	1.62	2.00	2.20
σ(2*e*2μ) (GeV)	Low	1.43	1.51	1.64	1.99	2.20
σ(2*e*2μ) (GeV)	High	1.64	1.68	1.84	2.10	2.28

Table 19-12 Overall efficiencies for identification and reconstruction of the various four-lepton final states from $H \rightarrow ZZ^* \rightarrow 4l$ decays with m_H = 130 GeV, together with the acceptances in the selected mass window (see text). The results are obtained from full simulation and reconstruction of events passing the kinematic cuts described in the text. The statistical error on the quoted acceptance numbers is about ± 0.006.

	4e		4μ		2e2μ	
	Low luminosity	High luminosity	Low luminosity	High luminosity	Low luminosity	High luminosity
Overall lepton efficiency	0.69	0.69	0.84	0.84	0.76	0.76
Acceptance in mass window	0.833	0.847	0.837	0.837	0.854	0.853

As discussed above, the lepton identification and reconstruction efficiencies have been evaluated from the full simulation and reconstruction. Although higher efficiencies of 91% per electron and 96% per muon have been obtained, the nominal value of 90% per lepton is used in Section 19.2.5.4 for the evaluation of the signal significances, for reasons of consistency with the other physics analyses in this document.

19.2.5.3 Rejection of reducible backgrounds

After the kinematic cuts are applied, the reducible backgrounds from $t\bar{t}$ and $Zb\bar{b}$ production are ten times higher than the irreducible one [19-40]. Since the overall uncertainties on these backgrounds are large, it is desirable to bring them well below the irreducible background from ZZ^* continuum production. To achieve this requires an additional rejection of 100, which can be obtained using lepton isolation and vertexing measurements, as described in this Section. All the results presented are based on the reconstruction of fully simulated large statistics samples of four-muon and four-electron final states from $H \rightarrow ZZ^* \rightarrow 4l$ events with m_H = 130 GeV and from $t\bar{t}$ and $Zb\bar{b}$ production.

Isolation cuts

In contrast to the Higgs-boson signal and the irreducible ZZ* continuum background, at least two of the selected leptons are non-isolated in the $t\bar{t}$ and $Zb\bar{b}$ backgrounds, since they originate from a *b*-quark decay. Isolation cuts are expected to reduce these backgrounds considerably. These cuts are applied to all four leptons in the final state and combine the information from:

- the calorimeter, where the summed transverse energy in a cone around the lepton can be required to be smaller than a given threshold E_T^{cut};
- the Inner Detector, where one may require that no charged track with p_T larger than a given threshold be reconstructed in a cone around the lepton.

These isolation criteria have been studied in detail in [19-40]. They are strongly correlated and the gain in combining them is small. The distribution of the maximal transverse momentum of all charged tracks reconstructed in the Inner Detector in a cone of radius ΔR = 0.2 around the leptons is shown in Figure 19-16, for the Higgs-boson signal and the reducible backgrounds. A significant background rejection can be achieved by this cut alone.

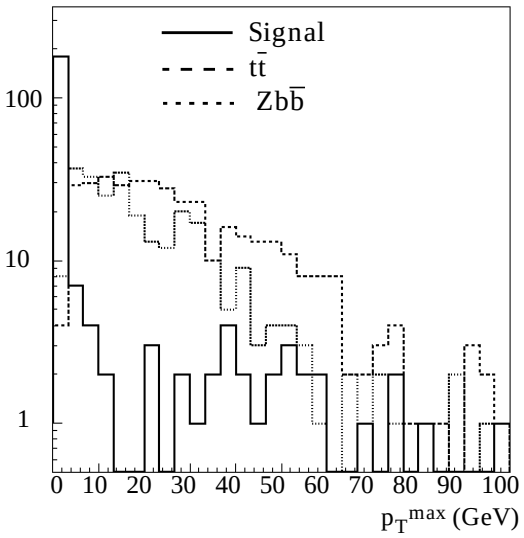

Figure 19-16 Distribution of the maximal transverse momentum, p_T^{max}, of all charged tracks reconstructed in the Inner Detector in a cone of radius $\Delta R = 0.2$ around the leptons for the $H \rightarrow ZZ^* \rightarrow 4l$ signal and the reducible backgrounds.

The p_T spectrum of *b*'s (and therefore of the leptons from *b*-decay) is softer in $Zb\bar{b}$ events than in $t\bar{t}$ events, leading to a less effective rejection of the non-isolated leptons using isolation cuts.

For the four-muon final state, the results for the background rejections as function of the efficiency for signal events with m_H = 130 GeV are shown separately for $t\bar{t}$ and $Zb\bar{b}$ events in Figure 19-17 both for low and high luminosity. At low luminosity, for a signal efficiency of 90%, a rejection of ~110 (~30) against $t\bar{t}$ ($Zb\bar{b}$) can be obtained. At high luminosity, similar rejections are obtained for an efficiency of 65% (75%) against the $t\bar{t}$ ($Zb\bar{b}$) backgrounds. For the four-electron final states, the results obtained are presented in Figures 19-18 and 19-19, respectively for the $t\bar{t}$ and $Zb\bar{b}$ backgrounds.

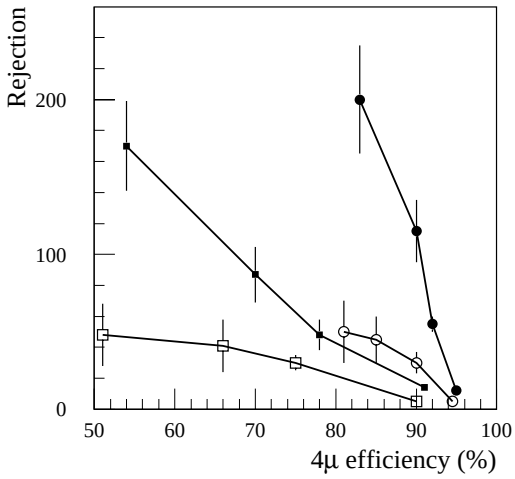

Figure 19-17 Rejection using track isolation of reducible backgrounds versus overall efficiency for $H \rightarrow ZZ^* \rightarrow \mu\mu\mu\mu$ final states with m_H=130 GeV. The results are shown for $t\bar{t}$ and $Zb\bar{b}$ as black and open symbols respectively and for both low (circles) and high (squares) luminosity.

The results are shown for track isolation at low luminosity and for calorimeter isolation at low and high luminosity.

- Compared to the results shown in Figure 19-17 for the four-muon final states, those for the four-electron final states using track isolation at low luminosity provide similar rejections at a somewhat lower efficiency. This is most likely due to the extra track multiplicity arising from conversions of bremsstrahlung photons in the four-electron case. The use of explicit electron-veto algorithms should improve the results of Figures 19-18 and 19-19 and bring them closer to the values of Figure 19-17.
- The calorimeter isolation at low luminosity is as effective as the track isolation for $t\bar{t}$ events. As mentioned above, the isolation cuts are much less effective for $Zb\bar{b}$ events because of the softer p_T spectrum of the b's.
- Finally, at high luminosity, the rejection using the calorimeter isolation is degraded in both cases because of the large fluctuations induced by pile-up noise in the energy depositions measured in the calorimeter towers.

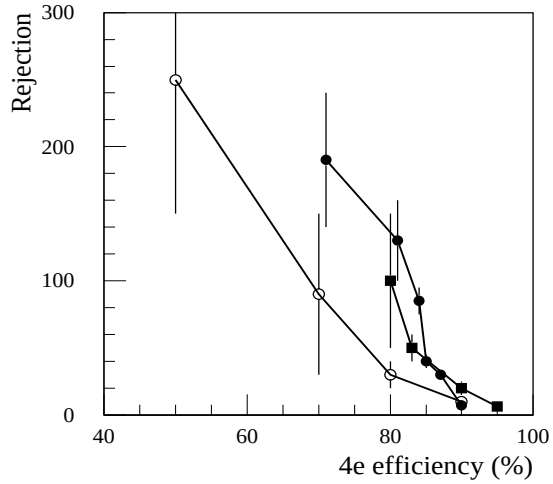

Figure 19-18 Rejection of $t\bar{t}$ background versus overall efficiency for $H \rightarrow ZZ^* \rightarrow eeee$ final states with m_H=130 GeV. The results are shown for track isolation at low luminosity (black circles), calorimeter isolation at low luminosity (black squares) and calorimeter isolation at high luminosity (open circles).

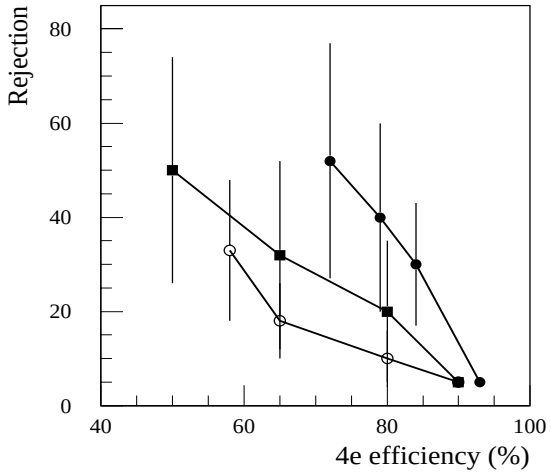

Figure 19-19 Same as Figure 19-18 for the $Zb\bar{b}$ background.

Impact parameter cuts

Further rejection against the reducible backgrounds can be obtained by using impact parameter cuts, since two of the leptons originate from b-decays. The largest of the normalised impact parameters (in the transverse plane) of the four reconstructed lepton tracks, is used as a discriminant variable. The distribution of this variable is shown in Figure 19-20 for four-muon final states from signal events and from the $t\bar{t}$ and $Zb\bar{b}$ reducible backgrounds. The long tails due to leptons from b-decays are clearly visible for both backgrounds.

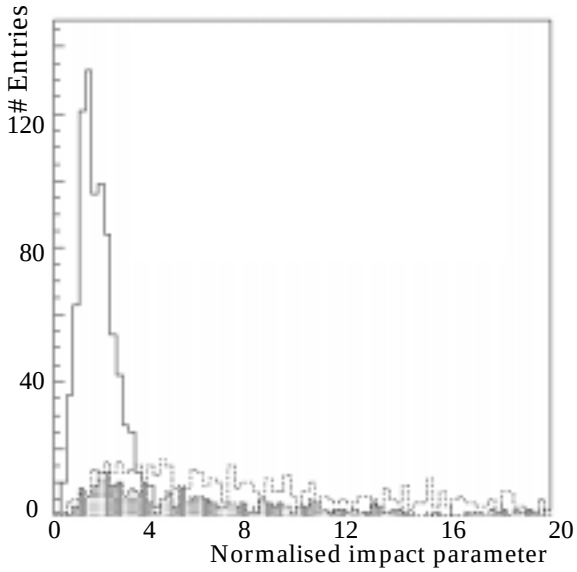

Figure 19-20 Largest of normalised impact parameters of the four muons, as reconstructed for fully simulated events from $H \rightarrow ZZ^* \rightarrow \mu\mu\mu\mu$ decays (solid histogram) and from the $t\bar{t}$ (dashed histogram) and $Zb\bar{b}$ (shaded histogram) backgrounds.

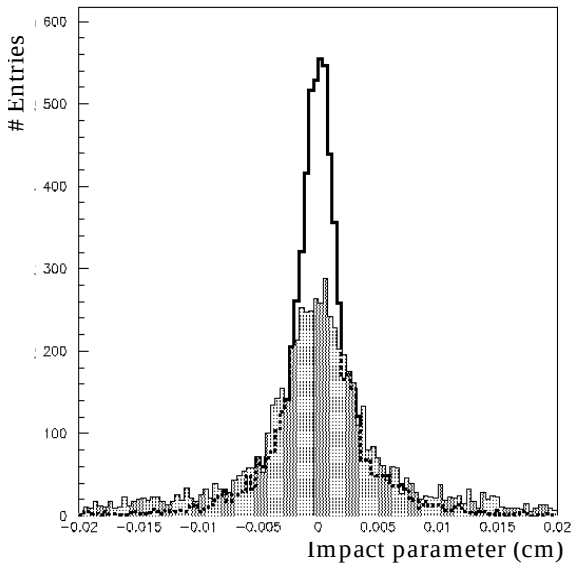

Figure 19-21 Distribution of largest (in absolute value) of the impact parameters of the four electrons as reconstructed for fully simulated events from $H \rightarrow ZZ^* \rightarrow eeee$ decays, before (shaded) and after (white) bremsstrahlung recovery.

For electrons, both inner and external bremsstrahlung induce tails in the impact parameter distributions. Figure 19-21 shows that these tails are significantly reduced by the bremsstrahlung recovery procedure of xKalman [19-41], see Section 7.2.1.1. The largest (in absolute value) of the impact parameters of the four reconstructed electron tracks is shown in Figure 19-21 before and after the recovery procedure is applied.

The spread of the primary vertex in x and y (in the transverse plane) induces a loss of impact parameter resolution. For four-muon final states, for example, the impact parameter resolution degrades from 19 μm to 29 μm if this spread is taken into account without correcting for it. This loss can be recovered by introducing the following kinematic variable [19-40]:

$$SUMDI = \sum_{i,\,j\,=\,1,\,4}^{i\,>\,j} \sqrt{(x_i - x_j)^2 + (y_i - y_j)^2}$$

where (x_i,y_i) are the coordinates in the transverse plane of the intersection point of two lepton tracks. Given the four tracks, there are six possible such intersection points. For signal events, for which all leptons come from the primary vertex, the intersection points of all lepton pairs should coincide, and hence the value of *SUMDI* is expected to be small. This is illustrated in Figure 19-22 for signal events and for $t\bar{t}$ and $Zb\bar{b}$ background events.

The rejection power of the lepton impact parameter information, as obtained from full simulation and reconstruction, is shown in Figure 19-23, for both $t\bar{t}$ and $Zb\bar{b}$ events as a function of the efficiency for the signal events. The results are shown for the normalised impact parameter method, both without and with vertex spread. The observed loss of rejection due to the vertex spread can be nearly fully recovered if the *SUMDI* variable is used. For the four-muon final states, a rejection of 12 against the $t\bar{t}$ background and of 5.5 against the $Zb\bar{b}$ background is ob-

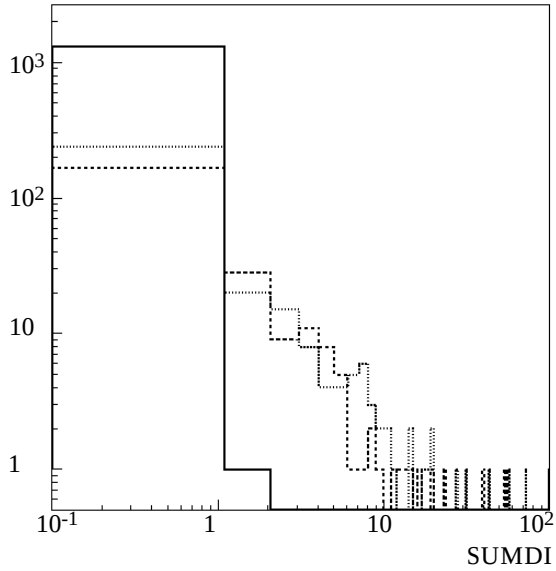

Figure 19-22 Distribution of *SUMDI* variable (cm) for $H \rightarrow ZZ^* \rightarrow \mu\mu\mu\mu$ signal events (solid) and for $t\bar{t}$ (dashed) and $Zb\bar{b}$ (dotted) background events (see text).

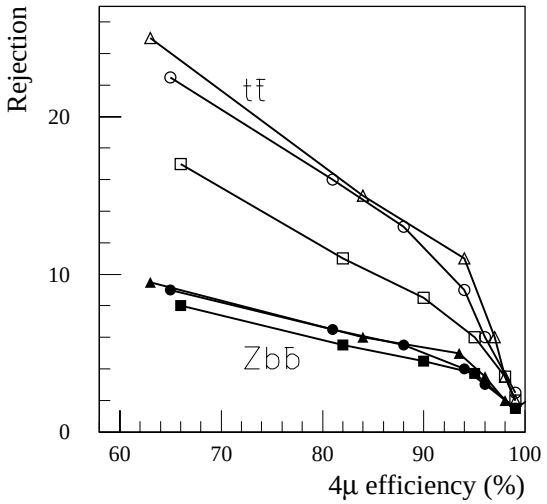

Figure 19-23 Rejection using impact parameter cuts of $t\bar{t}$ (open symbols) and $Zb\bar{b}$ (black symbols) backgrounds versus efficiency for $H \rightarrow ZZ^* \rightarrow \mu\mu\mu\mu$ final states with m_H = 130 GeV. The results are shown for the normalised impact parameter method without (triangles) and with (squares) vertex spread and for the method (circles) using the *SUMDI* variable (see text).

tained, for a signal efficiency of 90%. For the same rejection factors, the signal efficiency is degraded by about 20% for the four-electron final states. The rejection is significantly lower for $Zb\bar{b}$ events because of the lower average p_T of the leptons, which results in a worse impact parameter resolution, dominated by multiple scattering effects.

At high luminosity, the rejection of the impact parameter cuts is conservatively assumed to be degraded by about 35% (this was estimated by removing the information from the pixel *B*-layer when reconstructing the fully simulated events).

Combined rejection of reducible backgrounds

The results of the isolation and impact parameter studies reported above are combined together to provide estimates of the overall rejection against $t\bar{t}$ and $Zb\bar{b}$ backgrounds, which can be achieved as function of the efficiency for the $H \rightarrow ZZ^* \rightarrow 4l$ signal events and as a function of luminosity. The combined results are shown in Table 19-13, separately for the various four-lepton final states (the values for $H \rightarrow ZZ^* \rightarrow ee\mu\mu$ decays are derived by interpolation from the results obtained for the four-muon and four-electron final states). It is important to note that:

- The correlation between the isolation and impact parameter rejections (obtained separately in the studies reported above) is taken into account, since it is large, namely -10% for $t\bar{t}$ and -40% for $Zb\bar{b}$ events. This correlation is highest for $Zb\bar{b}$ events, since the isolation cuts soften the lepton p_T spectrum, which is in a range where the impact parameter resolution is limited by multiple scattering and therefore also dependent on p_T.
- The efficiency for four-electron final states is significantly lower than for four-muon final states (10% loss for isolation cuts and 20% loss for impact parameter cuts). The difference decreases at high luminosity because pile-up effects systematically degrade the isolation.

- The overall goal of a factor 100 rejection can be achieved, easily for the higher-p_T leptons from $t\bar{t}$ events, and also for the more difficult case of $Zb\bar{b}$ events (except for final states containing electrons at high luminosity).

Table 19-13 Combined rejections (using isolation and impact parameter cuts) against the $t\bar{t}$ and $Zb\bar{b}$ reducible backgrounds and efficiencies for the $H \rightarrow ZZ^* \rightarrow 4l$ final states with m_H=130 GeV. The results are given separately for the various four-lepton final states and for low and high luminosity.

	4e		**4μ**		**2e2μ**	
	Low luminosity	**High luminosity**	**Low luminosity**	**High luminosity**	**Low luminosity**	**High luminosity**
Signal efficiency	0.57	0.47	0.81	0.58	0.69	0.52
Rejection of $t\bar{t}$	1200	800	1200	800	1200	800
Rejection of $Zb\bar{b}$	130	50	110	90	120	70

It has also been investigated whether the background rejection could be further increased by using the missing transverse energy, E_T^{miss}. Although an E_T^{miss} cut would provide extra rejection, it would require the use of a very low cut, typically $E_T^{miss} < 20$ GeV. As shown in Section 19.2.5.4, the reducible backgrounds are rejected to a level well below the irreducible backgrounds, and this additional cut has therefore not been used. It could be used in future studies, however, to further optimise the signal efficiency with respect to the rejection of the reducible backgrounds.

19.2.5.4 Results

The numbers of signal and residual background events have been estimated for various Higgs masses in the range between 120 and 180 GeV. In order to compute the signal event rates, the cross-sections and kinematic cut efficiencies (Tables 19-9 and 19-10), the mass window acceptances (Table 19-12), the lepton identification and reconstruction efficiencies, and the isolation and impact parameter cut efficiencies (Table 19-13) are taken into account. For the evaluation of the signal significances, a lepton identification and reconstruction efficiency of 90% has been used to be consistent with the other results presented in this document. For this channel, this is conservative, given the results from the full simulation and reconstruction. The background numbers are computed from the cross-sections (Table 19-10), the mass windows (Table 19-11) the lepton identification and reconstruction efficiencies and the rejection factors obtained with the isolation and impact parameter cuts against the reducible backgrounds (Table 19-13).

The results are shown in Tables 19-14 and 19-15, respectively for integrated luminosities of 30 fb^{-1} and 100 fb^{-1}:

- the signal rates decrease very rapidly for $m_H < 130$ GeV and appear marginal for a Higgs boson discovery in this channel in this mass region;
- the dominant background is the irreducible continuum background from $ZZ^*/Z\gamma^*$ production;
- the reducible background is well below the irreducible background, thanks to the isolation and impact parameter cuts, and the dominant residual background remains the $Zb\bar{b}$ background;

- the significances have been evaluated using the Gaussian $S/\sqrt{B}$ approximation, but, given the small event rates, have also been calculated assuming Poisson statistics for both signal and background.

Table 19-14 Signal and background rates after all cuts and signal significances as a function of m_H, for $H \rightarrow ZZ^* \rightarrow 4l$ events and for an integrated luminosity of 30 fb^{-1} (low luminosity performance).

Higgs mass (GeV)	120	130	150	170	180
Signal	4.1	11.4	26.8	7.6	19.7
$t\bar{t}$	0.01	0.02	0.03	0.02	0.02
$Zb\bar{b}$	0.08	0.12	0.19	0.17	0.19
ZZ^*	1.23	2.27	2.51	2.83	2.87
$ZZ \rightarrow \tau\,\tau\,ll$	0.13	0.20	0.25	0.08	0.02
Significance ($S/\sqrt{B}$)	3.4	7.0	15.5	4.3	11.2
Significance (Poisson)	2.4	4.8	15.5	3.2	11.2

Table 19-15 Same as Table 19-14, but for an integrated luminosity of 100 fb^{-1} (high luminosity performance).

Higgs mass (GeV)	120	130	150	170	180
Signal	10.3	28.7	67.6	19.1	49.7
$t\bar{t}$	0.05	0.10	0.13	0.12	0.12
$Zb\bar{b}$	0.53	0.79	1.14	1.01	1.02
ZZ^*	3.53	6.36	7.03	7.54	7.61
$ZZ \rightarrow \tau\tau ll$	0.33	0.51	0.62	0.20	0.06
Significance ($S/\sqrt{B}$)	4.9	10.3	22.6	6.4	16.7
Significance (Poisson)	3.8	10.3	22.6	5.3	16.7

In conclusion, the $H \rightarrow ZZ^* \rightarrow 4l$ signal can be observed with a better than 5σ significance over most of the range $130 < m_H < 180$ GeV (except for a narrow region around 170 GeV) for an integrated luminosity of 30 fb^{-1}. For an integrated luminosity of 100 fb^{-1}, the signal can be observed with a better than 5σ significance over the complete mass range $125 < m_H < 180$ GeV.

19.2.6 $H \rightarrow WW^{(*)} \rightarrow l\nu l\nu$

For Higgs-boson masses close to 170 GeV, the signal significance in the $H \rightarrow ZZ^* \rightarrow 4l$ channel is reduced, due to the suppression of the ZZ^* branching ratio as the WW decay mode opens up (see Section 19.2.5). For $m_H = 170$ GeV, the $H \rightarrow WW^* \rightarrow l\nu l\nu$ branching ratio is approximately 100 times larger than that of the $H \rightarrow ZZ^* \rightarrow 4l$ channel. In the case of $H \rightarrow WW^* \rightarrow l\nu l\nu$ decays, however, it is not possible to reconstruct the Higgs-boson mass peak. Instead, an excess of events may be observed, and then used to identify the presence of a Higgs-boson signal and to extract information on its mass.

Based on the method suggested in [19-19], the potential for a discovery of the Higgs boson in the $H \rightarrow WW^* \rightarrow l\nu l\nu$ decay mode has been investigated for Higgs-boson masses in the range between 150 and 190 GeV [19-42]. The analysis presented here is based on fast detector simulation for final states containing electrons and muons. The signal cross-section times leptonic branching ratio for the $H \rightarrow WW^* \rightarrow l\nu l\nu$ decay is found to be between 0.55 and 0.80 pb over the mass range considered. Decays into τ-leptons, where the τ-leptons decay leptonically into electrons or muons have been taken into account in the analysis.

Table 19-16 Cross-sections for the most important background processes to the decay $H \rightarrow WW^* \rightarrow l\nu l\nu$ (leptonic τ-decays are included). The $W \rightarrow l\nu$ and the $\tau \rightarrow e\nu\bar{\nu}$, $\mu\nu\bar{\nu}$ branching ratios are included (leptonic branching ratios for b-decays are not included).

Process	$\sigma \times$ **BR (pb)**
$WW^* \rightarrow l\nu l\nu$	4.8
$WZ / ZZ \rightarrow ll\nu + X$	1.1
$t\bar{t} \rightarrow WWb\bar{b} \rightarrow l\nu l\nu + X$	38.6
$q\,g \rightarrow W\,t \rightarrow WW\,b \rightarrow l\nu l\nu + X$	4.8
$Wb\bar{b} \rightarrow l\nu b\bar{b} + X$	82.3
W+jet(s), $p_T > 10$ GeV	19300
$b\bar{b}$ inclusive (BR not included)	500×10^6

There are many irreducible and reducible background contributions, and the most important ones are listed in Table 19-16:

- The dominant irreducible background arises from WW continuum production, which has a cross-section times branching ratio between six and nine times larger than that of the Higgs-boson signal.
- WZ production with $W \rightarrow l\nu$, $Z \rightarrow ll$ and ZZ production with $Z \rightarrow ll$ and $Z \rightarrow \nu\nu$ also constitute a source of potentially irreducible background;
- $t\bar{t}$ and Wt production are the source of the largest reducible backgrounds with isolated leptons in the final state;
- $Wb\bar{b}$ and direct $b\bar{b}$ production, containing one or two leptons from semileptonic b-decays, are the dominant sources of reducible background with non-isolated leptons in the final state. These are considerably suppressed by the lepton p_T-threshold cuts and by isolation cuts.
- Finally, W+jet production, where a jet is mistaken as an electron, may also be a source of significant background.

In order to discriminate the signal from the most dangerous background processes, the following selection cuts are applied:

- Two isolated leptons with opposite sign are required within $|\eta| < 2.5$ and with transverse momenta, $p_T^1 > 20$ GeV and $p_T^2 > 10$ GeV. At high luminosity, the cut on the leading lepton is raised to 30 GeV for trigger purposes.
- Significant missing transverse momentum is required, $E_T^{miss} > 40$ GeV.
- The dilepton invariant mass is required to be smaller than 80 GeV.
- The opening angle ($\Delta\phi$) between the two leptons in the transverse plane is required to be smaller than 1.0 (measured in rad).
- The absolute value of the polar angle Θ_{ll} of the di-lepton system is required to be smaller than 0.9.
- The absolute value of the pseudorapidity difference ($\Delta\eta$) between the two leptons is required to be smaller than 1.5.

- Events with one or more jets with $p_T > 15$ GeV and $|\eta| < 3.2$ are rejected. At high luminosity, the p_T-threshold of this jet-veto cut is raised to 30 GeV.
- The transverse mass computed from the leptons and the missing transverse momentum,

$$m_T = \sqrt{2 p_T^{ll} E_T^{miss} (1 - \cos(\Delta\phi))}$$

  is required to fall in the mass window m_H - 30 GeV $< m_T < m_H$. Since the WW^* background is falling with increasing transverse mass, the lower cut value is reduced to m_H - 40 GeV for Higgs-boson masses above 170 GeV, in order to recover signal efficiency.

The dilepton invariant-mass cut mainly rejects background events where the lepton pair originates from a Z-boson. This cut has a large rejection against the WZ and ZZ background. The jet-veto cut is introduced to reject the $t\bar{t}$ and Wt backgrounds, which are characterised by large hadronic activity. The p_T-threshold of this jet-veto cut has unfortunately to be raised at high luminosity, which makes it much less effective and results in an increased residual $t\bar{t}$ background. The dominant irreducible background from WW* production is reduced by the angular cuts on the di-lepton system. The small angular separation between leptons in signal events results from the opposite spin orientation of the W pair originating from the decay of the scalar Higgs boson [19-43].

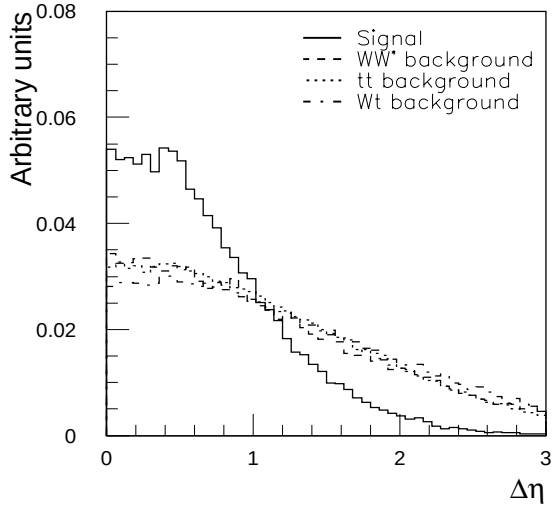

Figure 19-24 Difference in pseudorapidity between the two leptons for $H \rightarrow WW^* \rightarrow l\nu l\nu$ signal events with m_H = 170 GeV, and for the WW*, $t\bar{t}$ and Wt background events. All distributions are normalised to unity.

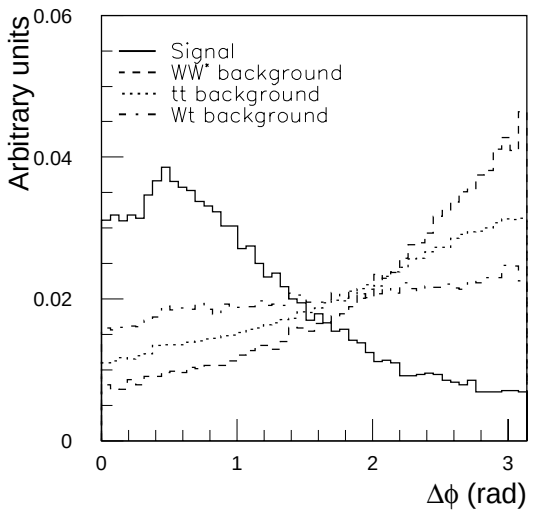

Figure 19-25 Difference in azimuth between the two leptons for $H \rightarrow WW^* \rightarrow l\nu l\nu$ signal events with m_H = 170 GeV and for the WW^*, $t\bar{t}$ and Wt background events. All distributions are normalised to unity.

The discrimination between the signal and the most important backgrounds is shown for the pseudorapidity difference, $|\Delta\eta|$, and the azimuthal difference, $\Delta\phi$, between the two leptons, respectively in Figures 19-24 and 19-25.

In Table 19-17, the cross-sections times branching ratios, the acceptances and the numbers of expected $H \rightarrow WW^* \rightarrow l\nu l\nu$ signal events are given as a function of m_H and for an integrated luminosity of 30 fb^{-1}. Over the mass range considered, the signal acceptance varies between 0.9 and 2.1%. In addition to this kinematic acceptance, a nominal identification and reconstruction efficiency of 90% per lepton has been assumed to obtain the signal event rates.

The numbers of expected background events in the selected transverse mass range are also given in Table 19-17, after all cuts are applied, for an integrated luminosity of 30 fb^{-1}. Due to the sliding window cut as a function of the Higgs-boson mass, also the background contribution is mass dependent. Thanks to the strict jet-veto cut applied at low luminosity, the $t\bar{t}$ background is at a level between 8 and 20 % of the irreducible WW^* background over the mass range considered. Single top production is found to be the dominant reducible background. A good signal-to-background ratio is obtained over this Higgs-boson mass range, with a maximum value of 0.7 for m_H = 170 GeV. At high luminosity, the $t\bar{t}$ and Wt background rejection is reduced and $t\bar{t}$ production is a significant reducible background, at the same level as the irreducible WW^* background.

The distribution of the transverse mass is shown in Figures 19-26 and 19-27 for the sum of signal plus background and for the background alone. The contribution from single top production and from $t\bar{t}$ production is also shown separately by the shaded histogram. The results are shown for m_H = 150 and 170 GeV and for an integrated luminosity of 30 fb^{-1}. Since there is no mass peak reconstructed in this channel, evidence for a Higgs-boson signal has to be deduced from an excess of events in the regions of transverse mass defined above. These regions are indicated by the two dotted lines.

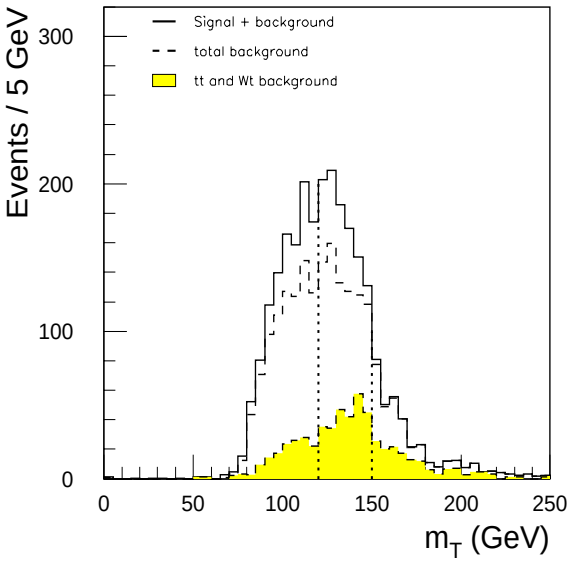

Figure 19-26 Transverse mass distribution for the summed $H \rightarrow WW^* \rightarrow l\nu l\nu$ signal (m_H = 150 GeV) and total background, for an integrated luminosity of 30 fb^{-1}. The distribution for the background alone is also shown separately. The shaded histogram represents the contributions from the Wt and $t\bar{t}$ background. The dashed lines indicate the selected signal region.

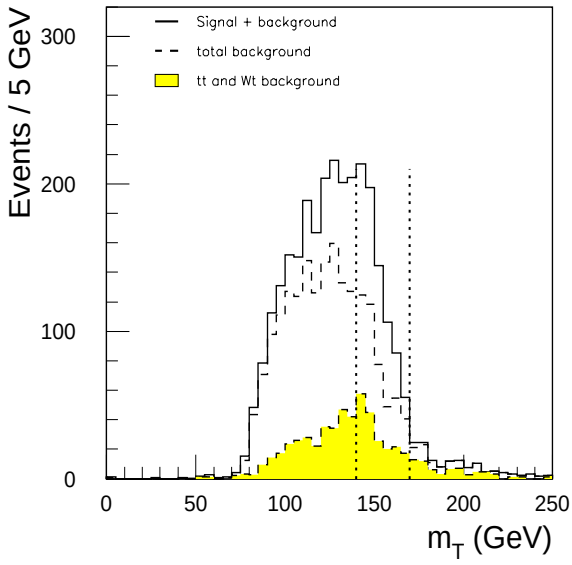

Figure 19-27 Same as Figure 19-26, but for m_H = 170 GeV.

The signal significance in this channel depends critically on the absolute knowledge of the various backgrounds. The cuts applied can be relaxed to some extent and a normalisation between the Monte Carlo prediction and the data can then be performed in regions, where only a small fraction of the signal is expected.

Table 19-17 Cross-sections times branching ratios, acceptances and numbers of expected signal and background events for $H \rightarrow WW^* \rightarrow l\nu l\nu$ decays and for an integrated luminosity of 30 fb^{-1}. The signal significances are computed assuming a systematic uncertainty of ±5% on the background.

Higgs mass (GeV)	**150**	**160**	**170**	**180**	**190**
$\sigma \times$ BR (fb)	610	790	800	705	550
Acceptance	0.016	0.021	0.017	0.016	0.009
Signal	240	400	337	276	124
WW* background	548	392	277	297	167
$t\bar{t}$ background	46	42	39	49	33
Wt background	215	195	149	163	85
WZ/ZZ background	25	17	9	10	6
W+jet background	< 10	< 10	< 10	< 10	< 10
Total background	844	656	484	529	301
Significance (including 5% systematic uncertainty)	4.7	9.6	10.3	7.8	5.4

Table 19-18 Same as Table 19-18, but for an integrated luminosity of 100 fb^{-1}.

Higgs mass (GeV)	**150**	**160**	**170**	**180**	**190**
Acceptance	0.024	0.032	0.027	0.026	0.016
Signal	1180	2050	1730	1490	700
WW* background	2320	1760	1200	1290	740
$t\bar{t}$ background	1010	960	850	1030	830
Wt background	2050	1890	1450	1590	920
WZ/ZZ background	105	75	45	50	35
W+jet background	25	25	25	25	25
Total background	5510	4710	3570	3985	2550
Significance (including 5% systematic uncertainty)	4.1	8.4	9.2	7.2	5.1
Significance (combined: 30 fb^{-1} + 70 fb^{-1}, including 5% systematic uncertainty)	5.4	11.4	12.7	9.7	7.2

To evaluate the significance, it has been optimistically assumed that such a normalisation can be performed to an overall accuracy of ±5%, *i.e.* that the summed WW*, $t\bar{t}$, and *Wt* background is known with a systematic uncertainty of ±5%. This uncertainty is larger than the statistical uncertainty on the background. Taking this into account, the signal significance estimated for an integrated luminosity of 30 fb^{-1} is above 5σ for ~150 < m_H < 190 GeV. Because of the less effective jet veto the residual $t\bar{t}$ and Wt backgrounds increase considerably at high luminosity. The numbers of expected signal and background events are given in Table 19-18, assuming high-luminosity running and an integrated luminosity of 100 fb^{-1}. Due to the strong increase of the $t\bar{t}$

and Wt background, the statistical significance does not improve compared to the low-luminosity running. The final signal significance which can be obtained with an integrated luminosity of 100 fb^{-1}, is computed from a combination of the significance achieved after low-luminosity operation over 30 fb^{-1} and high-luminosity operation over 70 fb^{-1}, assuming a fully correlated systematic error on the background.

The comparison of Tables 19-14 and 19-17 shows that the $H \rightarrow WW^* \rightarrow l\nu l\nu$ channel may have better sensitivity than the $H \rightarrow ZZ^* \rightarrow 4l$ channel for $160 < m_H < 175$ GeV, provided the small systematic uncertainty of ±5% Figure 19-28on the total background can be achieved.

Finally, it is important to note that constraints on the Higgs-boson mass can be extracted from the transverse mass distribution. As an example, the transverse mass distributions for m_H = 160 and 170 GeV are compared for the summed signal plus background in Figure 19-28. A sensitivity to the Higgs-boson mass is obtained from the upper edge of the distribution. The experimental resolution on the missing transverse energy defines the shape of this upper edge.

The distributions in Figure 19-28 can be separated with a purely statistical significance of 6σ [19-42]. Systematic uncertainties have not been studied yet, but the Higgs-boson mass can hopefully be constrained to better than ±5 GeV in this channel.

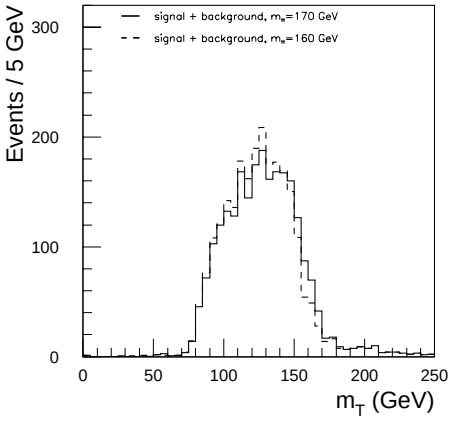

Figure 19-28 Transverse mass distributions of the summed signal plus background for m_H = 160 GeV (dashed histogram) and m_H = 170 GeV (full histogram).

19.2.7 WH with $H \rightarrow WW^* \rightarrow l\nu l\nu$ and $W \rightarrow l\nu$

It has been suggested recently [19-44], that the associated production of a Higgs boson with a W boson, with $W \rightarrow l\nu$ and $H \rightarrow WW^* \rightarrow l\nu l\nu$ provides an additional discovery channel at the LHC. The three-lepton final state appears as promising, since low background levels are expected. This channel is the associated production channel to the inclusive $H \rightarrow WW^* \rightarrow l\nu l\nu$ channel discussed in Section 19.2.6. Hence, the same general arguments about the signal extraction apply, and, in particular, evidence for a Higgs-boson signal has also in this case to be extracted from an excess of events above the expected background from Standard Model processes.

This channel is also interesting for the determination of the coupling parameters of the Higgs boson, since in its production and decay chain, only the couplings to gauge bosons appear. In almost all production and / or decay processes considered so far, Yukawa couplings of the Higgs boson to fermions are involved. In an extreme scenario, where there would appear only weak couplings of the Higgs boson to fermion pairs, this channel would remain unaffected, whereas all the others, except WH with $H \rightarrow \gamma\gamma$, would be suppressed.

A first study has been carried out [19-45], in which the ATLAS sensitivity in this channel has been investigated using fast simulation for Higgs-boson masses between 150 and 190 GeV. The signal cross-sections times leptonic branching ratios for this associated production channel are small, at the level of 4 fb. The values are given as a function of the Higgs-boson mass in Table 19-20.

There are two important backgrounds to this channel: WZ production, with a cross-section times leptonic branching ratio of 380 fb, and $t\bar{t}$ production with a cross-section times $W \rightarrow l\nu$ branching ratio of 28 pb. In the case of the $t\bar{t}$ background, the third lepton originates from semi-leptonic *b*-decays. In addition to these two major backgrounds, also the contributions from all other background sources studied for $H \rightarrow WW^* \rightarrow l\nu l\nu$ decays have been estimated. In order to achieve the necessary rejection against these backgrounds, the following cuts have been applied:

- Three isolated leptons (electrons or muons) with $p_T > 30$ GeV in the pseudorapidity interval $|\eta| < 2.5$.
- Same-flavour lepton veto: events which contain at least one pair of opposite-charge same-flavour leptons with an invariant mass between 60 and 120 GeV are rejected.
- $H \rightarrow WW$ tag: out of the three possible lepton pairs at least one should fulfil the tight angular cuts as used in the $H \rightarrow WW^* \rightarrow l\nu l\nu$ analysis (see Section 19.2.6). It is required that there is at least one pair with opposite charge, $\Delta\phi < 1.00$, $\Delta\eta < 1.5$ and an invariant dilepton mass smaller than 80 GeV. If none of the three possible lepton pairs fulfils these requirements the event is rejected.
- Jet veto: events with one or more jets with $p_T > 30$ GeV and $|\eta| < 3.2$ are rejected.

The second and third cut have a large rejection against the WZ background. The same flavour lepton veto rejects events containing $Z \rightarrow ll$ decays: this cut alone rejects the WZ background by about a factor 100 for a signal efficiency of about 70%. The residual WZ background contains either an off-shell Z or a $Z \rightarrow \tau\tau \rightarrow l\nu\, l\nu + X$ decay. Since the signal events contain two W bosons which originate from the decay of the scalar Higgs boson, the arguments on the angular separation between the decay leptons are still valid. The $H \rightarrow WW$ tag, based on this angular separation, therefore leads to another significant rejection of both the WZ and $t\bar{t}$ backgrounds for a reasonable signal efficiency. For the cuts applied, a rejection of about 3 is obtained for a signal efficiency of 85%. The large $t\bar{t}$ background can be further rejected in two different ways. A strict jet veto can be applied, where it is required that there be no jets with $p_T > 15$ GeV over $|\eta| < 3.2$. This jet veto can be applied at low luminosity, whereas at high luminosity the p_T-threshold has to be raised to 30 GeV. Since for $t\bar{t}$ events the third lepton originates from a semileptonic b-decay, the p_T-spectrum of the third lepton is more steeply falling for leptons from $t\bar{t}$ events than the one from signal events. There-

Table 19-19 Cross-sections times $W \rightarrow l\nu$ and $Z \rightarrow ll$ branching ratios and expected background rates for $WH \rightarrow WWW^* \rightarrow 3l$ decays. The rates are given for an integrated luminosity of 100 fb^{-1} and for various combinations of lepton and jet veto cuts. All other cuts are applied in addition, as described in the text.

Background process	**WZ**	**$t\bar{t}$**	**Wt**
σ x BR (fb)	380	28000	3500
Expected background events:			
$p_T(l) > 30$ GeV, Jet veto: 30 GeV	8.9	3.8	< 0.1
$p_T(l) > 20$ GeV, Jet veto: 15 GeV	4.7	8.1	10.0
$p_T(l) > 20$ GeV, Jet veto: 30 GeV	20.8	135	48.5

fore, a high p_T-threshold on the three leptons largely rejects the $t\bar{t}$ background, while keeping still a significant fraction of the signal. Both methods have been applied in the present study and the results are summarised in Table 19-19, where the expected background event rates are given for an integrated luminosity of 100 fb^{-1}. It should be noted that on top of the jet veto and lepton p_T-cuts indicated in the Table the same flavour lepton veto and the $H \rightarrow WW$ tag, as described above, have also been applied. As can be seen from these numbers, the largest background rejection is obtained if strict lepton p_T cuts are applied. For looser lepton cuts, the $t\bar{t}$ and Wt backgrounds are significant, in particular if a loose jet veto has to be applied, which is the case for high-luminosity operation. Since for these backgrounds the third lepton comes from a *b*-decay, an additional background rejection could be achieved using impact parameter and isolation criteria. An accurate estimation of these rejections requires a full simulation of the events. Since this has not yet been done, results based on the strict lepton cuts are quoted in the following.

The signal acceptance and the expected rates for signal and background events are summarised in Table 19-20 for Higgs boson masses in the range between 150 and 190 GeV and for an integrated luminosity of 100 fb^{-1}. For the cuts listed above, a total background of 12.7 events is found, which is dominated by the irreducible WZ background. The signal rate is largest for m_H =160 GeV, for which 28.5 signal events are expected. Therefore, a good signal-to-background ratio can be achieved in this channel for Higgs boson masses around 160 GeV. In the evaluation of the signal rates a lepton identification efficiency of 90% per lepton has been assumed.

The signal significance has been evaluated using Poisson statistics and assuming, as in the search for $H \rightarrow WW^* \rightarrow l\nu l\nu$ decays, a systematic uncertainty of ±5% on the total background. Due to the small background, however, this systematic uncertainty does not strongly degrade the significance. At high luminosity, a 5σ discovery of a SM Higgs boson in this channel seems to be possible in the mass range between ~155 GeV < m_H < 175 GeV, assuming an integrated luminosity of 100 fb^{-1}. For an ultimate integrated luminosity of 300 fb^{-1} the full range between 150 GeV and 190 GeV can be covered. For an integrated luminosity of 30 fb^{-1}, this channel is still rate-limited and a signal significance at the level of 3σ is obtained for m_H in the range between 160 and 170 GeV.

Table 19-20 Cross-sections times branching ratios, acceptances and numbers of expected signal and background events for WH, $H \rightarrow WW^* \rightarrow l\nu l\nu$ and $W \rightarrow l\nu$ decays and for an integrated luminosity of 100 fb^{-1}. The signal significances are computed assuming a systematic uncertainty of ±5% on the background and Poisson statistics.

Higgs mass (GeV)	**150**	**160**	**170**	**180**	**190**
σ × BR (fb)	3.95	4.60	4.10	3.30	2.35
Acceptance	0.063	0.085	0.084	0.077	0.067
Signal	18.1	28.5	25.2	18.5	11.5
Total background	12.7	12.7	12.7	12.7	12.7
Statistical significance (100 fb^{-1})	4.3	6.4	5.7	4.5	3.0
Statistical significance (30 fb^{-1})	2.2	3.3	3.0	2.3	1.5

Like for $H \rightarrow WW^* \rightarrow l\nu l\nu$ decays discussed in Section 19.2.6, the transverse mass of the E_T^{miss} and di-lepton system can be reconstructed for those di-lepton pairs fulfilling the angular separation and di-lepton mass cuts ($H \rightarrow WW$ tag). Although the E_T^{miss} is affected by the decay neutrino from the associated W boson, it is still peaked in the mass range between 100 and 200 GeV. As an example, the reconstructed transverse mass distribution is shown in Figure 19-29. The signal to background ratio can still be improved if appropriate transverse mass cuts are applied.

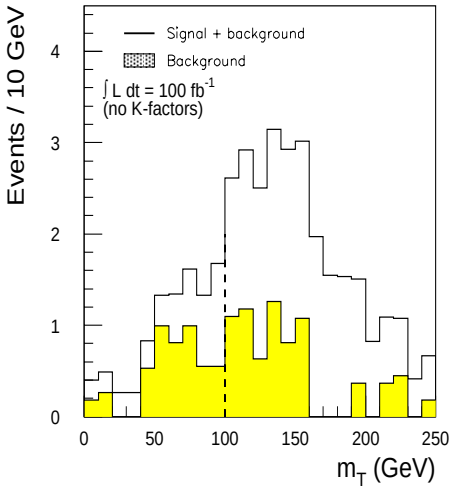

Figure 19-29 Transverse mass distributions of the summed signal plus background (histogram) for m_H = 160 GeV and for the background (shaded area).

In conclusion, the three-lepton channel represents an interesting possibility to enhance the observability of a Higgs-boson signal in the mass region between 150 and 190 GeV. It should finally be mentioned that, in addition to the three-lepton channel discussed here, the $WH \rightarrow WWW \rightarrow lljj$ channel with like-sign-leptons in the final state should also be considered. Although it suffers potentially from much larger backgrounds than the three-lepton channel, this channel is considered as interesting for Higgs-boson searches at the upgraded TeVatron collider [19-46].

19.2.8 Sensitivity to the SM Higgs boson in the intermediate mass range

The potential of the ATLAS experiment for the discovery of a SM Higgs boson in the intermediate mass range, 80 GeV < m_H < 2m$_Z$, is summarised in Figure 19-30 for integrated luminosities of 30 and 100 fb^{-1}. The signal significances are shown for individual channels, as well as for the combination of all channels.

For an integrated luminosity of 100 fb^{-1}, a SM Higgs boson can be discovered with a high significance over the full intermediate mass range. For all masses, the Higgs boson would be discovered in at least two different decay channels. A Higgs boson discovery with the ATLAS detector is already possible over the full intermediate mass range after a few years of running at low luminosity. It should be noted once again that no *K*-factors are included in the estimates of the signal significance, since these *K*-factors are generally not known for most background processes. This approach is conservative as long as the K-factor for the signal is larger than the square root of the *K*-factor for the background.

The most important channels in the intermediate mass region, for which a mass peak would be reconstructed, are the four-lepton channel, $H \rightarrow ZZ^* \rightarrow 4l$, the direct two-photon channel, $H \rightarrow \gamma\gamma$, as well as the associated production channels, where the Higgs boson is produced in association with a vector boson or a $t\bar{t}$ pair. In these channels, both the $\gamma\gamma$ and $b\bar{b}$ decay modes can be discovered at the LHC. For Higgs-boson masses around 170 GeV, for which the ZZ^* branching ratio is suppressed, the discovery potential can be enhanced by searching for the $H \rightarrow WW^* \rightarrow l\nu l\nu$ decay. In this case, the Higgs-boson signal would only be observed as an excess of events.

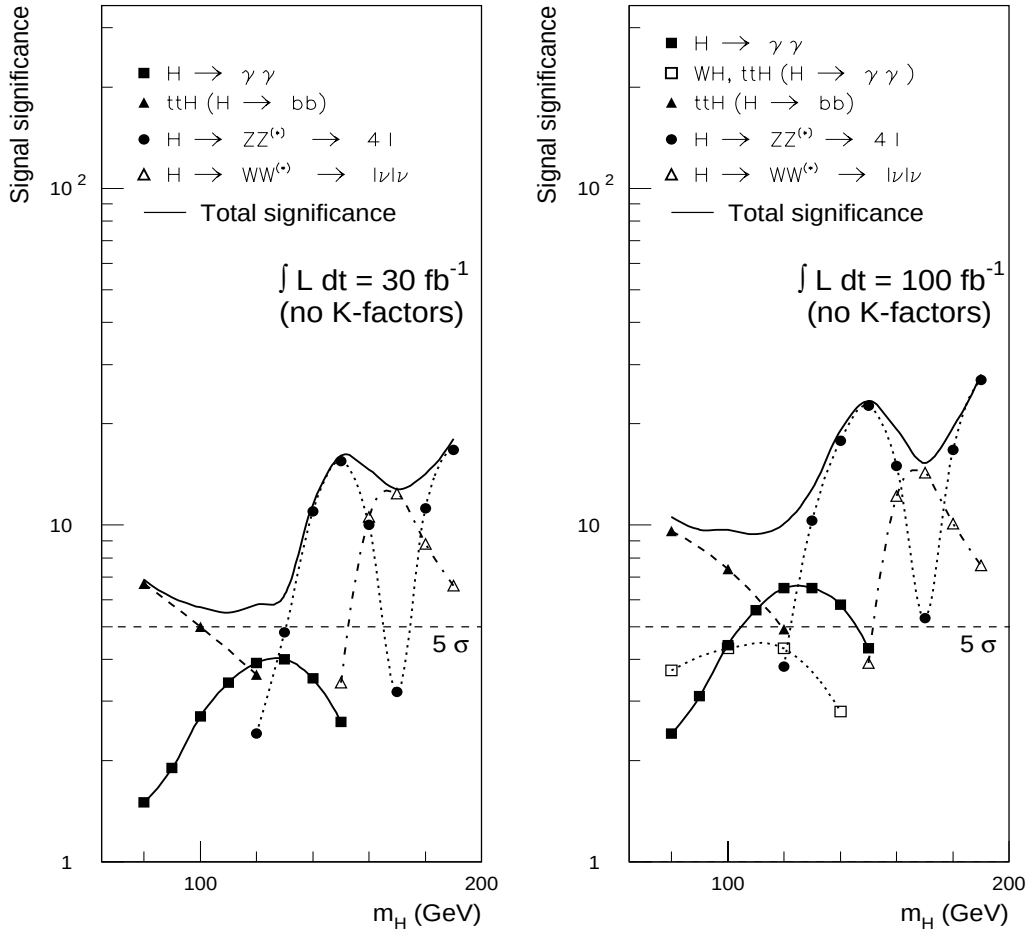

Figure 19-30 Sensitivity for the discovery of a Standard Model Higgs boson in the intermediate mass range. The statistical significances are plotted for individual channels as well as for the combination of all channels, assuming integrated luminosities of 30 fb^{-1} (left) and 100 fb^{-1} (right). Depending on the numbers of signal and background events, the statistical significance has been computed as $S/\sqrt{B}$ or using Poisson statistics. In the case of the $H \rightarrow WW^* \rightarrow l\nu l\nu$ channel, a systematic uncertainty of ±5% on the total number of background events has been included (see Section 19.2.6).

Most of the decay channels studied in the intermediate mass range are challenging in terms of detector performance. Even though the natural width of the Standard Model Higgs boson in this mass range is narrow, the backgrounds are relatively large and thus, an excellent detector performance in terms of energy resolution and background rejection is required. The $H \rightarrow \gamma\gamma$ decay mode requires high performance of the electromagnetic calorimetry in terms of photon energy resolution, photon direction measurements, and γ/jet separation. Impact parameter measurements in the Inner Detector are crucial for the discovery of the $b\bar{b}$ decay mode: efficient tagging of b-jets with a high rejection against light-quark and gluon jets allows a rather clean and complete reconstruction of $t\bar{t}$ final states together with the $b\bar{b}$ mass peak from Higgs boson decays. Finally, excellent performance in terms of the identification, reconstruction and measurement of isolated leptons with $p_T > 7$ GeV is required to discover the Higgs boson in the $H \rightarrow ZZ^* \rightarrow 4l$ channel. Due to the low expected rates over most of the mass range of interest, the Higgs boson cannot be discovered separately in the $H \rightarrow ZZ^* \rightarrow eeee$ or $H \rightarrow ZZ^* \rightarrow \mu\mu\mu\mu$ decay modes.

The performance of the ATLAS detector in its final optimised layout has been simulated in detail to assess whether it is able to meet the demanding requirements for the search for a Standard Model Higgs boson in the intermediate mass range. All the key performance characteristics have been evaluated with full GEANT simulation, both at low and high luminosity. These include the mass resolutions for the $H \rightarrow \gamma\gamma$, $H \rightarrow b\bar{b}$ and $H \rightarrow ZZ^* \rightarrow 4l$ channels, the performance of the *b*-tagging algorithms, and the rejections of many reducible backgrounds from various abundant Standard Model processes.

In conclusion, the ATLAS detector performance is adequate to guarantee that, if a Standard Model Higgs boson exists with a mass in the intermediate range, it will be discovered after only a few years of operation at low luminosity. Such a discovery would be confirmed and consolidated with better statistical significance at high luminosity. The results presented in the preceding Sections and summarised in Figure 19-30 could be compared to recent estimates based on work done in the context of studies performed for the future Tevatron runs [19-47]. Work is in progress to assess in a consistent way within ATLAS the comparative potentials of the detector to discover a SM Higgs boson in the intermediate mass range, in *pp* collisions at $\sqrt{s}$ = 14 TeV versus $p\bar{p}$ collisions at $\sqrt{s}$ = 2 TeV for an integrated luminosity of 30 fb^{-1} [19-48].

19.2.9 $H \rightarrow ZZ \rightarrow 4l$

For Higgs-boson masses in the range 180 GeV < m_H < ~700 GeV, the $H \rightarrow ZZ \rightarrow 4l$ decay mode is the most reliable channel for the discovery of a Standard Model Higgs boson at the LHC. The expected background, which is dominated by the continuum production of *Z* boson pairs, is smaller than the signal. In this mass range, the natural width of the Higgs boson grows rapidly with increasing m_H, and dominates the experimental mass resolution for m_H > 300 GeV. The momenta of the final-state leptons are high and their measurement does not put severe requirements on the detector performance. Therefore, the discovery potential in this channel is primarily determined by the available integrated luminosity.

The signal is reconstructed by requiring four identified leptons in the pseudorapidity range $|\eta| < 2.5$. The two leading leptons are required to have transverse momenta above 20 GeV, whereas the other two are required to have $p_T > 7$ GeV. For the lepton identification, an efficiency of 90% per lepton is assumed. The continuum $Z(\gamma^*)\, Z(\gamma^*) \rightarrow 4l$ production is the dominant background source in this mass range and its total production cross-section times branching ratio is 44 fb for $m_{ZZ} > 200$ GeV.

Since the Higgs-boson width varies rapidly over the mass range considered in this Section, a variable mass window of width σ_m, given by the convolution of the Higgs decay width and of the experimental resolution, $\sigma_m = ((\Gamma_H / 2.36)^2 + (0.02\ m_H)^2)^{1/2}$, was used to evaluate the observability of the signal. The acceptance was assumed to be 90% in a mass window of $\pm 1.64\ \sigma_m$ around m_H. Better estimates would require taking into account the correct line-shape for a broad Higgs boson, as well as interference effects between the resonant signal and the non-resonant background [19-49]. Given the very large sensitivity expected in this channel, these effects are not deemed critical for the evaluation of the signal observability, but would have to be included for *e.g.* a measurement of m_H.

The signal and background events expected in the mass window after applying only the simple kinematic cuts listed above are given in Table 19-21 (see [19-15] for more details). These numbers demonstrate that the signal can be easily identified above a small background over the full mass range from 200 to 600 GeV.

Since the Z-bosons from Higgs-boson decays are produced through the two-body decay of a heavy object, a significant rejection of the continuum ZZ background can be achieved by requiring that the transverse momentum of the harder of the two Z-bosons, $p_T^{max}(Z_1, Z_2)$, be larger than a given threshold value. As can be seen from the numbers in Table 19-21, the significance improves substantially if a moderate requirement, $p_T^{max}(Z_1, Z_2) > m_H/3$, is applied. Harder cuts on this maximum p_T would improve even further the signal significance. The efficiency of these harder cuts for the signal events is, however, subject to possibly significant theoretical uncertainties on the p_T distribution of the Higgs boson. In addition, the ZZ continuum background is known to be subject to higher-order QCD corrections [19-49], which increase substantially the background for high values of p_T^Z.

Table 19-21 Branching ratios and production cross-sections times branching ratios for the $H \rightarrow ZZ \rightarrow 4l$ decay mode, and expected numbers of signal and background events as a function of m_H. The expected event rates are given for an integrated luminosity of 30 fb^{-1} and for two sets of selection criteria, without and with an additional cut on the p_T of the harder of the two Z-bosons ($p_T^{max}(Z_1, Z_2) > m_H/3$).

Higgs mass (GeV)	**200**	**240**	**280**	**320**	**360**	**400**	**500**	**600**
$BR(H \rightarrow ZZ)$	0.26	0.29	0.30	0.31	0.30	0.28	0.27	0.27
$\sigma \times$ BR (fb)	12.4	11.2	9.6	8.9	8.7	6.8	3.2	1.6
Signal (no p_T cut)	134	127	110	105	105	86	44	23
Background (no p_T cut)	74	57	43	33	29	29	17	15
$S/\sqrt{B}$ (no p_T cut) for 30 fb^{-1}	15.6	16.8	16.8	18.2	19.3	15.9	10.7	5.9
Signal (with p_T cut)	54	88	90	90	91	76	39	19
Background (with p_T cut)	7	15	17	16	13	14	7	6
$S/\sqrt{B}$ (with p_T cut) for 30 fb^{-1}	20.4	22.7	21.8	22.5	25.2	20.3	14.7	7.8
$S/\sqrt{B}$ (with p_T cut) for 100 fb^{-1}	37.3	40.9	40.1	41.2	46.9	37.3	27.1	15.0

In conclusion, the $H \rightarrow ZZ \rightarrow 4l$ signal would be observed easily above the $ZZ \rightarrow 4l$ continuum background after less than one year of low luminosity operation for $200 < m_H < 600$ GeV. As an example of signal reconstruction above background, Figure 19-31 shows the expected signal from a Higgs boson with $m_H = 300$ GeV for an integrated luminosity of only 10 fb^{-1}. The signal is shown before (left) and after (right) the p_T^{max} cut is applied, and is clearly visible above the background from ZZ continuum production.

For larger values of m_H, the Higgs-boson signal becomes very broad and the signal rate drops rapidly, but a signal in the $H \rightarrow ZZ \rightarrow 4l$ channel could be observed up to $m_H \sim 800$ GeV, possibly even through the WW/ZZ fusion process if jet tagging in the forward regions is required [19-13].

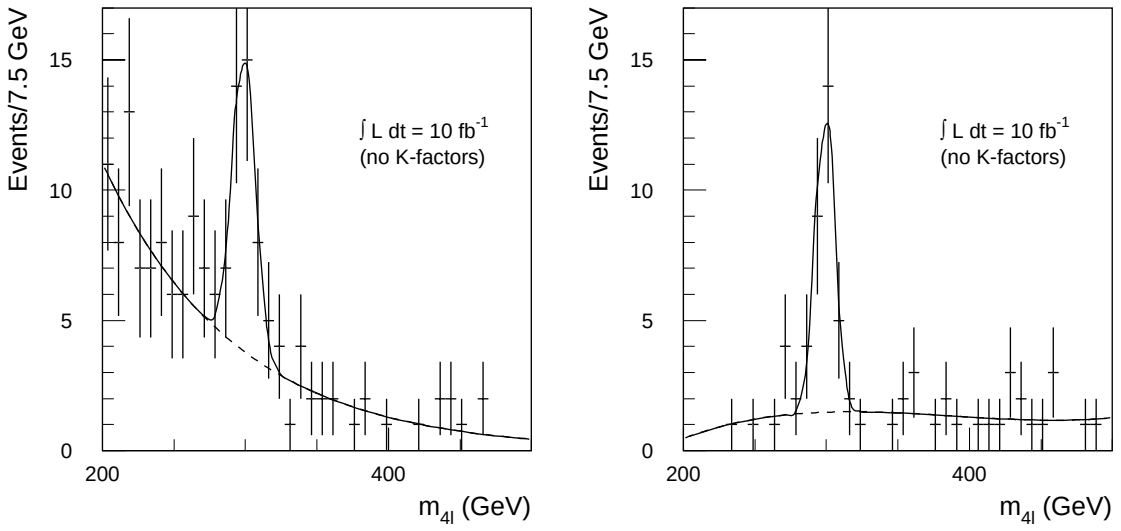

Figure 19-31 Expected $H \rightarrow ZZ \rightarrow 4l$ signal for m_H = 300 GeV and for an integrated luminosity of 10 fb^{-1}. The signal is shown on top of the ZZ continuum background before (left) and after (right) the $p_T^{max}(Z_1, Z_2)$ cut is applied (see text).

19.2.10 Heavy Higgs boson

As discussed in Section 19.2.9, the $H \rightarrow ZZ \rightarrow 4l$ decay mode can be observed up to $m_H \sim 800$ GeV, but it becomes rate-limited around $m_H = 700$ GeV. If no Higgs-boson signal were found for $m_H < 600$ - 800 GeV, searches in the TeV mass range would be essential to understand the electroweak symmetry-breaking mechanism. To access this mass range, one needs to detect Higgs-boson decays containing neutrinos or jets in the final state. If a Higgs-boson signal were found in the $H \rightarrow ZZ \rightarrow 4l$ channel, these channels could confirm the discovery and provide additional information on the Higgs couplings (WW-fusion production mechanism and $H \rightarrow WW$ decays).

The channels considered in this Section are the $H \rightarrow ZZ \rightarrow ll\nu\nu$ mode with a rate six times larger than the four-lepton mode and with a large E_T^{miss} signature, the $H \rightarrow WW \rightarrow l\nu jj$ mode with a rate 150 times larger than the four-lepton mode, and the $H \rightarrow ZZ \rightarrow lljj$ mode which has a rate 25 times larger than the four-lepton mode (six times smaller than the $H \rightarrow WW \rightarrow l\nu jj$ mode).

To reject the large QCD backgrounds in these channels excellent E_T^{miss} measurements and accurate reconstruction of $W/Z \rightarrow jj$ decays are needed. In addition, for the large values of m_H, a big fraction of the Higgs bosons are produced via gauge-boson fusion, materialised by forward-backward jets emitted at large pseudorapidities ($|\eta| > 2$). Good jet identification and energy measurements over $2 < |\eta| < 5$ are therefore essential [19-50].

19.2.10.1 *Search for $H \rightarrow ZZ \rightarrow ll\nu\nu$*

The signal in this channel is characterised by two high-p_T leptons from $Z \rightarrow ll$ decay in the central region and a large E_T^{miss} from $Z \rightarrow \nu\nu$ decay. The production cross-section times branching ratio is a few fb for $m_H \sim 500$ - 700 GeV, with a 25 - 30% contribution from vector boson fusion.

The largest background arises from reducible Z+jet production, where large E_T^{miss} can be created by neutrinos or by badly reconstructed jets due to cracks, dead material and the limited calorimeter pseudorapidity coverage. In addition, the ZZ irreducible continuum background, as well as the reducible $t\bar{t}$ and WZ/WW backgrounds have to be considered.

It has been shown in [19-51] and [19-52] (see also Section 9.2.2) that, for $E_T^{miss} > 150$ GeV, the instrumental background from jets mis-measured in the calorimeter or escaping outside the calorimeter coverage is much smaller than the background from Z+jet and ZZ production, where the E_T^{miss} is genuine (it originates from neutrinos produced in semi-leptonic decays of b-jets in the case of Z+jet production).

The selection cuts chosen for the $H \rightarrow ZZ \rightarrow ll\nu\nu$ channel are:

- Two same-flavour opposite-sign leptons with $p_T > 40$ GeV and $|\eta| < 2.5$ and no other isolated lepton.
- Z mass window: $m_{ll} = m_Z \pm 6$ GeV.
- Cut on p_T of $Z \rightarrow ll$: $p_T^{ll} >$ 150 (250) GeV for $m_H = 500$ (700) GeV.
- $E_T^{miss} > 150$ GeV.
- Forward jet tagging: one or two tag jets with $|\eta| > 2$ and $p_T > 25$ GeV.

The cumulative acceptances of these cuts, evaluated with fast simulation, are shown in Table 19-22. The efficiencies for the reconstruction of the tag jets in the signal events and the probabilities for fake tags in the background events are taken from fully simulated events [19-53][19-54] (see also Section 9.1.4).

Table 19-22 Cumulative acceptances (in %) of the various selection cuts for the $H \rightarrow ZZ \rightarrow ll\nu\nu$ signal and backgrounds.

Process	Lepton cuts	Z mass window	p_T^{ll} cut	E_T^{miss} cut	One tag jet	Two tag jets
$H \rightarrow ZZ \rightarrow ll\nu\nu$ ($m_H = 500$ GeV)	66.8	54.4	38.8	33.0	16.0	2.9
$H \rightarrow ZZ \rightarrow ll\nu\nu$ ($m_H = 700$ GeV)	70.4	57.4	45.7	41.1	21.6	4.8
ZZ continuum	36.2	29.2	1.9	1.4	0.24	0.016
WZ continuum	35.5	25.6	0.11	0.075	0.016	0.0018
WW continuum	36.7	1.1	0.005	0.002	0.001	$<< 10^{-3}$
$t\bar{t}$	3.1	0.09	0.005	3×10^{-4}	$< 10^{-5}$	$<< 10^{-5}$
Z+jets	64.0	51.6	3.4	1.6×10^{-5}	4×10^{-6}	1.3×10^{-6}

Figure 19-32 shows the E_T^{miss} distribution for the signal and various backgrounds which satisfy all the cuts of Table 19-22, including a double jet tag. The results are shown for $m_H = 600$ and 900 GeV. The signal appears as an excess of events with large E_T^{miss} above the backgrounds. After all selection cuts, including the double jet tag, the different backgrounds listed in Table 19-22 are all present (with the exception of the WW background) at approximately the same level.

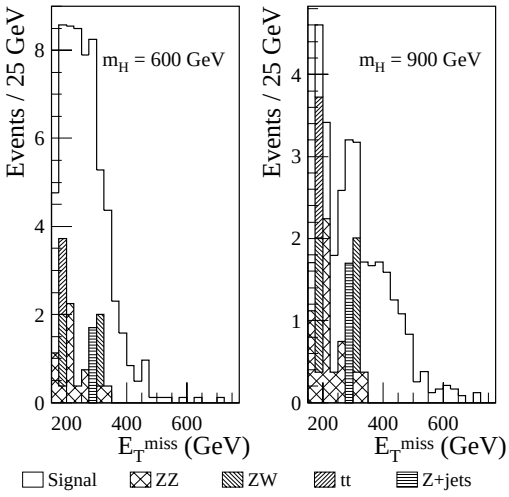

Figure 19-32 For an integrated luminosity of 100 fb^{-1} and for m_H = 600 GeV (left) and m_H = 900 GeV (right), reconstructed E_T^{miss} distribution for the $H \rightarrow ZZ \rightarrow ll\nu\nu$ signal and for the various backgrounds after requiring a double jet tag.

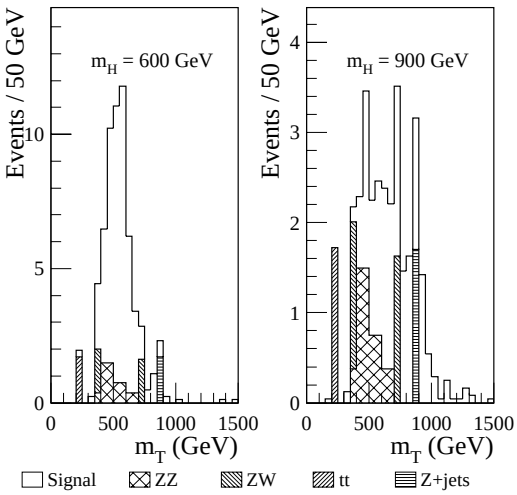

Figure 19-33 Same as Figure 19-32, but for the distribution of m_T, the transverse mass of the (ll E_T^{miss}) system.

In order to extract a more convincing signal, the transverse mass of the (ll E_T^{miss}) system, m_T, is calculated and shown in Figure 19-33. For m_H = 600 GeV, the width of the Higgs boson is still narrow enough that the peak of the m_T distribution can be observed close to the nominal Higgs-boson mass, and the signal is large with respect to the background. For m_H = 900 GeV, this is no longer the case, and a clear evidence for the signal would only be obtained if less stringent kinematic cuts (to provide a smoothly falling shape of the background as a function of E_T^{miss} or m_T) and variable jet tagging cuts (to vary the signal-to-background ratio) were studied, in a way similar to that described in more detail for the case of $H \rightarrow WW \rightarrow l\nu jj$ decays (see Section 19.2.10.2).

In addition, higher-order corrections to gauge-boson pair production (see Section 15.7.5) lead to significant increases in the background. For example, the E_T^{miss} distribution of the ZZ continuum background in Figure 19-32 corresponds to the p_T spectrum of the Z-boson decaying to a neutrino pair; for large values of E_T^{miss}, this spectrum might be underestimated by a factor of about two, in particular if the jet tagging cuts are assumed to be uncorrelated to the expected increase in rate due to the higher-order corrections.

With these caveats, the signal-to-background ratios and significances have been evaluated for the selection cuts described above and are shown in Table 19-23 as a function of the jet tagging cuts for m_H = 500 and 700 GeV and for an integrated luminosity of 100 fb^{-1}.

Without any jet tagging, the signal-to-background ratio is somewhat below one and decreases by a factor two when m_H increases from 500 to 700 GeV. The requirement of a single jet tag increases the signal-to-background ratio by a factor of about 2.5, and also increases the signal significance. As stated above, this significance does not correspond to a clear observation of a peak above a well-constrained background and should therefore be taken as an optimistic estimate. The requirement of a double jet tag further improves the signal-to-background ratio, and may be sufficient to demonstrate the discovery of a signal from $H \rightarrow ZZ \rightarrow ll\nu\nu$ decays.

Table 19-23 For an integrated luminosity of 100 fb^{-1}, expected numbers of $H \rightarrow ZZ \rightarrow ll\nu\nu$ signal and background events, signal-to-background ratios (*S/B*) and significances ($S/\sqrt{B}$), for m_H = 500 and 700 GeV and for various jet tagging cuts.

	Jet tagging	Signal	Background	*S/B*	$S/\sqrt{B}$
m_H = 500 GeV	None	707	763	0.9	25.6
	Single tag	345	147	2.4	28.5
	Double tag	66	12	5.3	18.7
m_H = 700 GeV	None	322	763	0.4	11.6
	Single tag	168	147	1.1	13.9
	Double tag	38	12	2.9	10.8

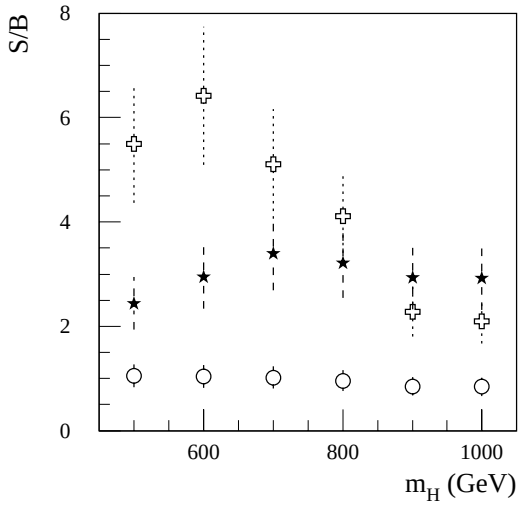

Figure 19-34 For an integrated luminosity of 100 fb^{-1} (high luminosity operation) and for the $H \rightarrow ZZ \rightarrow ll\nu\nu$ channel, optimised signal-to-background (*S/B*) ratio as a function of m_H for three jet tagging requirements: no jet tag (open circles), a single jet tag with p_T > 25 GeV (black stars), and a double jet tag with p_T > 25 GeV (open crosses).

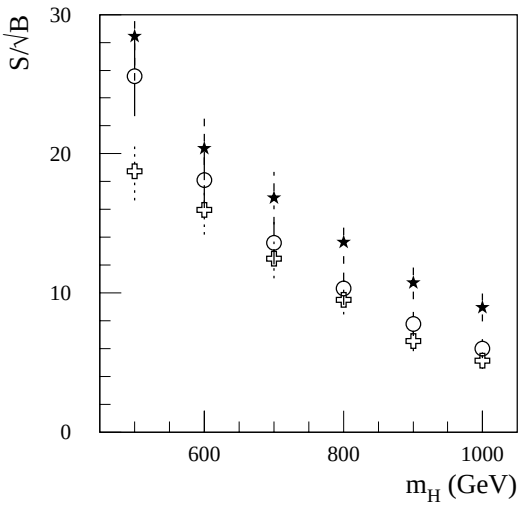

Figure 19-35 Same as Figure 19-34, but for the signal significance $S/\sqrt{B}$ as a function of m_H.

The p_T^{ll} and E_T^{miss} cuts have been varied as a function of m_H in an attempt to optimise the discovery potential of the $H \rightarrow ZZ \rightarrow ll\nu\nu$ channel over the range 400 < m_H < 1000 GeV. The results in terms of signal-to-background ratio and signal significance are shown in Figures 19-34 and 19-35, respectively, for an integrated luminosity of 100 fb^{-1}. All the results discussed above are obtained for high luminosity operation in the presence of pile-up, which affects the jet tagging efficiencies and fake tag rates (see Section 9.1.4). In the case of low luminosity operation, the signal-to-background ratios are therefore somewhat better than those of Figure 19-34, but the observability of a signal from $H \rightarrow ZZ \rightarrow ll\nu\nu$ decays would be limited to m_H < 600 GeV for an integrated luminosity of 30 fb^{-1}, due to the low rates expected after requiring a double jet tag.

If a signal is observed in this channel, the transverse mass of the (ll E_T^{miss}) system, m_T, can be used to measure the mass of the Higgs boson. Figure 19-36 shows as a crude example the variation of the average value of m_T as a function of m_H, including the expected purely statistical error for an integrated luminosity of 100 fb^{-1}.

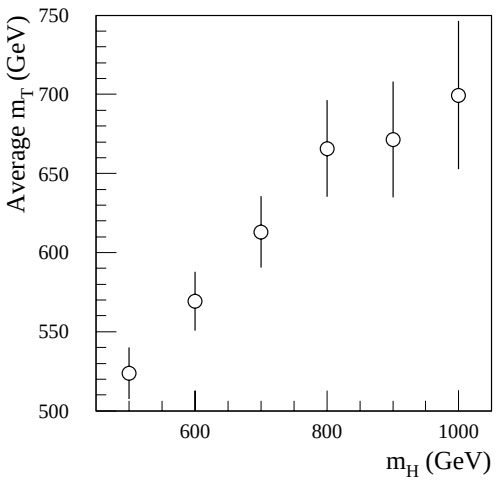

Figure 19-36 Average value of the reconstructed transverse mass, m_T, as a function of m_H, for the $H \rightarrow ZZ \rightarrow llνν$ signal with a double jet tag and for an integrated luminosity of 100 fb^{-1} (the error bars are purely statistical).

In conclusion, the $H \rightarrow ZZ \rightarrow llνν$ channel should be observable over a wide mass range from 400 to 900 GeV, and thus provide a reliable confirmation of the discovery of the Higgs boson in the gold-plated $H \rightarrow ZZ \rightarrow 4l$ channel for $m_H < 700$ GeV. For larger values of m_H, the demonstration of the observability of a convincing signal above the background requires careful studies of the evolution of the background shape as a function of the kinematic and jet tagging cuts, as well as a better understanding of the theoretical predictions for the p_T spectrum of individual vector bosons in gauge-boson pair production.

19.2.10.2 $H \rightarrow WW \rightarrow lνjj$ and $H \rightarrow ZZ \rightarrow lljj$ in $qq \rightarrow qqH$ production with $m_H \sim 1$TeV

The signal from this channel has a large enough rate to be observed during low luminosity operation and a very distinctive signature [19-55]:

- A high-p_T central lepton ($|\eta| < 2$).
- Large missing transverse energy from the escaping neutrino.
- Two high-p_T jets from the $W \rightarrow jj$ decay in the central region. Due to the large boost of the W-boson, the two jets are close-by in space ($\Delta R \sim 0.4$) and their energy deposition overlap.
- Two low-p_T tag jets in the forward regions ($|\eta| > 2$) coming from the WW/ZZ fusion production process.
- Small hadronic activity in the central region, except for the jets from $W \rightarrow jj$ decay.

The main backgrounds, before requiring any tag jets are:

- W+jet production with $W \rightarrow lν$. This background is potentially the largest and suffers from significant theoretical uncertainties due to higher-order corrections (K-factors) and to the procedure used to generate the events (see [19-56] for a comparison of the matrix-element and parton-shower approaches).
- $t\bar{t} \rightarrow lνjjb\bar{b}$ production. This background contains a real $W \rightarrow jj$ decay, but also additional hadronic activity from the b-jets when they fall in the central region.
- $WW \rightarrow lνjj$ continuum production, which has much lower rates than the W+jet and $t\bar{t}$ reducible backgrounds, but which is irreducible in the central region.

The main issues linked to the signal reconstruction and the background rejection are therefore the experimental efficiency and resolution for reconstructing high-p_T $W \to jj$ decays (see also Section 9.3.1.3) and the performance of the jet-veto cuts in the central region (see also Section 9.1.3). All the background processes will be rejected with high efficiency by the additional requirement of one or two tag jets in the forward region ($|\eta| > 2$) [19-50] and a realistic assessment of the performance of jet tagging has also to be included (see Section 9.1.4).

A set of cuts, called high-p_T central cuts, which are optimised exclusively in terms of the statistical significance of the signal above the background, without any study of the actual visibility of the signal, is used in the first stage of the analysis:

- Lepton cuts: p_T^l, $E_T^{miss} > 100$ GeV, $p_T^{W \to l\nu} > 350$ GeV.
- Jet cuts: two jets reconstructed within $\Delta R = 0.2$ with $p_T > 50$ GeV and $p_T^{W \to jj} > 350$ GeV.
- W mass window: $m_{jj} = m_W \pm 2\sigma$, where σ is the resolution on m_{jj} (see below).

Table 19-24 shows the cumulative efficiencies for $H \to WW \to l\nu jj$ decays with $m_H = 1$ TeV, as obtained for the high-p_T central cuts described above, for fast simulation compared to full simulation and reconstruction. The results are in good agreement for all cuts, and the full-simulation studies without and with pile-up show that these efficiencies are not affected strongly by pile-up, except possibly for the mass window on the W mass (see below).

Table 19-24 For the $H \to WW \to l\nu jj$ channel with $m_H = 1$ TeV, comparison of the cumulative efficiencies of the high-p_T central cuts (see text) for the fast and the full simulation and for low luminosity operation (no pile-up) and high luminosity operation (with pile-up).

Cuts	Fast simulation	Full simulation (no pile-up)	Full simulation (with pile-up)
Lepton cuts	43.3%	42.6%	42.6%
Jet cuts	29.0%	29.8%	29.8%
W mass window (no pile-up)	25.2%	24.8%	
W mass window (with pile-up)	23.6%		24.4%

The reconstruction of high-p_T $W \to jj$ decays is described in detail in Section 9.3.1.3. Various methods to overcome the problems of jet overlap and to optimise the resolution on the reconstructed W mass have been studied [19-54], and the one chosen for the studies reported here calculates the mass of the two jets, selected within a cone of size $\Delta R = 0.2$ and with $p_T > 50$ GeV, by using the four-momenta of each calorimeter cell (assumed to have zero mass) in two cones of size $\Delta R = 0.4$ with barycentres determined by the cones of size $\Delta R = 0.2$. Figure 19-37 shows the distributions of the reconstructed dijet mass with this method in the case of low luminosity operation (no pile-up) and of high luminosity operation (with pile-up). The distributions are obtained from a sample of fully simulated and reconstructed $H \to WW \to l\nu jj$ decays, and have been corrected as a function of the p_T of the dijet system for the systematic bias due to the finite size of hadronic showers, which results in a linear increase of the measured W mass as a function of the p_T of the W-boson (see Section 9.3.1.3).

Figure 19-37 shows that the resolution σ increases only from 5.0 GeV to 6.9 GeV when pile-up at high luminosity is added. The fraction of $W \to jj$ decays with $m_{jj} = m_W \pm 2\sigma$ decreases from 83% without pile-up to 82% with pile-up. The results for these efficiencies are also in good agreement between the fast and full simulation, as shown in Table 19-24.

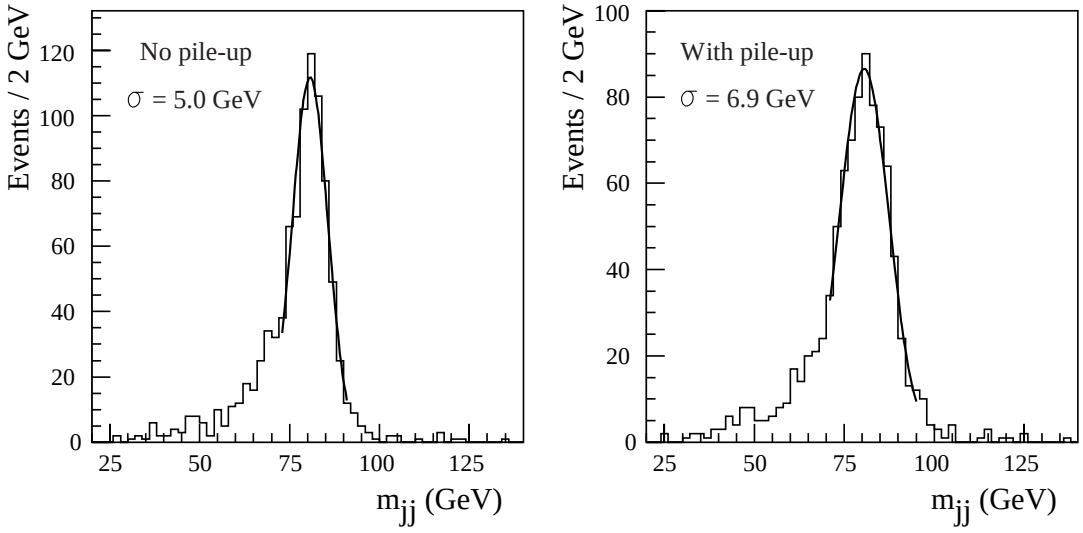

Figure 19-37 For fully simulated and reconstructed $H \rightarrow WW \rightarrow l\nu jj$ decays with m_H = 1 TeV, distributions of the dijet mass using the mass reconstruction method described in the text for low-luminosity operation (left) and high-luminosity operation (right).

Table 19-25 shows the numbers of signal and background events produced for an integrated luminosity of 30 fb^{-1}, the cumulative efficiencies of the high-p_T central cuts, and the numbers of events accepted after these cuts. Additional cuts are clearly needed, as mentioned above (jet veto in the central region and jet tagging in the forward regions).

Table 19-25 Numbers of events produced for an integrated luminosity of 30 fb^{-1} and cumulative efficiencies of the high-p_T central cuts (see text), as obtained from fast simulation for the $H \rightarrow WW \rightarrow l\nu jj$ signal with m_H = 1 TeV and for the $t\bar{t}$ and W+jet backgrounds.

	Higgs signal	**$t\bar{t}$ (p_T > 300 GeV)**	**W + jets (p_T > 250 GeV)**
Events produced	486	192 000	448 000
Efficiency of lepton cuts	43.3%	6.2%	11.5%
Efficiency of jet cuts	29.0%	3.3%	2.3%
Efficiency of W mass window	25.2%	1.0%	0.52%
Events accepted	122	1900	2300

Jet profile and asymmetry cuts have been investigated [19-54], to explore whether any significant additional rejection can be obtained against the dominant W+jet background. For the latter background the dijet system reconstructed with $m_{jj} = m_W \pm 2\sigma$ does not originate from the decay of a colour singlet and the jets are therefore expected to be broader than in the case of a real $W \rightarrow jj$ decay. Unfortunately, efficient cuts against the W+jet background would substantially bias the final mass distributions used to extract the signal (as described below) and this approach has not been pursued any further.

The performance of jet-veto cuts in the central region is described in detail in Section 9.1.3 as a function of the p_T threshold. Section 9.1.3 also compares the results from fast simulation to those from full simulation and reconstruction. The efficiency for signal events is found to be about 5% higher for fast simulation and is about 60% for a central jet veto ($|\eta| < 2$) with a p_T threshold of 25 GeV at low luminosity. The rejection of the $t\bar{t}$ background events is in excellent agreement between fast and full simulation.

This is illustrated in Figure 19-38 using a fast simulation, of the $H \rightarrow WW \rightarrow l\nu jj$ signal and of the $t\bar{t}$ and W+jet backgrounds. Efficiency here is defined as the fraction of events with no additional jet with p_T larger than threshold. The p_T thresholds chosen here are 15 GeV at low luminosity and 25 GeV at high luminosity, such that the efficiency for the $H \rightarrow WW \rightarrow l\nu jj$ signal is about 55%. The efficiency for the W+jet background is significantly lower than for the Higgs-boson signal because of the larger jet activity in these events. Finally, the central jet-veto cut provides a rejection factor of 10-15, depending on the p_T threshold at low and high luminosity, against the $t\bar{t}$ background which always has two additional b-jets in the final state.

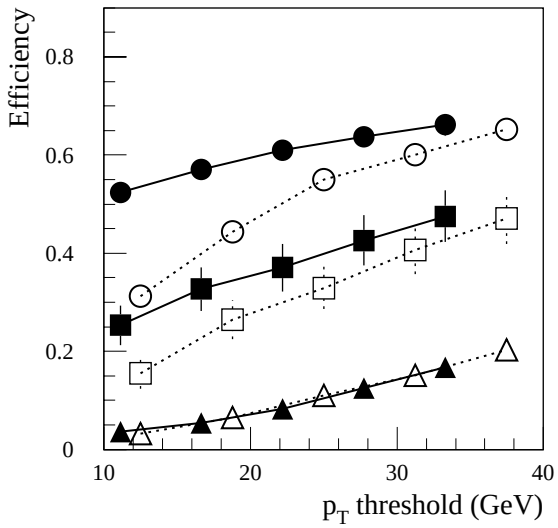

Figure 19-38 Efficiency of the central jet-veto cut as a function of the p_T threshold, as obtained from the fast simulation after the high-p_T central cuts (see text), for the $H \rightarrow WW \rightarrow l\nu jj$ signal (circles), the $t\bar{t}$ background (triangles) and the W+jet background (squares). The results are shown both without pile-up (black symbols) and with pile-up (open symbols).

Table 19-26 For an integrated luminosity of 30 fb^{-1} and for the $H \rightarrow WW \rightarrow l\nu jj$ channel with m_H = 1 TeV and 800 GeV, expected numbers of produced and accepted signal and background events, signal-to-background ratios and signal significances. The events are accepted if they pass all cuts, namely the high-p_T central cuts, the central jet veto and a double jet tag E_{tag} > 300 GeV (see text).

	Higgs signal	**$t\bar{t}$ (p_T > 300 GeV)**	**W+jets (p_T > 250 GeV)**	**WW (p_T > 50 GeV)**	**S/B**	**$S/\sqrt{B}$**
Events produced		192 000	448 000	255 000		
m_H = 1 TeV	486					
m_H = 800 GeV	1000					
Events accepted						
m_H = 1 TeV	37.9	3.3	9.2	1.0	2.8	10.3
m_H = 800 GeV	43.5	3.3	9.2	1.0	3.2	11.8

The final step of the event selection requires forward jet tagging (see [19-54] and Section 9.1.4 for details). The study is based on fully simulated and reconstructed events and includes the most up-to-date geometry of the forward calorimeters and a jet-finding algorithm optimised to minimise the effects of pile-up in the forward regions. The results presented in Section 9.1.4

show that the efficiency for reconstructing the tag jets is in agreement between fast and full simulation over $2 < |\eta| < 4$. For $|\eta| > 4$, the finite size of hadronic showers degrades the efficiency significantly and this effect has been corrected for in the fast simulation.

For the choice of a double jet tag requiring $E_{\mathrm{tag}} > 300$ GeV for both jets, the results are presented in Tables 19-26, for an integrated luminosity of 30 fb^{-1}. The expected numbers of produced and accepted signal events are shown for the $H \rightarrow WW \rightarrow l\nu jj$ signal with $m_H = 800$ and 1000 GeV. The same numbers are presented for the $t\bar{t}$, W+jet and WW backgrounds, which were generated with appropriate thresholds set on the p_{T} of the hard-scattering process. It is important to note that at the high luminosity the inclusion of all relevant pile-up effects and the use of a higher p_{T} threshold for the jet-veto cut reduces the signal-to-background ratio.

Large signal significances with a signal-to-background ratio around three can be obtained even at low luminosity. These values are optimistic, since the background rates suffer from significant uncertainties, but most of all because the broad signal expected from $H \rightarrow WW \rightarrow l\nu jj$ decays is difficult to separate clearly from the background. This is illustrated in Figure 19-39, which shows as an example the reconstructed spectrum of the invariant mass of the ($l\nu jj$) system, m_{lvjj}, summed for the $H \rightarrow WW \rightarrow l\nu jj$ signal with $m_H = 1$ TeV and for the backgrounds. The distributions are shown separately for the background and the summed signal+background, for an integrated luminosity of 30 fb^{-1} and for somewhat looser jet tagging cuts requiring two tag jets with $E_{\mathrm{tag}} > 100$ GeV. The signal and background shapes are very similar. This is due to the very strict central cuts applied to the reconstructed $W \rightarrow l\nu$ and $W \rightarrow jj$ decays. The thresholds of 350 GeV applied to ${p_{\mathrm{T}}}^{W \rightarrow l\nu}$ and ${p_{\mathrm{T}}}^{W \rightarrow jj}$ remove most of the background with $m_{\mathrm{lvjj}} < 800$ - 900 GeV.

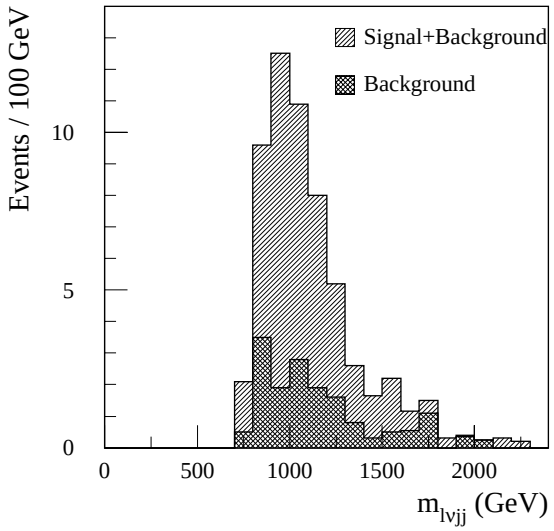

Figure 19-39 For an integrated luminosity of 30 fb^{-1} and for the $H \rightarrow WW \rightarrow l\nu jj$ channel with $m_H = 1$ TeV, distribution of reconstructed mass of the $l\nu jj$ system, m_{lvjj}, for the background (dark shaded histogram) and for the summed signal and background (light shaded histogram) after applying the high-p_{T} central cuts (see text), a central jet veto and a double jet tag ($E_{\mathrm{tag}} > 100$ GeV).

For the above reasons, a looser set of kinematic cuts in the central region, called loose central cuts, is defined:

- Lepton cuts: ${p_{\mathrm{T}}}^{l}$, ${E_{\mathrm{T}}}^{\mathrm{miss}} > 50$ GeV, ${p_{\mathrm{T}}}^{W \rightarrow l\nu} > 150$ GeV.
- Jet cuts: two jets reconstructed within $\Delta R = 0.2$ with $p_{\mathrm{T}} > 50$ GeV and ${p_{\mathrm{T}}}^{W \rightarrow jj} > 150$ GeV.
- W mass window: $m_{jj} = m_W \pm 2\sigma$, where σ is the resolution on m_{jj}.

The central jet-veto cut is applied with a p_{T} threshold of 20 GeV at low luminosity and two tag jets are required with $E_{\mathrm{tag}} > 300$ GeV. The results are shown in Table 19-27 for an integrated luminosity of 30 fb^{-1} and for $m_H = 1$ TeV. Table 19-27 shows the numbers of events produced, the acceptances of the loose central cuts, of the central jet veto and of the double jet tag, together with the numbers of events passing the successive sets of cuts for the signal and the various backgrounds.

Table 19-27 For an integrated luminosity of 30 fb^{-1} and for the $H \to WW \to l\nu jj$ channel with m_H = 1 TeV, expected numbers of signal and background events as a function of the cuts applied (see text). The acceptances and event rates are given separately for the loose central cuts, the central jet veto and the double jet tag.

	Higgs signal (m_H = 1 TeV)	**$t\bar{t}$ (p_T > 120 GeV)**	**W+jets (p_T > 100 GeV)**	**WW (p_T > 50 GeV)**
Events produced	486	2 250 000	10 400 000	255 000
After loose central cuts:				
Acceptance	45.7%	1.7%	0.15%	0.8%
Events	222	38,300	15,700	2070
After central jet veto (p_T > 20 GeV):				
Acceptance	64.5%	7.4%	44.0%	56.4%
Events	143	2800	6900	1170
After double jet-tag (E_{tag} > 300 GeV):				
Acceptance	50.7%	3.0%	0.9%	0.3%
Events	73	85	62	3

Compared to the results shown in Table 19-26 for the high-p_T central cuts, the signal-to-background ratio has degraded from about 3:1 to about 1:2 and the overall signal rate has increased by a factor 2. The choice of looser central cuts provides nevertheless the possibility to demonstrate the existence of a Higgs-boson signal from a study of the reconstructed invariant mass of the ($l\nu jj$) system, m_{lvjj}. Figure 19-40 shows the distribution of m_{lvjj} before and after the double jet tag is required for m_H = 1 TeV. The broad signal from $H \to WW \to l\nu jj$ decays now clearly emerges from the background, which is unbiased down to values of m_{lvjj} around 500 GeV.

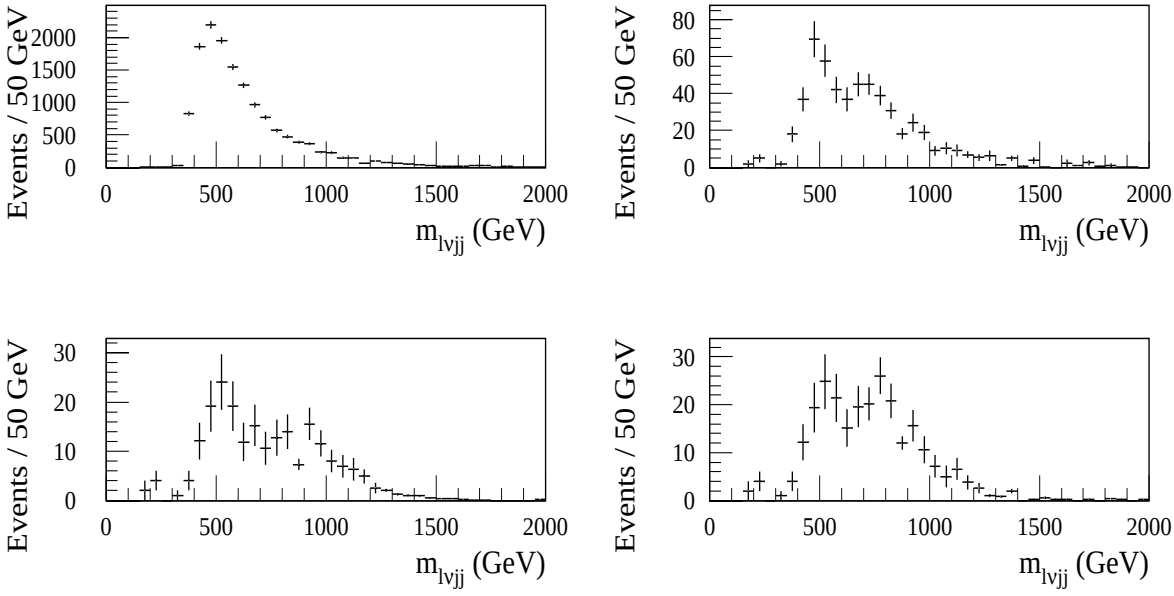

Figure 19-40 For an integrated luminosity of 30 fb^{-1} and for m_H = 1 TeV, distribution of m_{lvjj} for the summed signal+background before jet tagging cuts (top) and after requiring two tag jets with E_{tag} > 300 GeV (bottom). The results are obtained for the loose central cuts (see text).

Figure 19-41 For an integrated luminosity of 30 fb^{-1} and for m_H = 800 GeV, distribution of m_{lvjj} for the summed signal+background after requiring two tag jets with E_{tag} > 200 GeV (top) and E_{tag} > 400 GeV (bottom). The results are obtained for the loose central cuts (see text).

Figure 19-41 shows for m_H = 800 GeV, that the emergence of the signal can be further demonstrated by varying the energy threshold on the tag jets around its nominal value. As the threshold increases, the ratio between the signal peak around m_H and the kinematic peak of the background around 500 GeV increases significantly, thereby demonstrating the very different nature of the production mechanisms for the signal and background processes.

Preliminary studies have been done how well one could extract the main parameters of the observed resonance, namely its mass, width and height. A simple exponential fit is used for the m_{lvjj} distribution of the background and the signal shape is fitted to a Breit-Wigner with a width proportional to m_H^3. The results obtained for an integrated luminosity of 30 fb^{-1} indicates that the Higgs-boson mass would be measured with a statistical accuracy of about 5% and the signal rate would be measured to about 20%. A better description of the line shape of a very heavy Higgs boson would of course be needed to evaluate the systematic uncertainties on these difficult measurements of $H \rightarrow WW \rightarrow l\nu jj$ with $m_H \sim 1$ TeV.

The $H \rightarrow ZZ \rightarrow lljj$ channel cannot compete with the $H \rightarrow WW \rightarrow l\nu jj$ channel, since its rate is about six times lower. Nevertheless, it does not suffer from any significant $t\bar{t}$ background, and could be used for integrated luminosities above 100 fb^{-1} to confirm the observation of a signal in the $H \rightarrow WW \rightarrow l\nu jj$ channel, and thereby to compare the couplings of the Higgs boson to W and Z bosons.

Table 19-28 For an integrated luminosity of 100 fb^{-1} and for the $H \rightarrow ZZ \rightarrow lljj$ channel with m_H = 1 TeV and 800 GeV, expected numbers of produced and accepted signal and background events, signal-to-background ratios and signal significances. The events are accepted if they pass all cuts, namely the high-p_T central cuts, the central jet veto, and a double jet tag with E_{tag} > 600 GeV or E_{tag} > 300 GeV. Also shown are the results from full simulation and reconstruction for E_{tag} > 300 GeV.

	Higgs signal	Z+jets (p_T > 100 GeV)	S/B	Significance (Poisson)
Events produced		4 600 000		
m_H = 1 TeV	260			
m_H = 800 GeV	540			
m_H = 1 TeV				
E_{tag} > 600 GeV	9.2	2	4.6	4.3
E_{tag} > 300 GeV	17.3	8	2.2	4.7
Full simulation with pile-up (E_{tag} > 300 GeV)	14.7	18	0.8	2.9
m_H = 800 GeV				
E_{tag} > 600 GeV	9.4	2	4.7	4.3
E_{tag} > 300 GeV	19.2	8	2.4	5.2
Full simulation with pile-up (E_{tag}> 300 GeV)	16.3	18	0.9	3.3

The extraction of the signal proceeds along exactly the same lines as for the $H \rightarrow WW \rightarrow l\nu jj$ channel [19-55], except that a narrow mass window around the nominal Z mass is applied to the invariant mass of the lepton pairs. The only significant background then arises from Z+jet production, and the expected event rates before cuts and after all cuts, including a double jet tag with E_{tag} > 300 GeV and E_{tag} > 600 GeV, are shown in Table 19-28 for an integrated luminosity of 100 fb^{-1} and for the high-p_T central cuts described in the previous Section.

Since high-luminosity operation is discussed here, Table 19-28 also shows the results obtained from full simulation and reconstruction including pile-up. The efficiency of the jet-tagging cuts is 15% lower than that obtained with fast simulation and the background increases by a factor two due to fake tag jets.

In conclusion, the $H \rightarrow ZZ \rightarrow lljj$ channel with $m_H \sim 1$ TeV can only be observed for the ultimate integrated luminosity of 300 fb^{-1} presently envisaged for ATLAS.

19.2.10.3 $H \rightarrow WW \rightarrow l\nu jj$ for $m_H <$ 800 GeV

The results presented in Section 19.2.10.2 naturally call for an extension of the search for $H \rightarrow WW \rightarrow l\nu jj$ decays for Higgs-boson masses below 800 GeV. A very similar study has therefore been performed for m_H = 600 GeV [19-57].

- As shown in Table 19-29, central cuts on the reconstructed $W \rightarrow l\nu$ and $W \rightarrow jj$ decays are applied. These cuts have to be relaxed with respect to the values used for m_H = 1 TeV and the signal-to-background ratio is therefore much worse in this case.
- Although the same method is used for the $W \rightarrow jj$ reconstruction as that described in the case of $m_H \sim 1$ TeV, the cone size for the calculation of m_{jj} using the cells has to be increased from $\Delta R = 0.4$ to $\Delta R = 0.8$, since the boost of the W boson decreases as m_H decreases (see also Section 9.3.1).
- The central jet-veto cuts are the same as for m_H = 1 TeV (threshold of 15 GeV at low luminosity and of 25 GeV at high luminosity).
- Two forward tag jets are required and the signal observability is studied as a function of the energy threshold, E_{tag}, applied to these jets.

Table 19-29 Efficiencies of the central cuts at low luminosity and numbers of signal and background events accepted after all cuts, for an integrated luminosity of 30 fb^{-1} and for the $H \rightarrow WW \rightarrow l\nu jj$ channel with m_H = 600 GeV.

Cuts	Higgs signal	$t\bar{t}$	W+jets
Lepton cuts	58%	9.8%	2.7%
Jet cuts	68%	21.2%	4.3%
Events accepted	733	93 000	68 000

Tables 19-30 and 19-31 show the expected signal and background rates, before and after the successive cuts, respectively for integrated luminosities of 30 fb^{-1} (low-luminosity operation) and 100 fb^{-1} (high-luminosity operation). As already stated, jet tagging in the forward regions is necessary to achieve a sufficiently high signal-to-background ratio. The signal appears to be observable even for an integrated luminosity of 30 fb^{-1}.

This is confirmed by studying the shape of the m_{lvjj} spectrum. In contrast to Section 19.2.10.2, where the Higgs-boson width entirely dominates the quality of the reconstruction of the signal peak, the experimental resolution on m_{lvjj} begins to play a significant role for m_H = 600 GeV. The experimental resolution is approximately 40 GeV at low luminosity and 46 GeV at high luminosity, as obtained from full simulation and reconstruction. The dominant contributions to the experimental resolution arise from the $W \rightarrow jj$ mass resolution, the $E_{\mathrm{T}}^{\mathrm{miss}}$ resolution, and the reconstruction of the longitudinal momentum of the neutrino using the W-mass constraint. The overall experimental resolution is comparable to the effective rms of the Higgs-boson width, $\Gamma_{\mathrm{H}}^{\mathrm{tot}} \sim 120$ GeV. Figures 19-42 and 19-43 show the distribution of m_{lvjj} for the background and for the summed signal+background, respectively for integrated luminosities of 30 fb^{-1} and 100 fb^{-1}. In both cases, the signal is clearly visible above the background, which peaks around 500 GeV.

Table 19-30 For an integrated luminosity of 30 fb^{-1} (low-luminosity operation) and for $H \to WW \to l\nu jj$ decay with m_H = 600 GeV, expected numbers of signal and background events before cuts, after central cuts, after jet-veto cut and after requiring a double jet tag (see text). Also shown are the signal-to-background ratios and the signal significances.

Cuts	Higgs signal	$t\bar{t}$	W+jets	S/B	$S/\sqrt{B}$
Events produced	1860	4 440 000	56 820 000	0.00003	0.23
After central cuts	733	93 000	68 000	0.005	1.8
After central jet veto (p_T > 15 GeV)	466	6 200	29 000	0.013	2.5
After double jet-tag:					
E_{tag} > 100 GeV	323	680	1530	0.06	6.9
E_{tag} > 400 GeV	187	145	570	0.26	7.0
E_{tag} > 600 GeV	114	45	280	0.35	6.3

Table 19-31 Same as Table 19-30, but for an integrated luminosity of 100 fb^{-1} (high-luminosity operation)

Cuts	Higgs signal	$t\bar{t}$	W+jets	S/B	$S/\sqrt{B}$
Events produced	6200	14 800 000	189 400000	0.00003	0.43
After central cuts	2470	340 000	240 000	0.004	3.2
After central jet veto (p_T > 25 GeV)	1500	17 000	84 000	0.015	4.7
After double jet-tag:					
E_{tag} > 100 GeV	1060	3100	5900	0.11	11.0
E_{tag} > 400 GeV	642	1200	1470	0.26	12.9
E_{tag} > 600 GeV	398	460	630	0.36	12.0

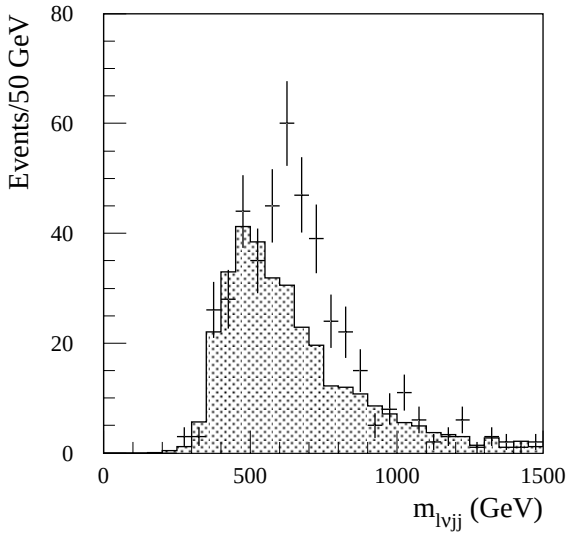

Figure 19-42 For an integrated luminosity of 30 fb^{-1} and for $H \to WW \to l\nu jj$ decays with m_H = 600 GeV, distribution of $m_{l\nu jj}$ for the background (shaded histogram) and for the summed signal+background (points with error bars).

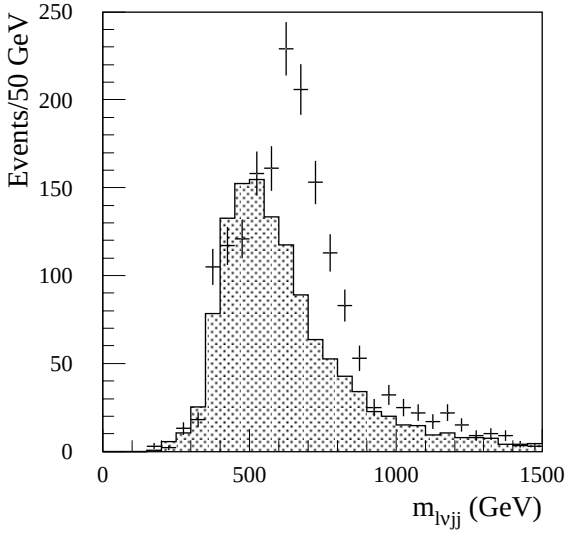

Figure 19-43 Same as Figure 19-42, but for an integrated luminosity of 100 fb^{-1}.

Finally, the study of the $H \rightarrow WW \rightarrow l\nu jj$ channel has been repeated for m_H = 300 GeV [19-57], to evaluate the overlap of this channel with the $H \rightarrow ZZ \rightarrow 4l$ and $H \rightarrow ZZ \rightarrow ll\nu\nu$ channels. For m_H = 300 GeV, the $W \rightarrow jj$ decays can be reconstructed using standard techniques, but the kinematic cuts have to be loosened even further, leading to an even lower signal-to-background ratio. Nevertheless, with the help of tight jet-veto and jet-tagging cuts, the signal can be observed above the background, as shown in Figure 19-44. The very similar shapes of the signal and background lead to the conclusion that this channel can only be used for confirmation of a discovery in another channel for m_H = 300 GeV.

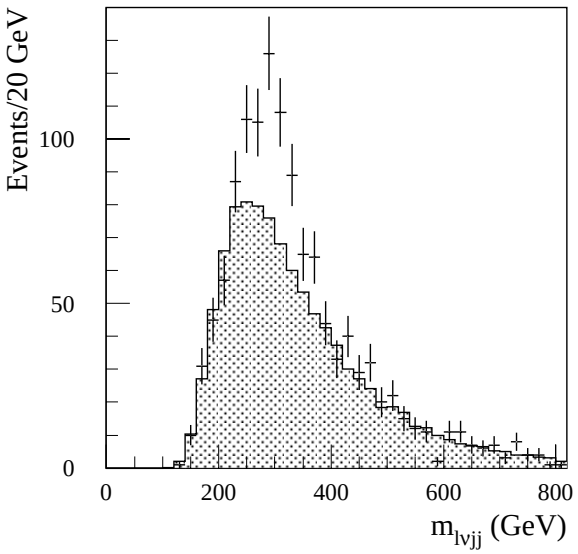

Figure 19-44 Same as Figure 19-42, but for m_H = 300 GeV.

19.2.10.4 Conclusions

The studies described above demonstrate that the SM Higgs boson would be observable in the $H \rightarrow ZZ \rightarrow ll\nu\nu$, $H \rightarrow ZZ \rightarrow lljj$ and $H \rightarrow WW \rightarrow l\nu jj$ decay modes, over most of the mass range from 300 GeV to 1 TeV. This can be achieved only through the requirement of two tag jets in the forward regions ($2 < |\eta| < 5$), which selects the $qq \rightarrow qqH$ production process and strongly reject the backgrounds from $t\bar{t}$ and W/Z+jet production.

The critical issues concerning the detector performance in these channels are the reconstruction of high-p_T $W \rightarrow jj$ decays, the efficiency of tight jet-veto cuts as a function of luminosity, the instrumental tails in the E_T^{miss} distribution from mis-measured jets, and the performance of jet tagging in the forward calorimeters. All these issues have been studied with full simulation and reconstruction, and the physics performance estimates have been updated to account for the results of these detailed studies.

The most recent efforts have concentrated on demonstrating the observability of the signal from $H \rightarrow WW \rightarrow l\nu jj$ decays above the background by using the reconstructed distribution of the mass of the $l\nu$jj system. At the same time, a first study of the sensitivity to the Higgs-boson mass, width and cross-section has been performed.

19.2.11 Overall sensitivity to the SM Higgs searches

The overall sensitivity for the discovery of a Standard Model Higgs boson over the mass range from ~80 GeV to ~1 TeV is shown in Figure 19-i. The sensitivity is given in units of $S/\sqrt{B}$ for the individual channels as well as for the combination of the various channels, assuming integrated luminosities of 30 and 100 fb^{-1}. A Standard Model Higgs boson can be discovered in the ATLAS experiment over the full mass range up to ~1 TeV with a high significance. A 5σ-discovery can already be achieved over the full mass range after a few years of running at low luminosity. As

already mentioned, no *K*-factors have been included in the evaluation of the signal significance. This is a conservative assumption, provided the *K*-factor for the signal process of interest is larger than the square root of the *K*-factor for the corresponding background process.

The requirements on the detector performance are the most demanding for the discovery of a Standard Model Higgs boson in the intermediate mass range, $80 < m_H < 2m_Z$, as discussed in Section 19.2.8. For $m_H > 2m_Z$, the dominant discovery channel is the four-lepton channel. In this case, the background is small and dominated by irreducible ZZ continuum production. For $m_H > 300$ GeV the requirements on the detector performance are rather modest in this channel, since the Higgs width is larger than the detector resolution. A high-significance discovery of the Higgs boson can be achieved for Higgs-boson masses up to 600 GeV over less than one year of data-taking at low luminosity.

A Standard Model Higgs boson in the mass range between 400 GeV and about 1 TeV would also be discovered with the $H \rightarrow WW \rightarrow l\nu jj$ mode providing the best discovery potential in this mass range. The good sensitivity to this channel for lower masses, provides independent and complementary information to the four-lepton channel. For $400 < m_H < 900$ GeV, the $H \rightarrow WW \rightarrow l\nu jj$ channel is complemented by the $H \rightarrow ZZ \rightarrow lljj$ and $H \rightarrow ZZ \rightarrow ll\nu\nu$ channels, which would provide additional robustness to a Higgs-boson discovery in this mass range.

As can be seen from Figure 19-i, at least two discovery channels are available over most of the Higgs-boson mass range. A comparison of the various production rates would provide valuable information for the determination of the Higgs-boson parameters, as discussed in the next Section.

19.2.12 Determination of the SM Higgs-boson parameters

Assuming that a Standard Model Higgs boson will have been discovered at the LHC, the ATLAS potential for the precision measurement of the Higgs parameters (mass, width, production rates, branching ratios) [19-58] is discussed in this section. Such measurements should give further insights into the electroweak symmetry-breaking mechanism and into the way the Higgs couples to fermions and bosons, and in some cases should allow a distinction between a SM and a MSSM Higgs boson (see also [19-59]).

The results presented here are limited to the mass region between 80 GeV and 700 GeV. For larger masses, the Higgs resonance becomes very broad ($\Gamma_H > 200$ GeV) and therefore precision measurements are meaningless. An integrated luminosity of 300 fb^{-1} is assumed in the following.

19.2.12.1 Measurement of the Higgs-boson mass

The ultimate experimental precision with which ATLAS should be able to measure the Higgs-boson mass is shown in Figure 19-45. The results obtained in the various decay channels, as well as the combination of all channels, are given. The quoted precision includes the statistical error in the determination of the peak position, coming from both the limited number of signal events and the error on the background subtraction (the background is assumed to be flat under the peak), and the systematic error on the absolute energy scale. The latter is assumed to be 0.1% for decay channels which contain leptons or photons (*e.g.* $H \rightarrow \gamma\gamma$, $H \rightarrow ZZ^{(*)} \rightarrow 4l$) and 1%

for decay channels containing jets (*e.g.* $H \rightarrow b\bar{b}$). Although the ATLAS goal is to determine the lepton energy scale to 0.02% (see Chapter 12 and Section 16.1), a more conservative error of 0.1% has been assumed as a baseline in this study.

For comparison, the precision of the Higgs-boson mass measurement has also been determined assuming a systematic uncertainty of 0.02% for the electromagnetic energy scale.

Figure 19-45 indicates that the Higgs mass can be measured with a precision of 0.1% up to masses of about 400 GeV if a scale uncertainty of ±0.1% is assumed. This number could be slightly improved in the mass range between ~150 and ~300 GeV if instead a better-scale uncertainty of ±0.02% could be achieved. For larger masses, the precision deteriorates because the Higgs-boson width becomes large and the statistical error increases. However, even for masses as large as 700 GeV, the Higgs-boson mass can be measured with an accuracy of 1%.

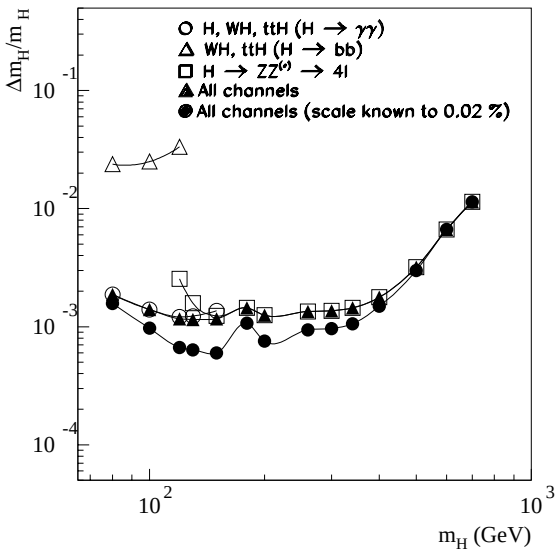

Figure 19-45 Relative precision $\Delta m_H/m_H$ on the measured Higgs-boson mass as a function of m_H, assuming an integrated luminosity of 300 fb^{-1}. The different open symbols correspond to different individual channels. The black triangles (black circles) correspond to the combination of all channels for an overall uncertainty of 0.1% (0.02%) on the absolute scale of the EM Calorimeter.

The precision of the measurement is determined by the four-lepton and two-photon channels, whereas the $H \rightarrow b\bar{b}$ channel contributes very little. This is due to both the larger systematic error on the absolute jet scale compared to the absolute lepton / photon scale and the larger statistical error because of worse mass resolution (~20 GeV for $H \rightarrow b\bar{b}$, compared to ~1.5 GeV for $H \rightarrow \gamma\gamma$ and $H \rightarrow ZZ^* \rightarrow 4l$).

No theoretical errors are included in the results presented in Figure 19-45. The uncertainty resulting from uncertainties on the structure functions is expected to be much smaller than 10 MeV [19-60]. A potentially larger error may come from the fact that, for $m_H > 700$ GeV, when the Higgs-boson width becomes large, interference effects between the resonant and the non-resonant processes tend to shift the position of the Higgs-boson peak towards lower values [19-49].

19.2.12.2 Measurement of the Higgs-boson width

The Higgs-boson width, Γ_H^{tot}, can be experimentally obtained from a measurement of the width of the reconstructed Higgs peak, after unfolding the contribution of the detector resolution. This direct measurement is only possible for Higgs-boson masses larger than 200 GeV, above which the intrinsic width of the resonance becomes comparable to or larger than the experimental mass resolution. This is the mass region covered mainly by $H \rightarrow ZZ \rightarrow 4l$ decays.

The ultimate precision on Γ_H, which can be achieved by ATLAS, is shown in Figure 19-46. These results include the statistical uncertainty coming from the number of signal events, and the systematic uncertainty coming from the measurement of the peak width and the knowledge of the detector energy and momentum resolution. In both cases, the systematic error is dominated by the uncertainty on the radiative decays and has been conservatively assumed to be 1.5% (see Section 16.1). As discussed in more detail in Section 16.1, the detector resolution will be obtained from the measurement of the Z width. The systematic uncertainty on the background subtraction has been neglected in this case since the signal-to-background ratio is large over most of the mass region relevant for this measurement.

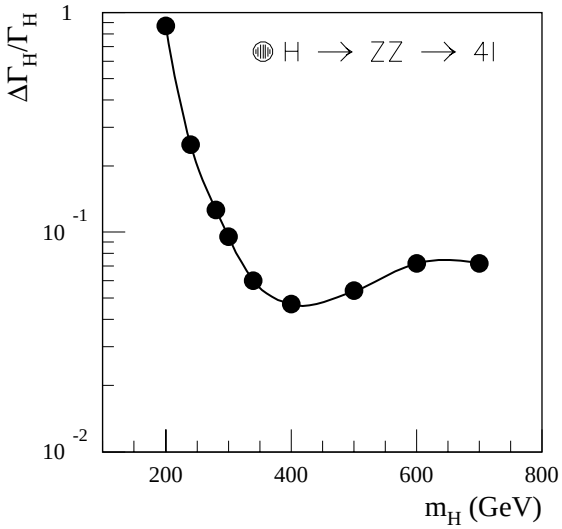

Figure 19-46 Relative precision $\Delta\Gamma_H/\Gamma_H$ on the measured Higgs-boson width as a function of m_H, assuming an integrated luminosity of 300 fb^{-1}.

Figure 19-46 shows that the precision improves with the Higgs-boson mass up to masses of ~300 GeV. For the higher masses the intrinsic width becomes larger and its contribution to the total resolution dominates compared to the detector resolution. Over the range $300 < m_H < 700$ GeV, the precision of the measurement is approximately constant and of the order of 6%.

19.2.12.3 Measurement of the Higgs-boson rate

The measurement of the Higgs-boson rate in a given decay channel provides a measurement of the production cross-section times the decay branching ratio for that channel. Such measurement in some cases would help to disentangle between SM and MSSM Higgs scenarios as discussed in Section 19.3.2.4.

The statistical error on such measurements is expected to be smaller than 10% over the mass region 120 - 600 GeV using the $\gamma\gamma$, $b\bar{b}$ and $4l$ final states. The main systematic error comes from the knowledge of the luminosity (see Chapter 13). Two values have been considered for the luminosity uncertainty: 5%, a somewhat ambitious goal, and 10% (a more conservative estimate).

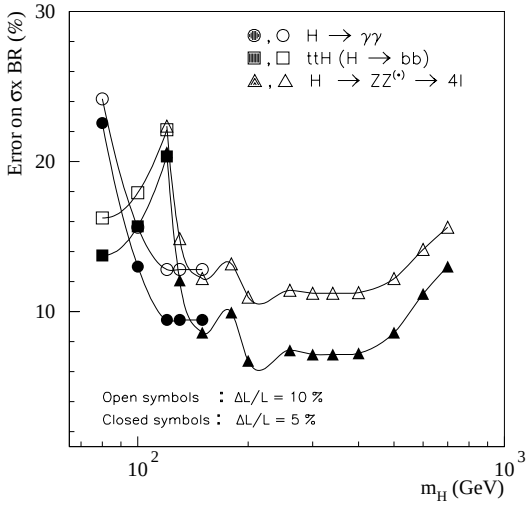

Figure 19-47 Relative precision on the measurement of the Higgs-boson rate ($\sigma \times$ BR) for various channels, as a function of m_H, for various channels, assuming an integrated luminosity of 300 fb^{-1}. The luminosity is assumed to be known to 10% (open symbols) or to 5% (black symbols).

An additional systematic error of 10% has been included to take into account the uncertainty on the background subtraction for channels where the background is not completely flat under the peak (*e.g.* $t\bar{t}H$ with $H \rightarrow b\bar{b}$).

Figure 19-47 shows the expected experimental uncertainty on the Higgs-boson rates, for various production and decay channels and for both assumptions on the luminosity uncertainty. Over the mass region 120 - 600 GeV, the Higgs-boson production rate can be measured with a precision of 12% (7%) if the luminosity is known to 10% (5%). These results stress the importance of future experimental and theoretical efforts to achieve a measurement of the absolute luminosity at the LHC to an accuracy at the level of a few percent.

19.2.12.4 Couplings and branching ratios

Once the Higgs-boson rate in a given decay channel is measured, an accurate theoretical prediction for the Higgs-boson production cross-section would allow a measurement of the branching ratio for the decay in that channel. Without theoretical assumptions, one can only measure ratios of rates for different channels, which in turn provide ratios of couplings and branching ratios. By performing these measurements for several channels, one can obtain several constraints on the Higgs-boson couplings to fermions and bosons, which can be used to test the theory.

A few examples of such measurements are given below, together with the expected precision for an integrated luminosity of 300 fb^{-1}:

- A measurement of the ratio of the $H \rightarrow \gamma\gamma$ and $H \rightarrow b\bar{b}$ rates in the associated production of Higgs bosons would provide the ratio between the $H \rightarrow \gamma\gamma$ and $H \rightarrow b\bar{b}$ branching ratios. Such a measurement can only be performed over the mass range, $80 < m_H < 120$ GeV, with an accuracy of about 30%, dominated by the statistical error.
- A measurement of the ratio between the $H \rightarrow \gamma\gamma$ and $H \rightarrow ZZ^* \rightarrow 4l$ rates would provide the ratio of the $H \rightarrow \gamma\gamma$ and $H \rightarrow ZZ^*$ branching ratios. Such a measurement can only be performed over the mass range $120 < m_H < 150$ GeV, with an accuracy of about 15%, dominated by the statistical error.
- A measurement of the ratio between the rate for $t\bar{t}H$ production and the rate for WH production both followed by $H \rightarrow \gamma\gamma$ or $H \rightarrow b\bar{b}$ decay, would provide the ratio of the Higgs couplings to the top quark (Yukawa coupling) and to the W boson. This measurement can only be performed over the mass range $80 < m_H < 120$ GeV, with an accuracy of about 25%, dominated by the statistical error.

In all the cases mentioned above, the statistical uncertainty dominates the measurement because the mass regions where two different channels overlap are at the edges of the sensitivity of one or the other channel. Furthermore, some systematic errors, such as the uncertainty on the absolute luminosity, cancel in the ratios.

It should be noted that, in addition to the measurements quoted above, other possibilities will also be studied. For example, the ratio between the $WW^{(*)}$ and $ZZ^{(*)}$ rates is sensitive to the couplings of the Higgs to the W and Z bosons. This ratio could be measured in the high mass region ($m_H > 300$ GeV) and, with a somewhat larger systematic uncertainty, in the mass range around 170 GeV. The $WH \rightarrow WWW^{(*)} \rightarrow 3l$ mode could provide additional information on the couplings of the Higgs boson to vector bosons. Finally, the ratio between the production cross-section via gg fusion and WW fusion can be measured, *e.g.* using forward jet tagging for $H \rightarrow ZZ \rightarrow 4l$. This could provide an indirect constraint on the Higgs-boson couplings to fermions and bosons.

19.2.12.5 Towards a determination of the spin and parity of the Higgs boson

The Standard Model predicts the Higgs boson to be a *CP*-even scalar particle. If the Higgs boson were discovered, these properties would have to be verified.

Only a few channels can give information on the spin and *CP*. *A priori* some general arguments, based on specific couplings, may be used to determine the spin. If, for example, the Higgs-boson is seen in the $H \rightarrow \gamma\gamma$ decay mode, then Yang's theorem implies that it is not a vector, and it must have a *CP*-even component. If the Higgs boson is observed in production and / or decay channels that require it to have substantial *WW* and / or *ZZ* couplings, it is very likely to have a large *CP*-even component, given that the *WW/ZZ* couplings of a pure *CP*-odd Higgs boson arise only at the one-loop level. Verifying that it is purely *CP*-even, as predicted by the Standard Model, will be much more challenging [19-61][19-62].

From the above, it is clear that a direct measurement of the Higgs-boson spin through the measurement of the angular distributions of its decay products is needed. A first study has therefore been performed [19-63], in which the sensitivity of the angular distributions to the spin of the Higgs boson is investigated. In this study, the $H \rightarrow \gamma\gamma$ and the $H \rightarrow ZZ \rightarrow 4l$ channels are used.

In the $H \rightarrow \gamma\gamma$ channel, the expected signal-to-background ratio is small, typically a few percent. This severely limits the potential to determine the spin structure from the angular distributions of the two photons. If only signal events are considered, it would be possible to discriminate with a significance of 10.7σ between the flat distribution, expected for the decay of a spin-zero particle, and a $(1+\cos^2\theta^*)$ distribution, where θ^* is the polar angle in the centre-of-mass of the decaying Higgs boson. The significance has been evaluated using a Kolmogorov-Smirnov test, assuming an integrated luminosity of 100 fb^{-1}. This sensitivity is substantially reduced, if the impact of the kinematic cuts, of the detector acceptance, and in particular of the background events are taken into account. The expected discrimination capability between the two hypotheses described above is reduced to a value below 1.5σ, even for an integrated luminosity of 300 fb^{-1}.

In the $H \rightarrow ZZ \rightarrow 4l$ channel, the expected signal-to-background ratio is much more favourable. For Higgs-boson masses between 200 and 400 GeV, it is about 20 (see Section 19.2.5). In this channel, in addition to the θ^* angular distribution of the Z bosons in the Higgs-boson centre-of-mass, the azimuthal separation $\Delta\phi$ between the two reconstructed Z bosons is sensitive to the spin of the Higgs-boson. For Higgs-boson decays into ZZ the azimuthal separation $\Delta\phi$ is expected to be smaller than for the ZZ continuum background. Both the $\cos(\theta^*)$ and the $\Delta\phi$ distributions depend on the ratio m_H / m_Z (particularly the θ^* distribution) and on the selection criteria. The optimisation of the signal-to-background ratio for higher Higgs-boson masses, with the selection cut requiring ${p_T}^Z{}_{\max} > m_H / 3$ causes the $\Delta\phi$ distribution to be more similar for the selected signal and background events. It can however still be demonstrated that, with a high significance, these angular distributions are incompatible with those expected for background events alone [19-63]. A more quantitative analysis of the discrimination between a spin-0 and a spin-1 particle, using this channel, is currently being carried out.

As suggested in [19-64], the $t\bar{t}H$ production channel could possibly be used to distinguish a *CP*-even from a *CP*-odd Higgs boson. This channel would however only provide sensitivity in the Higgs-boson mass window between 80 and 130 GeV. The method proposed requires the reconstruction of the momenta of both top quarks, which then could be used in a variety of simple variables. These variables are products of the reconstructed top-quark momenta and should

have sensitivity to the *CP* quantum number of the Higgs boson. Although this method looks interesting, its application at the LHC is difficult and might be limited by the available signal rates:

- For an integrated luminosity of 300 fb^{-1} and the $H \rightarrow \gamma\gamma$ decay mode the expected number of signal events is 20, before top-quark reconstruction, with a signal-to-background ratio of 1 (see Section 19.2.2). The expected efficiency for the reconstruction of both top-quarks (in the *jjb* and *lνb* channels) does not exceed 20% [19-35]. If *b*-tagging efficiencies are included, less than five reconstructed signal events are expected, with a signal-to-background ratio of about one.
- More events can be expected in the $H \rightarrow b\bar{b}$ mode, see Section 19.2.4.3. For an integrated luminosity of 30 fb^{-1} and m_H = 100 GeV, about 61 signal and 150 background events are expected to be reconstructed within the mass windows.

In addition, the systematic uncertainties linked to the reconstruction of the top-quark momenta have to be understood.

19.2.12.6 Conclusion

The results presented in the previous Sections demonstrate that ATLAS has a large potential, not only for the discovery of a Standard Model Higgs boson, but also for precision measurements of the Higgs-boson parameters. In particular, with an integrated luminosity of 300 fb^{-1} ATLAS would measure the Higgs-boson mass with a precision of 0.1% over the mass range 80 - 400 GeV, the Higgs-boson width with a precision of 6% over the mass range 300 - 700 GeV, the Higgs-boson production rate with a precision of 10%, and several of the most important couplings and branching ratios with a precisions of the order of 25%.

The determination of the spin and the *CP* quantum number of the Higgs boson from angular distributions is not straightforward at the LHC. Most channels suffer from too large backgrounds or too few events, and hence detailed studies of angular distributions are difficult. The most promising channel for a meaningful measurement is the $H \rightarrow ZZ^{(*)} \rightarrow 4l$ channel.

19.3 Minimal Supersymmetric Standard Model Higgs boson

19.3.1 Introduction

The investigation of the Higgs sector of the MSSM [19-10] is complex, since one has to deal with a rich spectrum of possible signals. The Higgs sector contains two charged ($H^{\pm}$) and three neutral (h, H, A) physical states. At the tree level, all Higgs-boson masses and couplings can be expressed in terms of two parameters only. They are usually chosen to be m_A, the mass of the *CP*-odd boson, and tanβ, the ratio of the vacuum expectation values of the Higgs doublets. However, the radiative corrections from loops containing top quarks or SUSY particles substantially modify the tree-level formulae for masses and mixing patterns in the Higgs sector [19-65][19-66] [19-67][19-68]. This has important implications for the strategies of MSSM Higgs-boson searches. At three-level the relation $m_h < m_Z \cos 2\beta$ holds, but the radiative corrections increase this upper limit to 150 GeV [19-11] in the most general case.

Over the past years, prospects for the detection of MSSM Higgs bosons at the LHC have been re-evaluated both theoretically [19-69] and experimentally [19-16]. These studies have selected sets of parameters, for which supersymmetric (SUSY) particle masses are large, so that Higgs-boson decays to SUSY particles are kinematically forbidden. The interest was focused on the discovery potential of various decay modes accessible also in the case of the SM Higgs boson: $h \to \gamma\gamma$, $h \to b\bar{b}$, $H \to ZZ \to 4l$, and of modes strongly enhanced at large tanβ: $H/A \to \tau\tau$, $H/A \to \mu\mu$. Much attention was given also to other potentially interesting channels such as: $H/A \to t\bar{t}$, $A \to Zh$, $H \to hh$. The conclusions drawn from these studies were that the complete region of parameter space, m_A = 50 - 500 GeV and tanβ = 1 - 50, should be accessible for Higgs-boson discovery by the ATLAS experiment. Over a large fraction of this parameter space, more than one Higgs boson and/or more than one decay mode would be accessible. The most difficult region was identified as the moderate tanβ and moderate m_A region, where only the lightest Higgs boson would be observable. Also, for larger values of m_A (m_A > 500 GeV), only the lightest Higgs boson, h, would most likely be observable. A summary of these studies is presented in Section 19.3.2 and Section 19.3.3.

If SUSY particles are light enough, decays of Higgs bosons to SUSY particles are kinematically allowed. The SM decay modes are then suppressed, competing in most cases with decays to charginos and neutralinos. The prospects for the observability of Higgs bosons under these conditions have also been evaluated [19-70] and are presented in Section 19.3.5. These studies have been performed using the more constrained SUGRA model [19-71]. With the allowed parameters combinations of SUGRA, the (m_A, tanβ) plane is still fully covered within the limits discussed above, but the possibility of discovering heavy Higgs bosons might be more limited. Some suppression of SM decay modes would occur in the low tanβ range, where, however new four-lepton signatures from Higgs-boson decays to SUSY particles would appear. Over a large fraction of the SUGRA parameter space, the possibility to observe the lightest Higgs boson, h, in SUSY cascade decays has also been systematically explored.

Some MSSM signatures have been investigated, even if the expected sensitivity is rather weak or if their observability is already almost excluded by searches at LEP2. These studies are nevertheless considered valuable, since they provide model-independent probes of possible Higgs-boson signatures and since they contribute to the general process of quantifying and optimising the detector performance for the exploration of new physics signatures.

Most studies presented below have been performed with the fast detector simulation, in particular to obtain a careful evaluation of the expected backgrounds. For several channels results obtained for mass resolutions, acceptances or reconstruction efficiencies have been confirmed with full simulation (see Section 2.5 and Section 9.3).

19.3.2 Scenarios with heavy SUSY particles

19.3.2.1 General considerations

In this study, two-loop equivalent calculations are used for the masses and couplings [19-66] [19-67][19-68], as well as one-loop calculations for some decay branching ratios [19-66][19-20]. QCD corrections are partially taken into account by including running quark masses in the calculations of branching ratios. As mentioned above, it is assumed that SUSY particles are sufficiently heavy that they do not play an important role in the phenomenology of MSSM Higgs-boson decays.

In addition, for the benchmark sets of MSSM parameters [19-11], where M_{SUSY} is fixed to 1 TeV, an extreme configuration of stop mixing parameters (A_t, μ) has been chosen, the so-called minimal mixing scenario (A_t, $\mu << M_{\mathrm{SUSY}}$). This scenario corresponds to the most pessimistic discovery scenario at the LHC, since these choices for the additional MSSM parameters give the lowest possible upper limit for m_h. This reduces the LHC potential for h-boson discovery in the $h \rightarrow \gamma\gamma$ channel, and also suppresses the $H \rightarrow ZZ^{(*)} \rightarrow 4\,l$ channel.

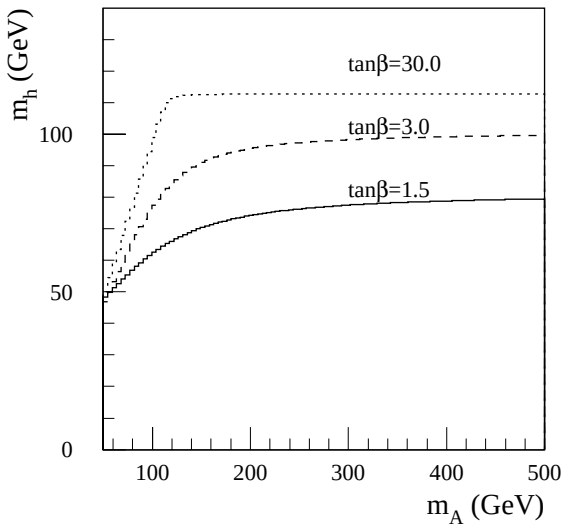

Figure 19-48 Two-loop equivalent predictions for m_h as a function of m_A and for tanβ = 1.5, 3, 30 in the minimal mixing scenario, as used throughout these studies.

In the minimal mixing scenario the predicted upper limit on m_h is 115 GeV for a top mass of 175 GeV [19-72]. This upper limit would increase to ~ 122 GeV, if maximal mixing were assumed. Figure 19-48 shows m_h as a function of m_A for three values of tanβ. The value of m_h depends very little on m_A for $m_A > 200$ GeV and reaches its maximum allowed value for $m_A > 200$ GeV and tanβ > 10. The masses of the charged Higgs-bosons $m_{H^{\pm}}$, and of the heavier neutral *CP*-even Higgs boson, m_H, vary nearly linearly with m_A. For large values of m_A all Higgs bosons except h are heavy and degenerate in mass.

The total decay widths of the MSSM Higgs bosons differ significantly from that of a SM Higgs boson of the same mass (see *e.g.* [19-16]). For large values of tanβ, the width of the h-boson is usually larger than that of a SM Higgs. However, it tends towards the SM value, as the h-boson mass approaches its maximal value for a given value of tanβ. This is the case for most of the relevant parameter space in the (m_A, tanβ) plane. Consequently, in most cases, the h-boson width is much smaller than the experimental resolutions expected for the decay modes observable at the LHC. The decay widths of the H- and A- bosons are also in general much smaller than that

of the SM Higgs boson of the same mass. However, they become relatively large with increasing m_A and / or tanβ. This has been taken into account whenever relevant for the evaluation of the significance of a possible signal from the decay of the heavy Higgs bosons.

In the (m_A, tanβ) region of parameter space relevant for the LHC searches, both the direct and associated production cross-sections and the branching ratios $h \to \gamma\gamma$ and $h \to b\bar{b}$ reach asymptotically the SM values as m_A and / or tanβ increases. In general, they are somewhat suppressed, except when m_h gets close to its maximum allowed value for a given value of tanβ. In this case, the $\sigma \times$ BR of the *h*-boson are even larger by 10 - 20% than the corresponding SM values. In this decoupling limit, the lightest MSSM Higgs-boson *h* behaves like a SM Higgs.

For the H / A bosons, the expected rates and decay channels vary rapidly with m_A and tanβ. As discussed in the next Sections, the variety of decay channels of interest is much richer than in the SM case. Typical features of MSSM Higgs decays are:

- the strong suppression of the HZZ and HWW coupling and absence of such couplings for the *A*-boson, which enhances the branching ratio of the other decay channels, such as $H/A \to \tau\tau$, $H/A \to t\bar{t}$;
- the strong enhancement of the $b\bar{b}H$, $b\bar{b}A$ coupling for large values of tanβ which leads to the dominance of this production mode;
- and the existence of decays with more than one Higgs boson involved, such as $H \to hh$ and $A \to Zh$.

19.3.2.2 h , H , $A \to \gamma\gamma$

h , $H \to \gamma\gamma$

The observability of the inclusive $H \to \gamma\gamma$ channel has been described in detail in Section 19.2.2.1 for the case of a SM Higgs boson. The search for the SM Higgs boson in $H \to \gamma\gamma$ decays can also be performed using associated WH and $t\bar{t}H$ production, as described in Section 19.2.2.2. The expected sensitivity for this channel can be combined with that for the inclusive one to improve the overall discovery potential for $H \to \gamma\gamma$ decays.

The expected MSSM rates, for both $h \to \gamma\gamma$ and $H \to \gamma\gamma$, are generally suppressed with respect to the SM case. However, they could also be slightly enhanced over limited regions of parameter space, as discussed above. In order to evaluate the overall sensitivity to γγ decays of the MSSM Higgs bosons, the results of the SM searches have been used. To obtain the 5σ-discovery contour curves in the (m_A, tanβ) plane, only *h*-boson masses above 70 GeV have been considered, since a proper experimental study of signal acceptance and background rates has not been performed for masses much below 80 GeV, and also since the present experimental limit from LEP2 is already of $m_h \sim 80$ GeV for any MSSM scenario [19-7].

The expected 5σ discovery contour curves in the (m_A, tanβ) plane are shown in Figures 19-49 and 19-50, respectively for integrated luminosities of 100 and 300 fb^{-1}. For the inclusive channel, the observability depends critically on the integrated luminosity. This is a consequence of the slow variation of m_h and $\sigma \times$ BR with increasing m_A.

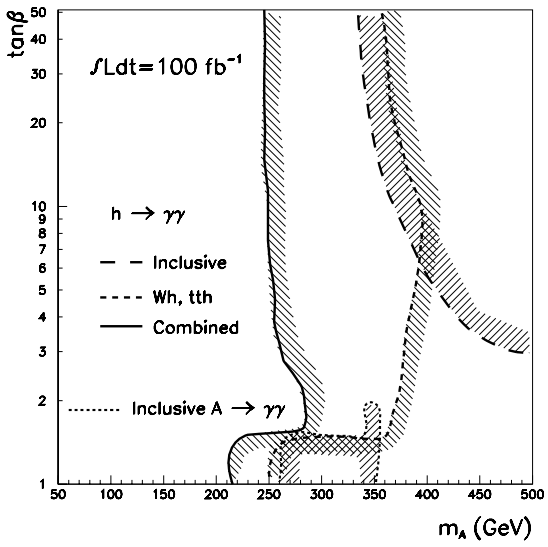

Figure 19-49 For an integrated luminosity of 100 fb^{-1}, 5σ-discovery contour curves for the $h \rightarrow \gamma\gamma$ (inclusive, associated *and* combined) and $A \rightarrow \gamma\gamma$ channels in the (m_A, tanβ) plane. The shaded areas indicate the side of the contour curves where the corresponding signal would be observable.

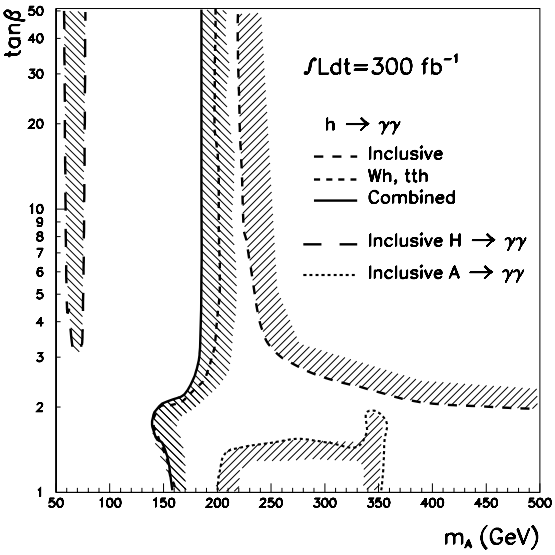

Figure 19-50 Same as Figure 19-49, but for an integrated luminosity of 300 fb^{-1}and including $H \rightarrow \gamma\gamma$.

Figures 19-49 and 19-50 show that a combined 5σ-discovery is possible for all values of tanβ provided m_A is larger than 180 GeV (260 GeV), for an integrated luminosity of 300 fb^{-1} (100 fb^{-1}). In the (m_A, tanβ) plane, the position of the 5σ-discovery contour curves is uncertain to $\sim \pm 30$ GeV along the m_A-axis, due to the rather large theoretical uncertainties still inherent to the calculation of m_h as a function of m_A.

The $h \rightarrow \gamma\gamma$ branching ratio has been computed here assuming that all SUSY particles have a mass of 1 TeV. More realistic mass spectra of SUSY particles usually contain lighter stop-quarks and charginos / neutralinos, and this may significantly decrease the $h \rightarrow \gamma\gamma$ branching ratio [19-73], which can also be affected by possible decays of the *h*-boson to the lightest neutralinos. In addition, SUSY particle masses lighter than 1 TeV could affect the $gg \rightarrow h$ production cross-section. For some specific choices of the SUSY model parameters, this cross-section could decrease by more than one order of magnitude. The $h \rightarrow \gamma\gamma$ channel would then only be observable at the LHC through the associated *Wh* and $t\bar{t}h$ production. While this would reduce the sensitivity, a significant fraction of the (m_A, tanβ) plane could still be covered with these processes alone. Since the SM and the MSSM h, $H \rightarrow \gamma\gamma$ rates are very similar over the accessible mass range, the observation of a Higgs boson decaying to γγ will not be sufficient to demonstrate the existence of a Higgs sector beyond the SM.

The heavy Higgs boson decay, $H \rightarrow \gamma\gamma$, would be observable only in a narrow strip for low m_A value (m_A = 70 - 80 GeV) corresponding to m_H = 110 - 120 GeV. This range of m_A is already almost excluded by searches at LEP2 [19-7].

$A \rightarrow \gamma\gamma$

The *CP*-odd Higgs boson A can also be searched for using the rare $\gamma\gamma$ decay mode. As in the case of the SM Higgs boson the $A \rightarrow \gamma\gamma$ decay mode is only observable over a limited region of parameter space, where the production cross-section (dominated by gg fusion) and the decay branching ratio are both relatively large. This region corresponds to small values of tanβ and to values of m_A between 200 - 350 GeV as shown in Table 19-32. For $m_A > 2m_t$ the $A \rightarrow t\bar{t}$ channel opens up and strongly suppresses the $A \rightarrow \gamma\gamma$ branching ratio.

Table 19-32 Cross-sections times branching ratios, acceptances and expected mass resolutions for the $A \rightarrow \gamma\gamma$ channel as a function of m_A.

m_A (GeV)	$\sigma \times$ BR (fb)	Accept.	σ_m (GeV)
200	7.3	15%	2.0
250	6.5	41%	3.0
300	10.3	57%	4.6
350	2.3	62%	6.3
400	0.2	66%	11.0

The signal reconstruction is performed exactly as for the SM $H \rightarrow \gamma\gamma$ decay mode, see Section 19.2.2. However, the p_T thresholds for the two photons can be raised considerably, given the higher Higgs-boson masses considered here. Thresholds of 125 GeV for the leading photon and 25 GeV for the second photon were found to give the best signal significance for 200 GeV < m_A < 400 GeV.

The acceptances of these simple kinematic cuts over this mass range are given in Table 19-32, which also includes the cross-sections and expected mass resolutions. Due to the narrow width of the A-boson in the MSSM, the mass resolution is determined by the experimental resolution of the EM Calorimeter.

Using a mass window of 1.4 σ_m and applying an efficiency factor of 80% for the photon identification, the expected numbers of signal and background events are given in Table 19-33 for an integrated luminosity of 100 fb^{-1}. The background is dominated by the irreducible $\gamma\gamma$ continuum, which itself is dominated by the $q\bar{q} \rightarrow \gamma\gamma$ Born process. As in the case of the search for SM $H \rightarrow \gamma\gamma$ decays, this background has been scaled up by a factor 1.5 to account for the quark-bremsstrahlung contribution. The reducible background is conservatively assumed to be 35% of the irreducible one, as estimated for lower masses in the SM Higgs case. Under these assumptions, the signal significances shown in Table 19-33 are expected.

Table 19-33 For the $A \rightarrow \gamma\gamma$ channel with tanβ = 1.1, expected number of reconstructed signal and background events inside the mass window, for an integrated luminosity of 100 fb^{-1}.

m_A (GeV)	Signal	Background	$S/\sqrt{B}$
200	52	210	3.6
250	121	1060	3.7
300	252	1660	6.2
350	68	810	2.4
400	5	130	0.5

The region of MSSM parameter space which can be covered by a search for the $A \rightarrow \gamma\gamma$ decay mode is shown in Figures 19-49 and 19-50 for integrated luminosities 100 fb^{-1} and 300 fb^{-1}, respectively. This channel is shown here for completeness as it provides coverage only over a limited range of m_A values for $m_A < 2m_t$ and for very low values of tanβ almost excluded already by LEP experiments.

19.3.2.3 $h \rightarrow b\bar{b}$

The SM $H \rightarrow b\bar{b}$ channel is discussed in detail in Section 19.2.4.2 for WH production (see also [19-34]) and in Section 19.2.4.3 for $t\bar{t}H$ production (see also [19-35]). Only the $t\bar{t}H$, $H \rightarrow b\bar{b}$ channel can be observed clearly above the background, provided the complete event is reconstructed. This requires excellent b-tagging performance (see Chapter 10 for more details), since each event contains four b-jets in the final state.

In the MSSM case, the rates can be enhanced by 10 - 20% compared to the SM, as discussed in [19-16]. The sensitivity to a $t\bar{t}h$, $h \rightarrow b\bar{b}$ signal has been computed from the results obtained for the SM search, after accounting for the different production and decay rates. The 5σ-discovery contours in the (m_A, tanβ) plane are shown in Figure 19-51. For an integrated luminosity of 30 fb^{-1}, the h-boson could be discovered in this channel for $m_A > 150$ GeV and tanβ < 4. For integrated luminosities above 100 fb^{-1}, the observability of the h-boson in this channel extends to 90% of the (m_A, tanβ) plane. For completeness, Figure 19-51 shows also the 5σ-discovery contour curve for the Wh, $h \rightarrow b\bar{b}$ channel for an integrated luminosity of 30 fb^{-1}, without including any systematic uncertainty on the background (see Section 19.2.4.2). This clearly demonstrates the superior discovery potential of the $t\bar{t}h$, $h \rightarrow b\bar{b}$ channel.

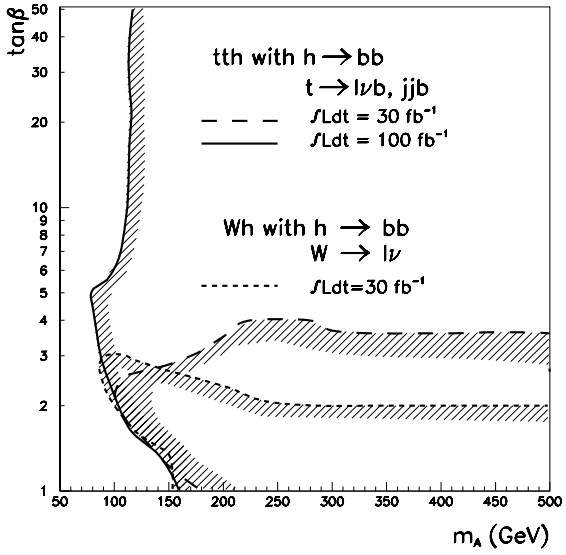

Figure 19-51 For integrated luminosities of 30 fb^{-1} and 100 fb^{-1}, the 5σ-discovery contour curves for the $t\bar{t}h$ and Wh with $h \rightarrow b\bar{b}$ channel in the (m_A, tanβ) plane.

In conclusion, the complete reconstruction of the $t\bar{t}h$, $h \rightarrow b\bar{b}$ final state has resulted in a very large improvement of the signal observability in this channel with respect to earlier studies [19-34], and the impact of this improvement is most striking in the MSSM case, as illustrated by Figure 19-51.

19.3.2.4 $H \rightarrow ZZ^{(*)} \rightarrow 4\,l$

As in the $h \rightarrow \gamma\gamma$ and $h \rightarrow b\bar{b}$ channels, the observability of the $H \rightarrow ZZ^{(*)} \rightarrow 4\,l$ channel in the MSSM is estimated by extrapolating the detailed studies performed in the SM case (see Section 19.2.5 and Section 19.2.9). For the intermediate mass range, 120 GeV < $m_H < 2m_Z$, the signal rates are small and the background rates are potentially very large. For the larger masses, above the ZZ threshold, the expected observability of this channel reaches values as high as 45σ, with a signal-to-background ratio of approximately 20:1. The only significant background arises from irreducible ZZ continuum production.

In the MSSM, the rates of $H \rightarrow ZZ^{(*)} \rightarrow 4\,l$ are strongly suppressed with respect to the SM case over the full tanβ range, except for values of tanβ smaller than one. This is due to the suppression of the HZZ coupling, to the opening of the $H \rightarrow hh$ decay channel, and to the enhancement of the $H \rightarrow t\bar{t}$ channel. These characteristics of the Higgs boson in the MSSM case limit the observability of this channel to the range $2m_h < m_H < 2m_t$ and to low values of tanβ.

Table 19-34 Observability of the $H \rightarrow ZZ^{(*)} \rightarrow 4\,l$ channels for an integrated luminosity of 30 fb^{-1}. The values for $\sigma \times$ BR are the ones for the SM Higgs boson and do not correspond to any fixed value of tanβ. For higher masses the numbers are given for the selection with the additional cut on $p_T{}^{max}(Z_1,Z_2)$ [19-16].

m_H (GeV)	130	150	170	200	240	300
$\sigma \times$ BR (fb)	3.0	5.5	1.4	12.4	11.2	9.1
Signal events	11.4	26.8	7.6	56	33	39
Background	2.6	3.0	3.2	5.3	1.1	1.2
Significance	4.8	15.5	3.2	24.2	31.8	36.1

In the SM case the Higgs-boson width increases rapidly with m_H, and therefore the chosen mass window is determined by the intrinsic Higgs-boson width for $m_H > 300$ GeV. Since the MSSM H-boson decay width remains much smaller than the experimental resolution over the relevant region of parameter space, the mass window chosen for the MSSM case is narrower. Since the observability in this channel is somewhat limited, cuts on the maximum p_T of the reconstructed Z-boson, $p_T{}^{max}(Z_1, Z_2)$, are used in the mass range $m_H > 200$ GeV [19-16]. Mass dependent requirements, $p_T{}^{max}(Z_1, Z_2) > m_H/3$ or $p_T{}^{max}(Z_1, Z_2) > m_H/2$, are applied to derive the observability in the MSSM case. The expected numbers of signal and background events are given in Table 19-34 for reference values of the cross-section times branching ratio, $\sigma \times$ BR, taken from the SM case. The expected 5σ-discovery contour curves are shown in Figure 19-52 for different values of the integrated luminosity. The highest possible integrated luminosity is needed to observe this channel in the MSSM case.

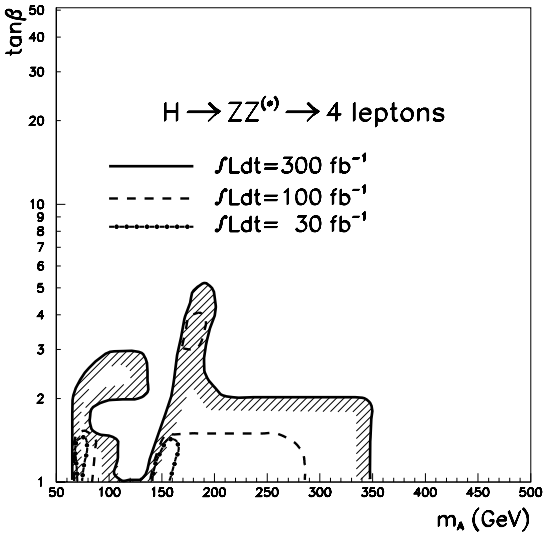

Figure 19-52 For integrated luminosities of 30 fb^{-1}, 100 fb^{-1} and 300 fb^{-1}, 5σ-discovery contour curves for the $H \rightarrow ZZ^{(*)} \rightarrow 4l$ channel in the (m_A, tanβ) plane.

If a signal were observed, the measured rate would provide the best information on its origin, since the $H \rightarrow ZZ^{(*)} \rightarrow 4\,l$ MSSM rates are suppressed by an order of magnitude with respect to the SM case over most of the parameter space. For values of m_H larger than ~250 GeV, the measured signal width would also distinguish between the SM Higgs boson with $\Gamma_H{}^{tot} \sim 10$ GeV and the MSSM Higgs boson with $\Gamma_H{}^{tot} << 10$ GeV for low values of tanβ.

19.3.2.5 *H/A* $\rightarrow \tau\tau$

Despite rather optimistic recent theoretical estimates [19-74], the $H \rightarrow \tau\tau$ decay mode is not expected to be observable at the LHC in the SM case, because the expected signal rates are too low compared to the large backgrounds from various SM processes [19-75]. However, in the MSSM case, the $H \rightarrow \tau\tau$ and $A \rightarrow \tau\tau$ rates are strongly enhanced over a large region of the parameter space. For low values of tanβ, the $gg \rightarrow A$, $A \rightarrow \tau\tau$ rates are dominant and significantly larger than in the SM case for a Higgs boson of the same mass. For large values of tanβ, the production is dominated by the strongly enhanced associated $b\bar{b}H$ and $b\bar{b}A$ production and the $H/A \rightarrow \tau\tau$

branching ratio is about 10% in the mass range 200 - 500 GeV. The relative contribution from the associated production is roughly 50% for $\tan\beta = 5$ and about 90% for $\tan\beta = 20$. For $m_A > 150$ GeV, the H and A bosons are almost degenerate in mass, so their signal rates in the $\tau\tau$-channel can be summed. A more complicated procedure, depending on the experimental resolution and on the mass difference $m_H - m_A$, has to be applied for $m_A < 150$ GeV [19-16]. Higgs-boson masses below 100 GeV have not been considered in this study due to the large resonant background from $Z \rightarrow \tau\tau$ decays.

This channel has been extensively used as a benchmark when optimising the detector for τ identification and E_T^{miss} reconstruction. The possible signal has improved as the detector design has evolved. Much effort has also gone into understanding in detail the topological features of the signal and background events. Since the ATLAS Technical Proposal [19-14] a combined analysis has been performed, using tagging of the spectator *b*-jets and a veto on the presence of other jets in the event. This has resulted in a significant improvement of the overall sensitivity to this channel.

The trigger for such decay modes is based on the leptonic decay of one of the τ-leptons. The other τ-lepton may then decay to hadrons (lepton-hadron channel) or to another lepton (lepton-lepton channel). The lepton-hadron channel turns out to provide the best sensitivity to a possible signal, due to both the larger rate (the fraction of $A \rightarrow \tau\tau$ resulting in a lepton-hadron final state is 46%) and to the more favourable kinematics of the τ-decay. This Section therefore only describes the extraction of the signal in this channel. The contribution from the lepton-lepton channel to the final observability is rather marginal and details on its analysis can be found in [19-76].

The backgrounds are a mixture of irreducible $Z \rightarrow \tau\tau$ background and of $t\bar{t}$, $b\bar{b}$ and *W+jet* processes, where a jet is misidentified as a τ–lepton. They can be significantly reduced by applying a selection based on a reconstructed lepton, τ identification and E_T^{miss}. Excellent τ identification performance to suppress the huge backgrounds containing hadronic jets from various sources [19-77], and excellent E_T^{miss}-resolution for the reconstruction of the $\tau\tau$ invariant mass, $m_{\tau\tau}$, are required to observe the signal [19-76].

A detailed discussion of the τ identification, the E_T^{miss} resolution and the reconstruction of the $\tau\tau$ invariant mass is presented already in Chapter 9. Only the main ingredients of the selection procedure are recalled here and only those aspects which are specific to the observability of this channel are discussed in some detail.

The standard $H/A \rightarrow \tau\tau$ analysis, as described already in [19-14] and [19-76], is based on a set of selection criteria, which include τ identification, kinematic cuts, and a mass window cut on the reconstructed $\tau\tau$ mass, $m_{\tau\tau}$. The energies of the two τ-leptons, used for the $m_{\tau\tau}$ calculation are evaluated from the energies of the τ decay products, which are assumed to have the direction of the parent τ-lepton, and the neutrino energies are obtained by solving a system of equations containing the two E_T^{miss} components (see the discussion on $Z \rightarrow \tau\tau$ mass reconstruction in Section 9.3.3.1).

This standard $H/A \rightarrow \tau\tau$ analysis includes the τ identification cuts described in detail in Section 9.1.5.2. Additional selections are then made:

- One isolated trigger lepton with $p_T > 24$ GeV within $|\eta| < 2.5$. The isolation requirement rejects leptons from $b\bar{b}$ production and decay by a factor of 100 for 90% efficiency for leptons from τ decays;
- $E_T^{jet} > 40$ GeV, $|\eta| < 2.5$ for the τ-jet;

- $E_T^{miss} > 18$ GeV;
- transverse mass m_T(lepton-E_T^{miss}) < 25 GeV;
- $1.8 < \Delta\phi^{(jet\text{-}lepton)} < 2.9$ or $3.4 < \Delta\phi^{(jet\text{-}lepton)} < 4.5$. This cut is necessary for the reconstruction of the ττ invariant mass.

Finally, events are accepted if the ττ invariant mass, $m_{\tau\tau}$, is within a mass window of $m_A \pm 1.5\,\sigma_m$.

The analysis presented above does not exploit the fact that the direct and associated production processes show substantial kinematic and topological differences. In associated production, spectator *b*-quarks are present in the signal events unlike in direct production. The $b\bar{b}H$ and $b\bar{b}A$ production processes can be selected by requiring a single tagged *b*-jet. This also reduces substantially the large W+*jet* and $Z \rightarrow \tau\tau$ backgrounds.

In $b\bar{b}H$, $b\bar{b}A$ events, the average transverse momentum of the Higgs boson is lower than in events from direct production. This difference increases with increasing Higgs-boson mass, from 14% to 42%, as m_H increases from 150 to 450 GeV. In $b\bar{b}H$, $b\bar{b}A$ events, the τ-leptons from the Higgs-boson decay are therefore more back-to-back, with the following consequences:

- A narrower $\Delta\phi^{(jet\text{-}lepton)}$ distribution, peaked around π, is observed for associated production with respect to direct production; the distribution is very similar to that of the $Z \rightarrow \tau\tau$ background.
- The fraction of events for which the neutrino system can be resolved is smaller by 30% for associated production compared to direct production (see Section 9.3.3.4).
- The ττ invariant mass resolution is degraded by about 50% for associated production compared to direct production (see Section 9.3.3.4).

Due to these topological features of the associated production the overall efficiency of the standard reconstruction procedure is reduced by 40 - 50% with respect to direct production.

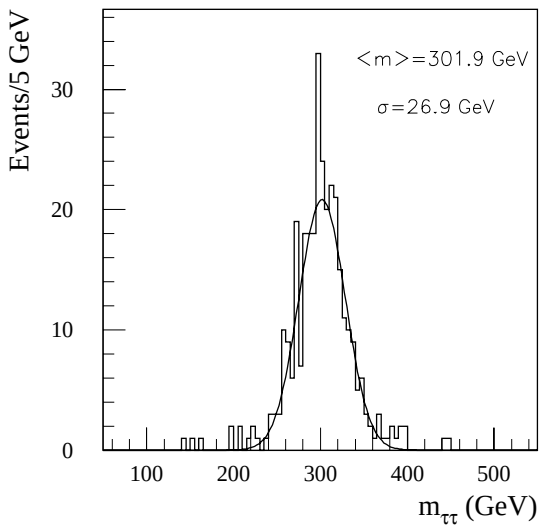

Figure 19-53 Reconstructed invariant mass, $m_{\tau\tau}$, from $A \rightarrow \tau\tau$ decays for direct Higgs-boson production and for m_A = 300 GeV.

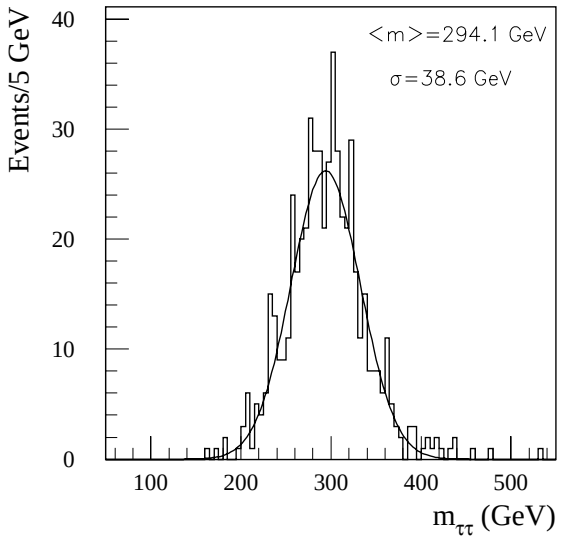

Figure 19-54 Same as Figure 19-53, but for associated Higgs-boson production.

Figures 19-53 and 19-54 show the $\tau\tau$ invariant masses obtained from fully simulated and reconstructed events at low luminosity for $m_A = 300$ GeV for events from direct and associated Higgs-boson production, respectively. Figure 19-55 shows the mass resolution, σ_m, expected at low luminosity as a function of m_A, separately for direct and associated Higgs-boson production. The general tendency of σ_m to increase with m_A is mostly due to the increase of $\sigma(E_T^{miss})$ as m_A increases (see Section 9.3.3.4).

Since the direct and associated production processes display substantial differences, both in their topological features and in the final state (two additional *b*-quarks in the case of associated production), a separate analysis for each production process has been performed to optimise the signal observability in the $H/A \rightarrow \tau\tau$ channel.

The analysis for direct production requires:

- A veto against *b*-jets for $p_T > 15$ GeV and $|\eta| < 2.5$ (to reject $t\bar{t}$ and $b\bar{b}$ backgrounds).
- Standard $H/A \rightarrow \tau\tau$ reconstruction (τ identification, kinematic and mass cuts).

The analysis for associated production requires:

- At least one tagged *b*-jet (to reject $Z \rightarrow \tau\tau$ and *W+jet* backgrounds).
- At most two non-*b* jets with $p_T > 15$ GeV and $|\eta| < 3.2$ (to reject $t\bar{t}$ backgrounds);
- Standard $H/A \rightarrow \tau\tau$ reconstruction (τ identification, kinematic and mass cuts), except for the $\Delta\phi^{(\text{jet-lepton})}$ cut.

In both analyses, the nominal *b*-tagging performance at low luminosity has been assumed (see Chapter 10).

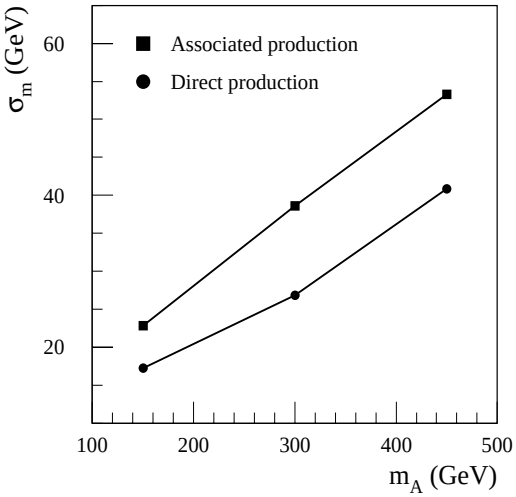

Figure 19-55 For $H/A \rightarrow \tau\tau$ decays at low luminosity, $\tau\tau$ invariant mass resolution, σ_m, as a function of m_A. The results are obtained from full simulation and reconstruction, and are shown separately for the direct (black circles) and associated (black squares) Higgs-boson production.

The analysis which enhances the fraction of events from direct production rejects more efficiently the $t\bar{t}$ and $b\bar{b}$ backgrounds because of the veto against *b*-jets. The analysis which selects mostly events from associated production will improve the sensitivity for moderate and large values of tanβ. In this case, the somewhat worse efficiency of the analysis is balanced by the improved *W+jet* and $Z \rightarrow \tau\tau$ background rejection.

Since events are accepted either by one analysis or the other, the expected overall signal significances are obtained by adding in quadrature the signal significances expected for each analysis separately. As explained in more detail in [19-78] and indicated in Table 19-35, the combination of these two analyses improves the overall sensitivity to the $H/A \rightarrow \tau\tau$ channel for masses in the range 150 - 450 GeV by 60 - 100% with respect to what would be obtained with the more inclusive analysis following the analysis presented in the ATLAS Technical Proposal.

Results at low luminosity

The $H/A \rightarrow \tau\tau$ reconstruction efficiency was estimated from high-statistics samples of fully simulated events for three different values of m_A (m_A = 150, 300 and 450 GeV) and separately for the direct and associated Higgs-boson production processes. High statistics samples of the various background processes (W+jet, $t\bar{t}$, $b\bar{b}$ and Z/γ^*) have also been fully simulated and reconstructed to evaluate the rejections of the two analyses described above as accurately as possible (see [19-78] for more details). Background from $Zb\bar{b}$ production has not been simulated in detail, since it has been shown to be very small in earlier studies [19-37]. The background rejections obtained after all the selection criteria (kinematic and topological cuts, mass window and τ identification) are very high for the reducible W+jet, $t\bar{t}$ and $b\bar{b}$ backgrounds. Therefore, for the background processes, the acceptance for the τ identification criteria has been factorised from the rest, since they are essentially uncorrelated to each other (the residual background from these processes contains only small contributions with real τ-leptons).

Table 19-35 Expected $H/A \rightarrow \tau\tau$ signal and background rates as a function of m_A for the lepton-hadron channel with tanβ = 10 and an integrated luminosity of 30 fb^{-1}. The rates are given separately for each production mechanism: direct ($gg \rightarrow H/A$) and associated ($b\bar{b}H$, $b\bar{b}A$) Higgs-boson production and for the direct/associated analyses (see text). The signal event rates correspond to the summed $H \rightarrow \tau\tau$ and $A \rightarrow \tau\tau$ rates. The expected signal significances are shown separately for the two analyses and for an integrated luminosity of 30 fb^{-1}. The overall combined significances are finally shown for integrated luminosities of 30 fb^{-1} and 300 fb^{-1}, accounting for the degraded performance expected at high luminosity (see text). For comparison the signal significance expected from an inclusive analysis, described in [19-76], is also shown.

m_A (GeV)	150	300	450
$\sigma \times$ BR for direct production (pb)	1.3	0.05	0.015
$\sigma \times$ BR for associated production (pb)	2.9	0.28	0.04
Mass window (GeV)	± 30 GeV	± 55 GeV	± 75 GeV
Inclusive analysis			
Signal significance for 30 fb^{-1}	5.7	1.2	0.6
Direct/associated analysis			
Event rates:			
Direct production	49 / 2	9.5 / 0.35	1.5 / 0.16
Associated production	56 / 72	6 / 18	1.3 / 6.3
Total signal	105 / 74	15.5. / 18	2.8 / 6.5
W+jet	530 / 46	740 / 43	228 / 22
$t\bar{t}$	7 / 6	9 /8	5 /4
$b\bar{b}$	14 / 29	4 / 21	1 / 6
$Z/\gamma^* \rightarrow \tau\tau$	163 / 5	41 / 2	7 / 0.5
Total background	714 / 86	794 / 74	241 / 32.5
Signal significance for 30 fb^{-1}	3.9 / 8.0	0.6 / 2.1	0.2 / 1.1
Combined significance for 30 fb^{-1}	8.9	2.2	1.2
Combined significance for 300 fb^{-1}	12.5	3.8	2.1

Table 19-35 gives the expected $H/A \rightarrow \tau\tau$ signal rates for three values of m_A and for an integrated luminosity of 30 fb^{-1}. The results are shown for tanβ = 10, separately for the direct and associated production processes and for each of the selection analyses. The signal from associated pro-

duction accounts for 70 - 80% of the total signal rate. The analysis requiring a tagged *b*-jet selects almost exclusively signal events from associated production, but a large fraction of these are also selected by the other analysis for low values of m_A, due to the limited acceptance in p_T and $|\eta|$ of the *b*-tagging algorithm.

The dominant background selected by the analysis optimised for direct Higgs-boson production arises from W+jet events, which have the largest production cross-section of all the background processes. For low values of m_A, the irreducible background from $Z \rightarrow \tau\tau$ is also significant for events selected with this analysis. In contrast, the analysis optimised for associated Higgs-boson production rejects much better the W+jet and $Z \rightarrow \tau\tau$ backgrounds, but due to their large production cross sections the dominant residual backgrounds remain to be W+jet and $b\bar{b}$ production.

In conclusion, the direct production analysis contributes significantly only for low values of m_A, but provides a signal-to-background ratio of only 0.15 for m_A = 150 GeV, even though it selects events with better mass resolution. In contrast, the associated production analysis provides a signal-to-background ratio close to 0.9 for the same values of m_A, and above 0.2 for the higher values of m_A.

Table 19-35 also shows the signal significances combined for both analyses for an integrated luminosity of 30 fb^{-1}. For m_A = 150 GeV, the inclusion of the direct production analysis improves the significance obtained with the associated production analysis by ~10%. This improvement increases as tanβ decreases, since the fraction of events arising from direct production increases. The combined method therefore improves the signal observability mostly for moderate values of tanβ. For large values of tanβ, the analysis requiring a tagged *b*-jet improves considerably the signal-to-background ratio and hence the signal observability with respect to previous more inclusive studies [19-14].

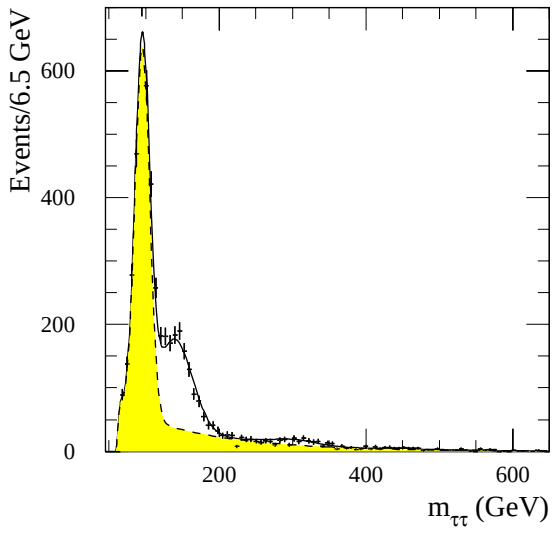

Figure 19-56 For the direct production analysis, for tanβ = 25 and for an integrated luminosity of 30 fb^{-1}, distribution of $m_{\tau\tau}$ shown for the total background (dashed shaded curve) and for the sum of the $H/A \rightarrow \tau\tau$ signals at m_A = 150, 300 and 450 GeV, and the background (solid curve and points with error bars).

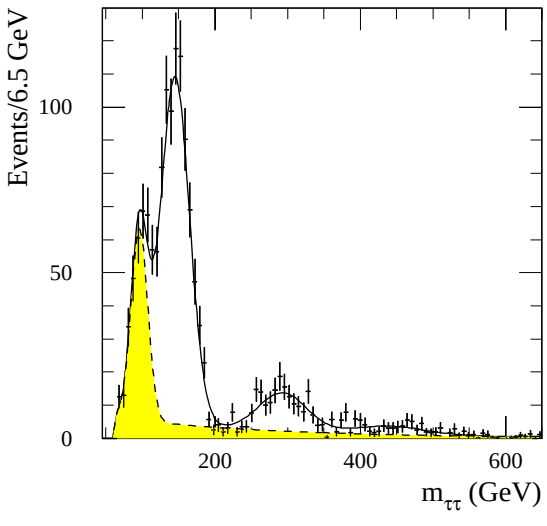

Figure 19-57 Same as Figure 19-56, but for the associated production analysis.

Table 19-36 shows for three values of m_A and for integrated luminosities of 30 fb^{-1} and 300 fb^{-1} the lower limit values of tanβ corresponding to a 5σ discovery for the $H/A \rightarrow \tau\tau$ channel. The errors assigned to the tanβ values are those which would arise if the overall background were assumed to have a systematic uncertainty of ±20%.

Table 19-36 For three values of m_A and for integrated luminosities of 30 fb^{-1} and 300 fb^{-1}, lower limits of tanβ corresponding to a 5σ discovery in the $H/A \rightarrow \tau\tau$ channel.

m_A (GeV)	30 fb^{-1}	300 fb^{-1}
150	7.5 ± 0.5	6.0 ± 0.5
300	14.5 ± 0.7	11.0 ± 0.5
450	19.5 ± 1.0	15.0 ± 0.6

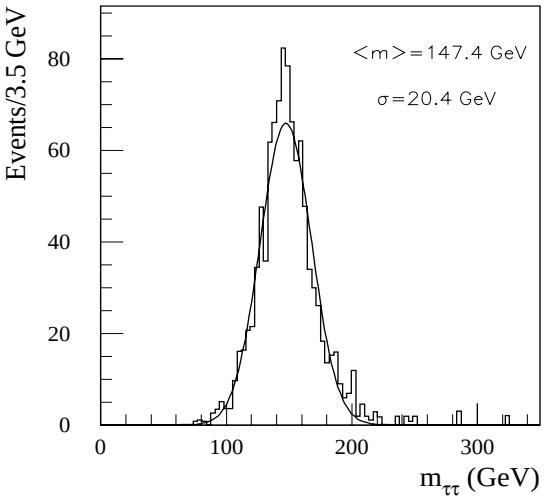

Figure 19-58 For the appropriate mixture of $H/A \rightarrow \tau\tau$ events from direct and associated production and for low-luminosity performance, distribution of reconstructed ττ mass for m_A = 150 GeV and tanβ = 7.5 (5σ discovery limit).

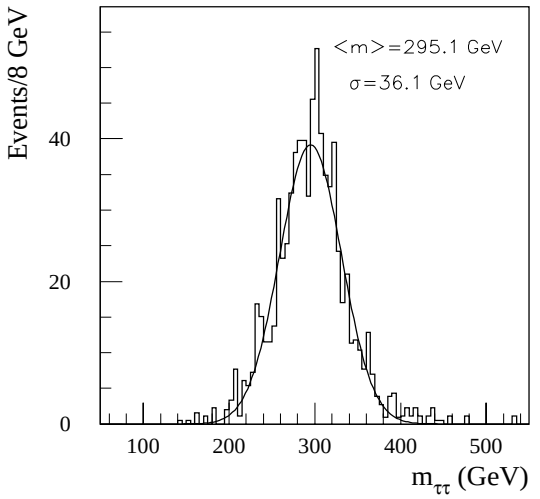

Figure 19-59 Same as Figure 19-58, but for m_A = 300 GeV and tanβ = 15.

Figures 19-56 and 19-57 show the $m_{\tau\tau}$ distributions expected for the summed signal and background, for three values of m_A with tanβ = 25 and for an integrated luminosity of 30 fb^{-1}, respectively for the direct and associated analyses. Finally, Figures 19-58, 19-59 and 19-60 show, respectively, for signal events with m_A = 150, 300 and 450 GeV, the $m_{\tau\tau}$ distribution for the appropriate mixture of direct and associated production events and for the value of tanβ corresponding to a 5σ-discovery for an integrated luminosity of 30 fb^{-1} (first column of Table 19-36).

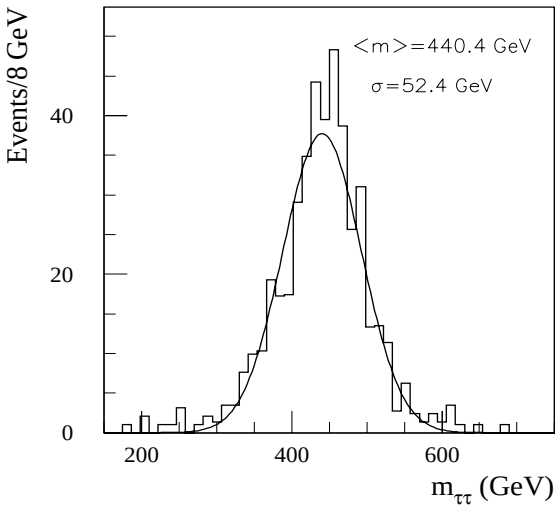

Figure 19-60 Same as Figure 19-58, but for m_A = 450 GeV and tanβ = 20.

Results at high luminosity

At high luminosity, the efficiency for τ identification and the background rejection can be maintained at their low-luminosity values, but the sensitivity to the $H/A \rightarrow \tau\tau$ channel is significantly degraded due to pile-up effects:

- The E_T^{miss} resolution is degraded by a factor of two at high luminosity and this directly affects the $m_{\tau\tau}$ reconstruction. The $m_{\tau\tau}$ resolution is degraded by a factor of two as can be seen from Figures 19-58 and 19-61.
- The acceptance in the mass window, which has to be twice as wide compared to its low-luminosity value, nevertheless decreases by about 30% (20%) for m_A = 150 GeV (m_A > 300 GeV).

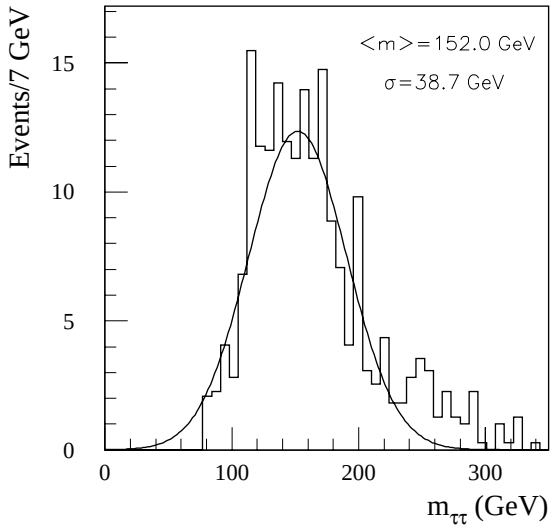

Figure 19-61 Same as Figure 19-58, but for tanβ = 6 and for high luminosity performance.

In addition, the acceptance for the signal is reduced at high luminosity due to:

- the reduced *b*-tagging efficiency (50% instead of 60%) for the same rejection of non-*b*-jets;
- the higher threshold on the jet p_T (30 GeV instead of 15 GeV);

The overall impact of high luminosity operation on the signal significance arises therefore mostly from the degradation of the ττ mass reconstruction due to pile-up and the *b*-tagging efficiency. The high luminosity signal significance is about 50% of the low luminosity significance for the same integrated luminosity. A real improvement on the 5σ discovery curve at low luminosity can be only expected after collecting the ultimate integrated luminosity of 300 fb^{-1}.

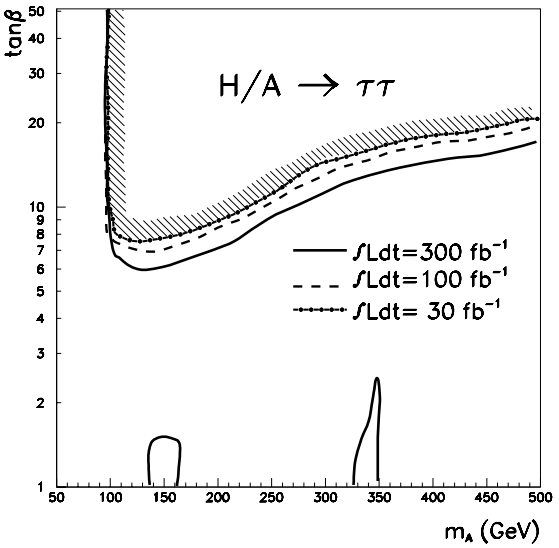

Figure 19-62 For integrated luminosities of 30 fb^{-1}, 100 fb^{-1} and 300 fb^{-1}, 5σ-discovery contour curves for the $H/A \rightarrow \tau\tau$ channel in the (m_A, tanβ) plane.

The expected 5σ discovery contour curves in the (m_A, tanβ) plane as a function of integrated luminosity are shown in Figure 19-62 for the combined $H/A \rightarrow \tau\tau$ signal. Even for a moderate integrated luminosity of 30 fb^{-1}, a signal should be observed over a large region of the (m_A, tanβ) plane. This region can be increased only for the largest integrated luminosities achievable with high luminosity operation, due to the degraded performance at high luminosity discussed above. For an integrated luminosity of 300 fb^{-1}, some sensitivity may also be achieved for low values of tanβ, in a region where the dominant signal contribution arises from direct $A \rightarrow \tau\tau$ production.

19.3.2.6 *H/A* $\rightarrow \mu\mu$

The $H \rightarrow \mu\mu$ decay channel cannot be observed for a SM Higgs because of both the very small signal rate and the large backgrounds from several SM processes. However, because of the large enhancement of rates through $b\bar{b}H$ and $b\bar{b}A$ production and of some enhancement of the branching ratio, both present at large tanβ, it can be observed in the MSSM case. The rates for this channel are governed by the same couplings as for the ττ channel, but the branching ratio scales as $(m_\mu/m_\tau)^2$.

This huge reduction in signal rates with respect to the ττ channel is compensated to some extent by the much better identification efficiency and experimental resolution, which can be achieved in the μμ channel. Also, in contrast to the $H/A \rightarrow \tau\tau$ channel, the efficiency of the reconstruction procedure and the mass resolution are comparable for the direct and associated production.

The final state contains isolated high-p_T muons and, for associated production, two additional spectator *b*-jets. In the standard event selection two muons with $p_T > 20$ GeV and $|\eta| < 2.5$ are required. This selection has a high acceptance, of 50 - 60%. The expected mass resolution, using the combined muon reconstruction, is σ_m / m = 2-3%. The intrinsic width of the Higgs boson increases with m_A and tanβ. It is of the order of ~1 GeV for tanβ = 10 and $100 < m_H < 500$ GeV and varies between 6 - 25 GeV for tanβ = 50. In the chosen mass window of $m_H \pm 1.64((\Gamma_H{}^{tot}/2.36)^2+\sigma_m{}^2)^{1/2}$, almost 90% of the signal events are contained, as described in Section 8.6.2.

The background in this channel is dominated by irreducible $Z/\gamma^* \rightarrow \mu\mu$ Drell-Yan production and reducible $t\bar{t}$ production with both top-quarks decaying into muons, $t \rightarrow \mu\nu b$. The expected cross-section for $Z/\gamma^* \rightarrow \mu\mu$ Drell-Yan production is 1400 pb for dimuon events with a mass above ~80 GeV and ~6 pb for $t\bar{t}$ events with two muons in the final state. A potential background source is also $b\bar{b}$ production with a total cross-section of 500 μb. After applying the kinematic cuts and muon isolation criteria, this background is found to be a negligible fraction of the total background. After an inclusive selection (see Table 19-37) the irreducible $Z/\gamma^* \rightarrow \mu\mu$ Drell-Yan background is dominant, while the $t\bar{t}$ background contributes only at the level of 20 - 30% of the total background over the mass range of interest. This fraction increases with increasing values of $m_{\mu\mu}$.

Since the direct and associated production result in substantially different final states, analyses, optimised separately for each production process [19-79], as in the $H/A \rightarrow \tau\tau$ case (see Section 19.3.2.5), are used. Moreover, it was found that both the irreducible and reducible backgrounds can be rejected further by applying cuts on the p_T of the dimuon system, $p_T{}^{\mu\mu}$, and on $E_T{}^{miss}$.

The optimised analyses require:

- $E_T{}^{miss} < 20$ GeV at low luminosity and $E_T{}^{miss} < 40$ GeV at high luminosity;
- $p_T{}^{\mu\mu} < 100$ GeV ;
- one *b*-tagged jet for the associated analysis, and a *b*-jet veto for the direct analysis. For low luminosity, the threshold on the *b*-tagged jet is set to 15 GeV, while for high luminosity, it is raised to 30 GeV.

Table 19-37 Expected $H/A \to \mu\mu$ signal and background rates within the chosen mass window as a function of m_A for tanβ = 15 and an integrated luminosity of 30 fb^{-1}. The rates are given separately for each production mechanism: direct ($gg \to H/A$) and associated ($b\bar{b}H$, $b\bar{b}A$) Higgs-boson production and for the direct/associated analyses (see text). The signal event rates correspond to the summed $H \to \mu\mu$ and $A \to \mu\mu$ rates. The expected signal significances are shown separately for the two analyses and for an integrated luminosity of 30 fb^{-1}. The overall combined significances are finally shown for integrated luminosities of 30 fb^{-1} and 300 fb^{-1}.

m_A (GeV)	125	150	200	300	450
σ × BR for direct production (fb)	9.6 (*A* only)	9.1	2.3	0.3	0.05
σ × BR for associated prod. (fb)	26 (*A* only)	24	10.	2.3	0.41
Inclusive analysis					
Events rates ($m_{\mu\mu} = m_A \pm 2\sigma$)					
Total signal	492	430	163	48.5	9.2
$Z/\gamma^* \to \mu\mu$	78 240	22 200	8 300	2 325	670
$t\bar{t}$	3 492	3 600	2 460	830	220
Total background	81732	25 800	10 760	3 150	890
Significance for 30 fb^{-1}	1.7	2.7	1.6	0.9	0.3
Direct/associated analysis					
Events rates ($m_{\mu\mu} = m_A \pm 2\sigma$)					
Direct production	121 / 2	116 / 2.8	29 / 0.7	2.7 / 0.07	0.4 / 0.01
Associated production	297 / 65	266 / 74	121 / 33	29.6 / 8.7	4.2 / 1.3
Total signal	418 / 67	382 / 77	150 / 33	32.3 / 8.7	4.6 / 1.3
$Z/\gamma^* \to \mu\mu$	60850 / 1180	15 300 / 430	8 840 / 220	1 700 / 27.4	102 / 7
$t\bar{t}$	57 / 137	56 / 174	41 / 98	12 / 32	1 / 4
Total background	60910 / 1317	15 354 / 604	8 880 / 318	1 712 / 59	103 / 11
Signal significance 30 fb^{-1}	1.7 / 1.9	3.1 / 3.1	1.6 / 1.9	0.8 / 1.1	0.4 / 0.4
Combined significance for 30 fb^{-1}	2.5 (*A* only)	4.4	2.4	1.4	0.6
Combined significance for 300 fb^{-1}	6.8 (*A* only)	11.6	6.4	3.3	1.8

Raising the E_T^{miss} threshold reduces the $t\bar{t}$ rejection, and thereby the sensitivity by 10%. Raising the jet threshold to 30 GeV implies an additional loss in significance of less than 10%. For high-luminosity operation, one expects a degradation of the nominal *b*-tagging efficiency from 60% to 50%, while the mass resolution and reconstruction efficiency for muons remain essentially the same.

The signal will be observed above the background as a narrow peak in the invariant dimuon mass distribution, $m_{\mu\mu}$, as shown in Figure 19-63. Table 19-37 gives the expected numbers of signal and background events in

Table 19-38 For five values of m_A and for integrated luminosities of 30 fb^{-1} and 300 fb^{-1}, lower limits of tanβ corresponding to a 5σ discovery in the $H/A \to \mu\mu$ channel.

m_A (GeV)	30 fb^{-1}	300 fb^{-1}
120	21.0	12.9
150	15.9	9.8
200	21.0	13.1
300	32.3	20.9
450	43.3	25.0

the appropriate mass window for an integrated luminosity of 30 fb^{-1} and tanβ = 15. For m_A = 120 GeV, only A-boson production is used, since the H and A masses are not degenerate and more complicated formulae have to be used for the calculation of the expected significance. For comparison, results are given for the inclusive analysis as well as for the more exclusive selections. There is a clear gain with the tighter selection, since the more favourable signal-to-background ratio leads to a better significance. Combining the results of both analyses enhances the sensitivity to this channel. Unlike in the $H/A \rightarrow \tau\tau$ case, there is no degradation in the mass resolution in the case of the associated production. The b-tagging of the spectator b-quark suppresses the dominant $Z/\gamma^* \rightarrow \mu\mu$ continuum background very effectively.

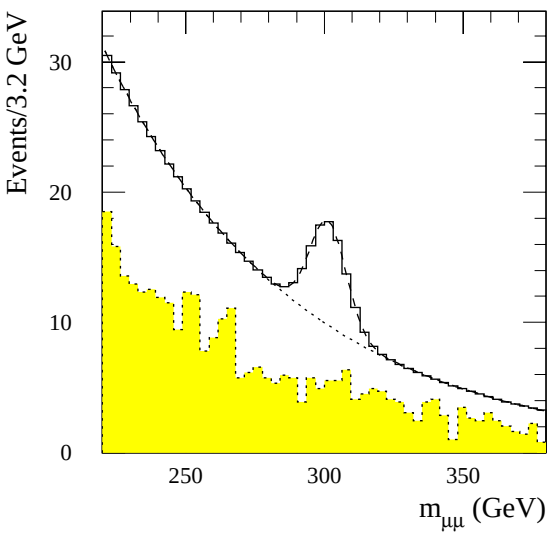

Figure 19-63 For an integrated luminosity of 30 fb^{-1} and for tanβ = 30, distribution of $m_{\mu\mu}$ shown for the reducible $t\bar{t}$ background (shaded histogram), for the total summed background (dashed curve) and for the sum of the $H/A \rightarrow \mu\mu$ signal with m_A = 300 GeV and the background (solid histogram). The $m_{\mu\mu}$ distribution is shown for the associated production analysis.

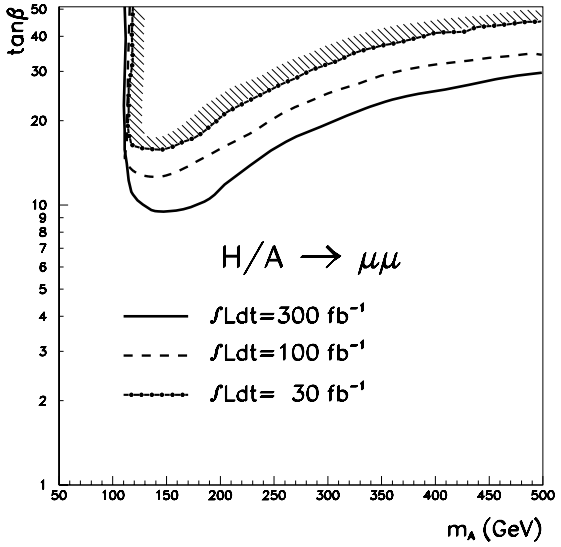

Figure 19-64 For integrated luminosities of 30 fb^{-1}, 100 fb^{-1} and 300 fb^{-1}, 5σ-discovery contour curves for the $H/A \rightarrow \mu\mu$ channel in the (m_A, tanβ) plane.

The expected significances for the inclusive, the associated and direct analyses and the combination of the latter two are given in Table 19-37 for integrated luminosities of 30 fb^{-1} and 300 fb^{-1}. The 5σ limit on tanβ for the combined analysis is given in Table 19-38 as a function of m_A. The expected 5σ-discovery contour curves for the combined $H/A \rightarrow \mu\mu$ signal are shown in Figure 19-64. The sensitivity to this channel is somewhat weaker than to the ττ channel as can be seen by comparing Tables 19-38 and 19-36. Nevertheless, the $H/A \rightarrow \mu\mu$ channel also covers a substantial fraction of the (m_A, tanβ) parameter space and provides a more precise measurement of the Higgs-boson mass (see Section 19.3.4.1).

19.3.2.7 $H/A \rightarrow t\bar{t}$

Due to the strong coupling of the SM Higgs boson to gauge-boson pairs, the $H \rightarrow t\bar{t}$ branching ratio is too small for this channel to be observable in the SM case. In the MSSM case, however, the $H \rightarrow t\bar{t}$ and $A \rightarrow t\bar{t}$ branching ratios are close to 100% for m_H, $m_A > 2\ m_t$ and for $\tan\beta \sim 1$. The $H \rightarrow t\bar{t}$ and $A \rightarrow t\bar{t}$ decays cannot be distinguished experimentally from each other, since the H- and A-bosons are almost degenerate in mass in the relevant region of parameter space.

As discussed in the literature [19-80], a signal from $H/A \rightarrow t\bar{t}$ decays would appear as a peak in the $t\bar{t}$ invariant mass spectrum above the $t\bar{t}$ continuum background for values of m_H smaller than 500 GeV. There is an interference between the signal and background amplitudes which causes an oscillating structure in the differential cross-section around $s = m_H^2$. This leads to a strong suppression of the observability of the signal at higher masses. As a consequence, for $m_H = 500$ GeV the total top-quark production cross-section differs very little from the cross-section with no Higgs boson being present. This interference effect is much stronger for the A than for the H boson. From the results presented in [19-80] this suppression of the total H+A rates is estimated to be roughly 30% for $m_H = 370$ GeV, 50% for $m_H = 400$ GeV and 70% for $m_H = 450$ GeV. These factors are taken into account in the analysis presented below (see also Table 19-39).

The signal is extracted [19-81] by searching for $WWb\bar{b}$ final states, with one $W \rightarrow l\nu$ and one $W \rightarrow jj$ decay. The lepton is required for the LVL1 trigger and all the jets, *i.e.* those from W-decay and the two b-jets, are required to have $p_T > 40$ GeV. It is expected that the experiment could trigger on such topologies and reconstruct them efficiently at both low and high luminosities. Both b-jets are required to be tagged, with an efficiency $\varepsilon_b = 60$ % (50%) at low (high) luminosity. Both top-quark decays are fully reconstructed (following the algorithm presented in Section 19.2.4.3) and a constraint on m_t is used to improve the resolution on the reconstructed $t\bar{t}$ invariant mass, $m_{t\bar{t}}$. The expected mass resolution, σ_m, on $m_{t\bar{t}}$ increases from 14 to 20 GeV as m_H increases from 370 to 450 GeV. After both top quark have been reconstructed, the background from continuum $t\bar{t}$ production is much larger than all other backgrounds (such as W+jet). The reconstructed $m_{t\bar{t}}$ distribution for signal and background events is shown in Figure 19-65 for $m_A = 370$ GeV and $\tan\beta = 1.5$.

The signal-to-background ratio varies between 9% and 1% over the mass range from 370 to 450 GeV. For an integrated luminosity of 30 fb^{-1} and $\tan\beta = 1.5$ about 2120 signal events and 4×10^4 background events are expected inside a mass windows of $\pm2\sigma_m$ around m_A for $m_A = 400$ GeV, see Table 19-39. For high luminosity operation and an integrated luminosity of 100 fb^{-1} one expects for a Higgs mass of 400 GeV about 4900 signal and 9×10^4 background events.

The mass resolutions quoted above imply that the width of a typical mass window for observing most of the signal would be between ±30 GeV and ±40 GeV. The extraction of the signal would only be possible for Higgs masses away from the kinematic peak of the background distribution, which is

Table 19-39 Observability of the $H/A \rightarrow tt$ channel for an integrated luminosity of 30 fb^{-1} and for $\tan\beta$ =1.5. The signal rates are computed using the rough estimate of the impact of the negative interference between the $H/A \rightarrow t\bar{t}$ signal and $t\bar{t}$ continuum production. For $m_A = 400$ GeV, a systematic uncertainty of 1% was assumed for the background.

m_A(GeV)	370	400	450
$\sigma \times$ BR (pb) (no interference)	11.8	8.4	4.8
$\sigma \times$ BR (pb) (with interference)	8.3	4.2	1.4
Signal	3190	2120	980
Background	34200	39500	52900
Significance	8.2	5.4	4.3

around $m_{t\bar{t}}$ = 400 GeV. Such an extraction assumes that the uncertainty on the shape of the continuum background is small and that it can be fitted from events outside the assumed Higgs mass window. Details on the fitting procedure can be found in [19-81]. This leads to the significance levels given in Table 19-39.

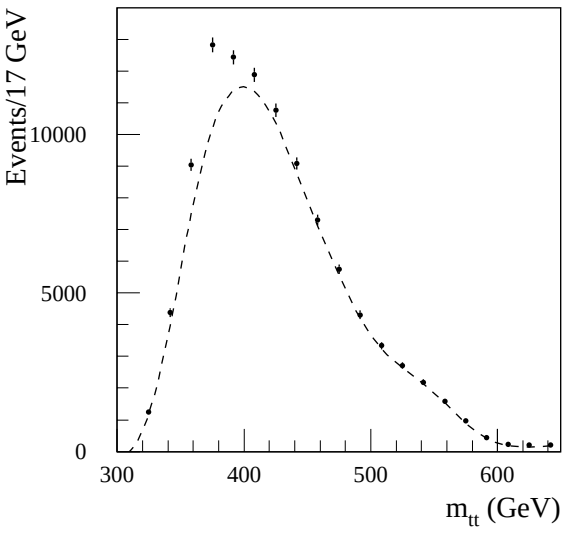

Figure 19-65 For an integrated luminosity of 30 fb^{-1} and for tanβ = 1.5, distribution of $m_{t\bar{t}}$ for the $t\bar{t}$ background (dashed histogram) and for the sum of the $H/A \rightarrow t\bar{t}$ signal with m_A = 370 GeV and of the signal+background (points with error bars).

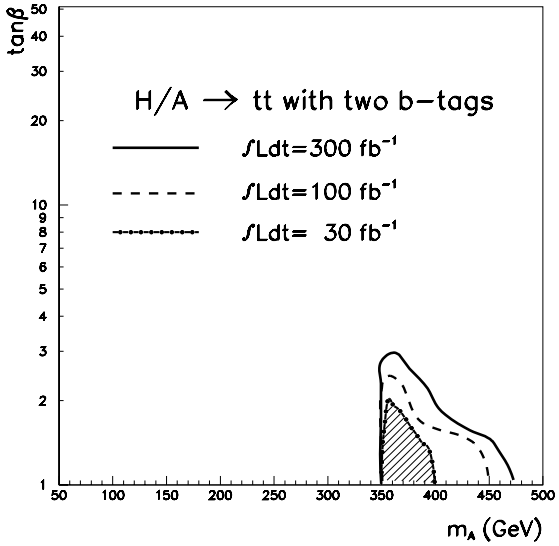

Figure 19-66 For integrated luminosities of 30 fb^{-1}, 100 fb^{-1} and 300 fb^{-1}, 5σ-discovery contour curves for the $H \rightarrow t\bar{t}$ channel in the (m_A, tanβ) plane.

For masses close to 400 GeV only an excess of events above the continuum background would be observed. This excess would be statistically significant, as shown in Table 19-39 and Figure 19-65, but this significance would only be meaningful if the theoretical uncertainties on the continuum background shape were not larger than about a percent. Although the theoretical uncertainties on the continuum $t\bar{t}$ production are much larger today, it is hoped that they would be reduced with time, and that the experimental data at the LHC would also contribute to a better understanding of heavy-flavour continuum production.

For the optimistic scenario assuming that the differential spectrum of $m_{t\bar{t}}$ would be known to better than 1% from a contribution of theory and experimental data, the signal significances including this systematic uncertainty for masses close to 400 GeV are shown in Table 19-39, and the 5σ-discovery contour curves in the (m_A, tanβ) plane for $H/A \rightarrow t\bar{t}$ decays are shown in Figure 19-66. These curves cover at best a limited region in parameter space, namely that corresponding to $2m_t < m_A < 470$ GeV. In conclusion, this channel will be only of very limited use as a discovery channel.

19.3.2.8 $b\bar{b}H$ and $b\bar{b}A$ production with $H/A \rightarrow b\bar{b}$

Final states containing four b-jets have been proposed in the literature [19-82] as signatures with a substantial discovery potential for heavy Higgs bosons in supersymmetric models. The channels of interest are:

- $b\bar{b}H$, $b\bar{b}A$ associated production with the subsequent $H/A \rightarrow b\bar{b}$ decay;

- $H \rightarrow hh \rightarrow b\bar{b}b\bar{b}$ (discussed in Section 19.3.2.9).

As described below, both channels have interesting features for the MSSM Higgs search. Their main drawback is the enormous background from QCD multijet production, and hence the very small signal-to-background ratio. In addition, triggering on purely hadronic final states is always a problem at hadron colliders. In order to maintain a LVL1 trigger rate from jets at a low enough level, rather high E_T thresholds have to be set on the individual jets [19-83] (see also Section 11.7.3). At present, ATLAS foresees three basic jet triggers at LVL1, a single jet trigger with a p_T threshold of 180 GeV, a three-jet trigger with a p_T threshold of 75 GeV on each jet, and a four jet-trigger with a p_T threshold of 55 GeV on each jet. These values apply to low-luminosity running. At high luminosity, they have to be raised to values of 290 GeV for single jet, 130 GeV for three jets and 90 GeV for four jets. These threshold settings limit the LVL1 jet trigger rate to the few kHz range, since the LVL2 trigger is not expected to reduce them by large factors.

For the particular Higgs-boson channels discussed here, these high thresholds lead to significant acceptance losses. If, on the other hand, efficient *b*-tagging could be performed with the LVL2 trigger, the LVL1 thresholds could be lowered. The possibility of applying *b*-tagging at LVL2 has been investigated already in some detail [19-83][19-84][19-85] and further work is in progress.

Given the difficulties described above, the analysis of these channels is performed in two steps. First, no acceptance losses at the trigger level are assumed, in order to determine the optimum physics coverage. In a second step, the events are subjected to the actual ATLAS LVL1 trigger thresholds, which represents a more realistic scenario, even if it could be considered pessimistic in certain cases (see below).

Analysis without trigger requirements

The $b\bar{b}H$ and $b\bar{b}A$ associated production with $H/A \rightarrow b\bar{b}$ is strongly enhanced for large values of tanβ and has been reported as a very promising channel [19-82]. This mode would be particularly interesting for large values of m_H and m_A for which the sensitivity to the $H/A \rightarrow \tau\tau$ channel slowly disappears (see Section 19.3.2.5). This channel has been studied carefully and the details are reported in [19-86].

For large values of m_A the final state has a very characteristic topology: the two hardest jets in the event come from the $H/A \rightarrow b\bar{b}$ decay, while the softer ones come predominantly from the associated $b\bar{b}$ pair and from initial / final-state radiation. These features can be used for the event selection, for which at least four reconstructed jets are required in the final state. A more favourable signal-to-background ratio is obtained, if the selection requires that the four jets of the highest transverse energies are tagged as *b*-jets. The background is dominated by events containing true *b*-jets. The contribution from events with at least one mis-identified jet is below 10%, if one assumes the default performance of the *b*-tagging algorithm at low luminosity (see Chapter 10).

The two leading jets are required to satisfy high p_T thresholds which are optimised as a function of m_A, as shown in Table 19-40. The p_T of the other two jets is required to be above 50 GeV and 30 GeV, respectively. For m_A = 200 GeV, the p_T threshold is lowered to 30 GeV for both jets. For the signal events, the expected acceptance, is of the order of 10% when four jets above these thresholds are required and the three most energetic ones are true *b*-jets (*b*-tagging efficiency is not included).

Table 19-40 p_T thresholds required for the two leading jets as a function of m_A for $H/A \rightarrow b\bar{b}$ decays from $b\bar{b}H$, $b\bar{b}A$ production.

m_A (GeV)	p_T^{min} (jet$_1$) (GeV)	p_T^{min} (jet$_2$) (GeV)
200	70	50
300	100	70
500	200	100
700	250	150
900	300	200

The two highest-p_T jets are used for the reconstruction of the Higgs-boson mass, $m_{b\bar{b}}$. The reconstructed $m_{b\bar{b}}$ peak, for tanβ = 50 and an integrated luminosity of 300 fb^{-1} is shown in Figure 19-67 for m_A = 500 GeV. Due to final-state radiation and hadronisation, the peak is rather broad, with a mass resolution of 50 GeV. About 20% of the $b\bar{b}$ combinations entering the distribution are incorrect. The acceptance in a mass window of ±80 GeV around m_A is about 70%.

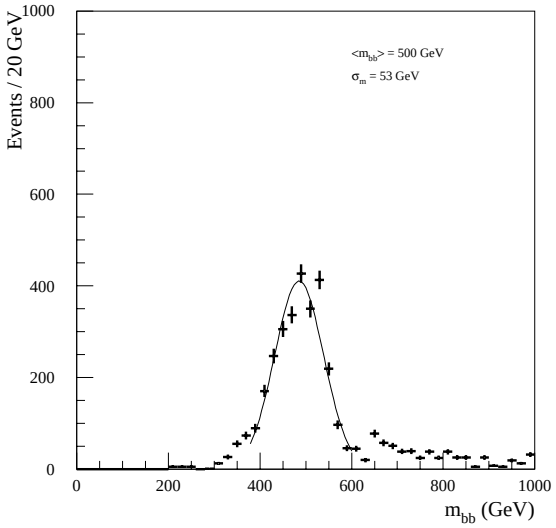

Figure 19-67 For $H/A \rightarrow b\bar{b}$ decays with m_A = 500 GeV from $b\bar{b}H$, $b\bar{b}A$ production with tanβ = 50 and for an integrated luminosity of 300 fb^{-1}, $m_{b\bar{b}}$ distribution obtained from the two leading *b*-jets in the event.

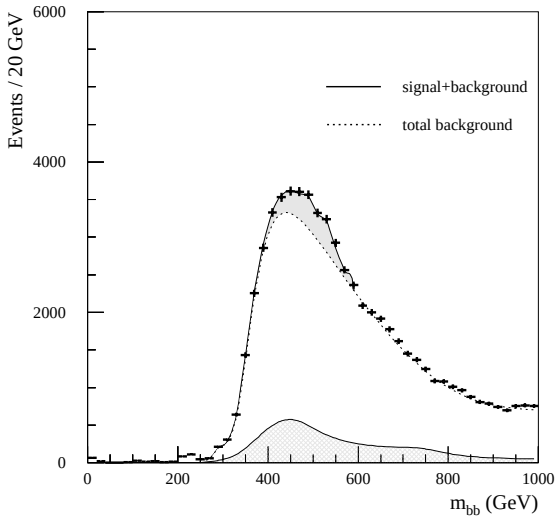

Figure 19-68 Same as Figure 19-67, but with the background included. The cross-hatched histogram shows the contribution from direct $b\bar{b}$ production and the dashed histogram represents the total background. The crosses show the summed signal and background. The signal events are clearly seen above the background (grey histogram).

This pure multi-*b*-jet final state will be very difficult to extract from the large QCD reducible and irreducible multi-jet background containing a variable number of real *b*-jets. A large sample of background events was generated using a shower approximation based on the hard-scattering dijet subprocess in the PYTHIA generator. The hard-scattering process was accompanied by initial- and final-state radiation, which both create additional jets with some fraction of *b*-jets from gluon splitting. After event selection but before applying the *b*-tagging procedure, the inclusive

background rates are approximately a factor of 10^4 to 10^5 higher than the signal rates in the mass window of interest. Requiring at least three identified *b*-jets reduces this factor to about 10^2 to 10^3.

Requiring in addition a fourth identified *b*-jet gains another factor of about two. In the sample containing at least three identified *b*-jets, approximately 40% of the background events contain at least three true *b*-jets, whereas in the sample containing at least four identified b-jets this fraction increases to 65%. The dominant remaining background arises from *gb* and *gg* production with gluon splitting into a $b\bar{b}$ pair. The contribution from direct $gg \rightarrow b\bar{b}$ production is found to be only at the level of 10% of the total background, as illustrated in Figure 19-68.

The final signal and background rates and the expected significances for an optimised selection procedure are given in Table 19-41 as a function of m_A, for $\tan\beta = 30$ and for integrated luminosities of 30 and 300 fb^{-1}.

As mentioned above, this channel has also been studied by requiring only 3 *b*-tagged jets [19-86]. Although the expected rates and significances are higher, the signal-to-background ratio is below 1%. It is rather unlikely that the systematic uncertainties on the background shape can be controlled to the precision required in this case. A selection requiring at least four identified *b*-jets, as presented in Table 19-41, yields a more favourable signal-to-background ratio (~3%) and also a more favourable ratio of irreducible-to-total background (~67%).

For a selection requiring four *b*-tagged jets and for an integrated luminosity of 300 fb^{-1}, a nominal significance larger than 5σ could be achieved for $\tan\beta > 29$ ($m_H = 500$ GeV) and for $\tan\beta > 20$ ($m_H = 300$ GeV), as illustrated in Figure 19-69. The overall conclusion is that, even for an integrated luminosity of 300 fb^{-1} and idealistic trigger conditions, the extraction of a $H/A \rightarrow b\bar{b}$ signal from $b\bar{b}$H, $b\bar{b}$A production will be very difficult. More detailed results are presented in [19-86].

The coverage in parameter space is smaller than the coverage of the $\tau\tau$ channel, see Section 19.3.2.5), which, for an integrated luminosity of 300 fb^{-1}, extends down to $\tan\beta > 11$ ($m_H = 300$ GeV) and to $\tan\beta > 15$ ($m_H = 500$ GeV). For an integrated luminosity of 30 fb^{-1}, the respective lower limits on $\tan\beta$ are $\tan\beta > 30$ and $\tan\beta > 50$ for the $b\bar{b}$ channel and $\tan\beta > 15$ and $\tan\beta > 20$ for the $\tau\tau$ channel.

It should be stressed that the significances quoted in Table 19-41 for the $b\bar{b}$ channel are rather optimistic, since the estimates of the QCD background are very uncertain (the background could be under-estimated by a factor of three) and the assumptions used for *b*-tagging are rather optimistic for such high-p_T jets. Systematic uncertainties due to the lack of knowledge of the background shape have not been taken into account in the significance estimates of Table 19-41**.** The results are optimistic also because the selection criteria are looser than those specified in the LVL1 / LVL2 trigger menu (see [19-83] and Section 11.7.3).

Acceptance with current trigger menu

If the currently planned LVL1 / LVL2 high-luminosity thresholds are applied (see Table 19-41), the acceptance for signal events is reduced by a factor of 4.7 (1.9) for $m_A = 300$ GeV ($m_A = 500$ GeV) while the background is reduced by a factor of three. This leads to a reduction in significance, for an integrated luminosity of 300 fb^{-1}, from 8.5 to 3.2 for $m_A = 300$ GeV and from 5.3 to 4.8 for $m_H = 500$ GeV. For $m_A = 200$ GeV the high-luminosity LVL1 / LVL2 thresholds reduce the acceptance for signal events by almost a factor of 18.

Table 19-41 Expected signal and background rates inside the signal mass window as a function of m_A, for $H/A \rightarrow b\bar{b}$ decays for $b\bar{b}H$ and $b\bar{b}A$ production with tanβ = 30, after applying an optimised selection procedure. The numbers are given for integrated luminosities of 30 fb^{-1} and 300 fb^{-1}(without and with the LVL1 trigger thresholds applied).

m_A(GeV)	200	300	500	700	900
σ × BR (pb)	107.0	29.0	3.5	0.9	0.2
Integrated luminosity of 30 fb^{-1}					
Signal	2 550	630	200	50	16
Background	43 000	24000	6100	1800	520
S/B	5.9%	2.6%	2.8%	2.8%	3.0%
$S/\sqrt{B}$	12.4	4.1	2.6	1.2	0.7
Integrated luminosity of 300 fb^{-1}					
Signal	12 440	3080	960	240	80
Background	230 000	130 000	33 000	10 000	2 800
S/B	5.4%	2.4%	2.9%	2.4%	2.8%
$S/\sqrt{B}$	26	8.5	5.3	2.4	1.5
Integrated luminosity of 300 fb^{-1} including LVL1 trigger thresholds					
Signal	710	650	510	240	80
Background	13 000	40 000	11 000	10 000	2 800
S/B	5.5%	1.6%	4.6%	2.4%	2.8%
$S/\sqrt{B}$	6.2	3.2	4.8	2.4	1.5

Figure 19-69 shows the 5σ-discovery contour curves in the (m_A, tanβ) plane before and after applying the LVL1/LVL2 trigger thresholds. The curves have not been extended to masses below m_A = 200 GeV since the acceptance of the LVL1/LVL2 trigger is reduced for m_A = 200 GeV to only 6% of that of the off-line selection.

In conclusion, the $b\bar{b}H$, $b\bar{b}A$ channel with $H/A \rightarrow b\bar{b}$ decay cannot be observed over most of the MSSM parameter space. Even for large values of m_A and tanβ, the large uncertainties on the QCD multijet backgrounds imply that the results shown in Figure 19-69 are optimistic and that therefore this channel cannot be considered as a discovery channel at LHC.

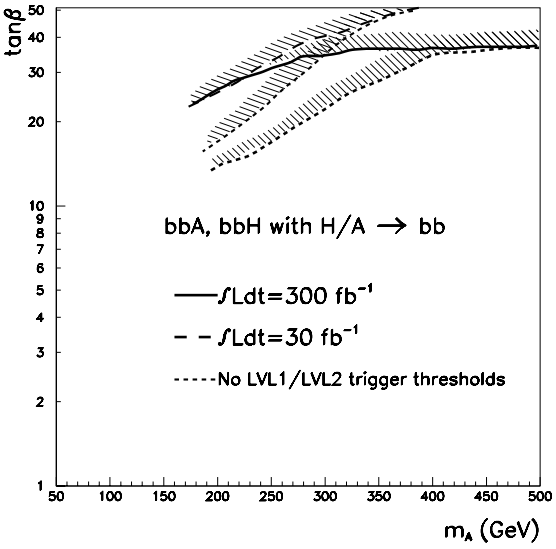

Figure 19-69 For integrated luminosities of 30 fb^{-1} and 300 fb^{-1}, 5σ-discovery contour curves in the (m_A, tanβ) plane for the $b\bar{b}H$, $b\bar{b}A$ with $H/A \rightarrow b\bar{b}$ channel. The dotted lines show the expected extension in coverage if the LVL1/LVL2 trigger thresholds are not applied.

19.3.2.9 $H \rightarrow hh$

This channel would be particularly interesting, since it would allow the simultaneous observation of two Higgs bosons. Possible final states of interest are:

- $H \rightarrow hh \rightarrow b\bar{b}b\bar{b}$. It would provide the largest signal rate, but would require a four-jet trigger with as low a p_T-threshold as possible and excellent *b*-tagging performance to control the overwhelming backgrounds from four-jet events.
- $H \rightarrow hh \rightarrow b\bar{b}\tau\tau$. The presence of at least one lepton from τ-decay would be required as a trigger, and the mass reconstruction of the ττ-pair would follow that described for $H/A \rightarrow \tau\tau$ decays. The dominant backgrounds would be from $t\bar{t}$ and *W+jet* production. This channel is difficult due to the poor mass resolution for the signal and the very large backgrounds.
- $H \rightarrow hh \rightarrow b\bar{b}\gamma\gamma$. This channel can be easily triggered upon and it offers good kinematic constraints and mass resolution for the reconstruction of m_H. The rate is however very limited.

The observability of the $H \rightarrow hh \rightarrow b\bar{b}\gamma\gamma$ and $H \rightarrow hh \rightarrow b\bar{b}b\bar{b}$ channels is discussed in this section. Similar final states occur from $A \rightarrow Zh$ decays. If the *Z*-boson and *h*-boson were degenerate in mass, the observability of the $H \rightarrow hh$ signal could be improved by $A \rightarrow Zh$ production with $Z \rightarrow b\bar{b}$ and $h \rightarrow \gamma\gamma$ or $h \rightarrow b\bar{b}$. The branching ratio $BR(A \rightarrow Zh) \times BR(Z \rightarrow b\bar{b})$ is much smaller than $BR(H \rightarrow hh) \times BR(h \rightarrow b\bar{b})$, but the cross-section for *A* production is larger than for *H* production, and therefore the additional contribution from the $A \rightarrow Zh$ channel would be at the level of 10 - 15%. This additional contribution has not been included in the studies presented below.

The $H \rightarrow hh \rightarrow b\bar{b}\gamma\gamma$ channel.

To extract a signal in this channel, events were selected to have:

- Two isolated photons, with $|\eta| < 2.5$ and $p_T > 20$ GeV which serve as a trigger.
- Two jets with $|\eta| < 2.5$ and $p_T > 15$ GeV ($p_T > 30$ GeV) at low (high) luminosity of which at least one is required to be tagged as a *b*-jet. The invariant mass of the two-jet system is denoted m_{bj} in the following.
- No other jet with $|\eta| < 2.5$ and $p_T > 15$ GeV ($p_T > 30$ GeV) at low (high) luminosity.
- The masses of the two-photon and dijet systems are required to be in a window of ±2 GeV and ±26 GeV around m_h, respectively. For events passing these cuts, the four-vectors of the photons and *b*-jets are rescaled to obtain $m_{\gamma\gamma} = m_{bj} = m_h$. This rescaling improves the invariant mass resolution for the $bj\gamma\gamma$ system, $m_{bj\gamma\gamma}$.
- The invariant mass of the $bj\gamma\gamma$ system is required to be within ±20 GeV of m_H. The signal acceptance in the mass window is 70% after the m_h constraints.

Figure 19-70 shows, for m_H = 300 GeV and m_h = 98 GeV, the reconstructed mass of the $\gamma\gamma$, *jb*, and $\gamma\gamma jb$ systems (without and with *h*-boson mass constraints).

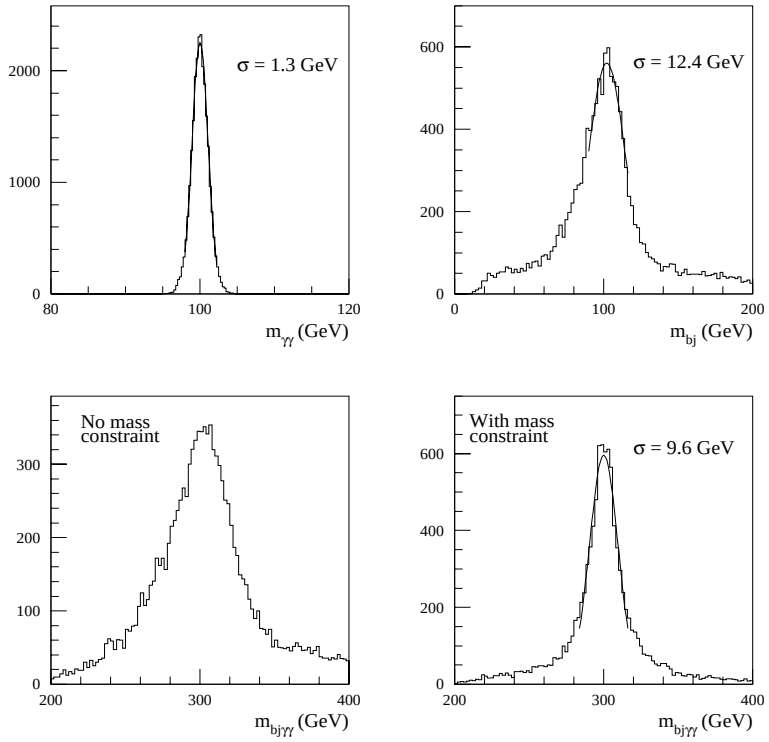

Figure 19-70 For m_H = 300 GeV and m_h = 98 GeV mass distributions from $H \rightarrow hh \rightarrow b\bar{b}\gamma\gamma$ decays (signal events only), shown for $m_{\gamma\gamma}$ (top left), m_{bj} (top right) and $m_{bj\gamma\gamma}$ before (bottom left) and after (bottom right) applying the *h*-boson mass constraints to $m_{\gamma\gamma}$ and m_{bj}.

At high luminosity, the expected $m_{bj\gamma\gamma}$ mass resolution increases by ~20% and the *b*-tagging efficiency decreases from 60% to 50%. In addition, since the p_T-thresholds on the jets have to be raised, the kinematic acceptance for the signal decreases from ~12% at low luminosity to ~6.5% at high luminosity.

The estimates for the observability of the $H \rightarrow bb\gamma\gamma$ signal given below can be considered as conservative at high luminosity, since a higher p_T threshold has been applied before recalibration of the jet energies.

Several background sources are considered: irreducible $b\bar{b}\gamma\gamma$ and reducible $bj\gamma\gamma$, $c\bar{c}\gamma\gamma$, $cj\gamma\gamma$ and jj$\gamma\gamma$, which are all estimated using the parton-shower approach in PYTHIA. There are large uncertainties on these background estimates, due to the poor knowledge of the total $b\bar{b}$, $c\bar{c}$ and jj cross-sections, and due to the procedure used to simulate photon bremsstrahlung in these processes. The various photon bremsstrahlung backgrounds were further reduced by requiring that the larger of the two h-boson transverse momenta be larger than a threshold value, typically of 60 - 80 GeV. Even for the requirement of only one tagged b-jet, the expected signal rates are rather low and they decrease rapidly with increasing tanβ.

For m_H = 320 GeV and an integrated luminosity of 300 fb^{-1}, about 106 events are expected for tanβ = 1 and 19 events for tanβ = 3, with a background of 1.7 and 4.2 events, respectively. Tables 19-42 and 19-43 give details on the number of expected signal and background events for an integrated luminosity of 30 fb^{-1} and 300 fb^{-1}, respectively. For a given value of m_H, the corresponding value of m_h increases as tanβ increases, and therefore the background rate varies.

The sensitivity to the $H \rightarrow hh \rightarrow b\bar{b}\gamma\gamma$ signal for a given value of m_H is estimated for two different values of m_h, and a simple linear interpolation or extrapolation is performed to obtain the 5σ-discovery contour curves in the (m_A, tanβ) plane. The result is shown in Figure 19-71. This channel is only observable for low values of tanβ, tanβ < 4, and for 2 $m_h < m_H < 2m_t$.

Table 19-42 Observability of the $H \rightarrow hh \rightarrow bb\gamma\gamma$ channel for an integrated luminosity of 30 fb^{-1} and for several values of m_H and m_h. The expected numbers of signal and background events are given together with the statistical significances (computed using Poisson statistics). The errors indicate the statistical precision of the simulation.

m_H (GeV)	230	270	320
m_h = 72 GeV	**(tanβ = 1)**		
σ × BR (fb)	6.0	5.0	4.6
Signal	18.4 ± 0.4	16 ± 0.3	16 ± 0.3
Background	1.7 ± 0.2	0.3 ± 0.05	0.3 ± 0.05
Significance	6.4	> 8.3	> 8.3
m_h = 97 GeV	**(tanβ = 3)**		
σ × BR (fb)	2.0	1.6	1.2
Signal	6.5 ± 0.1	4.8 ± 0.1	4.5 ± 0.1
Background	4.5 ± 0.4	1.5. ± 0.1	0.8 ± 0.1
Significance	2.1	2.0	2.7

Table 19-43 Same as Table 19-42, but for an integrated luminosity of 300 fb^{-1}.

m_H (GeV)	230	270	320
m_h = 72 GeV	**(tanβ = 1)**		
Signal	58.5 ± 1.2	40 ± 1.2	106 ± 0.3
Background	6.0 ± 0.7	2.1 ± 0.2	1.7 ± 0.3
Significance	23.5	26.1	77.8
m_h = 97 GeV	**(tanβ = 3)**		
Signal	16.5 ± 0.2	15.5 ± 0.2	18.6 ± 0.2
Background	8.8 ± 0.9	3.4 ± 0.3	4.2 ± 0.3
Significance	4.4	5.5	6.0

The $H \rightarrow hh \rightarrow b\bar{b}b\bar{b}$ channel

This channel, similarly to the channels $b\bar{b}A$, $b\bar{b}H$, presents another example of a multi-b-jet channel with no lepton present for triggering. It has been studied in some detail in [19-86], and the results of the analysis for m_H = 300 GeV and m_h = 80 GeV are presented below. As in Section 19.3.2.8, the discussion is split into two parts. First, an optimistic analysis without trigger requirements is presented, after which the impact of the current LVL1 / LVL2 trigger thresholds is discussed.

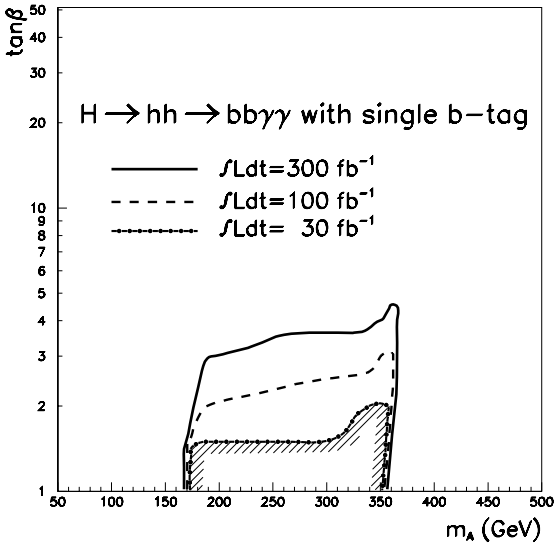

Figure 19-71 For integrated luminosities of 30 fb^{-1}, 100 fb^{-1} and 300 fb^{-1}, 5σ-discovery contour curves for the $H \rightarrow hh \rightarrow b\bar{b}\gamma\gamma$ channel in the (m_A, tanβ) plane.

Analysis without trigger requirements

The detector response is parametrised using fast simulation. Pile-up effects are included and a b-tagging procedure is applied to the reconstructed jets after recalibrating their four-momenta. For signal events, the jet spectrum is relatively hard, with an average p_T of 100 GeV for the hardest and 36 GeV for the fourth jet within $|\eta| < 2.5$. Requiring at least four jets reconstructed with $p_T > 40$ GeV (before energy recalibration) yields an acceptance of 25% for the signal events.

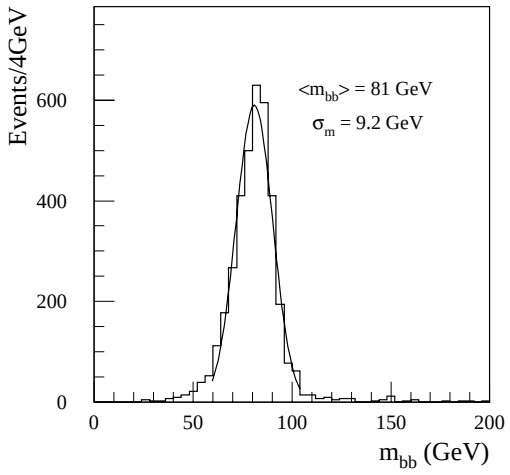

Figure 19-72 For fully simulated $H \rightarrow hh \rightarrow b\bar{b}b\bar{b}$ decays with m_H = 300 GeV and m_h = 80 GeV and for low-luminosity performance, distribution of $m_{b\bar{b}}$ for the best combination of two pairs of b-tagged jets (two entries per event).

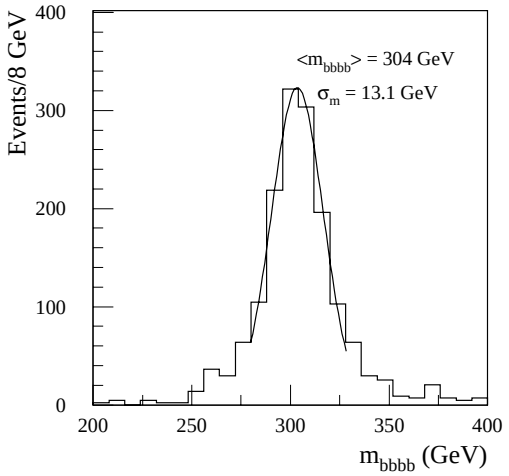

Figure 19-73 Same as Figure 19-72 but for the distribution of $m_{b\bar{b}b\bar{b}}$ after applying the h-boson mass constraint to both pairs of b-tagged jets.

The signal can be extracted by:

- Requiring the four highest-p_T jets to be identified as b-jets.
- Finding the best combination of two pairs of b-tagged jets with invariant masses, $m_{b\bar{b}} = m_h \pm 20$ GeV.

- Requiring $m_{b\bar{b}b\bar{b}} = m_H \pm 26$ GeV after applying the h-boson mass constraint to both pairs of b-tagged jets.

The results of this procedure for fully simulated and reconstructed events with $m_h = 80$ GeV and $m_H = 300$ GeV (see Section 9.3.2 and [19-87]) are illustrated in Figures 19-72 and 19-73 for the distributions of $m_{b\bar{b}}$ (two entries per event) and $m_{b\bar{b}b\bar{b}}$, respectively. At low luminosity, the acceptance for finding two $b\bar{b}$ pairs with $m_{b\bar{b}} = m_h \pm 20$ GeV is 76%, and that for finding $m_{b\bar{b}b\bar{b}} = m_H \pm 26$ GeV after applying the h-boson mass constraint in 82%.

Background events arise predominantly from QCD multijet production with a mixture of irreducible backgrounds (containing only b-jets) and reducible backgrounds (containing at least one non-b-jet in the final state). After requiring four jets within $|\eta| < 2.5$ and with $p_T > 40$ GeV, the expected number of inclusive four-jet events is $2\text{x}10^8$ from direct $gg \rightarrow b\bar{b}$ production, $1.2\text{x}10^9$ from $gb \rightarrow gb$ production and $1.7\text{x}10^{10}$ from $gg \rightarrow gg$ production.

Even though the direct $gg \rightarrow b\bar{b}$ production process contains initially two real b-jets, it contributes to only about 20% of the total background after requiring four b-tagged jets. Due to their much larger initial production rates, the dominant background arises from $gb \rightarrow gb$ and $gg \rightarrow gg$ production. The background from four real b-jets amounts to 70% of the total background.

Before any invariant mass combinations are selected, the multijet background is huge compared to the signal. As an example, for $m_H = 300$ GeV and $m_h = 97$ GeV ($\tan\beta = 3$), the signal-to-background ratio is about 0.1% after requiring events with four b-tagged jets with $p_T > 40$ GeV. This ratio increases to 1% after selecting the two best $b\bar{b}$ pairs in the mass window around m_h. These numbers show clearly that this channel cannot be used as a stand-alone discovery channel. Table 19-44 gives the expected signal and background rates for an integrated luminosity of 300 fb^{-1} and for two cases, $m_H = 300$ GeV and $m_h = 71$ GeV ($\tan\beta = 1.5$), and $m_H = 300$ GeV and $m_h = 97$ GeV ($\tan\beta = 3$). The signal observability is comparable to than that for $H \rightarrow hh \rightarrow b\bar{b}\gamma\gamma$

Table 19-44 For an integrated luminosity of 300 fb^{-1} and for $H \rightarrow hh \rightarrow b\bar{b}b\bar{b}$ decays with $m_H = 300$ GeV and two values of $\tan\beta$, $\tan\beta = 1.5$ and 3.0, expected cross-section times branching ratio, numbers of signal and background events, signal-to-background ratios and signal significances. No trigger requirements are imposed.

	$\tan\beta = 1.5$ ($m_h = 71$ GeV)	**$\tan\beta = 3.0$ ($m_h = 97$ GeV)**
$\sigma \times$ BR (pb)	1.73	0.76
Signal	1360	360
Background	4000	4000
S/B	34%	9.0%
$S/\sqrt{B}$	21.5	5.7

Table 19-45 For an integrated luminosity of 30 fb^{-1} and for $H \rightarrow hh \rightarrow b\bar{b}b\bar{b}$ decays with $m_H = 300$ GeV and $m_h = 97$ GeV ($\tan\beta = 3.0$), expected numbers of signal and background events, signal-to-background ratios and signal significances as a function of the p_T threshold for the softest jet.

p_T-threshold (GeV)	**20**	**30**	**40**
Signal	231	132	50
Background	48 000	10 000	800
S/B	0.5%	1.3%	6.2%
$S/\sqrt{B}$	1.1	1.3	1.8
$p_T^{bb} > 60$ GeV and $p_T > 80$ GeV			
Signal	132	75	30
Background	2 500	1 500	400
S/B	5.3%	5.0%	7.5%
$S/\sqrt{B}$	2.6	1.9	1.5

decays (see Table 19-43) but would be sufficient to confirm a discovery in this latter channel. However, the results of Table 19-44 are only indicative since they do not yet include any trigger requirements (see below).

Without optimised cuts, see upper part of Table 19-45, the background increases much faster than the signal as the p_T threshold is lowered and the sensitivity deteriorates rapidly. With optimised cuts, however, it would appear advantageous to lower the jet p_T threshold, but the already large uncertainties of about a factor of three on the modelling of the multijet background using the parton-shower approach would be even larger in this case. Even with optimised selection cuts, see lower part of Table 19-45, the sensitivity at low luminosity is weaker than or at most comparable to that for the $H \rightarrow hh \rightarrow b\bar{b}\gamma\gamma$ channels (see Section 19.3.2.9 and Table 19-42) and with much less favourable and more uncertain signal-to-background ratio.

Impact of current trigger menu

The present LVL1 trigger menu (see Section 11.7.3) imposes a p_T threshold of 90 GeV for the four-jet trigger at high luminosity, as compared to the 40 GeV threshold used in the analysis described above. The only other possibilities would be to trigger on single jets with $p_T > 290$ GeV or three jets with $p_T > 130$ GeV. These thresholds are very high compared to the expected p_T spectrum of jets from $H \rightarrow hh \rightarrow b\bar{b}b\bar{b}$ decays. Fulfilling the present LVL1 requirements would strongly suppress the possible sensitivity in this channel. A possible trigger on multijet final states including b-tagging at LVL2 is at present under study [19-83]. This would permit a lower threshold to be applied at LVL1.

19.3.2.10 $A \rightarrow Zh$

The observation of this channel would be particularly interesting, since it would correspond to the simultaneous discovery of two Higgs bosons. It is the dominant A-boson decay mode for low values of tanβ and for $m_Z + m_h < m_A < 2m_t$. Possible final states of interest are:

- $A \rightarrow Zh \rightarrow b\bar{b}b\bar{b}$. The channel is similar to $H \rightarrow hh \rightarrow b\bar{b}b\bar{b}$, but with smaller rates, because $BR(Z \rightarrow b\bar{b})$ is much smaller than BR($h \rightarrow b\bar{b}$). This would provide the largest signal rate, but would require a four-jet trigger with as low p_T-threshold as possible. Such a trigger is under consideration as discussed already in Section 19.3.2.9.
- $A \rightarrow Zh \rightarrow llb\bar{b}$. This channel is the only one discussed below, because it can be easily triggered upon and it offers the largest rates apart from the dominant four b channel.

Table 19-46 Expected cross-sections times branching ratios for background channels to the $A \rightarrow Zh \rightarrow llb\bar{b}$ searches.

Process ***lljj* final state**	$\sigma \times$ **BR (pb)**
$Zb\bar{b}$	36.0
Zjj with $m_{ll} > 80$ GeV	1880
ZZ with $Z \rightarrow bb$ $\sqrt{s'} > 150$ GeV	0.22
ZW, with $W \rightarrow jj$ $\sqrt{s'} > 150$ GeV	1.16
$t\bar{t}$	26.0

- $A \rightarrow Zh \rightarrow ll\gamma\gamma$. This channel would provide better kinematic constraints in the final state than the preceding one, but the expected rates are too low for it to be observable at the LHC.

The conclusions for the four-b channel are similar to that for the $H \rightarrow hh \rightarrow b\bar{b}b\bar{b}$ channel described previously. Below only the $A \rightarrow Zh \rightarrow llb\bar{b}$ channel is discussed.

The $A \rightarrow Zh \rightarrow llb\bar{b}$ events are selected to have [19-16]:

- Two isolated leptons, with opposite sign and same flavour in $|\eta| < 2.5$ and $p_T > 20$ GeV.
- Two additional jets with $|\eta| < 2.5$ and $p_T > 15$ GeV at low and $p_T > 30$ GeV at high luminosity. Both jets are required to be tagged as *b*-jets.
- The dilepton and dijet masses are required to be within ± 6 GeV and ± 22 GeV of m_Z and m_h respectively. For events in the mass window the four-vectors of the *b*-jets are rescaled, such that the peak position in the invariant mass of the $b\bar{b}$-system corresponds to the assumed nominal mass m_h.

After rescaling of the jet four-momenta a resolution of ~8 GeV is found for the reconstructed $llb\bar{b}$ invariant mass. These resolution has been confirmed with full simulation of the ATLAS detector [19-87]. The rescaling reduces significantly the non-Gaussian tails, as already illustrated in the case of $H \rightarrow hh \rightarrow b\bar{b}\gamma\gamma$.

The overall acceptance for the signal with $m_A = 300$ GeV is ~6.2% (3.0%) at low (high) luminosity including a lepton reconstruction efficiency of 90%, the *b*-tagging efficiency quoted above, and the acceptance of the selection cuts and mass windows. In this analysis, the threshold on the jet transverse momenta was applied, as for the $H \rightarrow hh \rightarrow b\bar{b}\gamma\gamma$ analysis, before energy recalibration. Since, in this channel, the average jet p_T is relatively low, such a procedure gives a significant loss of acceptance at high luminosity.

Several background sources have been considered: the irreducible $Zb\bar{b}$ and ZZ as well as the reducible ZW, Zjj and $t\bar{t}$ backgrounds. Cross-sections for these backgrounds are given in Table 19-46. After the selection cuts are applied, the $Zb\bar{b}$ and $t\bar{t}$ backgrounds are dominant.

Table 19-47 Cross-sections times branching ratios, expected number of signal and background events and statistical significance for the $A \rightarrow Zh \rightarrow llb\bar{b}$ channel for an integrated luminosity of 30 fb^{-1} and for several values of m_H and m_h (two different values of tanβ).

m_H (GeV)	200	250	300
m_h = 71 GeV tanβ = 1			
σ × BR (fb)	560	470	340
Signal	675	786	642
$Zb\bar{b}$	830	315	125
ZZ, Zjj	50	25	10
$t\bar{t}$	90	90	45
Total background	970	430	180
Significance	21.7	37.8	47.6
m_h= 97 GeV tanβ = 3			
σ × BR (fb)	9.0	21	17
Signal	15	39	37
Total background	1140	1120	650
Significance	0.5	1.2	1.4

Table 19-48 Same as Table 19-47, but for an integrated luminosity of 300 fb^{-1}, assuming high luminosity performance.

m_H (GeV)	200	250	300
m_h = 71 GeV tanβ = 1			
Signal	1008	2520	3000
$Zb\bar{b}$	375	375	60
ZZ, Zjj	20	20	10
$t\bar{t}$	210	405	190
Total background	600	800	260
Significance	40.8	89.0	186
m_h= 97 GeV tanβ = 3			
Signal	36	140	170
Total background	1830	2700	2000
Significance	0.8	2.7	3.8

The background can be further reduced by applying cuts on the transverse momenta of the reconstructed $h \to b\bar{b}$ or $Z \to ll$ and on the missing transverse momentum E_T^{miss}. A cut of $E_T^{miss} < 60$ GeV is found to optimise the signal-to-background ratio and leads to the event numbers given in Table 19-47. The results are given for two different values of tanβ and for an integrated luminosity of 30 fb^{-1}. The expected signal rates decrease rapidly with increasing tanβ, even though larger values of m_h improve the signal acceptance by nearly a factor of 2 between m_h = 70 GeV and m_h = 97 GeV. For tanβ = 1, the signal-to-background ratio increases from ~2:3 for m_A = 200 GeV to ~4:1 for m_A = 300 GeV. For a given value of m_A, the corresponding value of m_h increases with increasing tanβ and so the background rate varies also. At high luminosity, as presented in Table 19-48, the $t\bar{t}$ background becomes more important**.** For low tanβ values a clear mass peak can be reconstructed on top of the background, as shown in Figure 19-74 for a 300 GeV Higgs boson, tanβ =1 and an integrated luminosity of 30 fb^{-1}.

Given the rapid falling signal rates with increasing tanβ, the $A \to Zh \to llb\bar{b}$ channel can only be observed for low values of tanβ and for 200 GeV < m_A < 2 m_t. The sensitivity to the signal for a given value of m_A was estimated for two different values of m_h, and a simple linear interpolation or extrapolation was performed to obtain the 5σ-discovery contour curves in the (m_A, tanβ) plane which are presented in Figure 19-75.

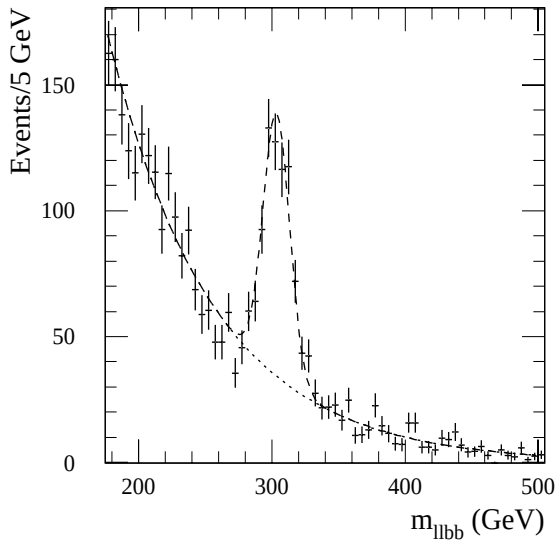

Figure 19-74 The expected signal+background distribution for $m_{llb\bar{b}}$ from a reconstruction of $A \to Zh \to llb\bar{b}$ events for m_A = 300 GeV and tanβ = 1 (m_h = 71 GeV) and for an integrated luminosity of 30 fb^{-1}.

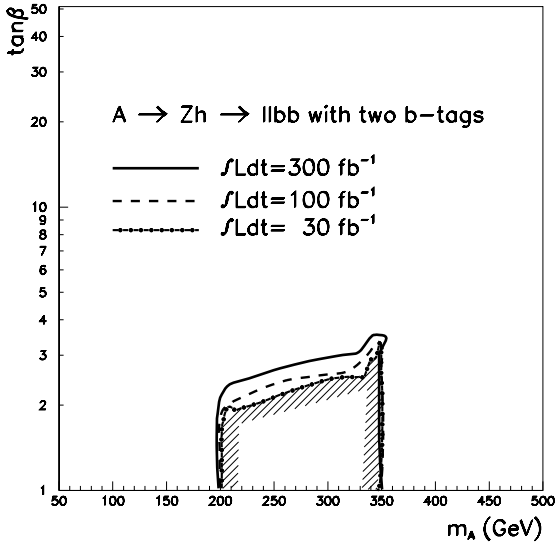

Figure 19-75 For integrated luminosities of 30 fb^{-1}, 100 fb^{-1} and 300 fb^{-1}, 5σ-discovery contour curves for the $A \to Zh \to llb\bar{b}$ channel in the (m_A, tanβ) plane.

19.3.2.11 Charged Higgs bosons

The charged Higgs bosons have masses which are almost degenerate with the masses of the *H*- and *A*-bosons. Although several mechanisms can be potential sources for their production, only a few seem promising for their detection:

- If the charged Higgs boson is lighter than the top quark, top quark decays represent a copious source of its production, via the decay $t \rightarrow H^+b$. Since top-quarks are expected to be produced with very large rates at the LHC, $\sigma_{t\bar{t}} \sim 600$ pb, a charged Higgs boson can be searched for in this channel for masses up to the kinematic limit imposed by the top-quark mass.
- If the charged Higgs boson is heavier than the top quark, it can be produced via the gluon-*b* and gluon-gluon fusion processes, $pp \rightarrow tH^{\pm}$ and $pp \rightarrow tbH^{\pm}$ respectively, in which the Higgs boson is emitted from a heavy quark [19-88].

The main decay channels of the charged Higgs bosons are the fermionic decays: $H^{\pm} \rightarrow \tau\nu$ below the *tb*-threshold and $H^{\pm} \rightarrow tb$ above. Below 150 GeV and for low values of tanβ, the $H^{\pm} \rightarrow cs$ and $H^{\pm} \rightarrow cb$ modes are not negligible. In the same mass range, the three-body off-shell decays $H^{\pm} \rightarrow hW^*$, $H^{\pm} \rightarrow AW^*$ and $H^{\pm} \rightarrow bt^* \rightarrow bbW$ [19-89] have also sizeable branching ratios. When the phase-space increases, 150 GeV < $m_{H^{\pm}}$ < 180 GeV, both the *bbW* and the *hW** mode could be enhanced with respect to the τν mode. Decays into the lightest chargino $\tilde{\chi}_1^{\pm}$ and neutralino $\tilde{\chi}_1^0$ or decays into sleptons would dominate whenever kinematically allowed. For large values of tanβ the importance of these SUSY decay modes would be reduced, however, for values as large as tanβ = 50, the decay $H^{\pm} \rightarrow \tilde{\tau}\,\tilde{\upsilon}$ would be enhanced, provided it is kinematically allowed and would lead to τ's in the final state. Their transverse momentum spectrum is, however, expected to be softer than that of τ's from the direct $H^{\pm} \rightarrow \tau\nu$ decays.

Charged Higgs lighter than the top-quark

The experimental strategies for the charged Higgs boson search below the top-quark mass rely on the $t \rightarrow H^+b$ decays, given the expected production of the $6\text{x}10^6$ $t\bar{t}$ pairs for an integrated luminosity of 10 fb^{-1}. Since the relevant $t \rightarrow H^+b$ branching ratio is proportional to ($m_t^2 \cot^2\beta + m_b^2 \tan^2\beta$), for a given value of $m_{H^{\pm}}$ the branching ratio for such decays is large at small and at large tanβ, but has a pronounced minimum at $\tan\beta \sim \sqrt{m_t/m_b} \sim 7.5$. The exact position of this minimum and its depth is sensitive to QCD corrections to the running *b*-quark mass.

Studies of $H^{\pm} \rightarrow \tau\nu$ and $H^{\pm} \rightarrow cs$ decay modes are presented below. The $H^{\pm} \rightarrow hW^*$, $H^{\pm} \rightarrow AW^*$ and $H^{\pm} \rightarrow bt^* \rightarrow bbW$ have not been studied so far by ATLAS. With the expected *b*-tagging efficiency, these multi-*b*-jets decays modes are very interesting for a more detailed investigation.

$H^{\pm} \rightarrow \tau\nu$

When the charged Higgs is produced in top decays, the $t \rightarrow H^+b$ decay competes with the standard $t \rightarrow Wb$ decay. The $H^{\pm} \rightarrow \tau\nu$ leads to an enhanced tau lepton rate in $t\bar{t}$ decays. The mass of the charged Higgs boson cannot, however, be directly reconstructed, because several neutrinos are produced in the final state.

The study was performed at the time of the Technical Proposal [19-14] (see also [19-90]), using a full detector simulation. Here only the main results are recalled and more details can be found in [19-90].

Events are selected to have:

- One isolated high p_T lepton within $|\eta| < 2.5$, which triggers the experiment. In signal events this lepton originates from semi-leptonic decays of the second top quark.
- One identified hadronic tau, using the same identification criteria as defined in Section 9.1.5 for the $H/A \rightarrow \tau\tau$ decays.
- At least three jets with $p_T > 20$ GeV and $|\eta| < 2.5$, of which two are required to be tagged as *b*-jets. This reduces the potentially large backgrounds from *W+jet* and $b\bar{b}$ production to a level well below the $t\bar{t}$ signal itself.

Table 19-49 Observability of the $H^{\pm} \rightarrow \tau\nu$ channel at low luminosity. The $\sigma \times$ BR values, the expected number of signal and background events and the signal significance are given for the production of one or two charged Higgs bosons in $t\bar{t}$ decay and for tanβ = 5. A systematic uncertainty of 3% on the background is assumed in the calculation of the signal significance.

m_{H^+} (GeV)	110	130	150
$\sigma \times$ BR (pb)	23.3	13.1	4.8
Signal	3050	1550	380
Background	7020	7170	9120
Significance	13.1	6.6	1.3

The selection cuts enhance the τ-lepton signal from $H^{\pm}$ decays with respect to that from *W* decay, and select mostly single-prong τ-decays.

As for the case of the $H/A \rightarrow \tau\tau$ decays discussed in Section 9.1.5 τ identification is a key element in extracting a possible signal from the large combinatorial background from jets. After the selection cuts and the τ identification criteria are applied, $t \rightarrow H^+b$ decays appear as final states with an excess of events with one isolated τ–lepton compared to those with an additional isolated electron or muon. Details on signal and background rates are given in Table 19-49 for tanβ = 5 and various H^+ masses. For example, for $m_{H^+} = 130$ GeV and tanβ = 5, an excess of ~1500 τ-leptons is expected from a charged Higgs-boson signal, above a background of ~3000 τ-leptons from *W*-decay, and of ~4000 fake τ-leptons.

When measuring such an excess, systematic uncertainties have to be taken into account. They arise mainly from the imperfect knowledge of the τ-lepton efficiency from fake τ-leptons present in the final sample. They were assumed to be ~3% from past experience [19-91], and were added to the statistical uncertainty to obtain the significances presented in Table 19-49. Since these systematic uncertainties dominate the overall uncertainty, the sensitivity to a charged Higgs-boson signal would not improve significantly with higher integrated luminosity unless increased statistics resulted in improved systematic uncertainties.

Figure 19-76 shows the expected 5σ-discovery contour curve for this channel in the (m_A, tanβ) plane for $m_t = 175$ GeV and for an integrated luminosity of 30 fb^{-1}. A signal from charged Higgs-boson production in $t\bar{t}$ decays

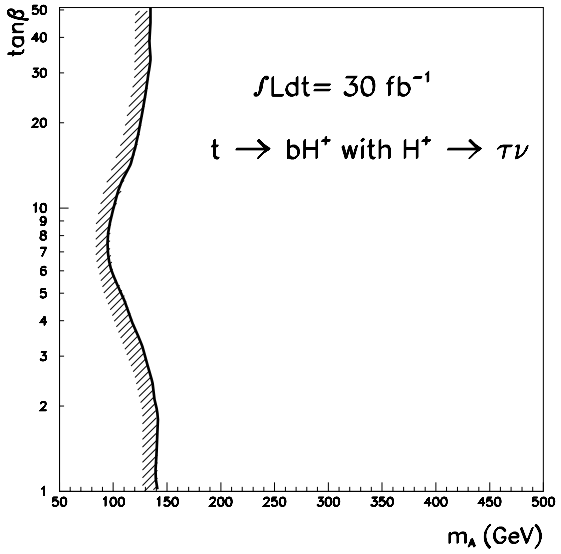

Figure 19-76 The 5σ-discovery contour curve for the $H^{\pm} \rightarrow \tau\nu$ channel in the (m_A, tanβ) plane for an integrated luminosity of 30 fb^{-1} and a top-quark mass of 175 GeV.

would be observed for all values of $m_{H^\pm}$ below m_t - 20 GeV over most of the tanβ-range. For moderate values of tanβ, for which the expected signal rates are lowest, the accessible values of $m_{H^\pm}$ are lower than this value by 20 GeV.

$H^\pm \to cs$

In the ATLAS Letter of Intent [19-13], the $H^\pm \to cs$ decay mode was considered as a complementary one to the $H^\pm \to \tau\nu$ channel for searches at low tanβ. Off shell decay modes such as $H^\pm \to hW^*$, $H^\pm \to AW^*$, $H^\pm \to bt^*$ were not considered in the original study. If these modes are taken into account, the prospects for the observability of the $H^\pm \to cs$ channel are reduced by a large factor. According to present theoretical calculations [19-89], assuming tanβ = 1.5 and $m_{H^\pm}$ = 110 - 150 GeV, for example, the $H^\pm \to cs$ branching ratio does not exceed ~3-6% while a branching ratio of ~26% is predicted by the default version of PYTHIA5.7, where off-shell decays are not included.

Table 19-50 Cross section times branching ratios for signal and $t\bar{t} \to WbWb$ background at tanβ = 1.5 and two different values of m_{H^+} for the production of a single charged Higgs boson in $t\bar{t}$ decays.

$t\bar{t}$ **with** $t \to Wb$, $W \to l\nu$ $t \to H^+b$, $H^\pm \to cs$	$t\bar{t}$ **with** $t \to Wb$, $W \to l\nu$ $t \to Wb$, $W \to jj$
m_{H^+} = 110 GeV	
$\sigma \times BR$ = 1.7 pb	$\sigma \times BR$ = 170 pb
m_{H^+} = 130 GeV	
$\sigma \times BR$ = 0.7 pb	$\sigma \times BR$ = 90 pb

The cross-section times branching ratios for the $H^\pm$ and the W decay modes of the top quark are compared in Table 19-50 for tanβ = 1.5 and two values of the $H^\pm$ mass. The original ratio of 1:10 of $t\bar{t} \to H^\pm bWb$ to $t\bar{t} \to WbWb$ events is reduced to 1:100 after branching ratios are taken into account. Given this ratio, the extraction of an $H^\pm \to cs$ peak in the m_{jj} distribution seems difficult.

For extracting this decay mode, the events are required to have:

- One isolated high p_T lepton within $|\eta| < 2.5$, to trigger the experiment. In signal events this lepton originates from semi-leptonic decays of the second top quark.
- Two b-tagged jet with $p_T > 15$ GeV and $|\eta| < 2.5$ and no additional b-jet.
- At least two non-b central jets $|\eta| < 2.0$ for the $H^\pm \to cs$ reconstruction, and no additional jets above 15 GeV in this central region.

Evidence for $H^\pm$ is searched for in the two-jet mass distribution. The mass peak from an $H^\pm$ decay can be reconstructed with a resolution of σ = 5 - 8 GeV if the mass of the $H^\pm$ is in the range between 110 and 130 GeV. In this mass range, the peak sits on the tail of the reconstructed $W \to jj$ distribution from $t\bar{t}$ background events which decay via a Wb instead of an H^+b. Examples are shown in Figures 19-77 and 19-78 for $H^\pm$ masses of 110 and 130 GeV. In this mass range the $H^\pm$ peak can be separated from the dominant $W \to jj$ background [19-92].

Table 19-51 The expected number of signal and background events for the $H^\pm \to cs$ channel for an integrated luminosity of 30 fb^{-1} and for m_H = 110 and 130 GeV and tanβ = 1.5.

m_{H^+} **(GeV)**	**110**	**130**
Signal	870	430
Background:	18 000	10 000
S/B	4.8%	4.5%
$S/\sqrt{B}$	6.5	4.4

The expected numbers of signal and background events for an integrated luminosity of 30 fb^{-1} are given in Table 19-51. This channel is complementary to the $H^{\pm} \rightarrow \tau\nu$ channel for low tanβ values. Whereas the $H^{\pm} \rightarrow \tau\nu$ channel allows only the observation of an excess of events, it is possible to reconstruct a mass peak in the $H^{\pm} \rightarrow cs$ decay mode, which makes a determination of the $H^{\pm}$ mass possible.

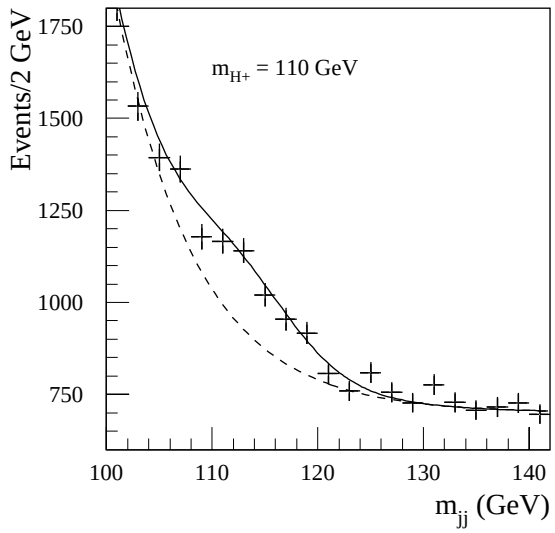

Figure 19-77 For the $H^{\pm} \rightarrow cs$ decays the expected m_{jj} distribution of signal+background events (solid line) and from the expected background (dashed) for $m_{H^{\pm}}$ = 110 GeV and tanβ = 1.5 and for an integrated luminosity of 30 fb^{-1}. The errors are statistical only.

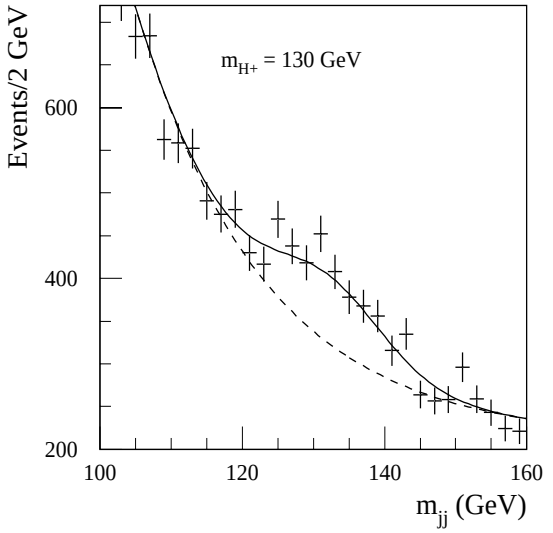

Figure 19-78 Same as Figure 19-77, but for m_{H^+} = 130 GeV.

Charged Higgs heavier than the top-quark

The possibility for discovering a charged Higgs heavier than the top-quark produced by *gg* and *gb* fusion [19-93] or by other *b*-quark initiated processes [19-94], has been investigated. Above the top-quark mass threshold the charged Higgs decays in almost 100% of the cases to *tb*. For charged Higgs bosons produced in *gb* fusion ($bg \rightarrow H^{\pm}t$) the final state would contain two top-quarks and a *b*-quark. The *gg* fusion with $H^{\pm}$ bremsstrahlung ($gg \rightarrow H^{\pm}tb$) would lead to two top-quarks and two *b*-quarks with the possibility of reconstructing top-quarks pairs. The $bq \rightarrow bH^{\pm}$ process would lead to two *b*-quarks and a top-quark in the final state. In all cases a multi-*b*-jet final state with at least one top-quark characterises the signal events. The only substantial background is expected to be the $t\bar{t}$ production.

The expected signal cross-section is driven by the $H^{\pm}$tb coupling squared, which is proportional to $(m_t^2 \cot^2\beta + m_b^2 \tan^2\beta)$. The cross-section reaches its minimum, for constant m_{H^+}, at $\tan\beta \sim \sqrt{m_t/m_b} \sim 7.5$. The branching ratio for $H^{\pm} \rightarrow tb$ decays is 100% for tanβ = 1.5 and decreases slowly to 80% with increasing tanβ where $H^{\pm} \rightarrow \tau\nu$ decays become relevant.

In the currently available Monte Carlo generator, PYTHIA 5.7, the $2 \rightarrow 2$ matrix-element for the process $bg \rightarrow H^{\pm}t$ has been implemented. The predicted rates for single $H^{\pm}$ production, including branching ratio for the semi-leptonic decay of one top-quark, are given in Table 19-52**.** More details on the analysis presented below can be found in [19-92].

Table 19-52 The expected cross section times branching ratios ($\sigma \times$ BR) for single charged Higgs production in $bg \rightarrow H^{\pm}t$ process with $H^{\pm} \rightarrow tb$ and one semi-leptonic top-quark decay $t \rightarrow l\nu b$ for various values of m_{H^+} and tanβ.

$m_{H^{\pm}}$	tanβ=1.5	tanβ= 10	tanβ= 30
200 GeV	3.4 pb	0.4 pb	1.6 pb
250 GeV	2.0 pb	0.18 pb	1.2 pb
300 GeV	1.2 pb	0.14 pb	1.0 pb
400 GeV	0.6 pb	0.08pb	0.4 pb

The applied reconstruction procedure requires:

- One isolated high p_T lepton within $|\eta| < 2.5$ to trigger the experiment. Both in signal and background events this lepton originates from semi-leptonic decays of one of the top quarks.
- Three b-tagged jets with $p_T > 30$ GeV, $|\eta| < 2.5$ and no additional b-jet.
- At least two non-b jets, which are used for the $W \rightarrow jj$ reconstruction of the second top quark.
- Both top-quarks must be reconstructed inside the mass window, as explained in Section 19.2.4.3.
- One of the reconstructed top-quarks is to be matched with the remaining b-jet for the reconstruction of the peak in the m_{tb} distribution from $H^{\pm} \rightarrow tb$ decay.

Thresholds on p_T are applied to improve the resolution of the reconstructed Higgs-boson mass ($p_T{}^t > 60$ GeV and $p_T{}^{H^{\pm}} > 80$ GeV).

For a Higgs boson mass of 200 GeV the initial signal-to-background ratio is in the order of 1:100 in the favourable low and high tanβ range. Requiring exactly three b-tagged jets improves this ratio to 1:20. The acceptance of the initial selection is about 2.5% (5.1%) for Higgs signal events of $m_{H^{\pm}} = 200$ GeV (500 GeV) and 0.1% for background events. After this selection, the background consists roughly of 70% $t\bar{t}b$ events and 30% $t\bar{t}j$ events. The mass resolution and acceptance of the top-pair reconstruction are comparable to those obtained in the $t\bar{t}H, H \rightarrow b\bar{b}$ analysis: namely, 12.5 GeV for $W \rightarrow jj$, ~10 GeV for $t \rightarrow jjb$ and $t \rightarrow l\nu b$ with ~60% acceptance for reconstructing both top-quarks inside their respective mass windows.

The mass resolution obtained for $H^{\pm} \rightarrow tb$, specified in Table 19-53, is not as good as could be expected from the reconstruction of other multi-jet multi-resonance channels, *e.g.* $H \rightarrow hh \rightarrow b\bar{b}b\bar{b}$ or $A \rightarrow t\bar{t}$. If only the true $H^{\pm} \rightarrow tb$ combinations are considered, the resolution is found to be $\sigma_m = 17$ GeV, with an acceptance of 86% inside a $\pm 2\sigma_m$ mass window for $m_H = 300$ GeV. When all combinations of the reconstructed tb events are allowed, including false $t \rightarrow Wb$ matching and/or false $H^{\pm} \rightarrow tb$ matching, a Gaussian peak with a resolution of $\sigma_m = 15$ GeV (39 GeV) is obtained, but with large tails. The event fraction inside a $\pm 2\sigma$ mass window becomes 42% (73%) for a Higgs-boson mass of 200 GeV (300 GeV). Nevertheless, the signal peak can be seen on top of the background as illustrated in Figures 19-79 and 19-80 for Higgs-boson masses of 200 and 300 GeV respectively.

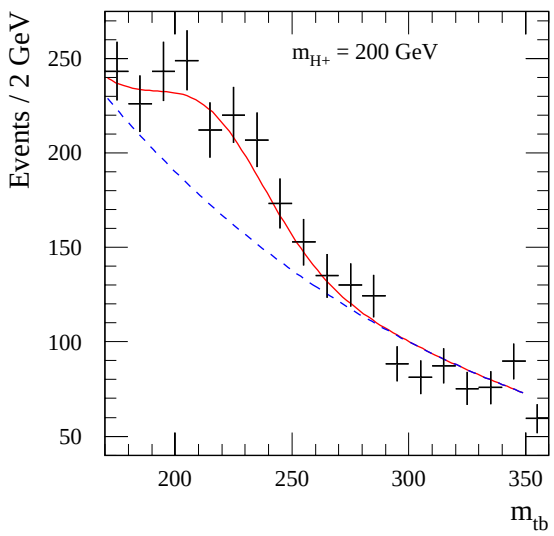

Figure 19-79 The signal+background (solid) and background only (dashed) distribution for reconstructed invariant mass m_{tb} for a Higgs boson mass of 200 GeV, tanβ = 1.5 and an integrated luminosity of 30 fb^{-1}. The errors are statistical only.

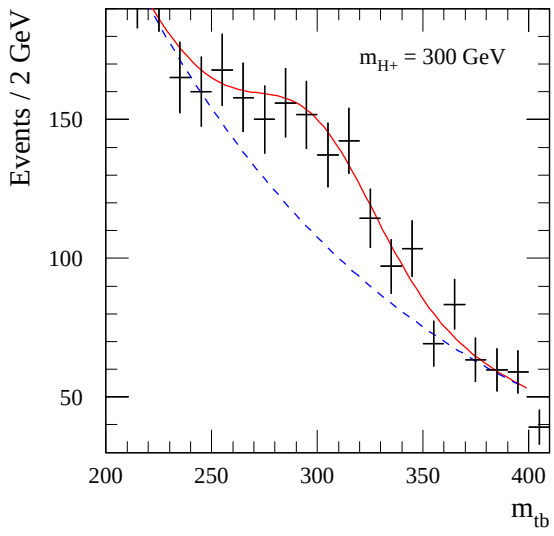

Figure 19-80 Same as Figure 19-79, but for a Higgs boson mass of 300 GeV.

Table 19-53 The mass resolution, acceptance inside the mass window, and the expected number of signal and background events for $H^{\pm} \rightarrow tb$ decays, for tanβ = 1.5 and 30 and for an integrated luminosity of 30 fb^{-1}.

$m_{H^{\pm}}$ (GeV)	200	250	300	400
σ_m (GeV)	15	37	39	49
Acceptance $m_{H^+} \pm 2\sigma_m$	42%	71%	73%	64%
tanβ = 1.5				
Signal	300	560	378	152
Background	760	1590	1650	1270
S/B	0.40	0.36	0.22	0.12
$S/\sqrt{B}$	10.9	14.0	9.3	4.3
tanβ = 30				
Signal	140	336	315	100
S/B	0.18	0.21	0.19	0.08
$S/\sqrt{B}$	5.4	8.4	4.4	2.8

The expected number of signal and background events in the mass window, which varies from ± 30 GeV for $m_{H^\pm}$ = 200 GeV to ±80 GeV for $m_{H^\pm}$ = 300 GeV, is given in Table 19-53 for an integrated luminosity of 30 fb^{-1} and for two different values of tanβ. The 5σ discovery contour curves in the (m_A, tanβ) plane are shown in Figure 19-81 for integrated luminosities of 30 fb^{-1}, 100 fb^{-1} and 300 fb^{-1} respectively. This channel would be observable for low and large values of tanβ. The kinematic limit for the on-shell $H^\pm \to tb$ decays is around m_A = 160 GeV.

Since not all the processes contributing to the single charged Higgs production were available for the Monte Carlo simulation, the signal rates given in Table 19-53 are underestimated. Therefore, the sensitivity to this channel, as presented above and shown in Figure 19-81, should be considered as a conservative estimate.

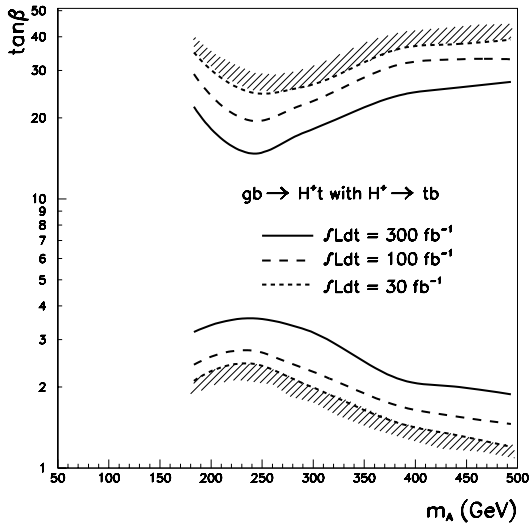

Figure 19-81 For integrated luminosities of 30 fb^{-1}, 100 fb^{-1} and 300 fb^{-1}, 5σ-discovery contour curves for the $H^\pm \to tb$ decays in the (m_A, tanβ) plane.

19.3.3 Overall sensitivity

The 5σ discovery contour curves, as determined in the previous Sections for the various channels in the (m_A, tanβ) plane, are superimposed in Figure 19-ii for integrated luminosities of 30 fb^{-1} and of 300 fb^{-1} and for the minimal mixing scenario (the most difficult case for the LHC). In Figure 19-82, the same overall picture is presented for the case of maximal mixing and an integrated luminosity of 300 fb^{-1}.

These Figures also display the present LEP2 limit ($\sqrt{s}$ = 189 GeV and 175 pb^{-1} per experiment), as well as the ultimate limit expected by the end of LEP2 operation in 2000 ($\sqrt{s}$ = 200 GeV and 200 pb^{-1} per experiment), assuming that no Higgs-boson discovery will be made. The present experimental limit from LEP2 already excludes values of tanβ below 2 - 3, and the expected ultimate limits will extend these excluded regions to tanβ < 3 (maximal mixing) or even tanβ < 7 (minimal mixing). This makes the prospects for the discovery of several channels presented in the previous Sections much less promising, since these channels do not provide any discovery potential for larger values of tanβ (this is the case for *e.g.* $H/A \to t\bar{t}$, $A \to Zh \to llb\bar{b}$ and $H \to hh \to b\bar{b}\gamma\gamma$).

Nevertheless these channels have been studied and presented here in some detail for two reasons.

- The level of detail with which the analyses of individual channels have been optimised at this stage is far below what has been done with LEP data for obvious reasons. The same is true for the scan of the (m_A, tanβ) parameter space. In addition, as discussed in Section 14.4, the presently available theoretical predictions for some of the signal process-

es and most of the background processes still suffer from large uncertainties. For these reasons, the signal observability reported here can be considered as conservative.

- More importantly, the MSSM scenario has been considered as a benchmark for the evaluation of the physics performance of the detector, given the rich spectrum of possible experimental signatures. The studies reported here would also be of interest for other models. Even if the search for a fundamental scalar particle with a mass below 130 GeV is considered to be the most important test of the MSSM [19-95], recent theoretical calculations show that this upper limit can be increased to masses of up to 200 GeV if additional Higgs doublets are introduced into the model [19-96]. The spectrum of possible scenarios is rather broad, whereas the spectrum of characteristic signatures is limited and the Standard Model background sources to such signatures are well established by now.

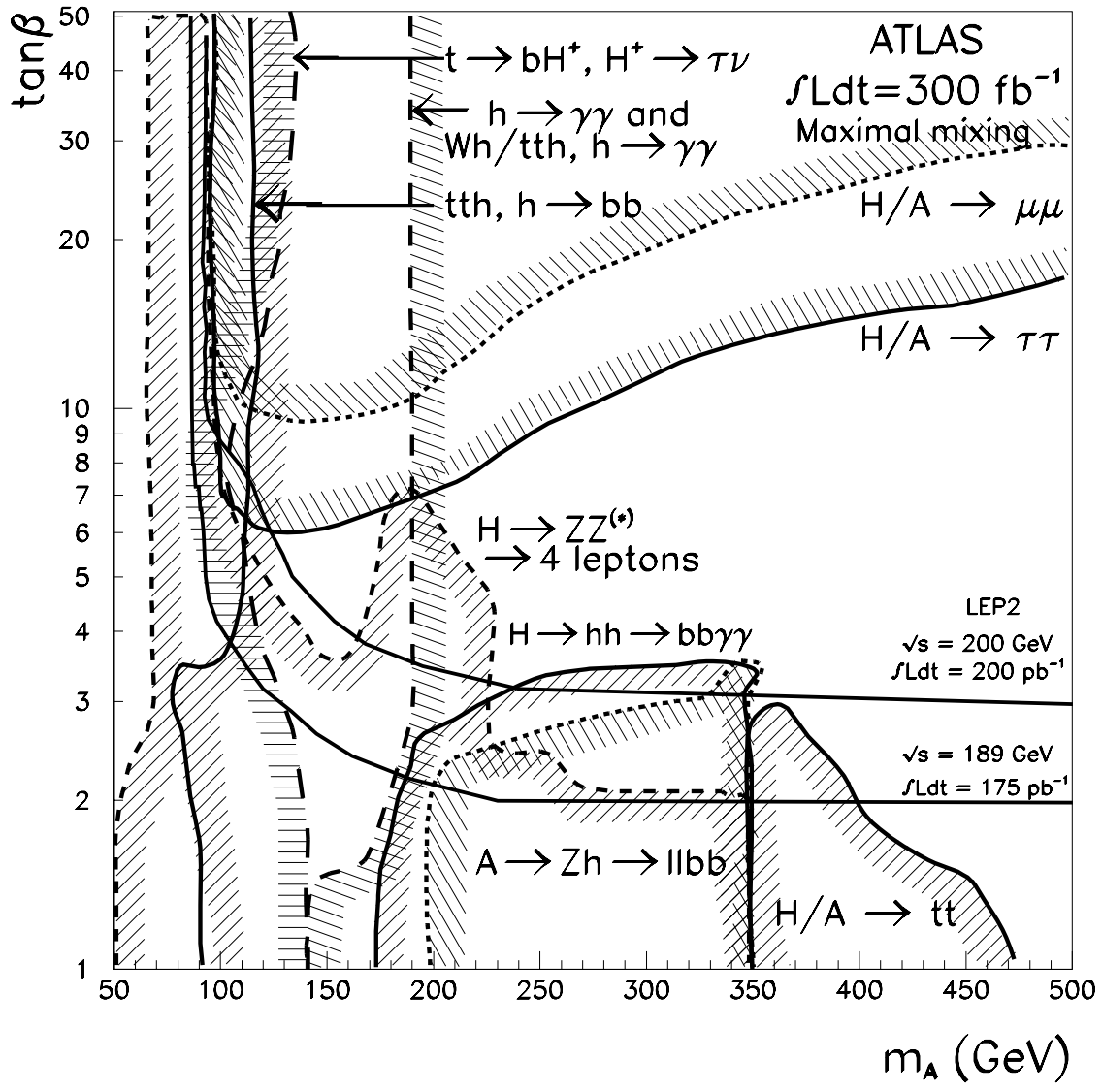

Figure 19-82 Same as Figure 19-ii, but for maximal mixing (see text).

Therefore, the conclusions concerning the observability of the various Higgs bosons in the MSSM are not limited by the strict validity of the model itself with respect to present (or expected) experimental limits. The goal was to evaluate the observability of a spectrum of signatures above the Standard Model background and to establish a full coverage of the parameter space.

As discussed already, the details of the 5σ-discovery contour curves presented in Figure 19-ii and Figure 19-82 may be affected by changes in some of the parameters in the MSSM model. This arises from kinematic shifts in the opening/closing of channels (determined by the value of m_h) or from changes in rates for signals or backgrounds. One of the important parameters governing such changes is the sensitivity to the mixing parameters A_t and A_b. As the so-called mixing varies from minimal to maximal, the predicted mass of the light *h*-boson rises for given values of m_A and tanβ, thereby increasing in many cases the discovery potential for the *h*-boson at the LHC and decreasing it at LEP.

The 5σ–discovery contour curves in the case of maximal mixing are shown in Figure 19-82. The main changes with respect to Figure 19-ii (bottom) arise from the fact that m_h is predicted to be 10 -20 GeV higher for the same values of m_A and tanβ. The expected coverage for $h \rightarrow \gamma\gamma$ is slightly degraded for $m_A \sim 150$ GeV and tanβ ~ 2. The coverage of the $H \rightarrow ZZ^{(*)} \rightarrow 4l$ channel is enhanced for low values of m_A, because the $H \rightarrow hh$ channel is closed for all values of tanβ. As a consequence, the $H \rightarrow hh$ and $A \rightarrow Zh$ channels become open only for higher values of m_A. More detailed differences between minimal and maximal mixing are beyond the precision of the evaluation presented here.

In summary, however, the overall picture remains the same:

- With a modest integrated luminosity of 30 fb^{-1}, the discovery potential covers a large fraction of the parameter space. For 80 % to 90 % of the cases, the discovery of a Higgs boson would allow discrimination between the SM and MSSM models.
- The overall discovery potential in the (m_A, tanβ) plane relies heavily on the $H/A \rightarrow \tau\tau$ channel and on the $t\bar{t}h$ with $h \rightarrow b\bar{b}$ and on the $h \rightarrow \gamma\gamma$ channels.
- For an integrated luminosity of 100 fb^{-1}, corresponding approximately to four years of LHC operation, the discovery potential covers the whole parameter space. For a very high integrated luminosity of 300 fb^{-1} the experiment would be able to distinguish between the SM and the MSSM models in most cases. In Figure 19-ii, the region with $m_A > 250$ GeV and $4 < \tan\beta < 5 - 10$ is only covered by the $h \rightarrow \gamma\gamma$ and $h \rightarrow b\bar{b}$ channels, and this distinction will be very difficult from these channels alone. However, $h \rightarrow b\bar{b}$ decays from SUSY particle decays should be observable above background in this region in many cases, thus providing a direct evidence for SUSY (see Section 19.3.5.4).
- In the case of the simultaneous discovery of the *h*- and *A*-bosons at LEP2, essentially only the charged Higgs boson would be seen directly in top-quark decays at the LHC. In the more likely case where only the *h*-boson was discovered at LEP2, several Higgs bosons would then be observed at the LHC (low tanβ region of Figure 19-ii).
- More generally, over large regions for $m_A > 160$ GeV, all three neutral Higgs bosons, and in some cases also the charged Higgs-boson would be discovered with ATLAS. Over most of this region, the *H*- and *A*- bosons are degenerate in mass and would be very difficult to distinguish. For ~10 % of the parameter space, *i.e.* for $\tan\beta > 7$ and $90 \text{ GeV} < m_A < 130$ GeV, the two heavy neutral Higgs bosons and the charged Higgs boson would be discovered with ATLAS.

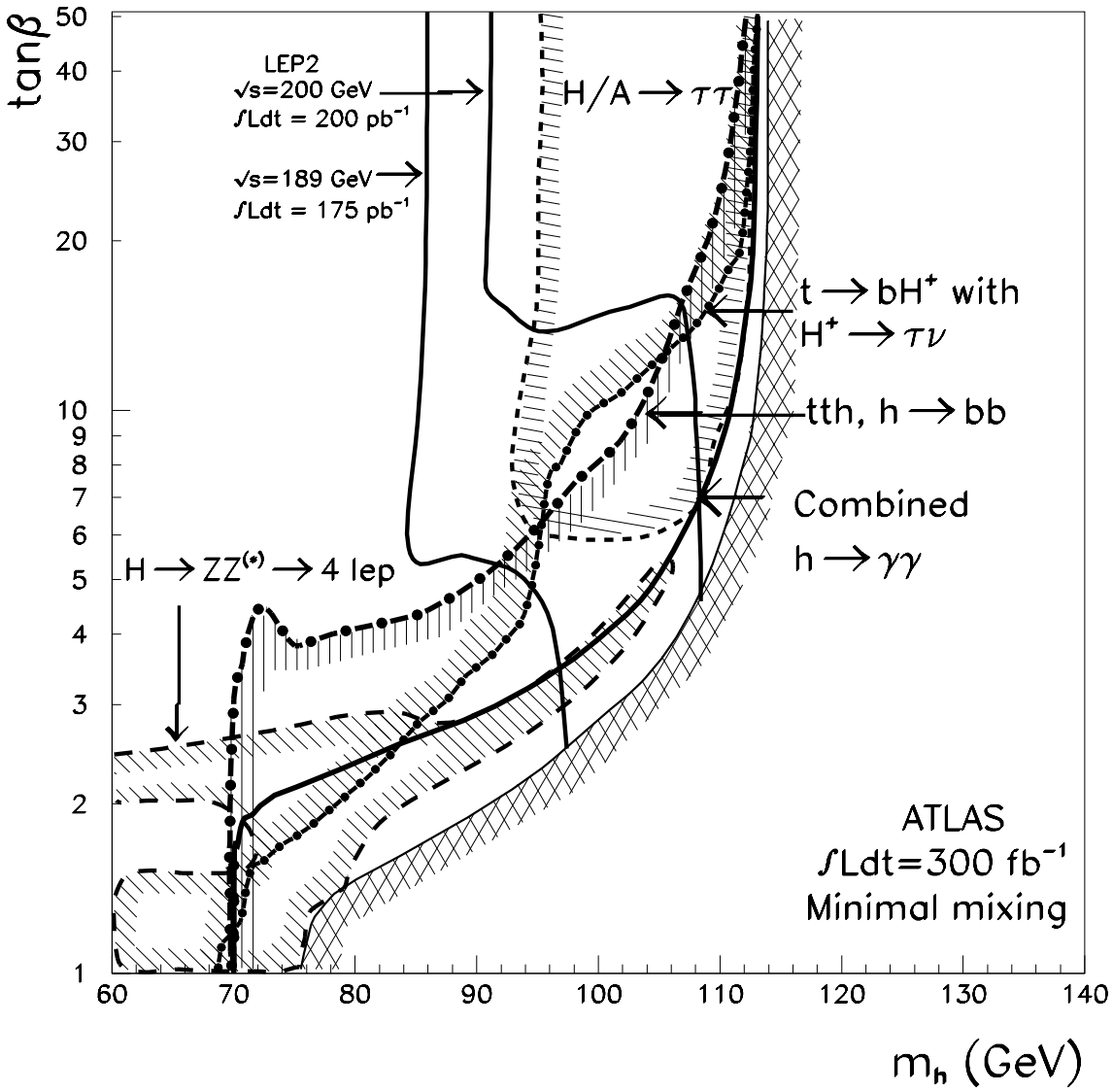

Figure 19-83 Same as Figure 19-ii but in the (m_h, tanβ) plane for an integrated luminosity of 300 fb^{-1}. The region on the right-hand side of the curve with the cross-hatched area is not allowed in the model (it corresponds to values of m_h larger than the maximum allowed value in the MSSM).

- The discovery potential of the heavy Higgs bosons for $m_A > 500$ GeV is limited to very large values of tanβ. In such cases the coverage of the (m_A, tanβ) plane would essentially be ensured only by the discovery of the h boson in the $h \to \gamma\gamma$ and $h \to b\bar{b}$ channels.
- The overall discovery potential can also be displayed in the (m_h, tanβ) plane, as shown in Figure 19-83 for an integrated luminosity of 300 fb^{-1}. This choice of parameter plane, although relevant for LEP2, where most of the sensitivity is related to the h-boson, is not the best one for displaying the LHC potential, because the large masses of the other Higgs bosons all collapse into the line delimiting the maximum allowed value of m_h. Figure 19-83 shows that, for large tanβ and for $m_h < 110$ GeV, a discovery of the h-boson through its direct production is not possible with ATLAS. However, if cascade decays of SUSY particles are also considered (see Section 19.3.5.4), the h-boson (produced in SUSY cascade de-

cays) would be discovered in the $h \rightarrow b\bar{b}$ channel in many SUSY scenarios, even for $m_h < 95$ GeV.

- The various channels described in the previous sections have also been studied for $\tan\beta < 1$ [19-16]. Even if such values are disfavoured for theoretical reasons, it is important to assess the experimental sensitivity in these cases. For this reason, each channel was studied for $0.3 < \tan\beta < 2$. In contrast to LEP2, which has very little sensitivity to values of $\tan\beta$ below ~ 0.8, the sensitivity with ATLAS is quite good for most channels of interest in this region of very low values of $\tan\beta$.
- It is important to recall here that all the SUSY particle masses were set to 1 TeV for this study. In some specific cases, the exact choice of the SUSY particle mass spectrum does affect the Higgs-boson production cross-sections and / or decay branching ratios, and therefore the discovery potential for specific channels. In particular, studies based on Minimal Supergravity (SUGRA) Models (see Section 19.3.5) indicate that the two heavy neutral Higgs bosons and the charged Higgs boson will have masses larger than 500 GeV in many cases and will therefore be outside the parameter space studied here. For given values of m_A and $\tan\beta$, different values of m_h would be allowed, depending on the exact mass spectrum of the SUSY particles, but, in most cases, these values would be close to the unique value allowed in the case of heavy SUSY particles.

19.3.4 Determination of the MSSM Higgs parameters

Assuming that a MSSM Higgs boson would be discovered, this section evaluates the potential for precision measurements of the model parameters, m_A and $\tan\beta$, and of the masses of the discovered Higgs bosons themselves (see [19-97] for more details).

The theoretical motivation for precision measurements in the MSSM is even stronger than in the Standard Model. In the SM, a precise knowledge of the profile of the Higgs boson (mass, width, branching ratios, couplings) would confirm the correctness of the model itself. However, since the sensitivity of the electroweak precision measurements to m_H through radiative corrections is only logarithmic, a precise knowledge of the Higgs-boson mass would not substantially overconstrain the model. The present data ($m_W = 80.394 \pm 0.042$ GeV and $m_t = 174 \pm 5$ GeV) and the electroweak precision measurements favour an area which is consistent with both the MSSM and the SM [19-98].

In the MSSM Higgs sector, the relations between the Higgs-boson masses, $\tan\beta$ and other parameters of the SUSY model are strongly constrained. Precise measurements of the Higgs-boson parameters and of the SUSY particle masses (see Chapter 20), if matched well by the precision of the theoretical calculations, would allow to overconstrain the SUSY model itself (see *e.g.* [19-99]).

If no SUSY particles are found, measurements of the Higgs-boson parameters should allow in some cases to distinguish between the SM and the MSSM models and to check the consistency with the relations between Higgs-boson masses predicted by the model. If, for example, the signal were to be observed in the $H \rightarrow ZZ^* \rightarrow 4l$ channel, the measured signal rate would provide the best tool to understand its origin, since the MSSM rates are suppressed by an order of magnitude with respect to the SM case over most of the parameter space. For values of m_H larger than ~250 GeV, the measured signal width would also provide a handle to disentangle the SM case ($\Gamma_H^{tot} \sim 10$ GeV) from the MSSM case ($\Gamma_H^{tot} < 1$ GeV).

The Higgs-boson couplings will be measured, but most likely with an accuracy not better than 10 - 20%, since in most cases these measurements will be based on signal rates. A measurement of obvious interest will be that of the Higgs-boson couplings to the top quark, either through the observation of $t\bar{t}h$ production with $h \to b\bar{b}$ decay, or through the observation of $H/A \to t\bar{t}$ decays.

As already discussed in Section 19.2.12 for the SM Higgs-boson, ratios of rates from different channels will also provide ratios of couplings in the MSSM. This would be the case of $H/A \to \tau\tau$ and $H/A \to \mu\mu$ for large values of tanβ. Over a very large range of tanβ and m_A values this would also be the case for the associated production with $h \to \gamma\gamma$ and $h \to b\bar{b}$ decay.

19.3.4.1 Measurement of the Higgs-boson masses

The precisions quoted in this section for Higgs-boson mass measurements are estimated with the same assumptions as already discussed in Section 19.2.12. They include the statistical error on the determination of the peak position, coming from both the limited number of signal events and from the error on the background subtraction (the background is assumed to be flat under the peak), and the systematic error on the absolute energy scale (see Chapter 12). This latter error is assumed to be 0.1% for decay channels which contain leptons or photons (*e.g.* $h \to \gamma\gamma$, $H \to ZZ^* \to 4l$) and 1% for decay channels containing jets (*e.g.* $h \to b\bar{b}$). No theoretical errors are included in the results presented below and an integrated luminosity of 300 fb^{-1} is assumed in the following.

In the MSSM model, the lightest Higgs boson is searched for over a very small range of mass values, with an upper limit of m_h = 115 - 130 GeV (depending on the model parameters) and a lower limit given by the experimental constraints. Since the present lower limit from LEP2 [19-11] is about 80 GeV for m_h and m_A, only results above these values are presented below. The couplings of the *h*-boson are similar to the couplings of the SM Higgs-boson over the accessible range of parameter space for the discovery channels: $h \to \gamma\gamma$ and $h \to b\bar{b}$. The precision expected for the mass measurements is therefore similar.

The heavy neutral Higgs bosons would be observable in decay channels not accessible otherwise for the SM Higgs-boson. The only exception is the $H \to ZZ^{(*)} \to 4l$ channel, for which, however, the expected rates are strongly reduced with respect to the SM case.

Table 19-54 Expected precision on the measurement of the MSSM Higgs boson masses for an integrated luminosity of 300 fb^{-1} and for the whole discovery region.

MSSM Higgs boson	Process	Precision $\Delta m/m$
h	Inclusive $h \to \gamma\gamma$	0.1% - 0.5%
	Wh, $t\bar{t}h$ with $h \to \gamma\gamma$	0.1% - 0.5%
	Wh, $t\bar{t}h$ with $h \to b\bar{b}$	1% - 3%
H	Inclusive $H \to \gamma\gamma$	0.1% - 0.5%
	$H \to ZZ^* \to 4l$	0.1% - 0.5%
	$H \to hh \to b\bar{b}\gamma\gamma$	1% - 2%
A	Inclusive $A \to \gamma\gamma$	0.1% - 0.5%
	$A \to Zh \to llb\bar{b}$	1% - 2%
H/A	$H/A \to \tau\tau$	1% - 12%
	$H/A \to \mu\mu$	0.1% - 2.0%

Table 19-54 summarises the expected precisions on the masses of the MSSM Higgs bosons over the complete set of possible discovery channels and over the full parameter space for an integrated luminosity of 300 fb^{-1}.

- If the *h* boson is discovered through the SM production processes (direct or associated production), the precision of the mass measurement is similar to that discussed already in Section 19.2.12. Over the range of parameter space covered by both the $h \to \gamma\gamma$ and $h \to b\bar{b}$

channels, the precision is determined by the $h \rightarrow \gamma\gamma$ channel and is ~0.1%. Over the region where only the $h \rightarrow b\bar{b}$ channel is observable the expected precision is 1 - 3%.

- Cascade decays of SUSY particles, discussed in Section 19.3.5.4, might be a source of copious production of $h \rightarrow b\bar{b}$ events. The precision which can be achieved in this channel varies with the rates associated with a given SUGRA parameter point (see Section 19.3.5.4). This channel is limited by the systematic error of 1% on the jet energy scale for signal rates above a few hundred events, which would be achieved over a large region of the SUGRA parameter space, for an integrated luminosity of 30 fb^{-1}.
- For low values of tanβ, the precision of the measurement of the mass of the H-boson will be determined by the $H \rightarrow ZZ^{(*)} \rightarrow 4l$ channel, if observable. It will vary strongly with tanβ, from 0.1% to 0.5%, following the rapid variation of rate. It will be worse than that expected for the SM Higgs-boson of the same mass, since the MSSM rates are strongly suppressed. If only the $H \rightarrow hh \rightarrow b\bar{b}\gamma\gamma$ decay mode were to be accessible, the expected precision would not be better than ~1%.
- The pseudoscalar A can be discovered for low values of tanβ in the $A \rightarrow Zh \rightarrow llb\bar{b}$ and $A \rightarrow \gamma\gamma$ modes with rates varying very rapidly with tanβ. The expected precision of the mass measurement is not better than 1 - 2% for $A \rightarrow Zh \rightarrow llb\bar{b}$ and 0.1% for the $A \rightarrow \gamma\gamma$ channel.
- For large values of tanβ, heavy Higgs bosons H and A will be discovered in the $\tau\tau$ or $\mu\mu$ decay mode. They cannot be disentangled from each other, being almost degenerate in mass and having almost identical decay modes. If both $H/A \rightarrow \tau\tau$ and $H/A \rightarrow \mu\mu$ decays are observable, the precision will be determined by the $\mu\mu$ decay mode, with a much better expected resolution and a smaller systematic error. For large values of tanβ where both channels are accessible, the precision is about 0.1%. For moderate values of tanβ, where the discovery reach of the $\tau\tau$ channel extends further than that of the $\mu\mu$ channel, the precision is degraded to 1-12%. For $H/A \rightarrow \tau\tau$ a systematic uncertainty of 1% coming from the jet energy scale has been included. The systematic uncertainty from the E_T^{miss} scale has not been included in the present study, but is expected to be of the same order of magnitude (see Section 12.5.2).

Figures 19-84 and 19-85 illustrate the expected precisions on the Higgs-boson masses discussed above, for an integrated luminosity of 300 fb^{-1} and for tanβ = 3 and tanβ = 30, respectively.

19.3.4.2 Measurement of tanβ

The measurement of the signal rates for the heavy Higgs bosons provides a good sensitivity to tanβ. The method proposed in [19-59] was followed for the evaluation of this sensitivity. The systematic error is dominated by the luminosity and is taken conservatively to be 10%. The expected precision on the measurement of m_A is also taken into account in the evaluation:

- If the signal were to be observed in the $H \rightarrow ZZ^{(*)} \rightarrow 4l$ channel, the measured signal rate would allow a measurement of tanβ with an accuracy of 10% to 25%, for an integrated luminosity of 300 fb^{-1}. For small tanβ its measurement is possible with the $H \rightarrow ZZ^{*} \rightarrow 4l$ channel. However, the precision is limited to 10% at best, since the signal rate for this channel is low.
- If the signal were to be obtained in the $H/A \rightarrow \tau\tau$ channel, the measured signal rate would provide good sensitivity to tanβ. As an example, for m_A = 150 GeV and an integrated luminosity of 300 fb^{-1}, tanβ can be measured to an accuracy of ±15 % for tanβ = 5 and of ±6 % for tanβ = 40.

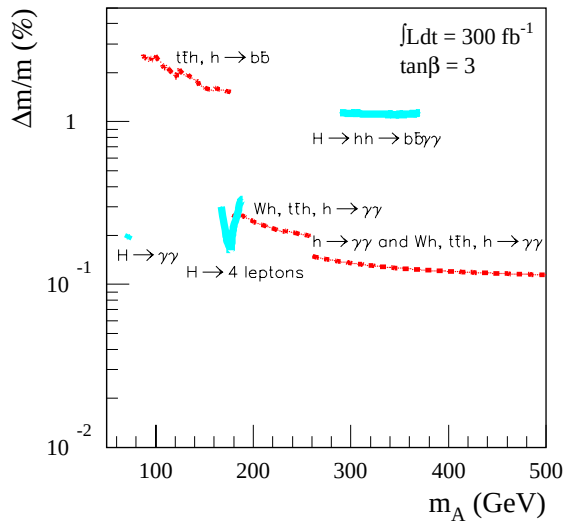

Figure 19-84 Expected precision on the measurement of the MSSM Higgs-boson masses for an integrated luminosity of 300 fb^{-1} and tanβ = 3.0

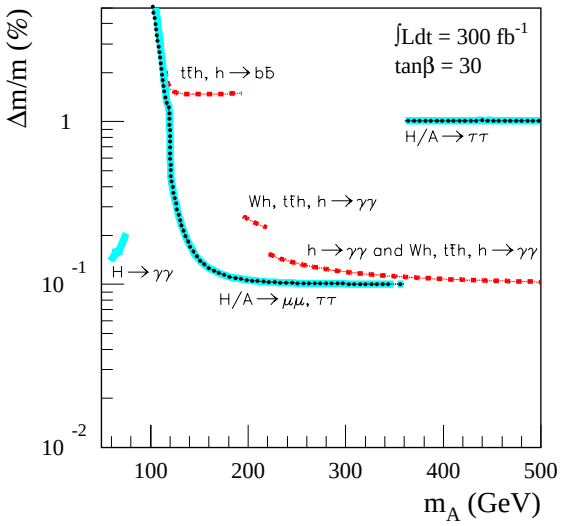

Figure 19-85 Same as Figure 19-84, but for tanβ = 30.

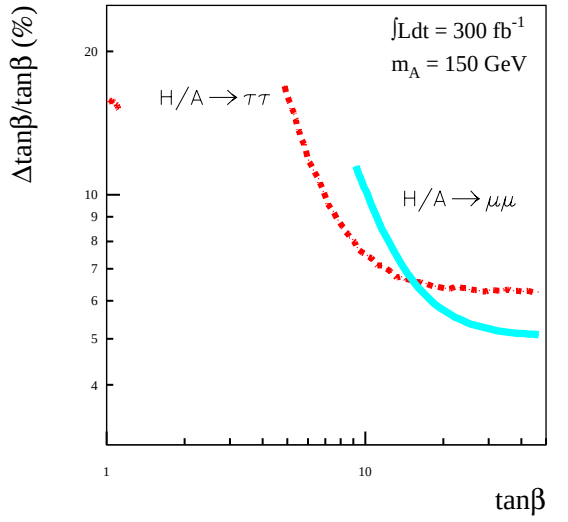

Figure 19-86 Expected precision on the measurement of tanβ, for an integrated luminosity of 300 fb^{-1} and for m_A = 150 GeV.

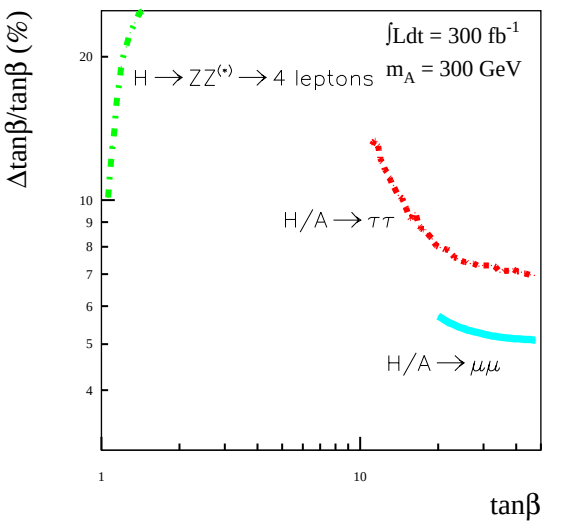

Figure 19-87 Same as Figure 19-84, but for m_A= 300 GeV.

- For large values of tanβ, a somewhat better sensitivity can be achieved with the $H/A \rightarrow \mu\mu$ channel, ±12 % for tanβ = 10 and ±5 % for tanβ = 40.

Figures 19-86 and 19-87 illustrate the expected precision on tanβ discussed above, for an integrated luminosity of 300 fb^{-1} and for m_A = 150 GeV and m_A = 300 GeV, respectively.

19.3.5 SUGRA scenarios

19.3.5.1 General considerations

As discussed in Section 19.3.3, the searches in the MSSM Higgs sector have been performed under the assumption that the SUSY mass scale is heavy and the influence of SUSY particles on the Higgs-boson decays could therefore been ignored. However, for a complete discussion of the MSSM Higgs sector, the influence of SUSY particles has to be considered [19-100]. In this section, other scenarii are discussed, where SUSY particles can appear among the decay products of supersymmetric Higgs bosons, and where the Higgs bosons themselves appear in the decays of SUSY particles. In general, the influence of the SUSY particle sector on the Higgs bosons arises from the following effects:

- Due to radiative corrections, the mass spectrum of the Higgs bosons is affected by the SUSY particle spectrum and the mixing parameters in the stop-sbottom sector [19-11].
- If SUSY particles are not too heavy, their contribution to loops can either enhance or suppress the $gg \rightarrow h, H, A$ production cross-sections and/or the branching ratios for the $\gamma\gamma$ channel [19-101].
- There are regions in parameter space, where the rates for Higgs-boson decays to SUSY particles are large and dominant. These decays reduce the rates for SM signatures, opening new modes for Higgs-boson detection [19-100][19-102]. Higgs-boson decays to charginos or neutralinos ($H \rightarrow \tilde{\chi}_2^0 \tilde{\chi}_2^0$, $\tilde{\chi}_1^\pm \tilde{\chi}_1^\pm$) which lead to multi-lepton final states, are among the most interesting signatures in this respect.
- There are regions in parameter space, where Higgs bosons are produced in decays of SUSY particles [19-100]. The most promising channel is the second lightest neutralino decay to the h-boson, followed by an $h \rightarrow b\bar{b}$ decay [19-103][19-104].

The many parameters of the MSSM render a systematic study of the interplay between the Higgs and SUSY sectors extremely difficult. Therefore these studies have been performed in the framework of the more constrained minimal SUGRA model [19-71]. For a detailed discussion of the parameters of this model, the reader is referred to Chapter 20.

Masses

The SUGRA parameters have been scanned over the ranges m_0, $m_{1/2}$ = 50 - 1000 GeV, tanβ = 1 - 50, for both signs of μ and for A_0 = 0. These ranges correspond to the region of parameter space over which SUSY would be discovered at the LHC (see Chapter 20). Parts of this parameter space are excluded theoretically or experimentally [19-105]. In the determination of these excluded parameter regions, the present experimental limit on m_h has not been included. Curves of constant m_h are

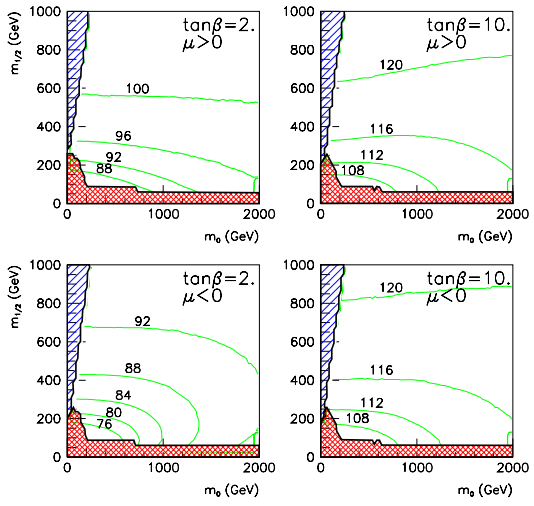

Figure 19-88 Curves of constant m_h in the (m_0, $m_{1/2}$) SUGRA parameter space for A_0 = 0, tanβ = 2 and 10, and for both signs of μ. The hashed and cross-hashed areas are excluded, respectively theoretically and experimentally.

shown over a subset of the SUGRA parameter space in Figure 19-88. For a given value of tanβ, these curves are almost independent of m_0 and increase only slowly with $m_{1/2}$. For low values of tanβ and for positive μ the predicted value for m_h is about 10 -15 GeV higher than for negative μ and for the same values of the m_0, $m_{1/2}$ parameters. This splitting disappears for large values of tanβ for which the mass of the *h*-boson reaches its upper limit.

The other supersymmetric Higgs bosons are predicted to be heavy in SUGRA models, even for relatively low values of (m_0, $m_{1/2}$). The *H*- and *A*- bosons are degenerate in mass over almost the whole parameter range. Curves of constant m_A are shown in Figures 19-89 and 19-90 for three values of tanβ (2, 10, 40) and for both signs of μ. For given values of m_0 and $m_{1/2}$, the predicted masses of the *H*- and *A*- bosons decrease with increasing tanβ. Note that the isoline m_A = 500 GeV reaches $m_{1/2} \sim 300$ GeV for tanβ = 10 and $m_{1/2} \sim 500$ GeV for tanβ = 40. For m_A = 500 GeV, the maximum possible value of $m_{1/2}$ increases from 250 GeV to 550 GeV when tanβ increases from 2 to 40. The heavy neutral Higgs bosons are only observable at the LHC for

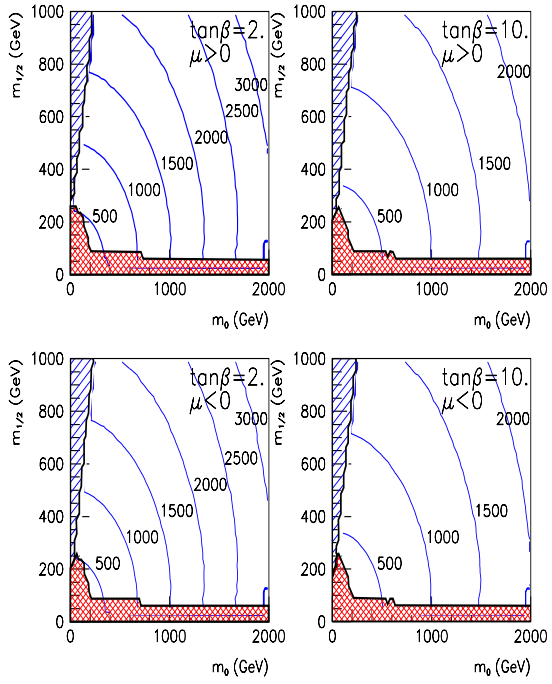

Figure 19-89 Same as Figure 19-88, but for curves of constant m_A.

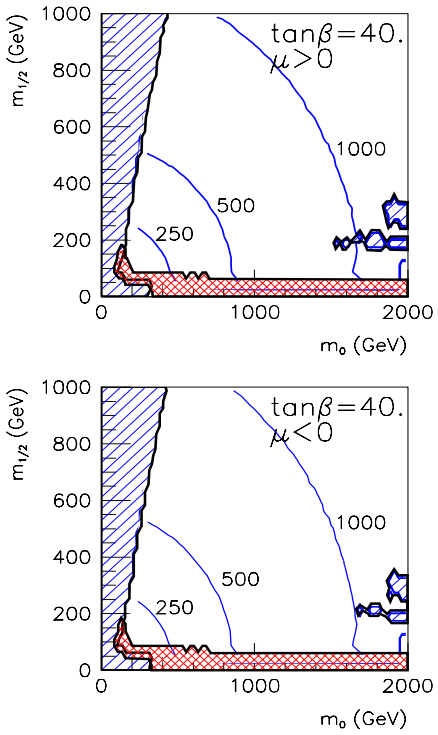

Figure 19-90 Same as Figure 19-89, but for tanβ = 40.

masses up to about 500 GeV, since their production cross-sections decrease rapidly with increasing mass. As shown in Figures 19-89 and 19-90, the region with m_A < 500 GeV represents, however, only a small fraction of the SUGRA parameter space.

If the excluded regions of the SUGRA parameter space are mapped onto the (m_A, tanβ) discovery plane discussed in Section 19.3.3, they correspond to regions with low values of m_A, so that only the region with m_A > 225 GeV is allowed. The discovery of a heavy neutral Higgs boson in SUGRA has therefore to rely on the $H/A \rightarrow \tau\tau$ and $H/A \rightarrow \mu\mu$ channels, or as shown in the next sections, on some of their possible SUSY decay modes [19-106].

Production and decay

For the evolution of the SUGRA parameters from the GUT scale to the weak scale, the ISASUSY package was used [19-107]. The output parameters were then used as input to the HDECAY package, which calculates the SUSY particle spectrum and the Higgs-boson branching ratios [19-20]. This package includes the most important higher-order QCD corrections to the decays into quark pairs and important decays to off-mass-shell particles. All SUSY particles contributions to the loop-mediated $h \to \gamma\gamma$ decay mode are included. The package calculates the Higgs-boson branching ratios in the so-called SUSY-ON and SUSY-OFF scenarios, where the latter omits SUSY particles in decays and loops but calculates the Higgs-boson masses and couplings for the chosen SUSY model.

Higgs-boson production via gluon-gluon fusion is a production process which is important to be estimated consistently in SUSY-ON / OFF scenarios. For this purpose, the decay width of the Higgs boson to *gg* pairs is calculated. A comparison of the cross-sections times branching ratios computed in the two scenarios provides an estimate of the difference between the effect of a variation of the couplings obtained from the MSSM parameters (m_A and tanβ) and the effect of SUSY loops or SUSY decay modes in the Higgs sector. The SUSY-OFF scenario is used as a reference model, since it corresponds to the one discussed extensively in Section 19.3.2. More details on the comparison between these two scenarios in SUGRA can be found in [19-70], where several plots illustrate the behaviour of $\sigma \times$ BR for different Higgs-boson decay channels in the SUGRA parameter space.

19.3.5.2 Standard Model decay modes

Observability of the h-boson

The SM decay modes of the *h*-boson may be suppressed due to the opening of SUSY decay modes or due to SUSY contributions to loops. Over the allowed SUGRA parameter space, the decay of $h \to \tilde{\chi}_1^0\ \tilde{\chi}_1^0$ (where $\tilde{\chi}_1^0$ denotes the lightest neutralino) is not accessible, and *h* only decays to SM particles.

The presence of SUSY particles in loops has a significant impact on the observability of the *h*-bosons over certain regions of the SUGRA parameter space:

- the $gg \to h$ production cross-section is somewhat enhanced;
- the $h \to \gamma\gamma$ branching ratio may be suppressed by up to 30%.

As a consequence, the $\sigma \times$ BR for $gg \to h \to \gamma\gamma$ is never below 90% of its SUSY-OFF value. The $\sigma \times$ BR for the *Wh* and $t\bar{t}h$ associated production with $h \to \gamma\gamma$ can be reduced to 70% of the SUSY-OFF values. The reduction of the $h \to \gamma\gamma$ rate occurs for low values of $m_{1/2}$ and is insensitive to m_0 [19-70]. On the other hand, the discovery potential for the $h \to b\bar{b}$ channel is essentially unaffected by the mass spectrum of the SUSY particles.

Figures 19-91 and 19-92 show how the 5σ-discovery contour curves in the (m_A, tanβ) plane for inclusive and associated $h \to \gamma\gamma$ searches, are modified by the changes in $\sigma \times$ BR from the SUSY-OFF values. In the SUGRA scenario, the region where m_A is less than 225 GeV, is excluded as explained in Section 19.3.5.1 and illustrated in Figures 19-91 and 19-92. Although the observability of the $h \to \gamma\gamma$ channel may be somewhat reduced the overall observability of the *h*- boson remains unchanged since the sensitivity of the $t\bar{t}h$, $h \to b\bar{b}$ channel is unaffected by SUSY particles.

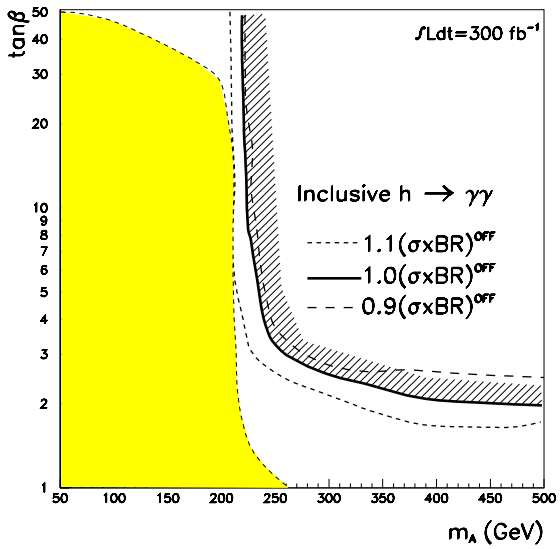

Figure 19-91 For an integrated luminosity of 300 fb^{-1}, 5σ-discovery contour curves for the inclusive $h \to \gamma\gamma$ channel in the (m_A, tanβ) plane as a function of $\sigma \times$ BR with respect to the SUSY-OFF scenario (see text).

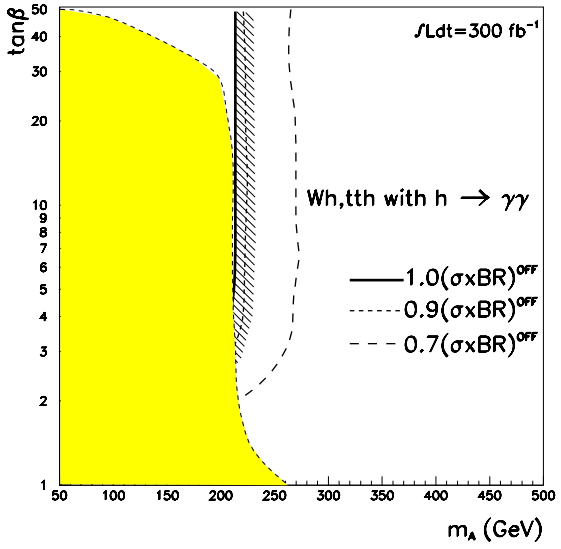

Figure 19-92 Same as Figure 19-91, but for the associated production of Wh and $t\bar{t}h$ with $h \to \gamma\gamma$.

Observability of the *H*- and *A*- bosons

In contrast to the h-boson, the SM decay modes of the heavy neutral Higgs bosons may be significantly affected by the opening of decay modes to SUSY particles (see Section 19.3.5.3). In many cases, the branching ratios to SM particles are strongly suppressed. These suppressions depend weakly on m_0 and are strongest for low values of $m_{1/2}$ and tanβ: for tanβ > 40, the suppression is always below 20% and for $m_{1/2} > 400$ GeV, it is always below 40% (see [19-70] for more details).

Figure 19-93 illustrates the impact of the opening of H/A SUSY decays modes on the observability of their SM decay modes in SUGRA. The top plots of Figure 19-93 show the possible regions of parameter space for a 5σ discovery of the heavy neutral Higgs bosons in the SUSY-OFF scenario (derived directly from the results reported in Section 19.3.2), both in the (m_0, $m_{1/2}$) and (m_A, tanβ) planes. The middle plots of Figure 19-93 indicate that these regions of possible discovery are not directly affected if SUSY decay modes are allowed, but the bottom plots of Figure 19-93 show that, over a large fraction of these regions, the suppression of the SM decay modes may be so large that their discovery is no longer possible.

Observability of the $H^{\pm}$ - boson

The production of a charged Higgs boson at the LHC can occur through $t\bar{t}$ production followed by a $t \to H^{+}b$ decay or through gg or gb fusion. A signal can be observed in the case of $t\bar{t}$ production in either the $H^{\pm} \to \tau\nu$ or $H^{\pm} \to cs$ decays. The decay $H^{\pm} \to tb$ is also observable for low and large values of tanβ (see Section 19.3.2.11).

In the SUGRA parameter region m_0, $m_{1/2}$ = 50 - 1000 GeV, the $H^{\pm}$ is heavier than the top quark, except at very large tanβ. $H^{\pm}$ could decay into charginos / neutralinos or squarks but, even above the top-quark threshold, the branching ratio to chargino / neutralino will not exceed 20 - 30%. Decay into stop-sbottom also may become important, with a branching ratio of the same order of magnitude as the branching ratio into SM fermions.

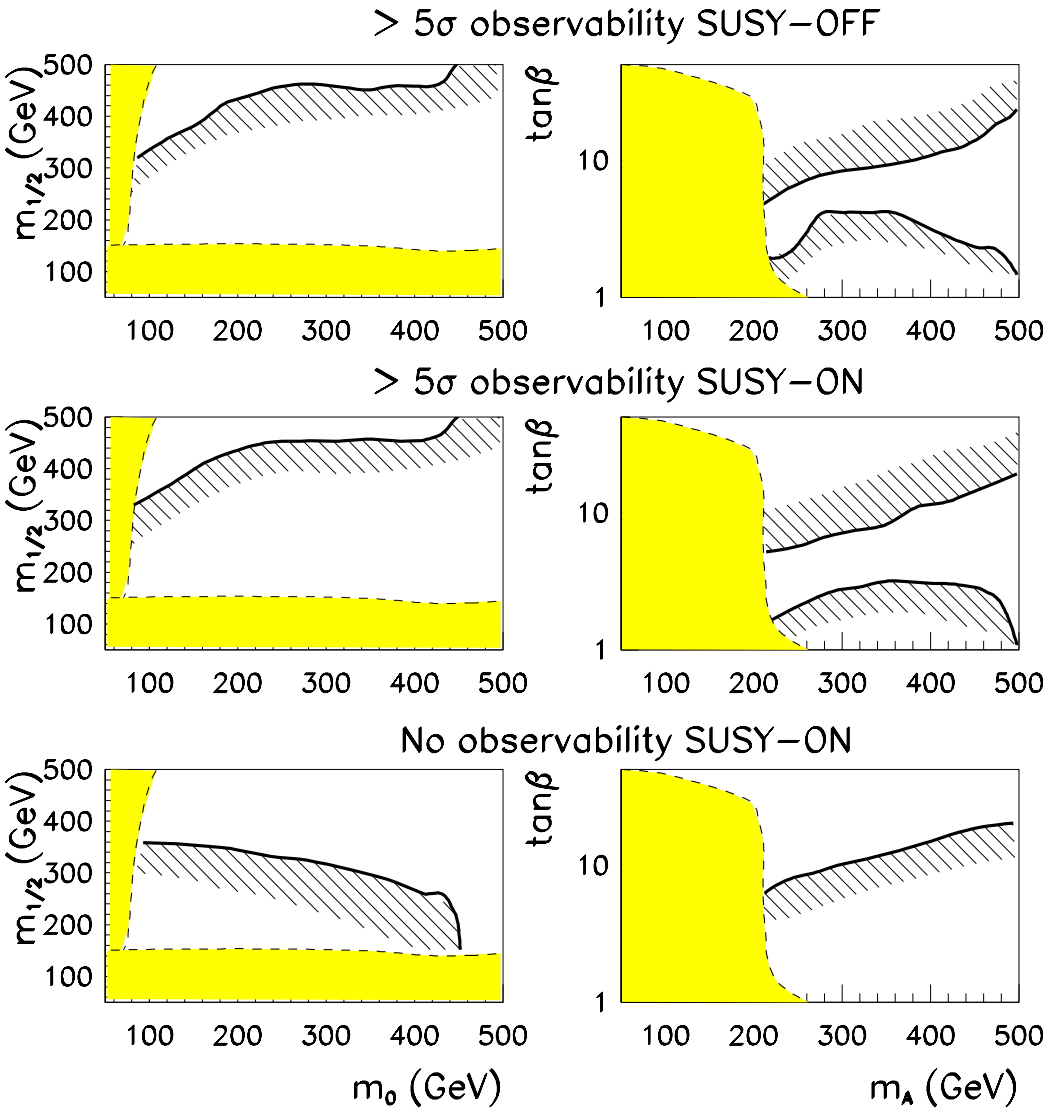

Figure 19-93 For SM decays of the heavy neutral Higgs bosons in SUGRA scenarios and for an integrated luminosity of 300 fb^{-1}, regions of the (m_0, $m_{1/2}$) plane (left) and of the (m_A, tanβ) plane (right), where a 5σ discovery would be possible in the absence of SUSY decay modes (top), in the presence of SUSY decay modes (middle) and where no discovery in SM decay modes would be possible in the presence of SUSY decay modes (bottom). The ττ, μμ, *tt* decays and $A \rightarrow Zh$ and $H \rightarrow hh$ modes are used. The shaded areas are excluded by theoretical and experimental constraints.

Overall sensitivity

Figure 19-94 shows the 5σ-discovery contour curves for SM decays of the various Higgs bosons and for an integrated luminosity of 300 fb^{-1}, as taken from the general MSSM studies reported in Section 19.3.2, but extrapolated to SUGRA scenarios with heavy SUSY particles (SUSY-OFF) and including the theoretical and experimental constraints described above.

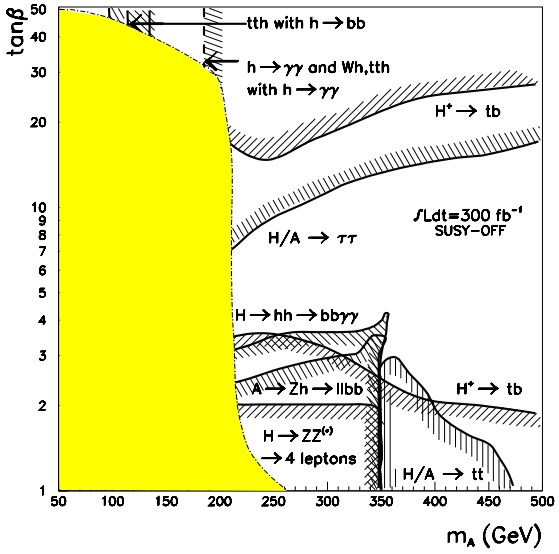

Figure 19-94 For an integrated luminosity of 300 fb^{-1} 5σ discovery contour curves for various SM Higgs-boson decay modes in the case of SUGRA scenarios with heavy SUSY particles (SUSY-OFF) and for an integrated luminosity of 300 fb^{-1}. The shaded area is excluded by theoretical and experimental constraints.

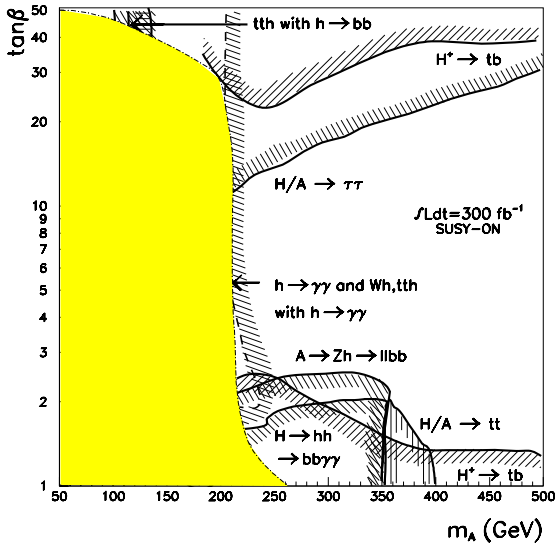

Figure 19-95 Same as Figure 19-94, but the impact of SUSY particles on Higgs-boson production and decay is included (SUSY-ON, see text).

In general, however, the other SUGRA parameters have an impact on these discovery curves through the opening of Higgs-boson decays to SUSY particles (mostly for H and A) and the presence of SUSY particles in loops. This impact is illustrated in Figure 19-95, where these effects are taken into account by reducing the SM decay rates of the heavy neutral Higgs bosons to 40% of their nominal SUSY-OFF values and by reducing the SM $h \to \gamma\gamma$ rates to their minimal predicted values (see Figures 19-91 and 19-92). Over most of the relevant region of SUGRA parameter space, the reduction is smaller so this is a conservative assumption. Despite the reduction in the decay rates of the Higgs bosons, the difference between Figures 19-94 and 19-95 is not very large (only the $H \to ZZ^{(*)} \to 4l$ channel disappears).

19.3.5.3 SUSY decay modes

In this section the sensitivity of the ATLAS experiment to decays of the heavy SUSY Higgs bosons via supersymmetric particles is discussed. There is a large branching ratio for neutralino and chargino decays, $H \rightarrow \tilde{\chi}_i^0 \tilde{\chi}_i^0$, or $H \rightarrow \tilde{\chi}_i^{\pm} \tilde{\chi}_i^{\pm}$, which could decay via cascades into multi-lepton final states. Such multi-lepton final states together with missing transverse energy provide a clean signature.

The strategy for the detection of these decays is shown first [19-106] for the SUGRA point 3 [19-108] (see Chapter 20). The method is then applied to other points in the SUGRA parameter space and the 5σ discovery regions are determined [19-109].

H/A $\rightarrow \tilde{\chi}\,\tilde{\chi}$ at SUGRA point 3

SUGRA point 3 [19-108] is characterised by the following parameters: m_0 = 200 GeV, $m_{1/2}$ = 100 GeV, A = 0, tanβ = 2 and sgn(μ) = -1. At this point the heavy Higgs bosons H and A are predicted to have masses of 375 GeV; decays: $H/A \rightarrow \tilde{\chi}_1^0 \tilde{\chi}_2^0$, $H/A \rightarrow \tilde{\chi}_2^0 \tilde{\chi}_3^0$ and $H/A \rightarrow \tilde{\chi}_2^{\pm} \tilde{\chi}_1^{\pm}$ are kinematically allowed and compete with the $t\bar{t}$ decay mode. The two lightest neutralinos have masses of 45 and 97 GeV, and the decay $\tilde{\chi}_2^0 \rightarrow \tilde{\chi}_1^0 l^+l^-$ has a relatively large branching ratio. The dominant contribution to the multi-lepton final states comes from the $H/A \rightarrow \tilde{\chi}_2^0 \tilde{\chi}_2^0$ decay, which leads to two lepton pairs with opposite sign and same flavour in 12% of the cases.

The dominant source of background are leptons produced in the decays of squarks and gluinos which cascade to charginos and neutralinos. Unlike the charginos / neutralinos from Higgs-boson decays they are however produced in association with quarks and gluons if they appear in the cascade of squarks / gluinos. This large hadronic activity can be used to suppress this type of SUSY background. An additional, smaller background source is the direct production of slepton or gaugino pairs via the Drell-Yan processes. Only a very small hadronic activity is expected in these events and their rejection is more difficult. The rate of direct production of $\tilde{\chi}_2^0$ pairs is comparable with the $H/A \rightarrow \tilde{\chi}_2^0 \tilde{\chi}_2^0$, also the background from the direct production of slepton / sneutrino pairs is non-negligible.

Events are selected as follows.

- Two pairs of isolated leptons with opposite sign and same flavour (OS-SF), with $p_T > 20$ GeV for the two hardest and $p_T > 7$ GeV for the other two leptons. The mass of the lepton pairs has to be above 4.5 GeV and outside of $m_Z \pm 10$ GeV.
- Jet veto of $p_T > 40$ GeV or 20 GeV in the pseudorapidity interval $|\eta| < 5$.

The jet veto acceptance for the signal is ~35% for the 40 GeV threshold and ~19% for the 20 GeV threshold, whereas the acceptance for the SUSY background is 0.56% and 0.025% respectively. The expected number of signal and background events passing these cuts are given in Table 19-55, assuming an integrated luminosity of 30 fb^{-1}. For the final selection a tight jet veto, 20 GeV for both low and high luminosity is needed. The expected additional loss in acceptance in the high luminosity case is 50% [19-110].

Table 19-55 Expected numbers of signal and background events with two OS-SF leptonic pairs for an integrated luminosity of 30 fb^{-1}.

Selection	Signal	Backg.	*S/B*
2 OS-SF pairs	493	3.6x10^5	0.001
Kinematic cuts	333	2.5x10^5	0.001
Jet veto 40 GeV	115	1545	0.07
Jet veto 20 GeV	80	140	0.57

With looser isolation criteria than those that were discussed in Section 19.2.5, the lepton reconstruction+isolation efficiency can be kept at the 66% per event (~90% per lepton) with still sufficient rejection power of 120 (20) against $t\bar{t}$ background and of 30 (10) against $Zb\bar{b}$ background for low (high) luminosity. The SM background (Z^*Z^*, $t\bar{t}$, $Zb\bar{b}$ events) is suppressed to a level below 10% (20%) of the SUSY background for low (high) luminosity.

In Figure 19-96 the invariant mass distribution of the four leptons, m_{llll}, is shown for the signal + background (black points) and for the background alone (histogram) after applying a jet-veto cut of 20 GeV and for an integrated luminosity of 300 fb^{-1}. The Higgs signal appears as an enhancement in the m_{llll} distribution and can be detected with a significance of $S/\sqrt{B}$ = 5.2 after 30 fb^{-1} and $S/\sqrt{B}$ = 11.9 after 300 fb^{-1} if the systematic error on the background is not taken into account. The shape of the distribution is sensitive to the Higgs-boson mass, as shown in Figure 19-97; a sensitivity of 10 GeV is expected for an integrated luminosity of 300 fb^{-1}.

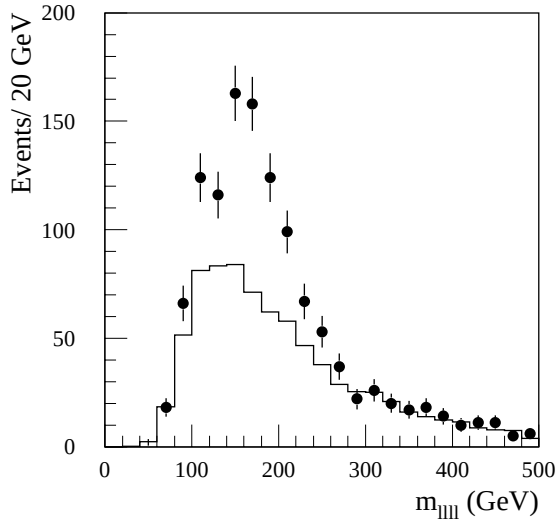

Figure 19-96 For $H/A \rightarrow \tilde{\chi}\,\tilde{\chi} \rightarrow 4l$+X decays with m_A = 371 GeV distribution of the four-lepton invariant mass for the background (solid line) and the summed signal+background (points with error bars) for an integrated luminosity of 300 fb^{-1}.

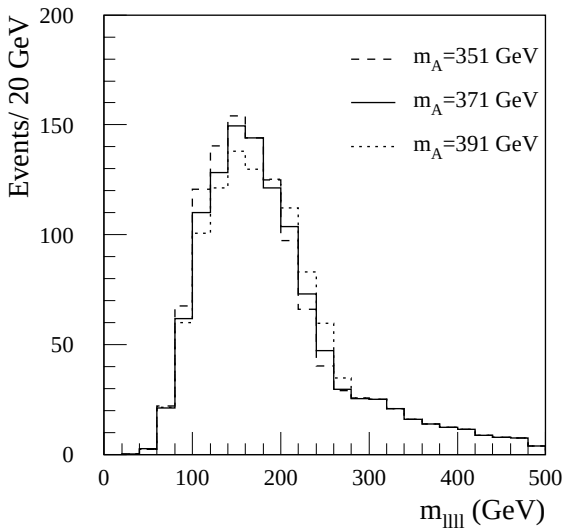

Figure 19-97 For $H/A \rightarrow \tilde{\chi}\,\tilde{\chi} \rightarrow 4l$+X and for an integrated luminosity of 300 fb^{-1}. The distribution is shown for three different values of m_A.

Complete reconstruction of the Higgs mass

If in the $\tilde{\chi}_2^0 \rightarrow \tilde{\chi}_1^0 l^+ l^-$ decay the dilepton pair has an invariant mass near its endpoint, then in the rest frame of the $\tilde{\chi}_2^0$ both the $\tilde{\chi}_1^0$ and the ll pair are forced to be at rest. One can then reconstruct the four-momentum of the $\tilde{\chi}_2^0$ if its mass is assumed. More details of this method can be found

in Section 20.2.4.1. The previous event selection was refined by requiring both OS-SF pairs to be in the $(m_{\tilde{\chi}_2^0} - m_{\tilde{\chi}_1^0}) - 10\ \text{GeV} < m_{ll} < (m_{\tilde{\chi}_2^0} - m_{\tilde{\chi}_1^0})$ window. To increase the statistics of the end-point events the jet veto is raised to 40 GeV.

The invariant mass of pairs of $\tilde{\chi}_2^0$'s is formed and shown in Figure 19-98. The mass distributions are shown for signal and background for values of the Higgs boson mass shifted by ±20 GeV around nominal one and for an integrated luminosity of 300 fb^{-1}. For a Higgs boson mass of m_A = 370 GeV 18 signal and 65 background events from the $ee\mu\mu$ sample are found in the mass window ±50 GeV around the nominal Higgs boson mass. This only corresponds to a signal significance $S/\sqrt{B}$ = 2.2. If all events with SF-OS lepton pairs are used about 33 signal and 132 background events are expected which give a statistical significance of $S/\sqrt{B}$ = 2.9. Figure 19-98 shows the expected distribution of the reconstructed Higgs boson mass for all OS-SF pairs and for three different values of the Higgs boson mass. Although the sensitivity in this particular point is rather weak for the full reconstruction of the Higgs boson mass, this method may be successfully used in other SUGRA scenarios.

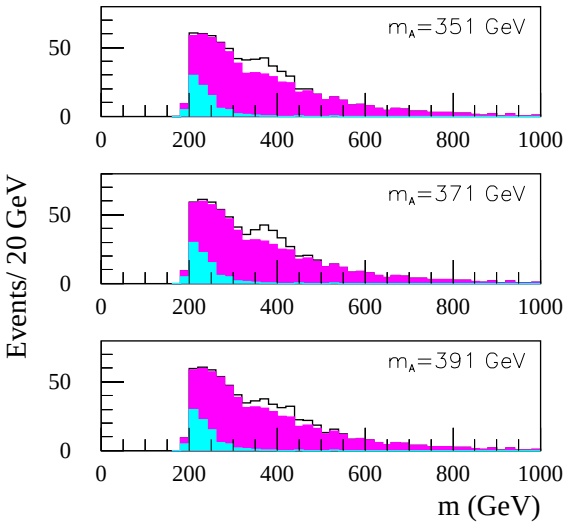

Figure 19-98 Expected reconstructed Higgs boson mass for all OS-SF pairs (see text) and an integrated luminosity of 300 fb^{-1}.

Scan of SUGRA parameter space

The same analysis as described above for the SUGRA point 3 has been applied to other points in the parameter space. The SUGRA parameter space has been scanned for fixed values of m_0 = 50, 100, 150, 200, 250 GeV in the range of $m_{1/2}$ = 100 - 300 GeV and tanβ = 1.5 - 50. The parameter A_0 had been set to zero. For this scan a dedicated package based on subroutines from ISAJET-7.37 was used. This calculates cross-sections and branching ratios for the signal and the SUSY backgrounds. Only the Higgs production via the gg fusion and the $b\bar{b}A$, $b\bar{b}H$ associated production gives a substantial contribution. The expected range in the SUGRA parameter space where the appropriate decay channel is open is determined. As the masses of the neutralinos $\tilde{\chi}_1^0$ and $\tilde{\chi}_2^0$ are proportional to $m_{1/2}$, the kinematic constraint $m_{\tilde{\chi}_2^0} - m_{\tilde{\chi}_1^0} < m_Z$, which is crucial for $\tilde{\chi}_2^0 \to \tilde{\chi}_1^0 l^+ l^-$ being dominant, gives the upper limit on $m_{1/2}$ of about 250 GeV for the Higgs searches in the four lepton channel.

Over most of the SUGRA parameter space the $H \to \tilde{\chi}_2^0\,\tilde{\chi}_2^0$ decay gives the main contribution to the four-lepton final state. In a small region of m_A in the range between 300 and 400 GeV and tanβ = 2, there is also a contribution from $H \to \tilde{\chi}_2^0\,\tilde{\chi}_3^0$ decays. If sleptons are lighter than the second lightest neutralinos, $m_{\tilde{e}_R}$ or $m_{\tilde{e}_L} < m_{\tilde{\chi}_2^0}$ the decay chain $\tilde{\chi}_2^0 \to \tilde{e}_R(\tilde{e}_L)^+\, e^-$ with the subsequent decay $\tilde{e}_R(\tilde{e}_L)^+ \to \tilde{\chi}_1^0\, e^+$ dominates the direct decay $\tilde{\chi}_2^0 \to \tilde{\chi}_1^0 l^+ l^-$.

The SUSY background was simulated including all SUSY production processes and those decay modes which give measurable contributions to the four lepton final state. For some SUGRA points the contributions from the neutralino/chargino production from sources other than $\tilde{\chi}_2^0\,\tilde{\chi}_2^0$-pair production are comparable with $\tilde{\chi}_2^0\,\tilde{\chi}_2^0$-pair production.

The $\tilde{\chi}\ \tilde{\chi}$, $\tilde{g}\ \tilde{\chi}$ and $\tilde{q}\ \tilde{\chi}$ production was included in the SUSY background. For large values of tanβ the $\tilde{\chi}$ decay to tau-leptons is dominant. For tanβ = 20 for example, the ratio $BR(\tilde{\chi}_2^0 \rightarrow \tilde{\chi}_1^0 \tau\tau) / BR(\tilde{\chi}_2^0 \rightarrow \tilde{\chi}_1^0 ee)$ is about 30 and the contribution from $\tau \rightarrow e\nu, \mu\nu$ decay is about 10% for the Higgs signal and about 30% for the background.

In some specific SUGRA parameter points the signal and background events were simulated and analysed with ATLFAST. The detection efficiencies depend on the particular parameters of the model. For example, the efficiency of the kinematic selection for leptons varies for signal events from ~40% for large m_A to ~10% for m_A = 200 GeV. For background events, the lepton cut efficiency is in the range 30 - 50% for most of the points. The analysis has been performed for jet-veto cuts, using thresholds of 20 and 40 GeV. At each point of parameter space the analysis with the higher significance is retained. For many SUGRA points, in contrast to the point 3 case, the SUSY background is not very high.

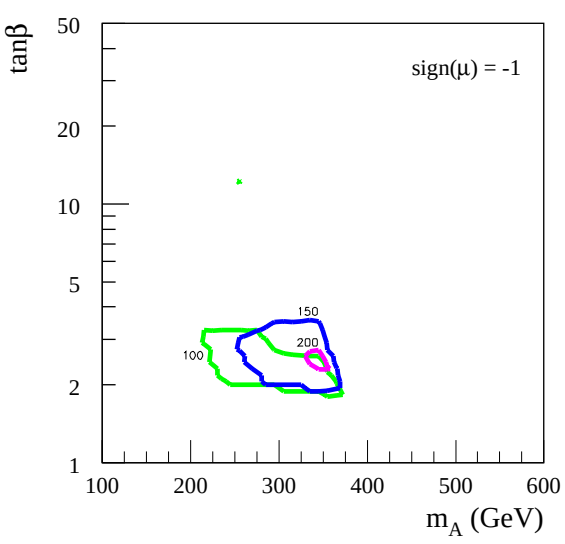

Figure 19-99 For an integrated luminosity of 30 fb^{-1}, 5σ-discovery contours for $H \rightarrow \tilde{\chi}\ \tilde{\chi} \rightarrow 4l$ channel in the (m_A, tanβ) plane for fixed m_0 = 50, 100, 150 and 200 GeV, and for sgn(μ) = -1.

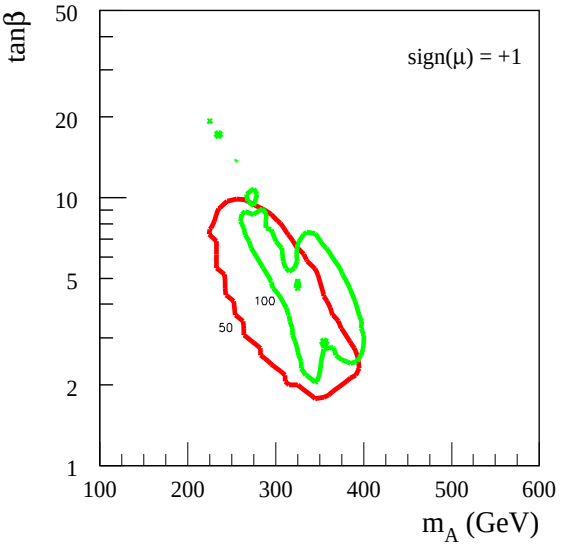

Figure 19-100 Same as Figure 19-99, but for sgn(μ) = +1.

The resulting 5σ-discovery contours are shown in Figure 19-99 to 19-102 projected onto the (m_A, tanβ) plane for both signs of μ, and for integrated luminosities of 30 fb^{-1} and 300 fb^{-1} [19-109]. The lines correspond to a 5σ significance. They are shown for fixed value of m_0 = 50, 100, 150 and 200 GeV. For positive μ values the significance is found to be slightly higher and a larger fraction of the (m_A, tanβ) plane can be covered. For both sgn(μ) the access to the large tanβ region, tanβ > 20, is restricted by the stau contribution. The complex structure of the significance region in the (m_A, tanβ) plane is mainly determined by the thresholds for the $\tilde{\chi}_2^0$ to sleptons decays.

In conclusion, while high luminosity running is required due to the small rate of Higgs production, this four lepton is promising for detection of heavy supersymmetric Higgs bosons via their decays to SUSY particles in the region of the (m_A, tanβ) plane which, using SM decay modes, was only accessible via the discovery of the light Higgs *h*. The sensitivity to the SUSY decay scenarios will be useful in the discrimination between the Standard Model and a supersymmetric Higgs model and for the investigation of the properties of the MSSM Higgs sector.

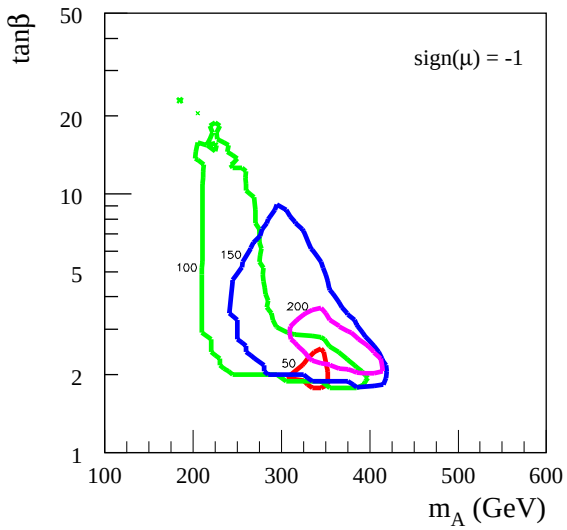

Figure 19-101 Same as Figure 19-99, but for an integrated luminosity of 300 fb^{-1}.

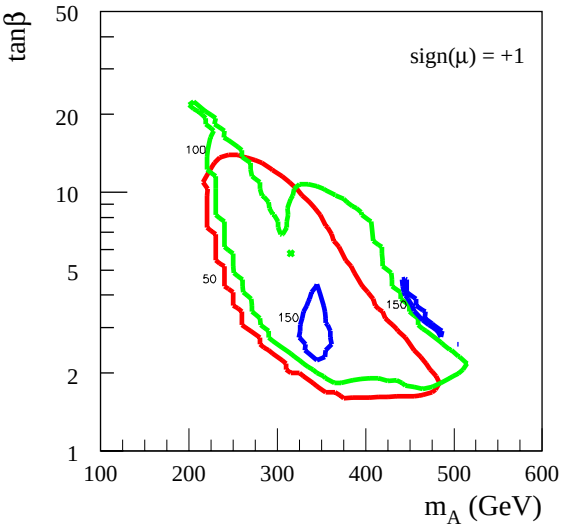

Figure 19-102 Same as Figure 19-100, but for an integrated luminosity of 300 fb^{-1}.

19.3.5.4 Higgs production in SUSY cascade decays

In this section the sensitivity to detect Higgs bosons in cascade decays of heavier SUSY particles is discussed. In particular, the lightest Higgs often appears at the bottom of cascades. One copious production source is the decay of the second lightest neutralino into the lightest neutralino, $\tilde{\chi}_2^0 \to \tilde{\chi}_1^0 h$; the former is produced with a large rate in the decays of squarks or gluinos such as $\tilde{q}_L \to \tilde{\chi}_2^0 q \to \tilde{\chi}_1^0 hq$. In R-parity conserving SUSY models the light Higgs h is always accompanied by missing transverse energy, carried away by the lightest SUSY particle. The presence of missing transverse energy and several energetic jets can be used to obtain a sample that consists mainly of the decay products of SUSY particles (see Section 20.2.5.). The discovery of the Higgs h in its dominant decay mode $h \to b\bar{b}$ without a lepton being present (as required in the Wh with $W \to l\nu$, case) then becomes possible.

In the following, the signal extraction is described using SUGRA point 1 as a typical example. The method established there [19-103] is then used at other points in the SUGRA parameter space and the discovery region in the SUGRA parameter space is determined [19-111].

$\tilde{\chi}_2^0 \to h\,(\to b\bar{b})\,\tilde{\chi}_1^0$ decay at SUGRA point 1

At point 1 (see Section 20.2) the SUSY particles are relatively heavy with squarks and gluinos in the 1 TeV range. The two lightest neutralinos have masses of 325 GeV and 170 GeV. Since the mass of the lightest Higgs h is 95 GeV, the decay $\tilde{\chi}_2^0 \to \tilde{\chi}_1^0 h$ is open and has a branching ratio of 90%. The Higgs boson h decays with a branching ratio of 80% into a $b\bar{b}$ pair.

The total cross-section for the production of SUSY particles is 3.6 pb and is dominated by squark-squark and squark-gluino production. About 25 000 events containing at least one h-boson are expected to be produced for an integrated luminosity of 30 fb^{-1}. About 90 % of them contain only one h-boson with an average p_T of about 200 GeV. In particular the cascade decay of the $\tilde{q}_L \to \tilde{\chi}_2^0 q \to \tilde{\chi}_1^0 hq$ leads to a very characteristic signature of multi-jet and multi-b-jet events associated with large E_T^{miss}. With further selection the reconstruction of the

$h \rightarrow b\bar{b}$ decays provides an accurate measurement of m_h, with a signal sample free of the large backgrounds from SM processes. Using this clean sample of $h \rightarrow b\bar{b}$ decays, a backward partial reconstruction of the SUSY cascade itself can also be performed (see Section 20.2.4.3).

Table 19-56 Numbers of expected events for SUSY and SM background events passing the selection cuts discussed in the text for an integrated luminosity of 30 fb^{-1} as a function of E_T^{miss} and *b*-jet-veto cuts. The third and fourth columns correspond to the choice of the final cuts.

Process	E_T^{miss} > 200 GeV Veto p_T^b > 15 GeV 30 fb^{-1}	E_T^{miss} > 300 GeV Veto p_T^b > 15 GeV 30 fb^{-1}	E_T^{miss} > 300 GeV Veto p_T^b > 50 GeV Final selection 30 fb^{-1}	E_T^{miss} > 300 GeV Veto p_T^b > 50 GeV Final selection 300 fb^{-1}
SUSY: $h \rightarrow b\bar{b}$	1190	920	980	6460
SUSY: other	190	160	180	1200
SM background	220	45	75	420
$S/\sqrt{B}$	59	64	61	160

To select a clean $h \rightarrow b\bar{b}$ signal above the SUSY combinatorial background and the SM background the following criteria are applied:

- $E_T^{miss} > 300$ GeV (or 200 GeV in some cases).
- Two tagged *b*-jets with $p_T > 50$ GeV, which are relatively close, $R^{b,b} < 2$. (The separation cut is mainly applied to reject $t\bar{t}$ background).
- There should be no additional *b*-jet with $p_T > 50$ GeV (or $p_T > 15$ GeV is some cases).
- Lepton-veto for isolated leptons with $p_T > 6$ GeV.
- Two additional jets with $p_T > 100$ GeV, one of them should be within $|\eta| < 2.0$.

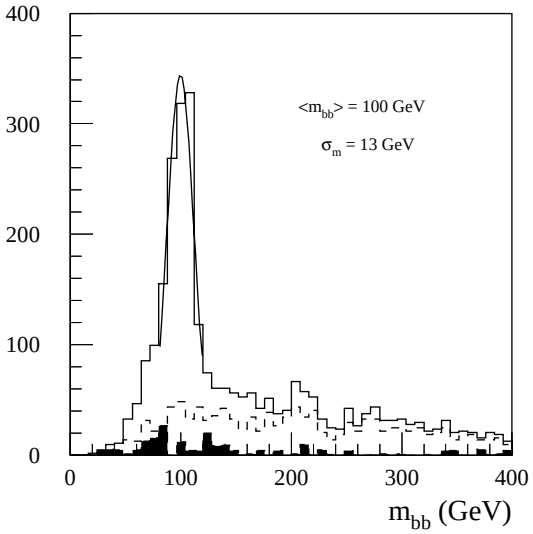

Figure 19-103 The reconstructed $m_{b\bar{b}}$ distribution for events passing the $h \rightarrow b\bar{b}$ selection cuts (see text). The distributions are shown for the SM background (shaded), the total SUSY+SM background (dashed) and the summed $h \rightarrow b\bar{b}$ signal and background for SUGRA point 1. An integrated luminosity of 30 fb^{-1} has been assumed.

Table 19-56 shows the number of expected events for the different selection cuts for integrated luminosities of 30 and 300 fb^{-1}. Already at low luminosity the signal can be clearly identified with a high significance above the backgrounds. At high luminosity, there is some degradation due to pile-up effects, and some degradation of the *b*-tagging efficiency which explains why the numbers in the Table do not scale with luminosity. In Figure 19-103 the reconstructed mass distributions $m_{b\bar{b}}$ of the two selected b-jets is shown after cuts. The contributions of the $h \rightarrow b\bar{b}$ signal + background (solid), of the Standard Model background (black) and of the total SM+SUSY background (dashed) are shown separately.

In the mass window $m_{b\bar{b}} = m_h \pm 25$ GeV, the SM background can be reduced well below 10% of the $h \to b\bar{b}$ signal. The SUSY combinatorial background is found to be small, at the level of 20% of the $h \to b\bar{b}$ signal itself.

Very similar conclusions are drawn from the analysis performed for SUGRA point 5 (see Section 20.2.5), where the SUSY particles have lower masses (gluino and squarks of 700 GeV) but similar cascade decay patterns [19-104].

Scan of SUGRA parameter space

The observability of the $h \to b\bar{b}$ signal was studied in the SUGRA parameter space for m_0 up to 2 TeV, $m_{1/2}$ up to 1 TeV, tanβ = 2, 10, and 30, sgn(μ) = ± 1 and $A_0 = 0$ [19-111]. For several points in the (m_0, $m_{1/2}$) plane where the channel $\tilde{\chi}_2^0 \to \tilde{\chi}_1^0 h$ is open, individual analyses similar to the one described above, were performed.

In most cases the same selection cuts were imposed. The E_T^{miss} threshold was increased with $m_{1/2}$ from 300 GeV for $m_{1/2}$ = 300 GeV to 600 GeV for $m_{1/2}$ = 1000 GeV. The E_T^{miss} cut was not so efficient at large m_0 and large $m_{1/2}$ where the E_T^{miss} results from the decay of rather light $\tilde{\chi}_2^0$, $\tilde{\chi}_i^{\pm}$ and not from decays of heavy $\tilde{q}$, as is the case for the low m_0, large $m_{1/2}$ region. The p_T thresholds for the *b* and non-*b* jets were optimised separately for different regions of the (m_0, $m_{1/2}$) parameter space.

Over a large region of the parameter space, the most important cascade for the *h* production, $\tilde{\chi}_2^0 \to \tilde{\chi}_1^0 h$, is open and has a branching ratio of about 90%. Also for $90 \le m_h \le 120$ GeV the branching ratio BR($h \to b\bar{b}$) is large and exceeds 75%. The total cross-section for SUSY production varies from ~ 10^3 pb at (m_0, $m_{1/2}$) ≈ (100 GeV, 100 GeV) to 10^{-1} pb for $m_{1/2} > 800$ GeV. The cross-section is almost independent of tanβ and sgn(μ).

All SUSY production processes available in PYTHIA 6.115 [19-112] were simulated, with $\tilde{q}\tilde{q}$, $\tilde{g}\tilde{q}$, $\tilde{g}\tilde{g}$, $\tilde{\chi}_1^{\pm}\ \tilde{\chi}_1^{\pm}$, $\tilde{\chi}_1^{\pm}\tilde{\chi}_2^0$ production being the most important ones. For low m_0 and large $m_{1/2}$, the $\tilde{q}\tilde{q}$ production is dominant (40%) since $m_{\tilde{g}} > m_{\tilde{q}}$, while at large m_0 and low $m_{1/2}$, where $m_{\tilde{g}} < m_{\tilde{q}}$, the $\tilde{g}\,\tilde{g}$ production is significant (30%). At the lower-left quarter of the (m_0, $m_{1/2}$) plane, where both the $\tilde{q}$ and the $\tilde{g}$ masses are low, $\tilde{g}\tilde{q}$ production contributions are larger than 35% of the total SUSY production. For large $\tilde{q}$ and $\tilde{g}$ masses, *i.e.*, at the upper-right part of the parameter space, gauginos lead the SUSY production via electroweak processes (50%). Mixed production processes, like $\tilde{g}\ \tilde{\chi}_1^{\pm}$, $\tilde{g}\,\tilde{\chi}_2^0$, $\tilde{q}\ \tilde{\chi}_1^{\pm}$, and $\tilde{q}\ \tilde{\chi}_1^0$ production, give contributions of order 1% or less.

In Figures 19-104 and 19-105 the 5σ-observability contours are shown for tanβ = 10, sgn(μ) = +1, and for integrated luminosity of 30 fb^{-1} and 300 fb^{-1} respectively. A line is superimposed which indicates where the branching ratio $BR(\tilde{\chi}_2^0 \to \tilde{\chi}_1^0 h)$ has a constant value of 50%. There is an obvious correlation between this branching ratio and the 5σ discovery contours. Once the channel $\tilde{\chi}_2^0 \to \tilde{\chi}_1^0 h$ is open, it quickly becomes dominant and the subsequent decay $h \to b\bar{b}$ becomes detectable. The expected number of $h \to b\bar{b}$ events, after selection cuts have been imposed, is indicated by the dashed and/or dotted lines in the figures. The 5σ discovery region depends only weakly on tanβ and sgn(μ). Similar plots exist for other values of tanβ and sgn(μ) and can be found in [19-111].

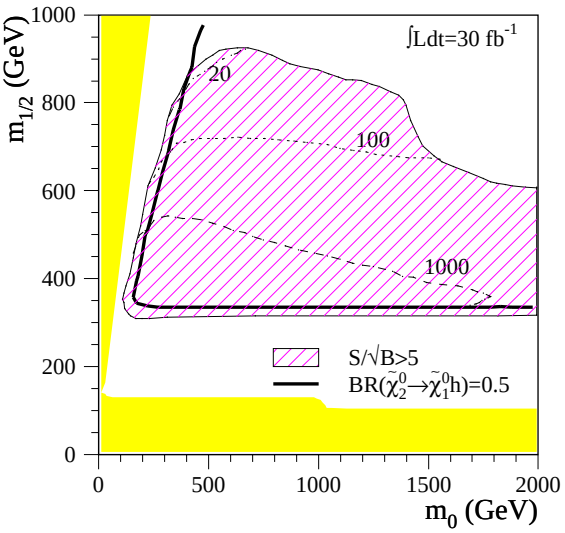

Figure 19-104 For an integrated luminosity of 30 fb^{-1}, 5σ-discovery area (hatched) for the $h \to b\bar{b}$ from SUSY cascade in the (m_0, $m_{1/2}$) plane for tanβ = 10, sgn(μ) = +1. The expected numbers of reconstructed $h \to b\bar{b}$ events are also shown. The dark shaded areas are excluded theoretically or experimentally.

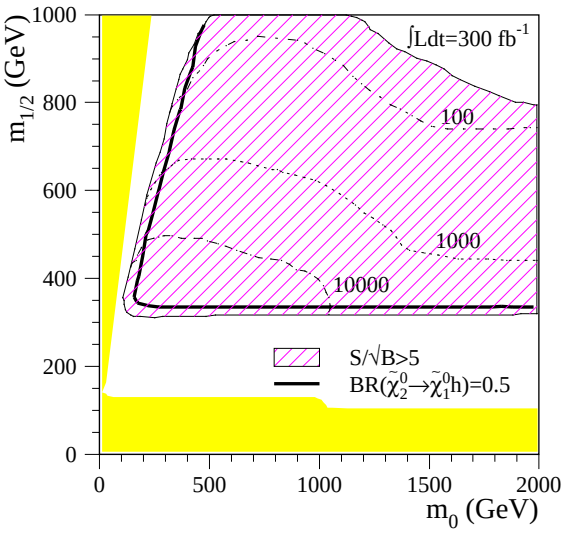

Figure 19-105 Same as Figure 19-104 but for an integrated luminosity of 300 fb^{-1}.

Outside the marked regions of the SUGRA parameter space the $h \to b\bar{b}$ decay will not be observed. Either the Higgs h is not produced in the SUSY cascade of heavy gaugino decays into lighter ones or a large $b\bar{b}$ irreducible background overwhelms the signal. This $b\bar{b}$ background arises from $\tilde{\chi}_2^0 \to \tilde{\chi}_1^0 Z \to \tilde{\chi}_1^0 b\bar{b}$, $\tilde{g} \to \tilde{\chi}_i^0 b\bar{b}$, or $\tilde{g} \to \tilde{\chi}_i^0 t\bar{t} \to \tilde{\chi}_i^0 WWb\bar{b}$ decays The non-observability of the signal in the upper right corner of the (m_0, $m_{1/2}$) plane is caused by a drop of the efficiency of the E_T^{miss} cut and by the lower cross-section for SUSY production. The results from the SUGRA parameter scan for both sgn(μ) were projected onto the (m_A, tanβ) plane. The results are shown in Figure 19-106 for integrated luminosities of 30 fb^{-1} and 300 fb^{-1}. In a large fraction of the (m_A, tanβ) parameter space above m_A= 500 GeV (m_A = 400 GeV) for tanβ > 5 (tanβ > 30) the $h \to b\bar{b}$ will be observable for an integrated luminosity of 30 fb^{-1}. It overlaps with the region where there is no sensitivity to the heavy Higgs bosons in the MSSM model.

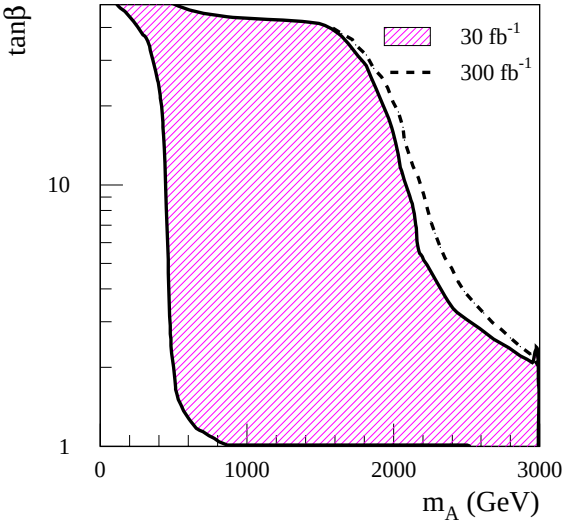

Figure 19-106 For integrated luminosities of 30 and 300 fb^{-1}, 5σ-discovery area (hatched) for the $h \to b\bar{b}$ from SUSY cascade in the (m_A, tanβ) plane. The dashed line indicates the improvement in the 5σ discovery for an integrated luminosity of 300 fb^{-1}

19.4 Strongly interacting Higgs sector

In the Standard Model, as the Higgs mass is increased, its coupling to gauge bosons increases, making the resonance wider and the interaction stronger, eventually leading to a violation of the unitarity bound ~1 TeV [19-3]. Requirements of vacuum stability and the validity of the running of the effective coupling, in next-to-leading order, should limit the allowed range for the mass of the Higgs boson [19-4], [19-5], [19-6].

While the Standard Model is renormalisable and consistent with all precision electroweak measurements, it has well known shortcomings [19-113]. It makes *ad hoc* assumptions about the shape of the potential, responsible for electroweak symmetry breaking, and provides no explanation for the values of the parameters. The theory becomes *trivial* (or non-interacting) if it is to remain valid at high energies. Radiative corrections to the Higgs mass diverge, leading to the *naturalness/hierarchy* problem. Supersymmetry is an appealing alternative which solves these problems, but at the cost of more particles and Higgs bosons, including a relatively light scalar not yet discovered.

It may well be, that no fundamental scalar particle exists. In that case, new physics must exist to account for the breaking of electroweak symmetry, for the regularisation of the vector boson coupling, and for generating fermion masses. In the absence of a low mass scalar Higgs particle, the study of electroweak symmetry breaking will require measurements, in the high energy regime, of the production rate of longitudinal gauge boson pairs since the longitudinal components are the Goldstone bosons of the symmetry breaking process. It will also be essential to search for the presence of new resonances which could exist in theories that regularise the vector boson scattering cross-section.

It has already been shown, in Section 19.2.10 that $V_L V_L$ fusion is detectable in the case of a heavy Higgs resonance, through the processes $H \rightarrow WW$ or $H \rightarrow Z\,Z$, up to $m_H \sim 1$ TeV. More generally, resonances could occur in vector, charged or neutral channels. Narrow resonances, predicted for example by technicolor models (see Section 21.2), should be detectable up to higher masses. Various other models exist for a unitarisation of the $V_L V_L$ coupling and experimental prospects have been evaluated in several recent reviews [19-114][19-115]. The search for a generic WZ resonance is presented below and the feasibility of measuring nonresonant behaviour of the $V_L V_L$ fusion process at high mass is assessed.

19.4.1 Detector performance issues

The same techniques are applied in the search for high mass gauge boson pairs as in the case of the heavy Higgs (see Section 19.2.10). Since the signals derive in large part from VV fusion, forward jet tagging is a powerful method of rejecting backgrounds. Central jet vetoing suppresses the large background from $t\bar{t}$ events, which produce pairs of W bosons accompanied by several jets. Searches which rely on reconstructing the hadronic decay of the W or Z will require optimisation of efficiencies and resolution in jet-jet masses.

19.4.2 Vector boson scattering in the Chiral Lagrangian model

Assuming an unbroken custodial $SU(2)_{L+R}$ symmetry, the scattering amplitudes for different $V_L V_L \to V_L V_L$ processes are related to each other by crossing. Defining a weak isospin I, the $W_L W_L$ scattering can be written in terms of isospin amplitudes, exactly as in low energy hadron physics. The isospin indices are assigned as follows,

$$W_L{}^a\, W_L{}^b \to W_L{}^c\, W_L{}^d$$

where W_L denotes either W_L or Z_L, where $W_L{}^{\pm} = (1/\sqrt{2})(W_L{}^1 \mp iW^2{}_L)$ and $Z_L = W_L{}^3$. The scattering amplitude is given by

$$M(W_L{}^a\, W_L{}^b \to W_L{}^c\, W_L{}^d) \sim A(s,t,u)\,\delta_{ab}\,\delta_{cd} + A(t,s,u)\delta_{ac}\delta_{bd} + A(u,t,s)\delta_{ad}\delta_{bc}$$

where a, b, c, d =1, 2, 3 and s, t, u are the usual Mandelstam kinematic variables.

Chiral Perturbation Theory (ChPT) [19-116] provides a theoretical framework capable of describing generically the strong interactions of electroweak gauge bosons [19-117]. In the chiral approach the low-energy Lagrangian is build as an expansion in derivatives of the Goldstone bosons fields. The form of the effective chiral Lagrangian, including operators up to dimension four, is only constrained by symmetry considerations which are common to any strong electroweak symmetry breaking sector [19-118]:

$$L^{(2)} = \frac{v^2}{4} trD_\mu U D^\mu U^\dagger$$

where $D_\mu U = d_\mu U - W_\mu U + UB_\mu$, $W_\mu = -(ig\sigma^a W_\mu^a)/2$, and $B_\mu = (ig\sigma^3 B_\mu)/2$. At higher-orders phenomenological parameters, L_1 and L_2 appear:

$$L^{(4)} = L_1(trD_\mu U D^\mu U^\dagger)^2 + L_2(trD_\mu U D^\nu U^\dagger)^2$$

The values of L_1 and L_2 depend on the model, but are expected to be in the range 10^{-2} to 10^{-3}. Given these parameters, it is possible to compute the function $A(s,t,u)$ in $O(p4)$ order [19-119]

$$A(s,t,u) = \frac{s}{v^2} + \frac{1}{4\pi v^4}(2L_1 s^2 + L_2(t^2+u^2)) + \frac{1}{16\pi^2 v^4}\left(-\frac{t}{6}(s+2t)\log\left(-\frac{t}{\mu^2}\right) - \frac{u}{6}(s+2u)\log\left(-\frac{u}{\mu^2}\right) - \frac{s^2}{2}\log\left(-\frac{s}{\mu^2}\right)\right)$$

The chiral Lagrangian approach does not respect unitarity. Among the methods used to unitarise chiral amplitudes, the Inverse Amplitude Method (IAM) [19-120][19-121], used here, has proved very successful in describing resonances in low energy π-π and πK scattering [19-122]. It is based on the assumption that the inverse of the amplitude has the same analytic properties as the amplitude itself.

In analogy to ππ scattering there are three possible isospin channels I = 0, 1, 2. At low energies states of lowest angular momentum J are most important, and thus only the $t_{I,J} = t_{0,0}$, $t_{1,1}$ and $t_{2,0}$ partial waves are considered here. The IAM is also able to reproduce, with proper choice of parameters, the broad Higgs-like resonance in the (I = 0, J = 0) channel. It has been shown [19-123]

that in the (I = 1, J = 1) channel there may exist narrow resonances up to masses of about 2500 GeV. The mass and width of this channel only depend on the combination $(L_2 - 2L_1)$ in this model and on v^2:

$$m_V^2 = \frac{v^2}{4(L_2 - 2L_1) - \frac{1}{18(4\pi)^2}} \text{ and } \Gamma_V = \frac{m_V^3}{96\pi v^2}$$

The $W_L Z_L \rightarrow W_L Z_L$ process is expected to be dominated by the (I = 1, J = 1) ρ-like resonance.

$W_L Z_L \rightarrow W_L Z_L \rightarrow lljj$

As a reference for this model, the process $W_L Z_L \rightarrow W_L Z_L$, with $Z \rightarrow ll$, $l = e, \mu$ and $W \rightarrow jj$ [19-124] is used. PYTHIA 5.7 was modified to generate the $V_L V_L$ scattering processes for any values of L_1 and L_2. The simulation was done for two values of $(L_2 - 2L_1) = 0.006$ and 0.01, which yield $\sigma \times$ BR of 1.5 fb and 2.8 fb, with mass peaks at 1.5 TeV and 1.2 TeV respectively.

The main features of the signal are:

- Two high-p_T leptons in the region $|\eta| < 2.5$ with the invariant mass consistent with the mass of Z-boson.
- Two high-p_T jets in the central region with the invariant mass consistent with the mass of W-boson.
- The presence of energetic jets in forward region ($|\eta| > 2$).

Requiring, at generator level, $\hat{s} > 1050$ GeV and $p_T^{\text{hard}} > 100$ GeV, the $\sigma \times$ BR of the Z+jet production, with leptonic decay of the Z boson is 0.276 pb. Irreducible background is from continuum WZ production and the main QCD background is from Z+multijet production. Two final-state jets can fake a W decay if the invariant mass of the jet pair is close to m_W. The $t\bar{t}$ background with leptonic decays of the W's is potentially dangerous because of the large cross-section, but can be efficiently suppressed by a cut on the invariant mass of the leptons from the W decay, since the two leptons have large transverse momenta and a wide opening angle. Figure 19-107 shows the invariant mass of two leptons from W decay for several values of the minimum lepton p_T allowed.

The vector bosons in $V_L V_L$ scattering are produced mostly in the central region and are characterised by large values of transverse momenta. These properties are used to suppress the background by selecting high p_T decay products. Figure 19-108 shows the p_T distribution of the leptons for the signal and Z+jet background (the background was generated here with a minimal p_T for Z of 30 GeV). The events are required to have two isolated and identified leptons of same flavour and opposite charge (e^+e^- or $\mu^+\mu^-$) in the region $|\eta| < 2.5$ with $p_T > 100$ GeV. The invariant mass of these two leptons was required to lie in the region $|m_{ll} - m_Z| < 6$ GeV. The total efficiency of this selection criteria was estimated at ~40% for signal events.

Jets were reconstructed by a cone algorithm with $\Delta R = 0.2$. Due to a large W boost, the cones of the jets could overlap. In that case, the reconstructed energy in the overlap region was shared between the jets according to their relative energies. A resolution of 10 GeV in the mass of the reconstructed W was obtained, consistent with what was found in Section 9.3.1. The events were required to have two jets with $p_T > 50$ GeV and $|\eta| < 2$ and the invariant mass of these two jets was $|m_{jj} - m_W| < 15$ GeV. Both Z and W bosons were required to have a transverse momentum larger than 200 GeV.

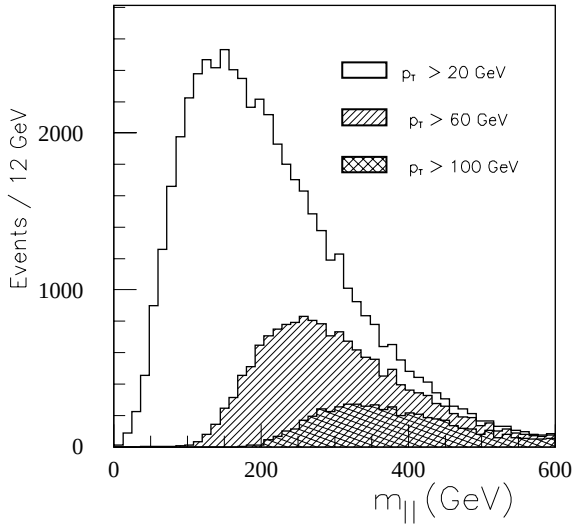

Figure 19-107 Invariant mass of the two leptons from the $t\bar{t}$ background, for the threshold on the leptons transverse momenta p_T = 20, 60 and 100 GeV.

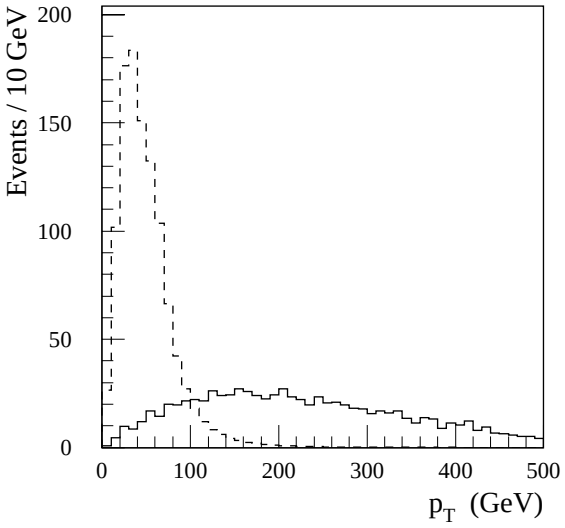

Figure 19-108 Transverse momentum distribution for leptons from signal (solid line) and from the Z+jet background (dashed). The histograms are normalised to a same number of events.

Forward jet tagging provides a powerful method of further rejecting background. Jets in the forward regions ($2 < |\eta| < 5$) were reconstructed by a cone algorithm with $\Delta R = 0.5$. Events were accepted if jets with $p_T >$ 30 GeV and energy larger than 500 GeV were present in each hemisphere. The total tagging efficiency of 0.25 for the signal process and 0.01 for Z+jet background was obtained.

The expected number of signal and background events after successively applied cuts and for an integrated luminosity of 100 fb^{-1} are presented in Table 19-57.

Table 19-57 Number of signal and background $W_L Z_L$ candidate events in a 2σ interval around the mass of the resonance, for an integrated luminosity of 100 fb^{-1}, for the cases (L_2 - 2L_1) = 0.01 and (L_2 - 2L_1) = 0.006, corresponding to Mρ = 1.2 TeV and 1.5 TeV respectively.

Number of events	**M_ρ = 1.2 TeV**		**M_ρ = 1.5TeV**	
	$W_L Z_L$	Z+jet	$W_L Z_L$	Z+jet
Central jets cut	284	2187	145	1781
$m_{jj} = m_W \pm 15$ GeV	101	154	46	82
Leptonic cuts	70	84	36	47
Forward jet tagging	14	3	8	1.3

The mass spectra for WZ candidates after all cuts show a clear peak with width 75 GeV for the 1.2 TeV resonance and 100 GeV for the 1.5 TeV resonance (Figure 19-109). The expected number of events in the window $|m_{WZ} - m_V| < 2\sigma$, for an integrated luminosity of 100 fb^{-1}, is 8 for m_V = 1.5 TeV and 14 for m_V = 1.2 TeV, with respectively 1.3 and 3 events from Z+jet background. The contribution from the irreducible continuum WZ background is negligible, below 0.05 events inside the mass window. It can therefore be concluded that such a narrow resonance process is detectable after a few years of high luminosity data taking.

The process of $W_L Z_L$ production can also be well measured in its purely leptonic final states, without jet tagging if the production by $q\bar{q}$ fusion dominates [19-14]. It is discussed in Section 21.2.1.1 in the framework of a multiscale technicolor model.

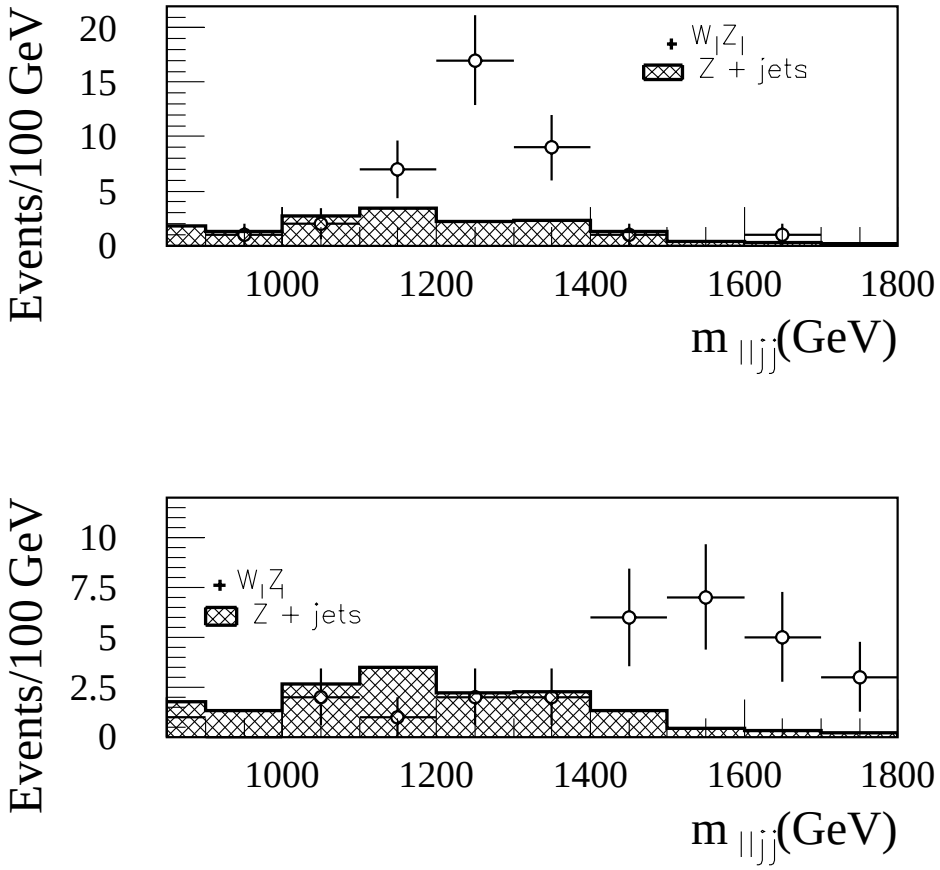

Figure 19-109 Reconstructed mass distribution for the WZ system for a 1.2 TeV and a 1.5 TeV resonance for an integrated luminosity of 300 fb^{-1}.

19.4.2.1 Non-resonant high mass gauge boson pairs

As a complement to measurements of resonances in $V_L V_L$ scattering, or in the absence thereof, the measurement of cross-sections at high mass for nonresonant channels will be a challenging task. It will be essential to understand very well the magnitude and energy dependence of backgrounds. Here, the observability of like-sign $W_L^{\prime}\ W_L^{\prime}$ production, followed by leptonic decay (μ or *e*) of the *W's* is discussed.This process has been considered in the literature as a potentially sensitive probe because of low background levels [19-125][19-126][19-127]. This channel can be particularly important since it has been shown that a complementary relationship between resonant *WZ* and nonresonant $W_L^{\prime}\ W_L^{\prime}$ exists [19-127].

As processes for the high mass $W_L\ W_L$ signal, the following are considered [19-128]:

- A t-channel exchange of a Higgs with m_H = 1 TeV, (W_LW_L only), simulated with PYTHIA: $\sigma \times \mathrm{BR}$ = 1.33 fb.
- A model with a K-matrix unitarised amplitude [19-127][19-129], $a_{IJ}^K = \frac{Re(a_{IJ})}{1 - iRe(a_{IJ})}$, with $\sigma \times \mathrm{BR}$ = 1.12 fb.
- The Chiral Lagrangian Model of Section 19.4.2, with the same parameters L1 = 0 and L2 = 0.006 or 0.01: $\sigma \times \mathrm{BR}$ = 0.484 fb and 0.379 fb respectively.

Backgrounds from continuum WW bremsstrahlung of $O(\alpha^2)$ in amplitude produce mostly transverse W's. Other backgrounds include processes involving non-Higgs exchange, as well as QCD processes of order $\alpha\alpha_s$ in amplitude, with gluon exchange and W bremsstrahlung from interacting quarks. The effects of $Wt\bar{t}$ and WZ backgrounds is also considered. The signal is generated with PYTHIA 6.2 [19-112], and backgrounds have been incorporated into PYTHIA using a generator code, obtained from [19-115], which takes into account all diagrams. The contributions from electroweak processes not involving the Higgs are estimated by assuming a low-mass Higgs (m_H = 100 GeV).

The analysis was performed using fast simulation. First, leptonic cuts were applied:

- Two positively charged isolated leptons in the central region (p_T > 40 GeV and $|\eta| < 1.75$).
- The opening angle between the two leptons, in the transverse plane must satisfy $\cos\Delta\phi < -0.5$. This cut selects preferentially events with longitudinal W's which have high p_T.
- The invariant mass of the two leptons m_{ll} > 100 GeV.

At the jet level, backgrounds can be reduced by requiring that:

- No jet (p_T > 50 GeV) be present in the central region ($|\eta| < 2$). This reduces significantly background from the $Wt\bar{t}$ process.
- Two of the jets must fall in the forward and backward regions: $\eta > 2$ and $\eta < -2$.
- A lower p_T is required from the forward jets: $p_T < 150$ GeV for the first and $p_T < 90$ GeV for the second.

The expected number of signal and background events is shown in Table 19-58, assuming an integrated luminosity of 300 fb^{-1}. Figure 19-110 displays the expected mass distribution of the $ll\nu\nu$ system (accounting only for transverse missing momentum). The major remaining background, especially at low values of $m_{ll\nu\nu}$ is from continuum transverse W's. Potentially large systematic uncertainties asso-

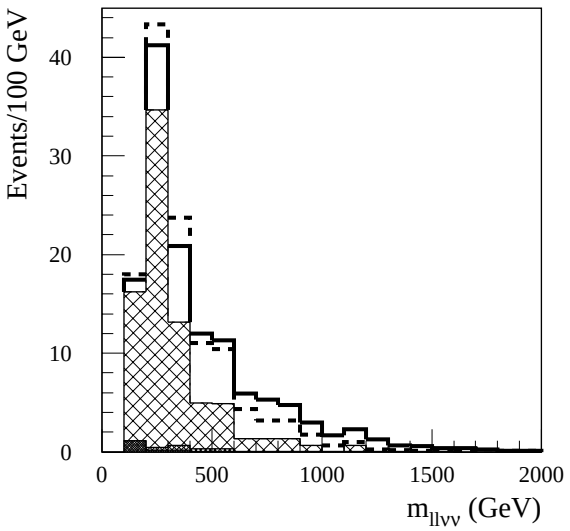

Figure 19-110 Distribution of invariant mass of the two leptons with E_T^{miss} in the $W_L\ W_L \rightarrow ll\nu\nu$ process expected for an integrated luminosity of 300 fb^{-1}. The scenarios are: K-matrix unitarisation (solid line) and 1 TeV Higgs (dotted histogram), shown on top of the backgrounds. The backgrounds are (from darkest to lightest): WZ, gluon exchange diagrams, and W_TW_T from electroweak bremsstrahlung.

ciated with the evaluated cross-section of this background, or of the cut efficiencies, can be estimated by analysing various distributions under different cut conditions.

The K-matrix scenario gives the highest signal, observable after a few years of high luminosity running, whereas a very low signal would be seen if the ρ resonance itself is clearly observable (Chiral Lagrangian Model, with L2 = 0.006 or 0.01 and L1 = 0, see Section 19.4.2).

Table 19-58 The expected number of events for the $W_L\ W_L$ signal and backgrounds after respective selection criteria and for an integrated luminosity of 300 fb^{-1}.

	Leptonic cuts	**Jet + leptonic cuts**	$m_{llνν}$**> 400 GeV**
Higgs m_H = 1 TeV	116	42.6	21.0
K-matrix	129	50.3	34.8
Chiral Lagrangian, L2 = 0.006	45	17.1	8.2
Chiral Lagrangian, L2 = 0.01	33.8	11.8	5.1
W_TW_T	648	76	14.5
Gluon exchange	127	1.35	0.54
Wt	281	0	0
WZ	555	1.2	0.3

19.5 Conclusions on the Higgs sector

The detailed studies described in this Chapter have demonstrated that the ATLAS detector has a large potential in the investigation of one of the key physics question at LHC, the origin of electroweak symmetry-breaking.

If a SM Higgs boson exists, discovery over the full mass range, from the LEP200 lower limit to the TeV scale will be possible after a few years of running at low luminosity.

- The most important channels in the intermediate mass region, $m_H < 2m_Z$, for which a mass peak would be reconstructed, are the four-lepton channel, $H \rightarrow ZZ^* \rightarrow 4l$, the direct two-photon channel, $H \rightarrow \gamma\gamma$, as well as the associated production channels, where the Higgs boson is produced in association with a vector boson or a $t\bar{t}$ pair. In these channels, both the γγ and $b\bar{b}$ decay modes can be discovered at the LHC. For Higgs-boson masses around 170 GeV, for which the ZZ^* branching ratio is suppressed, the discovery potential can be enhanced by searching for the $H \rightarrow WW^* \rightarrow l\nu l\nu$ decay. In this case, the Higgs-boson signal would only be observed as an excess of events.
- For $m_H > 2m_Z$ the dominant discovery channel is the four-lepton channel.
- In the mass range between 600 GeV and about 1 TeV, a Higgs boson would be discovered with the $WW \rightarrow l\nu jj$ mode. The sensitivity in this channel can also be extended down to lower masses, where it provides independent and complementary information to the four-lepton channel. For $400 < m_H < 900$ GeV the $H \rightarrow WW \rightarrow l\nu jj$ channel is complemented by the $H \rightarrow ZZ \rightarrow lljj$ and $H \rightarrow ZZ \rightarrow ll\nu\nu$ channels, which would provide additional robustness to a Higgs boson discovery in this mass range.

Over a large fraction of the mass range the discovery of a SM Higgs boson will be possible in two or more independent channels. It has also been shown that, if discovered, important Higgs-boson parameters like the mass and the width can be measured. Together with measurements of the production rates and some couplings and branching ratios they will provide useful constraints on the Higgs couplings to fermions and bosons which in turn can be used to test the Standard Model predictions and to determine the nature of the resonance.

The ATLAS experiment has also a large potential in the investigation of the MSSM Higgs sector. If the SUSY mass scale is large and supersymmetric particles do not appear in the Higgs decay products, the full parameter space in the conventional (m_A, tanβ) plane can be covered assuming an integrated luminosity of about 100 fb^{-1}.

- The interest was focused on the discovery potential of various decay modes accessible in the case of the SM Higgs boson: $h \to \gamma\gamma$, $h \to b\bar{b}$, $H \to ZZ \to 4l$, and of modes strongly enhanced at large *tan*β*: H/A* $\to \tau\tau$, *H/A* $\to \mu\mu$. Much attention was given to other potentially interesting channels such as: $H/A \to t\bar{t}$, $A \to Zh$, $H \to hh$, $H^{\pm} \to tb$.
- The overall discovery potential in the (m_A, tanβ) plane relies heavily on the $H/A \to \tau\tau$ channel, on the $t\bar{t}h$ with $h \to b\bar{b}$ and on the direct and associated $h \to \gamma\gamma$ channels.
- Over a large fraction of this parameter space more than one Higgs boson and / or more than one decay mode would be accessible.
- For almost all cases, the experiment would be able to distinguish between the SM and the MSSM models.

This complete coverage can also be reached independent on the mixing scenario in the stop-sbottom sector. The evidence for Higgs-boson signals would not constitute a direct proof of the existence of supersymmetry, unless supersymmetric particles are discovered themselves.

The interplay between SUSY particles and the Higgs sector has also been addressed. SUSY scenarios have an impact on the discovery potential through the opening of Higgs-boson decays to SUSY particles (mostly for *H* and *A*) and through the presence of SUSY particles in loops (mostly for production via *gg* fusion and for $h \to \gamma\gamma$ decays). Scenarios in which SUSY particles are light and appear as Higgs decay products have been studied in the framework of SUGRA models. The discovery potential of the lightest neutral Higgs *h* in the SM production processes would not be significantly different from what is obtained in the heavy SUSY scenario, since within the model, given present experimental constraints, the decay of *h* to the lightest SUSY particles is kinematically forbidden. Moreover, over a large fraction of the SUGRA parameter space, the *h*-boson would appear at the end of the decay cascade of SUSY particles in the channel $\tilde{\chi}_2^0 \to \tilde{\chi}_1^0 h$ which will be observable with the ATLAS detector. The neutral heavy Higgs bosons would be detected in some cases via their decays into neutralinos and charginos, using multi-lepton final states.

In the absence of a scalar Higgs boson, the principal probe for the mechanism of electroweak symmetry breaking will be gauge boson scattering at high energies. It has been shown that ATLAS will be sensitive to the presence of resonances, such as in the *WZ* system, up to masses around 1.5 TeV. Nonresonant processes, such as in the W^+W^+ production, will require a few years of high luminosity running and a good understanding of the underlying backgrounds.

Many scenarios discussed in this chapter have served as benchmark processes for optimising the detector design and performance. This includes the MSSM model, which should be considered as one theoretical model among many others, but one which provides a variety of signatures to test and to optimise the detector performance. The important detector requirements in

the investigation of electroweak symmetry breaking include electromagnetic calorimetry, jet-jet mass resolution in the reconstruction of multijet final states, good measurement of missing transverse energy, *b*-tagging, good electron, muon, tau and photon identification as well as forward jet tagging. The ATLAS detector in its final layout and optimisation is well matched to achieve the necessary requirements. It is also expected that the present design provides a firm basis for exploring areas of new and unexpected physics.

19.6 References

19-1 P.W. Higgs, Phys. Rev. Lett. **12** (1964) 132 and Phys. Rev. **145** (1966) 1156;
F. Englert and R. Brout, Phys. Rev. Lett. **13** (1964) 321;
G.S. Guralnik, C.R. Hagen and T.W. Kibble, Phys. Rev. Lett. **13** (1964) 585.

19-2 S. Glashow, Nuc. Phys. **22** (1961) 579;
S. Weinberg, Phys. Rev. Lett. **19** (1967) 1264; A. Salam, in: 'Elementary Particle Theory', W. Svartholm, ed., Almquist and Wiksell, Stockholm,1968;
H.D. Politzer, Phys. Rev. Lett. **30** (1973) 1346; D.J. Gross and F.E. Waltzed, Phys. Rev. Lett. **30** (1973)1343.

19-3 B.W. Lee *et al.*, Phys. Rev. Lett. **38** (1977) 883;
M. Quiros, 'Constraints on the Higgs boson properties from the effective potential', hep-ph/9703412;
A. Ghinculov and T. Binoth, Acta Phys. Polon. **B30** (1999) 99**.**

19-4 L. Maiani, G. Parisi and R. Petronzio, Nucl. Phys. **B136** (1979) 115;
N. Cabibbo *et al.* Nucl. Phys. **B158** (1979) 295;
R. Dashen and H. Neunberger, Phys. Rev. Lett. **50** (1983) 1897;
D.J.E. Callaway, Nucl. Phys. **B233** (1984) 189;
M.A. Beg *et al.*, Phys. Rev. Lett. **52** (1984) 883;
M. Linder, Z. Phys. **C31** (1986) 295.

19-5 G. Altarelli and G. Isidori, Phys. Lett. **B337** (1994) 141.
J.A. Casas, J.R. Espinosa and M. Quiros, Phys. Lett. **B342** (1995) 171; Phys. Lett. **B383** (1996) 374.

19-6 B. Grzadkowski and M. Linder, Phys. Lett. **B178** (1986) 81;
T. Hambye and K. Riesselmann, Phys. Rev. **D55** (1997) 7255.

19-7 The present LEP preliminary limits, presented at the 1999 winter conferences: ALEPH 99-007 CONF-99-003, March 1999; DELPHI 99-8 CONF-208; L3 Notes 2382,2383, March 1999; OPAL Note PN382, March 1999.

19-8 P. Janot, Proc. of the workshop on LEP-SPS performance, Chamonix IX, CERN-SL-99-007 DI (1999) and references therein.

19-9 The LEP Collaborations ALEPH, DELPHI, L3, OPAL, the LEP Electroweak Working Group and the Heavy Flavour and Electroweak Groups, CERN-EP/99-15.

19-10 For a review on the MSSM, see H. P. Nilles, Phys. Rep. **110** (1984) 1,
P. Nath, R. Arnowitt and A. Chamseed, *Applied N=1 Supergravity*, ICTP Series in Theoretical Physics, Vol. I (World Scientific, Singapore, 1984);
H.Haber and G. Kane, Phys. Rep. **117** (1985)

19-11 *E.g.* see 'Higgs Physics at LEP2', M. Carena, P. M. Zerwas (conv) *et al.*, Proceedings of the LEP2 Workshop, G. Altarelli, T. Sjöstrand and F. Zwirner (eds), CERN 1995.

19-12 S. Weinberg, Phys. Rev. **D13** (1979) 974, *ibid.* **D19** (1979) 1277;
L. Susskind, Phys. Rev. **D20** (1979) 2619.

19-13 ATLAS Letter of Intent, CERN / LHCC / 92-4, CERN 1992.

19-14 ATLAS Technical Proposal, CERN / LHCC 94-43, CERN 1994.

19-15 E.Richter-Was *et al.* 'Standard Model and Minimal Supersymmetric Standard Model Higgs rates and backgrounds in ATLAS', ATLAS Internal Note ATL-PHYS-95-048 (1995).

19-16 E. Richter-Was *et al.*, 'Minimal Supersymmetric Standard Model Higgs rates and backgrounds in ATLAS', ATLAS Internal Note ATL-PHYS-96-074 (1996), published in Int. J. Mod. Phys. **A13** (1998) 1371.

19-17 E. Richter-Was, D. Froidevaux and L. Poggioli, 'ATLFAST 2.0 a fast simulation package for ATLAS', ATLAS Internal Note, ATL-PHYS-98-131 (1998).

19-18 For a review see for example, M. Spira, Fortsch. Phys. **46** (1998) 203 and references therein.

19-19 M. Dittmar and H. Dreiner, Phys. Rev. **D55** (1997) 167; Contributed paper to the EPS Conference, hep-ph / 9703401.

19-20 A. Djouadi, J. Kalinowski and M. Spira, Comput. Phys. Commun. **108** (1998) 56.

19-21 ATLAS Collaboration, Calorimeter Performance Technical Design Report, CERN / LHCC 96-40 (1996).

19-22 V. Tisserand, 'The Higgs to Two Photon Decay in the ATLAS Detector', ATLAS Internal Note ATL-PHYS-96-090 (1996).

19-23 L. Fayard and G. Unal, 'Search for Higgs decays into photons with EAGLE', ATLAS Internal Note ATL-PHYS-92-001 and Addenda 1&2 (1992).

19-24 P. Aurenche *et al.*, in Proc. Large Hadron Collider Workshop, Aachen, 1990, edited by G. Jarlskog and D. Rein, CERN 90-10 / ECFA 90-133.

19-25 E. Richter-Was, 'Hard photon bremsstrahlung in the process $pp \rightarrow Z/\gamma^* \rightarrow l^+l^-$: a background for the intermediate mass Higgs' ATLAS Internal Note ATL-PHYS-94-034, published in Z. Phys. **C61** (1994) 323.

19-26 G. Eynard, 'Etude de la production associee du boson de Higgs WH, $t\bar{t}H$, ZH with $H \rightarrow \gamma\gamma$ avec le detecteur ATLAS, aupres du LHC', ATLAS Ph. D. Thesis 1997, LAPP Annecy.

19-27 E. Barberio and Z. Was, Comput. Phys. Commun. **79** (1994) 291; E. Barberio, B. van Eijk and Z. Was, Comput. Phys. Commun. **66** (1991) 115.

19-28 CMS Technical Proposal, CERN / LHCC 94-38, CERN 1994.

19-29 S. Abdulin *et al.*, INP MSU 98-13 / 514 (1998).

19-30 S. Zmushko,' Search for $H \rightarrow \gamma\gamma$ in association with jets', ATLAS Communication ATL-COM-PHYS-99-040 (1999).

19-31 R.K. Ellis, I. Hinchliffe, M. Soldate and J.J. van der Bij, Nucl. Phys. **B297** (1988) 221.

19-32 S. Kiourkos and J. Schwindling, 'H $\rightarrow$ Zγ channel in ATLAS. A study on the Standard Model and Minimal Supersymmetric SM case', ATLAS Communication ATL-COM-PHYS-99-009 (1999).

19-33 A. Stange, W. Marciano and S. Willenbrock, Phys. Rev. **D50** (1994); J. F. Gunion and T. Han, Phys. Rev. **D51** (1995) 1051.

19-34 D. Froidevaux and E. Richter-Was, 'Is the channel $H \to b\bar{b}$ observable at LHC ?', ATLAS Internal Note ATL-PHYS-94-043 (1994), published in Z. Phys. **C67** (1995) 213.

19-35 E. Richter-Was and M. Sapinski, 'Search for the SM and MSSM Higgs boson in the $t\bar{t}H$, $H \to b\bar{b}$ channel', ATLAS Internal Note ATL-PHYS-98-132 (1998), published in Acta Phys. Polon. **B30** (1999) 1001.

19-36 B.J. Dick, 'Further work on WH, $H \to b\bar{b}$', ATLAS Communication ATL-COM-PHYS-99-019 (1999).

19-37 B. van Eijk, R. Kleiss, in [19-130], vol. II, p. 183.

19-38 L. Guyot, D. Froidevaux and L. Poggioli, 'Physics Performance for Various Muon System Configurations', ATLAS Internal Note ATL-PHYS-95-076, (1995).

19-39 O. Linossier and L. Poggioli, 'Final state inner-Bremsstrahlung effects on $H \to ZZ^* \to 4l$ channel with ATLAS', ATLAS Internal Note ATL-PHYS-95-075, (1995).

19-40 O. Linossier and L. Poggioli,'H to ZZ^* to 4 leptons channel in ATLAS. Signal reconstruction and reducible backgrounds rejection ', ATLAS Internal Note ATL-PHYS-97-101, (1997).

19-41 I. Gavrilenko, 'Description of Global Patern Recongnition Program (xKalman)', ATLAS Internal Note ATL-INDET-97-165 (1997).

19-42 K. Jakobs and T. Trefzger, 'SM Higgs Searches for $H \to WW^* \to l\nu l\nu$ with a mass between 150-190 GeV at LHC', ATLAS Communications, ATL-PHYS-COM-99-031 (1999).

19-43 C.A. Nelson Phys. Rev. **D37** (1988) 1220).

19-44 H. Baer and J. D. Wells, Phys. Rev. **D57** (1998) 4446.

19-45 K. Jakobs, 'A study of the associated production WH, $H \to WW \to l\nu l\nu$', ATLAS Communication ATL-PHYS-COM-99-062 (1999); W. Bonivento, 'Higgs search in trilepton signal', ATLAS Communication ATL-PHYS-COM-99-046 (1999).

19-46 T. Han *et al.*, Phys. Rev. **D59** (1998).

19-47 Report of the Physics at RUN II Supersymmetry / Higgs Workshop, Fermilab,1999, eds. M. Carena and J. Lykken, in preparation; J. Conway, 'Higgs discovery potential in Run 2 at Tevatron', conference talks, La Thuile, 3 March 1999; Sitges, 30 April 1999; M. Carena, conference talk, PLANCK'99, 19 April, 1999.

19-48 D. Froidevaux *et al.*, 'Comparison of the physics potential of the ATLAS detector for searches for the intermediate Higgs boson in pp collision as $\sqrt{s}$ = 14 TeV and $p\bar{p}$ collision at $\sqrt{s}$ = 2 TeV', ATLAS Communication ATL-COM-PHYS-99-058.

19-49 U. Baur and E.W.N Glover, in [19-130], Vol. II, p.570.

19-50 R.H. Cahn *et al.*, Phys. Rev. **D35** (1987) 1626.

19-51 I. Zuckerman *et al.*,'MC simulation of backgrounds to the $H \to ZZ \to ll\nu\nu$ signal at the LHC', ATLAS Internal Note ATL-PHYS-92-007 (1992).

19-52 M. Bosman and M. Nessi, 'Study of *Z+jets* background to $H \to ZZ \to ll\nu\nu$ signal using full simulation of ATLAS calorimetry', ATLAS Internal Note ATL-PHYS-94-050, 1995.

19-53 H. Ruiz, 'Discovery potential of a heavy Standard Model Higgs boson through the $H \to ZZ \to ll\nu\nu$ channel at the LHC with the ATLAS detector', ATLAS Communication ATL-COM-PHYS-99-031 (1999).

19-54 P. Savard and G. Azuelos, 'The discovery potential of a Heavy Higgs (m_H= 800 GeV) using full GEANT simulation of ATLAS', ATLAS Internal Note ATL-PHYS-98-128 (1998).

19-55 S. Zmushko *et al.*, 'Study of $H \rightarrow WW \rightarrow l\nu jj$ and $H \rightarrow ZZ \rightarrow lljj$ decays for m_H = 1 TeV', ATLAS Internal Note ATL-PHYS-92-008 (1992).

19-56 M. Cobal *et al.*,' VECBOS: a Lowest Order Matrix Element Calculation to simulate direct QCD W + n jet events', ATLAS Internal Note ATL-PHYS-96-084 (1996).

19-57 V. Cavasinni *et al.*, 'Search for $H \rightarrow WW \rightarrow l\nu jj$ with the ATLAS detector (m_H= 300-600 GeV)', ATLAS Internal Note ATL-PHYS-98-127 (1998).

19-58 F. Gianotti, 'Precision physics at LHC', ATLAS Internal Note ATL-PHYS-99-001 (1999).

19-59 J.F. Gunion *et al.*, 'Higgs boson discovery and properties', Snowmass 96, hep-ph/9703330.

19-60 F. Abe *et al.*, CDF Collaboration, Phys. Rev. **D52** (1995) 4784.

19-61 J.F. Gunion, A. Stange, S. Willenbrock, 'Weakly Coupled Higgs boson', hep-ph/9602238

19-62 M. Kramer *et al.*, Z. Phys. **C64** (1994) 21.

19-63 E. Richter-Was, 'A first look at the Higgs spin determination with ATLAS', ATLAS Communication ATL-COM-PHYS-99-051 (1999).

19-64 J.F. Gunion and X-G. He, Phys.Rev.Lett.**76** (1996) 4468.

19-65 S. P. Li and M. Sher, Phys. Lett. **140B** (1984) 339;
Y. Okada, M. Yamaguchi and T. Yanagida, Prog. Theor. **85** (1991) 1;
H. E. Haber and R. Hempfling, Phys. Rev. Lett. **66** (1991) 1815;
P. Chankowski, S. Pokorski and J. Rosiek, Phys. Lett. **274B** (1992) 191; and Nucl. Phys. **B423** (1994) 437;
R. Hempfling and A. H. Hoang, Phys. Lett. **331B** (1994) 99;
J. Ellis, G. Ridolfi and F. Zwirner, Phys. Lett **257B** (1991) 83; and Phys. Lett **262B** (1991) 477.

19-66 J. Ellis, G. Ridolfi and F. Zwirner, Phys. Lett. **271B** (1991) 123;
M. Dress and M. Noijiri, Phys. Rev. **D45** (1992) 2482.

19-67 J. Kodaira, Y. Yasui and K. Sasaki, Phys. Rev. **D50** (1994) 7035. J. A. Casas, J.R. Espinosa, M. Quiros and A. Riotto, Nucl. Phys. **B436** (1995) 3.

19-68 M. Carena, J.R. Espinosa, M. Quiros and C.E.M. Wagner, Phys. Lett **355B** (1995) 209.

19-69 I. Dai, J. F. Gunion and R. Vega, Phys. Lett. **B315** (1993) 355. J. F. Gunion and L. Ohr, Phys. Rev. **D46** (1992) 2052; J. F. Gunion, in 'Perspectives on Higgs Physics', edited by G. Kane (World Scientific, Singapore, 1992) and references therein;
J. F. Gunion, R. Bork, H. E. Haber and A. Seiden, Phys. Rev. **D46** (1992) 2040;
J. F. Gunion, H. E. Haber C. Kao, Phys. Rev. **D46** (1992) 2907.

19-70 E. Richter-Was and D. Froidevaux, 'MSSM Higgs bosons in SUGRA model: observability in SM decay modes with ATLAS', ATLAS Communication ATL-COM-98-012 (1998).

19-71 L. Alvarez-Gaume, J. Polchinski, and M.B. Wise, Nucl. Phys. **B221** (1983) 495;
L. Ibanez, Phys. Lett. **118B** (1982) 73;
J. Ellis, D.V. Nanopolous, and K. Tamvakis, Phys. Lett. **121B** (1983) 123; K. Inoue *et al.*, Prog. Theor. Phys. **68** (1982) 927;
A.H. Chamseddine, R. Arnowitt, and P. Nath, Phys. Rev. Lett. **49** (1982) 970

19-72 The CDF Collaboration, W. Yao, 'Top mass at CDF', talk presented at ICHEP 98, Vancouver, B. C. Canada, 23-29 July, 1998.
The D0 Collaboration, B. Abbott *et al.*, Phys. Rev. **D58** (1998) 5201.

19-73 B. Kileng, Z. Phys. **C63** (1994) 87; B. Kileng *et al.*, Z. Phys. **C71 (1996)** 87.

19-74 D. Rainwater, D. Zeppenfeld, Phys. Rev. **D59** (1999) 14037.

19-75 L. Di Lella in [19-130], Vol. II, p.530.

19-76 D. Cavalli *et al.*, 'Search for $H/A \rightarrow \tau\tau$ decays', ATLAS Internal Note ATL-PHYS-94-051 (1994).

19-77 D. Cavalli and S. Resconi, 'Tau-jet separation in ATLAS detector ', ATLAS Internal Note ATL-PHYS-No-98-118 (1998).

19-78 D. Cavalli and S. Resconi, 'Combined Analysis of $A \rightarrow \tau\tau$ Events from Direct and Associated $b\bar{b}A$ Production ', ATLAS Communication ATL-COM-PHYS-99-010 (1999).

19-79 D. Cavalli and P. Bosatelli, 'Combined Analysis of $H/A \rightarrow \mu\mu$ Events from Direct and Associated $b\bar{b}A$ / $b\bar{b}H$ Production', ATLAS Communication, ATL-COM-PHYS-99-053 (1999).

19-80 K.J.F. Gaemers and G. Hoogeveen, Phys Lett. **146B** (1984) 347; D. Dicus, A. Stange and S. Willenbrock, Phys. Lett. **B333** (1994) 126.

19-81 S. Gonzalez de la Hoz, 'MSSM Higgs decay to top quarks', ATLAS Communication ATL-COM-PHYS-99-016 (1999).

19-82 J. Dai, J. F. Gunion and R. Vega, Phys. Lett. **B345** (1995) 29, Phys. Lett **B387** (1996) 801.

19-83 ATLAS Trigger performance Status Report, CERN-LHCC / 98-15 (1998).

19-84 ATLAS Collaboration, Inner Detector Technical Design Report, Volume I, CERN / LHCC / 97-16 (1997).

19-85 ATLAS Collaboration, Pixel Detector Technical Design Report, CERN / LHCC / 98-13 (1998).

19-86 E. Richter-Was and D. Froidevaux, 'MSSM Higgs searches in multi-b-jet final states', ATLAS Internal Note ATL-PHYS-97-104 (1997), published in Z. Phys. **C76** (1997) 665.

19-87 D. Cavalli and M. Sapinski, 'Full and fast simulation and reconstruction of Higgs decay channels with multi-b-jet final states', ATLAS Communication ATL-PHYS-COM-99-033 (1999).

19-88 J. Gunion, H. E. Haber, F. Paige, Wu-ki Tung and S. S. D.Willenbrock, Nucl. Phys. **B294** (1987) 621;
S. Moretti and K. Odagiri, Phys. Rev. **D55** (1997) 5627.

19-89 A. Djouadi, J. Kalinowski and M.P. Zerwas, Z. Phys. **C57** (1993) 569; Z. Phys. **C70** (1996**)** 435.

19-90 D. Cavalli *et al.*, 'Search for $H^{\pm} \rightarrow \tau\nu$ decays', ATLAS Internal Note ATL-PHYS-94-53 (1994).

19-91 UA2 Collaboration, Phys. Lett. **B280** (1992) 137.

19-92 K. Assamagan, 'The Charged Higgs in Hadronic Decays with the ATLAS Detector', ATLAS Communication ATL-COM-PHYS-99-030 (1999).

19-93 R.M. Barnett, H. E. Haber and D. E. Soper, Nucl. Phys **B306** (1988) 697.

19-94 S. Moretti and K. Odagiri, Phys. Rev. **D55** (1997) 55.

19-95 H. Baer, B. W. Harris and X. Tata, Phys. Rev. **D59** (1999) 15003; M. Carena, S. Mrenna and C.E.M. Wagner,' MSSM Higgs boson phenomenology at the Tevatron collider', ANL-HEP-PR-98-54, hep-9808312.

19-96 M. Quiros and J. R. Espinosa, 'What is the upper limit on the lightest supersymmetric Higgs mass?', CERN preprint CERN-TH-98-292 (1998), hep-ph / 9809269.

19-97 V. Mitsou, 'Precision measurements in MSSM with ATLAS', ATLAS Communication ATL-COM-PHYS-99-035 (1999).

19-98 W. Hollik, 29th International Conference on High-Energy Physics (ICHEP 98), Vancouver, British Columbia, Canada, July 23-30, 1998.

19-99 D. Froidevaux *et al.*,'Precision SUSY measurements with ATLAS: Extraction of SUGRA model parameters and conclusions', ATLAS Internal Note ATL-PHYS-97-112 (1997).

19-100 H. Baer, M. Bisset, X. Tata J. Woodside, Phys. Rev. **D46** (1992) 46.

19-101 G.L. Kane, G.D. Kribs, S.P. Martin, J.D. Wells, Phys. Rev. **D50** (1996) 213.

19-102 H. Baer, D. Dicus, M. Drees and X. Tata, Phys. Rev. **D36** (1987) 1363;
K. Griest and H. Haber, Phys. Tev. **D37** (1986) 719;
D. Choudhury, D. P. Roy, Phys. Lett. **B322** (1994) 368;
J. F. Gunion, Phys. Rev. Lett. **72** (1994) 199;
H. Baer, M. Bisset, C. Kao, X. Tata, Phys. Rev. **D50** (1994) 316.

19-103 E. Richter-Was, D. Froidevaux and J. Soderqvist, 'Precision SUSY measurements with ATLAS for SUGRA points 1 and 2', ATLAS Internal Note ATL-PHYS-97-108 (1997).

19-104 G. Polesello, L. Poggioli, E. Richter-Was and J. Soderqvist, 'Precision SUSY measurements with ATLAS for SUGRA point 5', ATLAS Internal Note ATL-PHYS-97-111 (1997).

19-105 J. Erler and D.M. Pierce, Nucl. Phys. **B526** (1998) 53.

19-106 S. Zmushko *et al.*, 'Search for the heavy Higgs in SUGRA point3', ATLAS Communication ATL-COM-PHYS-98-009 (1998).

19-107 F. Paige and Protopopescu, in Supercollider Physics, p.41, editor D. Soper, World Scientific Singapore, 1986.

19-108 I. Hinchliffe et al, 'Precision SUSY Measurements with ATLAS: Introduction and Inclusive Measurements', ATLAS Internal Note ATL-PHYS-97-107; 'Precision SUSY measurements at LHC: Point 3*', ATLAS Internal Note ATL-PHYS-97-109 (1997).

19-109 S. Zmushko et al, 'The $H \rightarrow \chi\chi \rightarrow 4l\ X$ observability with ATLAS (predictions within SUGRA model)', ATLAS Communication ATL-COM-PHYS-99-005 (1999).

19-110 S. Zmushko, D. Froidevaux and L. Poggioli,' $H \rightarrow WW \rightarrow l\nu jj$ and $H \rightarrow ZZ \rightarrow lljj$ Particle level studies', ATLAS Internal Note ATL-PHYS-97-103 (1997).

19-111 V. Mitsou, 'Observability of $h \rightarrow b\bar{b}$ in SUSY cascade in SUGRA parameter space', ATLAS Communication ATL-COM-PHYS-99-036 (1999).

19-112 T. Sjostrand, Comput.Phys.Commun. **82** (1994) 74. The supersymmetry extensions are described in S. Mrenna, Computer Physics Commun. **101** (1997) 232.

19-113 R.S. Chivukula, 'NATO Advanced Study Institute on Quantum Field Theory Since 1970: Perspective and Prospectives', Les Houches, 1998 (hep-ph/9803219).

19-114 R.S. Chivukula *et al.*, 'Strongly coupled electroweak symmetry breaking: implication of models', published in Electroweak Symmetry Breaking and New Physics at the TeV Scale, World Scientific, 2996, hep-ph/9503202;
T. Barklow, ed.; C.P. Yan, 'Proposals for studying TeV $W_L W_L \rightarrow W_L W_L$ interactions experimentaly', hep-ph/9712513,
M. Chanowitz, 'Strong WW scattering at the end of the 90's: theory and experimental prospects', hep-ph/9812215.

19-115 V. Barger, K. Cheung, A. Djouadi, B. A. Kniehl and P. M. Zerwas, Phys.Rev.**D49** (1994) 79.

19-116 S.Weinberg, Physica **96A** (1979) 327; J. Gasser and H. Leutwyler, Ann. of Phys. **158** (1984) 142; Nucl. Phys. **B250** (1985) 465 and 517.

19-117 A. Dobado and M.J. Herrero, Phys. Lett. **B228** (1989) 495 and **B233** (1989) 505; J. Donoghue and C. Ramirez, Phys. Lett. **B234** (1990) 361.

19-118 T. Appelquist and C. Bernard, Phys. Rev. **D22** (1980) 200, A. C. Longhitano, Nucl. Phys. **B188** (1981) 118.

19-119 M. Golden et al, UCD-95-32, hep-ph/9511206.

19-120 Tran N. Truong, Phys. Rev. Lett. **61** (1988) 2526; *ibid* **D67** (1991) 2260.

19-121 A. Dobado, M.J. Herrero and T.N. Truong, Phys.Lett **B235** (1990) 134.

19-122 A. Dobado and J.R. Pelaez, hep-ph/9604416.

19-123 J.R. Pelaez, Phys. Rev. **D55** (1997) 4193.

19-124 A. Miagkov, 'Vector boson scattering in Chiral Lagrangian model', ATLAS Internal Note ATL-PHYS-99-006 (1999).

19-125 V. Barger, K. Cheung, T. Han and R.J.N. Phillips, Phys. Rev. **D42** (1990) 3052.

19-126 J. Bagger *et al.*, Phys. Rev. **D52** (1995) 3878.

19-127 M.S. Chanowitz and W. Kilgore, Phys. Lett. **B322** (1994) 147.

19-128 G. Azuelos, A. Miagkov and R. Mazini, 'Measuring the rate of non-resonant high mass longitudinal gauge boson pairs in ATLAS', ATLAS Communication ATL-COM-PHYS-99-048.

19-129 M.S. Chanowitz, private communication.

19-130 Proceedings of the Large Hadron Collider Workshop, Aachen, 1990, edited by G. Jarlskog and D. Rein, CERN 90-10/ECFA 90-133.